TESIS DE LA UNIVERSIDAD DE ZARAGOZA

2020 13

Elisa Ruiz Chóliz

Ultra-low background Micromegas X-ray detectors for Axion searches in IAXO and BabyIAXO

Departamento
Física Teórica

Director/es
García Irastorza, Igor
Luzon Marco, Gloria

ISSN 2254-7606

Prensas de la Universidad
Universidad Zaragoza

ISSN 2254-7606

Universidad Zaragoza
1542

Tesis Doctoral

ULTRA-LOW BACKGROUND MICROMEGAS X-RAY DETECTORS FOR AXION SEARCHES IN IAXO AND BABYIAXO

Autor

Elisa Ruiz Chóliz

Director/es

García Irastorza, Igor
Luzon Marco, Gloria

UNIVERSIDAD DE ZARAGOZA

Física Teórica

2019

Ultra-low background microbulk Micromegas X-ray detectors for Axion searches in IAXO and BabyIAXO

Memoria presentada por
Elisa Ruiz Chóliz
para optar al grado de doctora en Física

y dirigida por
Igor García Irastorza
Gloria Luzón Marco

Laboratorio de Física Nuclear y Astropartículas
Área de Física Atómica, Molecular y Nuclear
Departamento de Física Teórica
Universidad de Zaragoza

Agosto 2019

Agradecimientos

En primer lugar, quiero agradeceros a mis directores de tesis, Gloria Luzón e Igor G. Irastorza, por darme la oportunidad de realizar la tesis doctoral en el grupo de investigación. Quiero agradeceros vuestra disponibilidad y vuestra paciencia, sobre todo en este último año. Gloria, desde que llegué al departamento has sido un gran apoyo para mi y agradezco mucho tu confianza. Has sido toda una inspiración para mi. Igor, tu dirección durante la tesis y tu profesionalidad y presencia en el mundo de la ciencia ha hecho que me esfuerce al máximo. Te tomo como ejemplo.

No puedo dejar de agradecer a Theopisti Dafni, que has sido como mi tercera directora y la mejor mentora y compañera de laboratorio que podría haber pedido. Te admiro mucho, tanto personal como profesionalmente, y trabajar contigo me ha hecho mejorar como científica. Por supuesto, agradeceros también a Susana Cebrián y a Jose Manuel Carmona por estar disponibles siempre que he necesitado ayuda. También quiero agradecer a Jorge Puimedón, por ser mi tutor en las prácticas de laboratorio y enseñarme el lado divertido de la docencia cuando los alumnos no se han leído el guión.

A Héctor Mirallas, por las aventuras en el laboratorio y los desahogos momentaneos (y por controlar mis horas de sueño). A Juan Castel y a Javier Mena por esos cinco minutos que siempre os pido y luego no son cinco minutos. A Cristina Margalejo por tu trabajo, tus ganas de trabajar, por tu apoyo y por los buenos ratos. A Javier Galán, porque aunque nos quejamos mucho, todos te agradecemos infinitamente tu trabajo con REST. También a Alfonso Ortiz, por echarme una mano siempre que he necesitado ayuda.

Quiero mencionar también a compañeros que acabaron la tesis antes que yo, pero que su trabajo ha sido indispensable para mi. Javier Gracia, tu tesis me ha servido de referente. Juanan García, gracias por enseñarme a moverme por el CERN. Laura Seguí, por ayudarme en mi primer año, cuando estaba verdaderamente perdida, y por tu apoyo durante mi estancia en Saclay. A Francisco Iguaz, por tu disponibilidad, tu ayuda y tu profesionalidad.

Por supuesto, agradecer infinitamente a Esther Ferrer por darme la oportunidad de trabajar contigo en el CEA Saclay, por tu confianza y tu disponibilidad siempre que he necesitado algo. Te admiro y me alegro mucho de haber podido trabajar contigo.

Finally, a huge thank you to my collegues at CERN, that made the CAST shifts actually enjoyable! A special mention to Martyn Davenport for your guidance, and to Madalin Rosu for all your help. Y por supuesto, muchas gracias a Jaime Ruz y Inaki Ortega por los buenos ratos, las barbacoas y los viajes en coche/moto.

En el terreno más personal, no puedo agradecer suficiente el apoyo, el amor y los ánimos a mis padres, Jesús y M. Carmen. Siempre habéis confiado en mi, y no habría llegado hasta aquí sin vosotros. Por supuesto, a Eduardo, mi compañero de viaje y mi support. Grracias por no dejar que me caiga. ¡Y no pueden faltar las frimas! Laura, tu confianza y tu cariño siempre saca lo mejor de mi. Sofi, Sara, Miriam, Marcos, por todo vuestro cariño, ánimo y por creer en mi hasta el infinito (mencion especial a Sara Chóliz por pintar la ilustración de la portada, eres increíble). También, a mi tío Mariano, por animarme a seguir tus pasos en el mundo de la investigación, por tu confianza, apoyo y los buenos consejos. A mi familia en general, por estar siempre ahí. Javi, Maria José, Ana, y la más importante, la yaya Consuelo.

A mis amigos de la carrera que me aseguraron por activa y por pasiva que se sobrevive al doctorado. Muchas gracias, Edu, por tu preocupación y tu apoyo. A Alberto, porque siempre que no voy, me llamas para que vaya. A Alba y a Ana, mis fisichicas, que no se qué haría sin vosotras. A Jorge Jover por tu paciencia y tu ayuda con todo. Jorge Calvo y Pablo, por los cafés que salvan vidas. A Dani, por las cervezas que no solo salvan vidas, sino que arreglan el mundo. Y a Andrés, Carlos y Adrián, por las tardes de rol que algún día volverán.

Y no querría acabar sin mencionar a compañeros que he conocido por los caminos del doctorado y que han dejado huella, como Marina o Nico. Y por supuesto, a Ana Escorza, por estar siempre aunque nos veamos poco. Y a Lena, por tirarme una cuerda siempre que me hace falta.

Contents

Part I

Micromegas detectors: physics and evolution

CHAPTER 1

Phenomenology of particle gaseous detectors

Contents

1.1 Introduction

Gaseous detectors have been broadly used in experimental particle physics since the very first cloud chambers in the early twentieth century, that allowed important discoveries in the field such as the positron or the muon. They have the charm of using very simple phenomenology for the detection processes and the many improvements and new techniques that have been developed during the years puts them in a very central position in the current particle physics scenario.

In this chapter, all the steps involved in the working principle of a particle gaseous detector will be explained: from the production of the charge in the ionization chamber and the various ionization mechanisms, to the properties of the charges moving within the gas, the amplification of the charge and the production of the detectable signal.

1.2 Working principle of a particle gaseous detector

The main concept of a particle gaseous detector is that radiation passing through a gas can ionize its atoms or molecules if the energy delivered by such particle is higher than the ionization potential of the gas. Then, the application of an external electric field in the medium can make the charge pairs that are produced to move within the gas. The result of this process is an electric pulse that can be measured by a readout placed at one of the electrodes.

A typical gaseous detector consists of a gas enclosure, like a chamber, a positive and a negative electrode. The electrodes are raised to a potential difference that creates an electric field (drift field) and allows the charges to move towards the electrodes. The creation and movement of charge pairs perturbs the external electric field and produces current at the electrodes (a detectable signal). The resulting charge, current, or voltage at one of the electrodes can then be measured, which together with proper calibration, gives information about the energy of the initial particle.

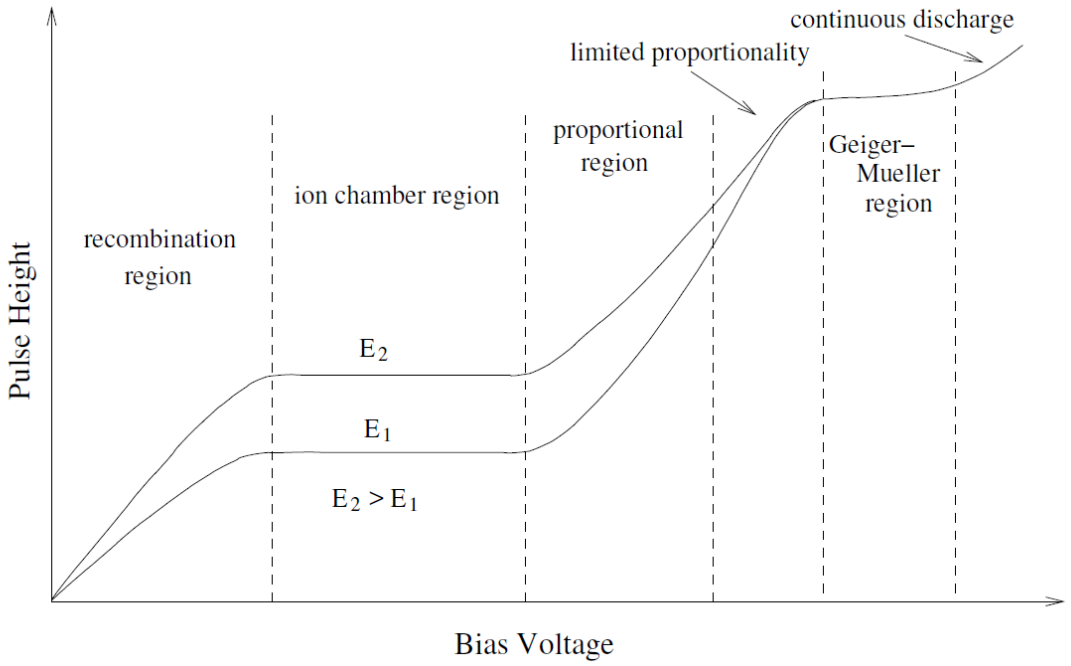

Figure 1.1: Variation of pulse height produced by different types of gaseous detectors with respect to applied voltage. The two curves correspond to two different energies of incident radiation [1].

A gaseous detector shows different regions of operation depending on the applied bias drift voltage, as it is shown in figure 1.1:

- In the absence of an external electric field, the electrons and ions produced by external radiation interacting with the gas are quickly recombined. At low voltages, some of the ions can reach the electrodes. This is the **recombination region**,

and it extends up to a voltage high enough to consider recombination negligible. The output signal at these voltages of operation is not proportional to the incident energy.

- As the voltage increases, the detector enters in the **ion chamber region**, where almost all the charges produced are collected. The current measured is therefore proportional to the energy left by the incident particle.

- Then, the detector enters the **proportional region**, where the charge pairs created have enough energy to produce additional pairs, a process that is called secondary ionization. This multiplication of charges is exploited to increase the amplitude of the output signal while keeping it proportional to the initial energy of the incident particle.

- Once the voltage is high enough to go above this region, the detected charge is no longer proportional to the initial energy of the incident particle, so only counter detectors such as Geiger-Muller detectors can take advantage of these conditions.

The object of study of this work are detectors based on two of these regions: ionization chambers, or Time Projection Chambers [2], for the charge conversion region, working together with Micromegas [3] readouts, that act as the proportional region, or more commonly called, amplification region.

1.3 Ionization in gaseous media: conversion

The first step in the detection process in a gaseous detector is the ionization in the gas itself. In order to detect a particle, it must interact with the detector active gas and transfer energy to the atoms or molecules of the medium. A particle passing through the gas creates excited an ionized particles though a variety of mechanisms along its path. These mechanisms depend on the type of particle and its energy, and they will be described below. In a nutshell, when an ionization occurs, one or more pairs of e^--ion are created, which ultimately is the detectable signal of an ionization detector.

When the e^--ion is created directly by the collision of an incident particle with the molecules of the gas, it is called a primary ionization. If this electron is expelled with enough energy, it can further ionize gas molecules and produce more e^--ion pairs. This process will continue until the energy of the ejected electron is lower than the ionization potential.

The ionization collisions occur randomly along the path of the charged particle, and the number of ionizing collisions follows a Poissonian distribution. This encounters are characterized by the mean free path, i.e., the mean distance between ionization processes, expressed as

$$\lambda = \frac{1}{n\sigma_I}, \tag{1.1}$$

where n is the electron density and σ_I is the effective ionization cross-section for the specific gas.

The practical parameter for experimental purposes is the number of e^--ion pairs N produced along the trajectory of a particle travelling inside the detector gas for a distance x:

$$N = \frac{1}{W}\frac{dE}{dx}x, \tag{1.2}$$

where dE is the absorbed energy by the gas and W is the energy required to produce a e^--ion pair for the particular gas, the so-called W-value. This value is experimentally determined and it is typically higher than the ionization potential due to some energy losses at excitation. Some relevant examples for this work are $W_{Ar} = 26\,\text{eV}$, $W_{Xe} = 22\,\text{eV}$ and $W_{Isobutane} = 26\,\text{eV}$ [4]. If the incident particle looses all its energy E in the interaction, then $N = E/W$. This allows determining the deposited energy of an incident particle that interacted in the detector gas through the number of e^--ion pairs generated.

Finally, since inelastic collisions are probabilistic, two identical charged particles depositing the same energy in the gas will not necessarily produce the exact same number of e^--ion pairs. The number of primary electrons produced in an ionization process will fluctuate according to quasi-Poissonian statistics with a reduced variance of

$$\sigma_N^2 = F\,N, \tag{1.3}$$

where F is the Fano factor. This factor indicates the magnitude of the fluctuation in the number of electrons (the smaller the factor, the smaller the variance), and it depends of the gas mixture and the electron energy.

This factor was first introduced by U. Fano [5] in 1947, and he defined it as

$$F = \frac{1}{N}\left\langle\left(N - \frac{E}{W}\right)^2\right\rangle, \tag{1.4}$$

where the average is carried out over the different collisions. Depending on the energy loss, Fano distinguished between three types of inelastic collisions:

1. if $E < I$, where I is the first ionization potential i.e. a simple excitation (labelled e),
2. if $I \leq E < 2I$, where an electron is ejected but it is incapable of further ionize more atoms (labelled $i1$),
3. if $E \geq 2I$, where an electron is ejected with energy $E - I$ and it is capable of further ionize more atoms in the gas (labelled $i2$).

Under the considerations that the number of ionizations per impact is $N = 0$ in the (e) case, and $N = 1$ in cases $(i1)$ and $(i2)$, and also, that the energy lost by the ionizing

radiation from case ($i2$) is only I, since $E - I$ can be utilized again, then the Fano factor can be written as

$$F = \frac{1}{\sum_j^{i1,i2} \sigma_j} \left(\sum_j^{e} \sigma_j \left(\frac{E_j}{W} \right)^2 + \sum_j^{i1} \sigma_j \left(1 - \frac{E_j}{W} \right)^2 + \sum_j^{i2} \sigma_j \left(1 - \frac{I}{W} \right)^2 \right). \tag{1.5}$$

Some significant examples for this work would be $F_{Ar} = 0.17$ for β particles [6], $F_{Xe} \leq 0.15 \pm 0.03$ for gammas (1.49 keV (K_α Al)) [7] or $F_{Isobutane} = 0.26$ also for gammas (1.49 keV (K_α Al)) [8].

This fluctuation in the number of primary e^--ion pairs is the first contribution to the energy resolution of a gaseous detector. The fact that an atom can only become ionized in a certain number of ways results in a better energy resolution than predicted by purely statistical considerations. The best energy resolution that can be reached will be given by

$$R(\%\text{FWHM}) = 2.35\sqrt{\frac{F\,W}{E}}, \tag{1.6}$$

where R is the *full width half maximum* (or FWHM) resolution. Along this chapter, other terms that affect the energy resolution will be mentioned.

In the following subsections, the main ionization mechanisms from different particles will be addressed.

1.3.1 Ionization mechanisms from heavy charged particles

There are several electronic and nuclear mechanisms through which charged particles can interact with the detector gas and ionize it. However the result of all these interactions is a reduction in the energy of the particles as they pass through the medium. The rate at which a charged particle loses energy as it passes through a material, or the stopping power, depends of the nature of both the incident and the target particles.

Figure 1.2 shows the energy loss dependence on the particle energy. At very low energies, the stopping power is described by the Lindhard approach [9], being proportional to β. Then, the phenomenological equation developed by Andersen and Ziegler [10] describes the stopping power until $\beta\gamma \sim 0.1$ (where $\gamma = 1/\sqrt{1-\beta^2}$). For intermediate energies, $0.1 \lesssim \beta\gamma \lesssim 1000$, the Bethe-Bloch equation [11, 12] is followed, which can be expressed as

$$\left\langle -\frac{dE}{dx} \right\rangle = K\, z^2\, \frac{Z}{A} \frac{1}{\beta^2} \left[\frac{1}{2} ln \left(\frac{2 m_e c^2 \beta^2 \gamma^2 W_{max}}{I^2} \right) - \beta^2 - \frac{\delta(\beta\gamma)}{2} \right], \tag{1.7}$$

where Z is the atomic number, A is the atomic mass, and I is the mean ionization potential of the target material; z is the charge and β is the velocity relative to c of the incident particle ($v = \beta c$); m_e is the electron mass and e is the electron charge; W_{max} is the maximum energy transfer to an electron in a single collision, that for a particle with

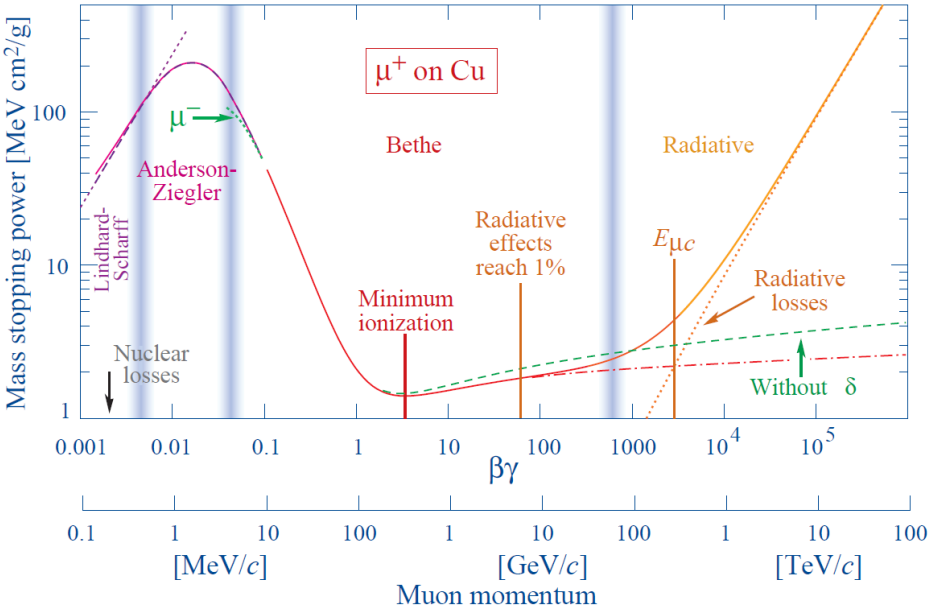

Figure 1.2: Stopping power for positive muons in copper as a function of $\beta\gamma = p/Mc$, from [4]. Solid curves indicate the total stopping power. Vertical bands indicate boundaries between different approximations.

mass M is expressed as

$$W_{max} = \frac{2m_e c^2 \beta^2 \gamma^2}{1 + (2\gamma m_e/M) + (m_e/M)^2}; \tag{1.8}$$

K is a coefficient defined as $K = 4\pi N_A r_e^2 m_e c^2 = 0.307\,\mathrm{MeV\,mol^{-1}\,cm^2}$, where N_A is the Avogadro's number and r_e is the classical electron radius. If this equation is multiplied by the density of the target material, ρ, it expresses the *linear stopping power* in $\mathrm{MeV\,cm^{-1}}$.

This equation shows that the energy loss decreases with the energy of the incoming particle as $1/\beta^2$ until it reaches a minimum, which is the minimum ionization value of the medium. This value is usually around 1-2 $\mathrm{MeV\,g^{-1}\,cm^2}$, and particles with energy close to this minimum are called minimum ionizing particles (MIPs). Then, at higher particle energies, the energy loss increases with energy as $ln(\beta\gamma)$.

This way, the energy loss depends on the material composition and the energy of the particle that travels through it. And although this equation is valid for moderate relativistic charged heavy particles, additional corrections are necessary for the density effect at high energies and shell corrections at very low energies. A more detailed description of such corrections and terms of this equation can be found in [4].

1.3.2 Ionization mechanisms from electrons

If an incident electron interacts with a gas atom with enough energy, it may eject one of its loosely bound electrons (known as δ-rays), resulting in the ionization of the atom. The

energy of the ejected electron depends on the incident electron energy as well as its binding energy. And if the energy of the ejected electron is high enough, it can produce ionization in the same manner in other gas atoms, being able to produce a chain of ionization. This chain will continue until the energy of the ejected electron is lower than the ionization potential of the gas atoms. These δ-rays can potentially leave detectable signals in the detector gas.

Electron collisions have a different behaviour than heavier particles because they happen between identical mass particles. From equation 1.8, the maximum energy transfer in a e^--e^- collision will be $W_{max} = m_e C^2(\gamma - 1)/2$ i.e. half of the entire kinetic energy. Therefore, the energy loss of electrons per unit length in a certain target material, or stopping power, can be written as

$$\left\langle -\frac{dE}{dx} \right\rangle = \frac{1}{2} K \frac{Z}{A} \frac{1}{\beta^2} \left[ln \left(\frac{m_e c^2 \beta^2 \gamma^2 [m_e c^2 (\gamma - 1)/2]}{I^2} \right) + (1 - \beta^2) - \frac{2\gamma - 1}{\gamma^2} ln2 + \frac{1}{8} \left(\frac{\gamma - 1}{\gamma} \right)^2 - \delta \right], \tag{1.9}$$

which is the first moment of the Moeller cross section divided by dx. For a more detailed explanation, see reference [4].

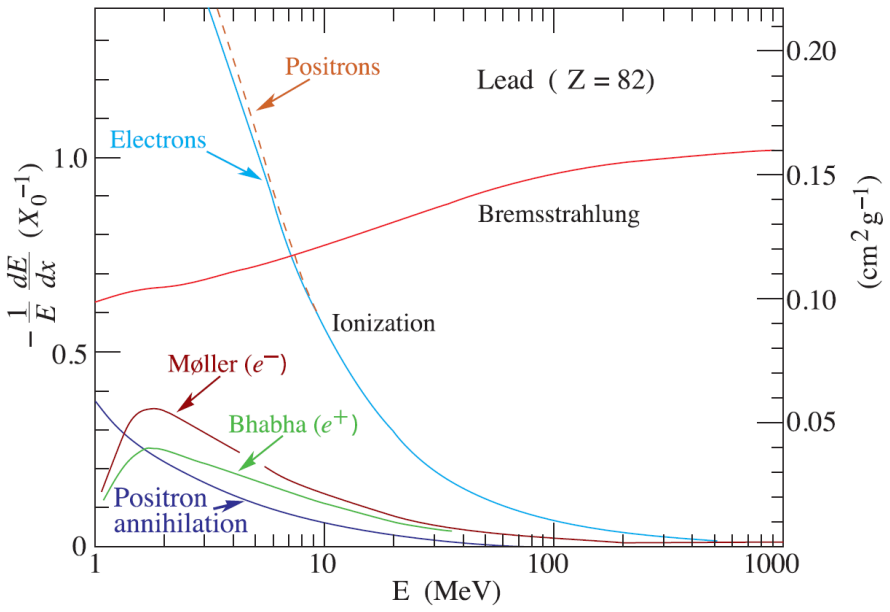

Figure 1.3: Fractional energy loss per radiation length in lead as a function of electron or positron energy [4].

Figure 1.3 shows the stopping power of electrons in lead. The energy loss for low energy electrons (below 10 MeV) is dominated by ionization, where also e^--e^- (and e^--e^+) scattering processes can occur (Møeller and Bhabha scattering respectively). On the other hand, the energy loss of high energy electrons (above 10 MeV) is dominated by radiative interactions called Bremsstrahlung. It is a process that refers to the emission of radiation when a charged particle accelerates in a material. In this interaction an incoming electron

can be deflected in the electric field of a nucleus and a portion of the kinetic energy of the electron is converted into a photon that can ionize the gas.

The point where the ionization and Bremsstrahlung energy losses meets is called the critical energy, that can is parametrized [4] as:

$$E_c \simeq \frac{a}{Z+b}\, MeV, \tag{1.10}$$

where for solid materials, $a = 610$ and $b = 1.24$; and for gases, $a = 710$ and $b = 0.92$. A relevant example for this work would be the critical energy in argon, which is around $\sim$37 MeV.

1.3.3 Ionization mechanisms from photons

In contrast with charged particles, photons can travel some considerable distances through a material without interacting. And when photons interact with matter, it leads to a partial or total energy transfer to the medium. The photon interaction probability with matter is usually parametrized by the intensity $I(x)$ of a beam of photons of a given energy after crossing a material with a thickness x, by the expression

$$I(x) = I_0\, e^{-\mu\,\rho\,x}, \tag{1.11}$$

where I_0 is the intensity of the beam before crossing the material, ρ is the density of the material and μ is the mass attenuation coefficient (in $\mathrm{cm^2\,g^{-1}}$), which is related with the mean free path as $\lambda = 1/(\mu\,\rho)$.

Photons interact with matter mainly by three processes: photoelectric effect, Compton scattering, and pair production. The probability for the photon to interact in one of these ways is defined by the specific interaction cross-section, and it depends of the energy of the photon and the atomic number of the target material. A relevant example for this work is shown in figure 1.4, where the photon interaction cross-sections of the different possible processes are shown for argon.

At low energies, the dominant process is the photoelectric effect. Then, at $\sim$100 keV, the Compton scattering process becomes the most probable one, and finally, pair production mechanism starts to be the most important at energies around $\sim$10 MeV. From these processes, only photoelectric and Compton scattering are relevant for detection purposes in gaseous detectors for low energy physics. Pair production has a very low cross-section with electrons, so this process is not significant.

The **photoelectric effect** consist of the absorption of an incoming photon of energy E_γ by an atom that becomes unstable. Then, this atom emits an electron from its atomic shells to recover the stable state. This process is allowed if E_γ is greater than the binding energy of the most external electron of the atom, E_{shell}, and this electron (or photoelectron) will escape the atom with a kinetic energy E_e of

$$E_e = E_\gamma - E_{shell}. \tag{1.12}$$

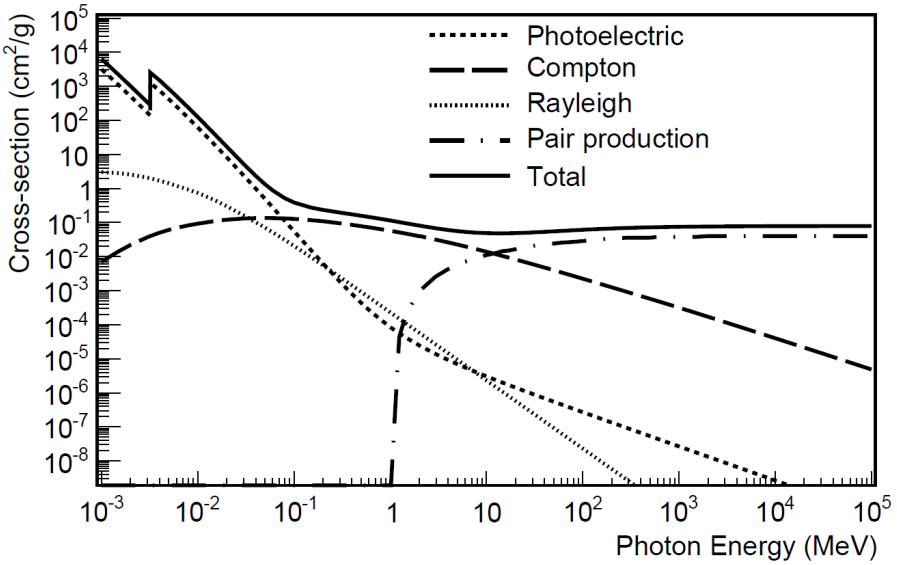

Figure 1.4: Interaction cross-sections of the photon in an argon medium as a function of its energy [13]. An increase in the photoelectric cross-section is observed at 3.19 keV because the electrons of the argon k-shell become available for this process.

When the energy of an incident photon is higher than the binding energy of one atomic shell, the electrons of that shell become available for the photoelectric effect. This results in a sharp increase in the photoelectric cross-section, what is known as shell edges: K-edge, L-edge, M-edge, etc. An example of this edge can be seen in figure 1.4 at energies around 3.19 keV for argon, that is the binding energy of its K-shell.

This way, the cross-section of the photoelectric effect is the sum of all the contributions of the allowed atomic shells for the specific energy of the incoming photon. This cross-section is highly dependent on the atomic number Z of the material, increasing with the electron density of the medium. This is why gaseous detectors are usually operated with noble high-Z gases like argon or xenon, and small quantities of other organic low-Z gases do not have a significant impact (they are known as *quencher* gases, and their role in gaseous detectors will be explained in section 1.4). In addition, the cross-section has a strong inverse relationship with the incident photon:

$$\sigma_{photoelectric} \propto \frac{Z^n}{E_\gamma^{3.5}}, \tag{1.13}$$

where n is a parameter that lies between 4 and 5.

After the emission of the photoelectron, a vacancy is created in the corresponding atomic shell. There are two main mechanisms for the excited atom to fill this vacancy that will result in secondary emissions:

- the emission of a **fluorescence x-ray**: the vacancy is filled by an outer shell electron, and a photon is emitted with an energy equal to the electronic levels energy difference. This emitted photon is in the x-ray energy range and it can interact in

the gaseous detection medium and produce a detectable signal. This x-ray can also escape from the gas without interacting, and this will translate into a *escape peak* in the detected energy spectrum for energies of $E_\gamma - E_{shell}$.

- the emission of an **Auger electron**: the vacancy is also filled by an outer shell electron, but in this case the energy difference between the atomic levels is transferred to an electron of the same atom. Then, if this energy is larger than the binding energy of the atom, this electron will be ejected to the gaseous detection medium where it can start an ionization process and therefore, produce a detectable signal.

These transitions can occur several times from one single initial excitation due to the vacancies left by the electrons, so they can result in more than one secondary emission. To illustrate these processes with an example, figure 1.5 shows a typical ^{55}Fe spectrum measured with a Micromegas detector in the energy range of [0,10] keV. The ^{55}Fe source emits mainly an x-ray of 5.9 keV, which is the main contribution to the energy spectrum. If these photons interact with the argon atoms by photoelectric effect, the atoms will relax by emitting either a 3.2 keV Auger electron or a 3.2 keV fluorescence x-ray, which can either ionize or escape the gas. The last case will be registered in the energy spectrum as an escape peak.

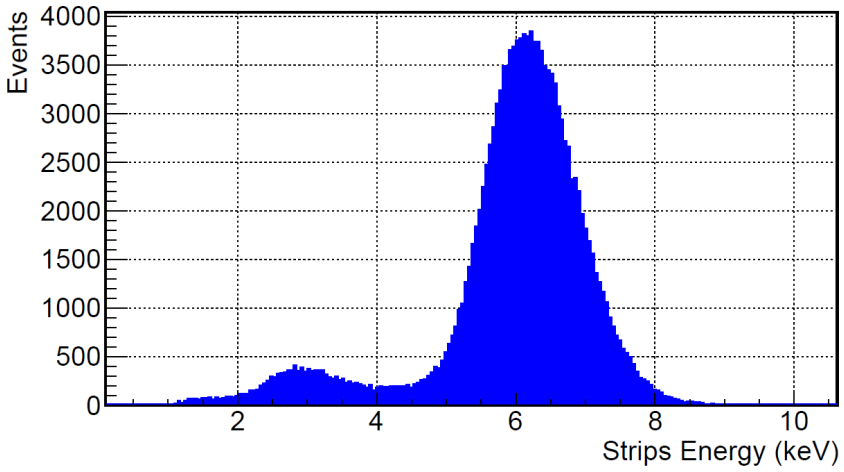

Figure 1.5: A typical ^{55}Fe calibration spectrum measured by a CAST-Micromegas detector (CAST-M18) [14]. The main x-ray peak from the source appears at 5.9 keV, as well as the escape peak at 2.7 keV.

On the other hand, the **Compton scattering** is a process where a photon is not absorbed but scattered by an electron. At the energies where the Compton scattering is dominant, the atomic binding energies are of the order of a few hundred eV, so the electrons are considered to be free in the medium and they may also get scattered in the process. In this interaction, the scattered photon transfers part of its energy to the atomic electron. From simple energy and linear momentum conservation laws, the relation between the wavelengths of incident photon, λ, and the scattered photon, λ_0, can

be deduced as

$$\lambda = \lambda_0 + \frac{h}{m_e c}[1 - cos\theta], \tag{1.14}$$

where h is the Plank constant, m_e is the electron rest energy and θ is the angle between the incident and scattered photons. The maximum energy transfer to the electron occurs when $\theta = 180\,\text{deg}$, producing the characteristic Compton edge in the energy spectra of gamma rays sources, and other scattering angles contribute to the rest of the Compton continuum. Low energy transfers to electrons via Compton scattering are relatively common and can have an important contribution to the background at low energies.

The differential cross-section of the Compton scattering is described by the Klein-Nishina [15] equation,

$$\frac{d\sigma_{Compton}}{d\Omega} = \frac{r_e^2}{2}\left[\frac{1 - cos^2\theta}{(1 + \alpha(1 - cos\theta))^2}\right]\left[1 + \frac{4\alpha^2 sen^4(\theta/2)}{(1 + \cos^2\theta)(1 + \alpha(1 - cos\theta))}\right], \tag{1.15}$$

where r_e is the classical electron radius, $\alpha = h\nu/m_e c^2$ and ν the frecuency of the incident photon.

In the classical limit for incident photons with low energy, the cross section becomes independent of this energy and equal to the Thompson cross section. Another coherent scattering is the Rayleigh scattering, which occurs when the wavelength of the incident photon is larger than the target atomic radius. In these coherent processes, the energy transfer to the atoms of the gas medium is negligible so they have no interest for particle detection.

1.3.4 Ionization mechanisms from non-charged particles

Chargeless particles like neutrons or the hypothetical WIMPs[1] are not be affected by the electric field of the atoms, but if they pass near the nuclei of the detector, they can interact with them via several processes, such as elastic and inelastic scattering, spallation, transmutation or radiative capture. As a secondary effect, some these processes can produce charged particles that are able to trigger ionization in the gas. The main processes by which a neutron can interact with nuclei are listed below.

- **Elastic scattering**: it is the neutron's principal mode of interaction with matter, where the target nucleus remains in the same state and the total kinetic energy of the neutron is conserved, so no extra particles are emitted.
- **Inellastic scattering**: in this process, the incoming neutron is absorbed by the nucleus forming an unstable compound, that quickly emits another neutron with a lower kinetic energy. The nucleus is left in an excited state, and some γ-decays can happen until it returns to the ground state.

[1] WIMPs, or Weakly Interacting Massive Particles, are hypothetical candidates to the dark matter of the universe.

- **Transmutation**: it is a reaction where an element captures a slow neutron and as a result, it changes into another element, emitting α or β particles in the process.

- **Radiative capture:** it is another common process for neutrons, where a nucleus absorbs it and becomes excited. To relax, the nucleus emits γ-rays. In this case, no transmutation occurs, but the element becomes a different isotope.

- **Spallation:** this process consist of the fragmentation of a nucleus into several parts due to the collision of a high energy neutron, such as the neutrons that come from cosmic rays.

- **Fission:** in this process, a slow neutron is captured by a heavy nucleus, which splits up in fragments emitting several neutrons and photons.

These non-charged particles interact mainly through the strong nuclear force because they can get very close to the nucleus of the atoms. Also, due to their neutrality, they do not loose their energy through electromagnetic interactions, so they can penetrate deeper into the material, although some attenuation is expected. The intensity of a neutron beam that travels a distance x through a certain material can be written as

$$I = I_0\, e^{-\mu_n x}, \tag{1.16}$$

where μ_n is the attenuation coefficient, that can be expressed as the inverse of the mean free path, λ_n, or in terms of the total nuclear cross-section,

$$\mu_n = N\sigma_{n,t} \tag{1.17}$$

where $\sigma_{n,t}$ is the sum of all the cross-sections of the possible processes described above, and N is the number density of the nuclei in the material.

1.4 Transport of electrons: drift

Once the gas has been ionized and the primary charges have been created, the free electrons find a medium with an electric field that avoid the e^--ion pair to recombine. Instead, electrons drift towards the anode, where the readout of the detector is placed, and the ion moves towards the cathode. In this type of detectors, the ions are not involved in the signal generation, so they will not be considered.

In this section, the drift of the electrons through the gas along with the physical processes that occurs and their properties will be explained. Since the analytical calculation of the properties of the drifting electrons in a gas is rather complex due to the quantum-mechanics processes involved in the collisions, a Monte Carlo simulation software called Magboltz [16] is commonly used for this purpose.

1.4.1 Drift velocity

The electrons and ions produced in a gas move randomly and are scattered by collisions with the gas molecules. In the absence of an external electric field, the free electrons in the gas scatter isotropically with the gas atoms or molecules with a mean instantaneous velocity u. But when an electric field is applied, the electrons are accelerated towards the anode. They are considered to move at a constant velocity during the drift because the acceleration due to the electric field is compensated by the collisions with the gas atoms, that slow down the electron. The resulting mean drift velocity v_d has been deduced in [17], and it is

$$v_d = \frac{e\,\tau}{m_e}\,E, \tag{1.18}$$

where e and m_e are the charge and mass of the electron, E is the value of the electric field and $\tau(E) = 1/(N\,\sigma_s\,u)$ is the mean time between collisions. This time is determined by the molecular density of the gas, N, the scattering cross-section, σ_s, and the mean instantaneous velocity, u. Since the drift velocity depends on the molecular density of the gas, it will change with the gas pressure.

The drift velocity of the electrons depends on the scattering cross-section of the gas (as seen in equation 1.18). The direction of the trajectory of the electron can change after a collision, due to the mass ratio between electrons and gas molecules. If the scattering is elastic, the fraction of energy loss per collision will be rather small. This is desirable because the primary charges are the responsible of producing the detectable signal. But if all the collisions are elastic, the trajectory of the electrons inside the gas will be very erratic and less efficient, translating into a slower drift velocity. On the other hand, if the scattering is inelastic, the energy loss will be bigger, which will minimize the deviations caused by the scattering and the electric field energy is invested in driving the charges only in the drift direction. However, inelastic collisions have the risk of reducing too much the energy of the primary charges so the gas molecule can capture it (known as attachment, and explained in subsection 1.4.3).

Particle gaseous detectors usually use noble gases as their active medium because they have simple molecular structures, they are very unlikely to absorb an electron, and they have low cross sections allowing long mean free paths. But on the other hand, inelastic collisions at low energies with electrons are not possible, so the main scattering process for electrons in a noble gas are elastic collisions, which is not ideal for a good drift velocity.

To improve the drift velocity of noble gases, they can be mixed with small quantities of another gas, called *quencher*. These are usually organic molecular gases such as CF_4, Trimethylamine (TMA) or Isobutane (C_4H_{10}), whose rotational or vibrational modes can be activated at energies much lower than the electronic excitation energies. This translates into a relatively high energy loss for the electron and therefore, an improvement of the drift velocity. Figure 1.6 shows the drift velocity of different argon based quenching gas mixtures for different electric field values.

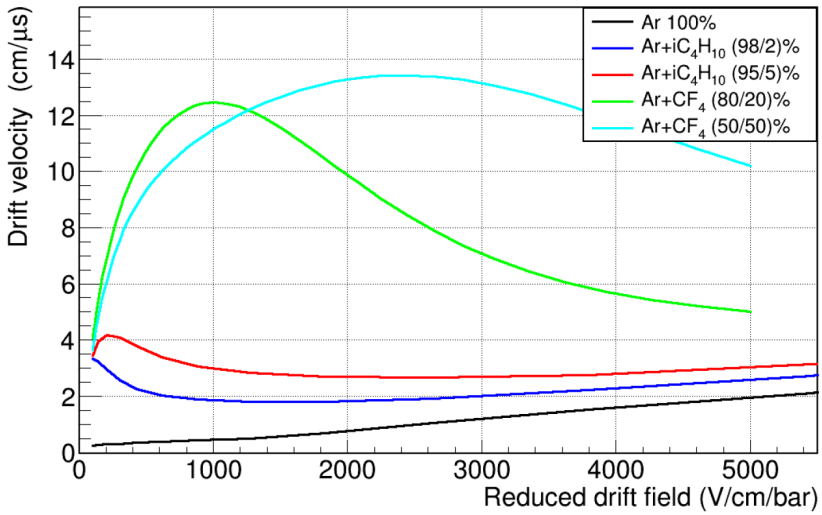

Figure 1.6: Dependence of the drift velocity of electrons with the reduced drift field for different argon based mixtures (obtained with Magboltz [16]).

1.4.2 Diffusion

Along the drift within the electric field, the electrons are deviated from its desirable trajectory due to collisions with the gas atoms or molecules. This phenomenon is called diffusion and it may affect the topological information of the gaseous detector.

In the absence of an external electric field, the diffusion is isotropic, so a point-like collection of free electrons will spread around the original point following a Gaussian spatial distribution, whose width will increase with time. This spread can be described for any direction as the number of charges dN that can be found in a differential element dx at a distance x from the center of the initial charge distribution after a time t as

$$dN = \frac{N}{\sqrt{4\pi\, D\, t}} \exp\left(\frac{-x^2}{4\, D\, t}\right) dx, \tag{1.19}$$

where D is known as a *diffusion coefficient*, and it is related to the standard deviation of the Gaussian distribution, σ, through

$$\sigma = \sqrt{2\, D\, t}. \tag{1.20}$$

In the presence of an electric field, the diffusion is no longer isotropic but a tensor with two non-zero components: a longitudinal component, D_L, in the direction of the drift electric field; and a transversal one, D_T, orthogonal to the drift electric field. With this consideration, the number of charges will be parametrized by

$$n(x,y,z,t) = N \left(\frac{1}{\sqrt{4\pi\, D_T\, t}}\right)^2 \left(\frac{1}{\sqrt{4\pi\, D_L\, t}}\right) \exp\left(\frac{-(x+y)^2}{4\, D_T\, t} - \frac{-(z+v_d\, t)^2}{4\, D_L\, t}\right). \tag{1.21}$$

The diffusion coefficients are usually expressed in units of $\mu\mathrm{m\,cm}^{-1/2}$ and can be determined by the spread of the electron cloud after a given drift length. A highly pixelized

readout allows measuring the mean squared deviation of the transversal diffusion, while the longitudinal one can be determined from the measurement of the drift velocity and the spread of arrival times of primary charges.

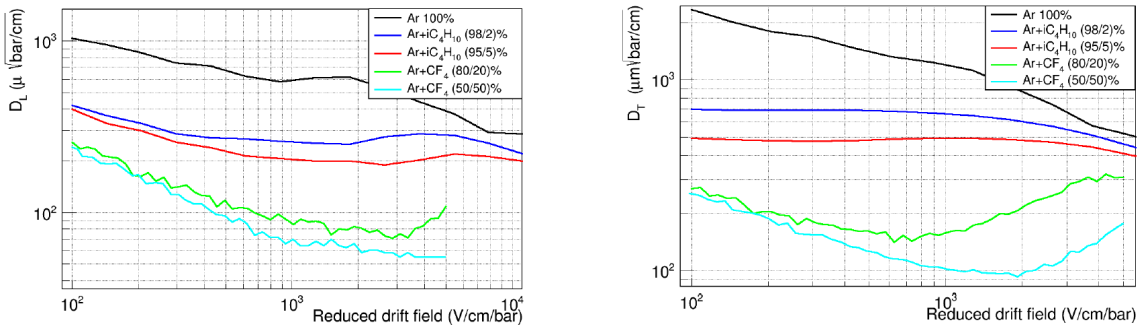

Figure 1.7: Dependence of the longitudinal **(left)** and transversal **(right)** diffusion coefficients with the reduced drift field for different argon based mixtures (obtained with Magboltz [16]).

Figure 1.7 shows examples of the diffusion coefficients of different argon based gas mixtures. In general, the longitudinal component is smaller than the transversal one, and the addition of a quencher to the target gas reduces the diffusion coefficients, as it was explained for the drift field.

1.4.3 Charge reduction

There are some processes that occur in the gas and reduce the number of the electrons produced by the primary emission, therefore modifying the final charge that will be measured by the readout. This could affect the detector performance and has to be taken into account. The main known processes that affect the final charge of the event in a gaseous detector are recombination and attachment.

Recombination refers to the process when the drift electrons meet the positive ions that are drifting in the opposite sense. This process implies a decrease in the number density of e^--ion pairs along a drift distance and depends of the number of charge carriers, n^+ and n^-, and of the so called recombination coefficient, p_r:

$$\frac{dn}{dt} = p_r\, n^+\, n^-. \tag{1.22}$$

Usually, the p_r coefficient is of the order of $\sim 10^{-7}\,\mathrm{cm}^{-3}\,\mathrm{s}^{-1}$. This process tends to increase with the e^--ion pair concentration, so the recombination rates of pure noble gases are usually higher than other gases [18]. However, this effect is strongly reduced by applying an electric field at the medium, so it is not usually very relevant. A deep study of the recombination in xenon+TMA mixture can be found in [19].

On the other hand, **attachment** is the absorption of the electron by a molecule present in the gas during the drift. All the molecules have a certain attachment cross-section, (the lowest correspond to noble gases), but attachment is generically caused by impurities with high electron affinity, specially air and water. A summary of the different attachment mechanisms can be found in [20].

Electron attachment can be reduced by minimizing the leaks of the gas system of the experiment and the outgassing[2] components inside it. A continuous flow of clean gas is also desirable, as well as pumping of the detector chamber.

1.5 Charge multiplication: avalanche

Inside a strong enough electric field ($\sim$kV cm^{-1}), electrons are accelerated and they are able to ionize more atoms along their way. As a result, a chain reaction of e$^-$-ion pairs production is triggered. This process is commonly called *electron avalanche*, and the number of charges dn produced after a certain distance dx can be parametrized as

$$dn = n(x)\alpha(E(x))\,dx, \tag{1.23}$$

where $n(x)$ is the final number of charges after the avalanche and α is the Townsend coefficient, that represents the number of collisions that will create a e$^-$-ion pair per unit length at a specific electric field $E(x)$. It can be expressed as $\alpha = \lambda^{-1}$, where λ is the mean free path of the electron. Figure 1.8 shows the dependence of the Townsed coefficient with the electric field for argon and some argon based mixtures.

Amplification regions with high electric fields are implemented in gaseous detectors to amplify the single electron charges that are formed in the ionization region, so they can produce a detectable signal. The amplification, or gain factor G, is defined as the number of ionizations created by a single electron in its path between two points, x_1 and x_2, as

$$G = \frac{n}{n_0} = \exp\left(\int_{x_2}^{x_1} \alpha(E(x))\,dx\right). \tag{1.24}$$

If the electric field is uniform, the Townsend coefficient will be constant, and the gain will simply be

$$G = \frac{n}{n_0} = e^{\alpha\, x}. \tag{1.25}$$

There exists a limit in the amplification factor due to an effect called *space charge*: the charges in the amplification region can modify the electric field in such a way that multiplication saturates, what is commonly called a *spark*. This happens at values of $G \sim 10^8$ (known as the Raether limit [22]), which corresponds to $\alpha\, x \sim 20$. The goal of any detector is to achieve a high enough gain at an stable operation point before this

[2]Outgassing is the release of a gas that has been dissolved, trapped, frozen, or absorbed in some material.

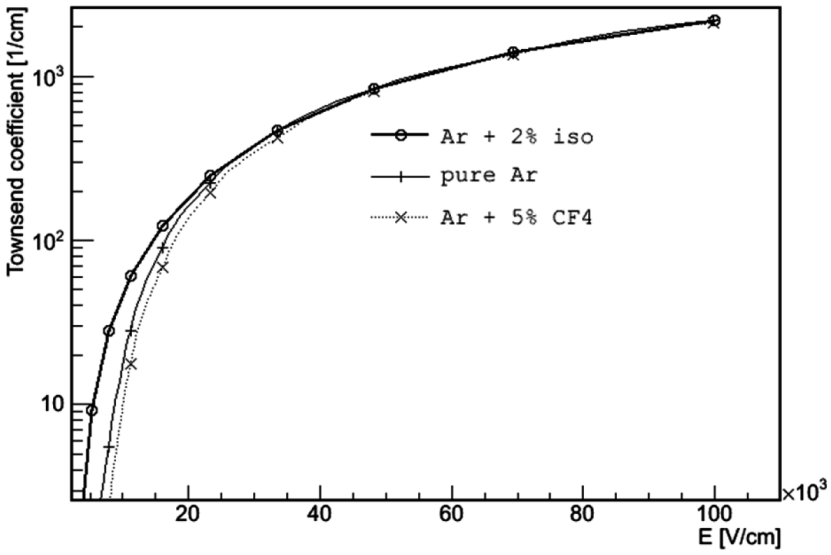

Figure 1.8: Townsend coefficient as a function of the electric field for pure argon and argon mixtures with two quencher gases (obtained with Magboltz [16], adapted from [21]).

spark breakdown. In the practice, the operation point is usually around four orders of magnitude less than the Raether limit, mainly due to imperfections in the anode or the absorption of secondary photons by the quencher gas.

The number of final electrons after the avalanche can fluctuate and affect the precision of the measurements of the detector. These fluctuations can be parametrized analytically [23] as a Polya distribution, b, that decreases with the electric field through a dependence $\alpha(E(x))x_0$ (where x_0 is the distance that an electron with an initial energy $\sim$0 has to travel before being able to ionize the gas). This parametrization typically assumes values between 0.2-0.9 in most gases operated at 20-100 kV cm^{-}1. The consequent fluctuation will affect to the energy resolution convoluted with the Fano factor, F, as

$$R(\%FWHM) = 2.35\sqrt{\frac{W}{E}(F+b)}. \tag{1.26}$$

Besides the statistical fluctuations, some other geometrical and operational parameters can influence the avalanche process and worsen the energy resolution, such as electronic noise, attachment, electron transmission from the conversion to the amplification regions, geometrical imperfections or space charge effect at high particle rates.

1.6 Signal generation

The e^{-}-ion pairs generated in the amplification region by the avalanche process will drift towards the corresponding electrodes, and this movement of the charges within the electric

field will generate current, i.e. a signal, in the electrodes. The instantaneous electric current $i(t)$ generated by a moving charge q near to an electrode is obtained by the theorem of Shockley-Ramo [24, 25]:

$$i(t) = q\,\overrightarrow{v}(t) \cdot \overrightarrow{E_w}, \tag{1.27}$$

where $\overrightarrow{v}(t)$ is the velocity of the moving charge and $\overrightarrow{E_w}$ is the weighted electric field, which is defined as the electric field at the instantaneous position of the charge, calculated with the condition that the electrode is at 1 V and the other electrodes are grounded.

The current induced in an electrode depends of the velocity of the charge. Since electrons are around 10^3 times faster than ions, they will induce signals with different characteristic times. However, the total charge generated in the electrode is the same for both, and can be expressed as $Q = \int_0^t i(t)dt$.

CHAPTER 2

TPC-Micromegas detectors for rare event searches

Contents

2.1 Introduction

The Rare Event Searches experiments are defined by the fact that they try to measure very unlikely phenomena for which very low detection rate is expected. It is an heterogeneous field containing experiments from high energy physics and astroparticle physics to nuclear physics. In this context, gaseous detectors are widely used and their evolution in the last century has been exponential from the first Geiger and Rutherford's single wire proportional counters [26], Geiger-Muller counters [27] and imaging detectors like cloud chambers [28]. One important milestone for instrumentation in such experiments happened in 1968 when G. Charpak invented the Multi Wire Propotional Chamber (MWPC) [29], that consisted of a gaseous chamber with an anode plane made of parallel closely-spaced wires, acting as independent proportional counters. This allowed reconstructing the two-dimensional trajectory of the particles that interacted in the gas.

Then, a new generation of detectors started to develop in order to obtain the position along the field direction using a drift chamber [17], with the idea of measuring the creation time of the primary electrons. With this concept, the Time Projection Chamber (TPC) [2] was designed by D. R. Nygren and J. N. Marx in 1978, which combines the two-dimensional positioning provided by the MWPCs and the temporal information of the drift chamber.

Another important milestone was reached in 1988, when A. Oed developed the

Micro Strip Gas Counters (MSGC) [30], which consisted of alternating cathode and anode strips printed on an insulating support with an electric field high enough to produce electron multiplication. This detector was the first of a new kind of readouts for gaseous detectors known as Micropattern Gaseous Detectors (MPGDs), with readouts implemented by means of printed-circuit-board (PCB) techniques. Nowadays, their combination with TPCs is widely spread along the experiments of rare event searches such as dark matter, high energy physics at colliders or neutrino physics.

Among the MPGDs, the MICRO MEsh GAseous Structure (Micromegas) [3] stands out in terms of gain and energy resolution. It was first introduced by J. P. Robert, Y. Giomataris, P. Rebourgeard and G. Charpak in 1996, and it meant another step in the readouts evolution. They implemented a near-parallel planes geometry to the electrode, which allowed both obtaining a constant amplification field in the amplification region, and also decoupling the drift and amplification regions, so independent electric fields could be applied to each region.

In this chapter, the detection concept of a TPC and its integration with a Micromegas readout will be explained. Then, the most relevant Micromegas designs, their manufacturing processes and their main features will be detailed.

2.2 Time projection chambers

The main idea behind a gaseous TPC is to define a rather long drift distance volume where a constant electric field is applied. The electrons produced by incident particles in the gas volume will follow the electrical field lines towards a readout plane, for example, a Micromegas. The electrodes can be placed at opposite sides of the volume, so only one readout plane is used, or alternatively, the cathode can be placed at the middle of the volume, creating two different drift regions with the possibility of using two readouts, one at each side of the volume.

If a segmented readout is placed at the anode (wired or pixelised), the two-dimensional topological information of the event that occurred in the gas can be obtained. On the other hand, the TPC provides temporal information from the drift time measurement, which will be total or relative depending on whether or not an extra detector is used to correlate the signals with the e^--ion pairs.

The gas or gas mixture used in the drift volume has to be carefully chosen to fulfil all the requirements discussed in the previous chapter in terms of drift velocity, diffusion and attachment. Usually, external gas systems are designed to provide a constant flow of clean gas to reduce the contaminants and optimize the detector performance. Also, it is important that the external electric field (usually 10^2-$10^3\,\mathrm{V\,cm^{-1}}$) is uniform and constant to assure a constant drift velocity of the charges. Internal field cages or shapers are implemented for this purpose.

Figure 2.1 shows a conceptual scheme of the detection concept of a TPC. In this

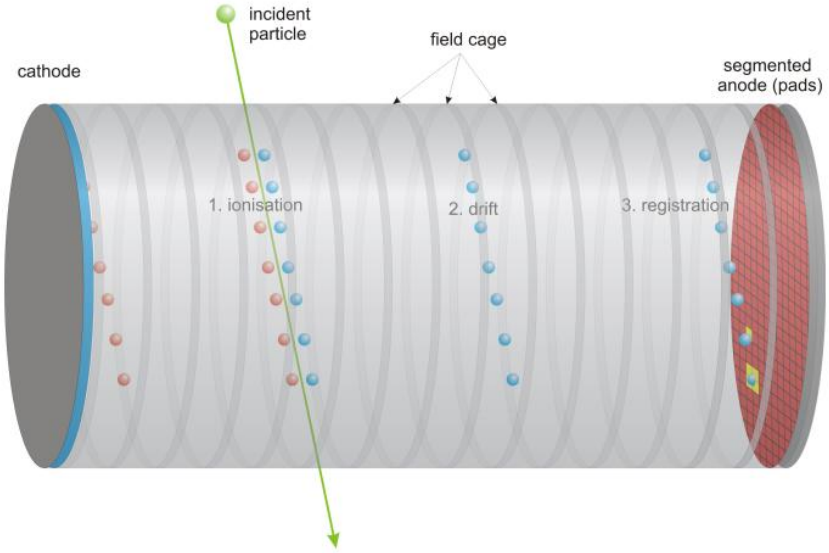

Figure 2.1: Working principle of a TPC (image from [31]). Incident particles enter in the chamber and ionize the gas molecules producing e^--ion pairs that drift towards the electrodes due to an external electric field. The charge is collected at the segmented anode and a signal is produced.

part of the detector the two first steps of the detection process happen: the ionization of the medium by an incident particle and the drift of the produced electrons towards the segmented anode. The two next steps, that are the amplification of the charge at the production of the signal occur in the actual segmented anode, which in the context of this work, it is a Micromegas readout.

2.3 Micromegas readouts

A Micromegas [3, 32] is a gaseous parallel plate detector where two parallel electrodes form a narrow amplification space, typically ∼50-100 μm, for charge multiplication. The cathode is made out of a thin metallic micro-mesh of a few microns thick, while the anode consist of micro-elements (strips, pads or pixels) of a conductor material printed on an insulator board. The separation between the cathode and the anode is done by means of insulating pillars deposited by standard photographic methods, covering a small part of the total readout surface (∼1%).

Usually, Micromegas are used as segmented anodes in TPCs, where the cathode of the chamber is placed parallel to the Micromegas mesh. Comprehensive schemes of a Micromegas+TPC detector are shown in figure 2.2. When electrons are released in the gas chamber by any ionization mechanism, they drift towards the mesh and they enter the amplification gap thanks to the shape of the field lines. There, they are multiplied in an avalanche process, resulting in a large number of e^--ion pairs that induce signals on the anode elements and on the cathode mesh respectively. A simulation of the field lines at the vicinity of the Micromegas mesh is shown in figure 2.3. The big difference

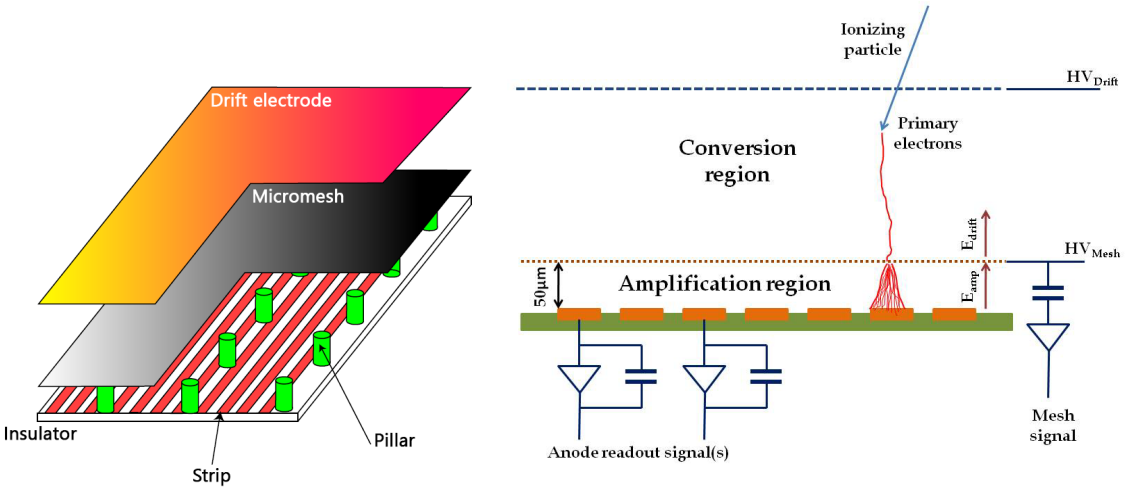

Figure 2.2: **(Lefft)** Scheme of a Micromegas detector design. A metallic cathode micromesh is suspended over a segmented readout anode by means of insulating pillars, creating an amplification region. Electrons are injected to this region from a conversion region above, defined by a third electrode. **(Right)** Scheme of the working principle of a gaseous Micromegas detector in a TPC. Particles ionize the gas in the conversion region and the electrons drift towards the anode due to an electric field. The electrons enter into the amplification region through the Micromegas mesh holes, where they are amplified due to the high electric field and finally, they produce a signal.

between amplification field (usually 10^4-10^3 V cm^{-1}) and drift field allows a high electron transmission from the conversion to the amplification region and a fast evacuation of the ions, avoiding charge space effect that could produce gain fluctuations in high rate environments.

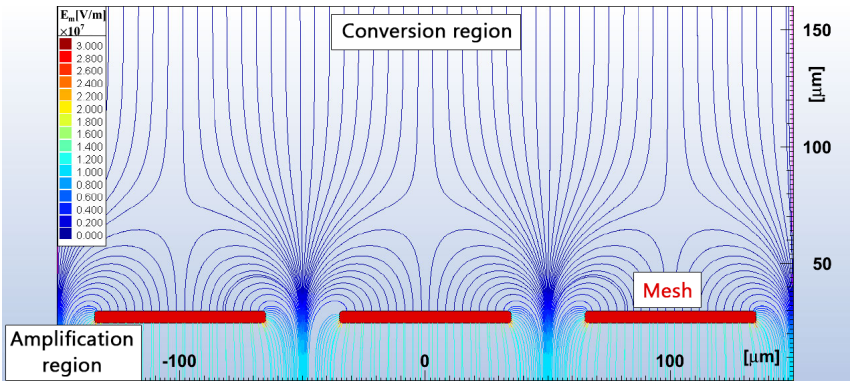

Figure 2.3: Field line simulation of a 25 μm amplification gap Micromegas detector. The field lines make the electrons produced in the conversion region to pass through the holes of the mesh to the amplification region. Image adapted from [33].

Micromegas detectors are being used in many experiments for different purposes, such as axion searches in CAST [34]; WIMP direct searches in TREX-DM [35]; neutrinoless double beta decay detection in PANDAX [36]; neutrino oscilations in T2K [37]; muon tracking in ATLAS [38]; particle tracking in COMPASS [39], NA48 [40] or CLAS12 [41]; or neutron physics in n-TOF [42]. Last but not least, Micromegas are the

main proposed detectors for the new IAXO axion observatory [43].

2.3.1 Micromegas designs and manufacture

The first Micromegas designs had the micro-mesh and the anode plane built separately over supporting frames. The anode consisted of gold-coated strips over an insulating substrate (PCB). Then, photolithographic techniques were applied to a photoresist film to form the insulating pillars, that were glued to a frame and mounted on the anode surface. Also, an electroformed[1] nickel micro-mesh was made and then glued on a supporting frame, which then was screwed to the anode frame. Finally, voltage was applied to the micro-mesh to stretch it over the insulating pillars, thus completing the fabrication process.

Later designs of Micromegas detectors took advantage of the photochemical etching mechanism to develop the insulating pillars directly on top of the micro-mesh [44]. Photoresisitive film was applied to both sides of copper clad kapton foils supported by a frame, and two different masks were used to set different designs on each side: a micro-mesh mask for the copper side and the pillars pattern for the kapton side. After the mask designs were set by photolithography, the coper-clad-kapton foil was chemically etched and it was mounted on top of the anode plate.

The main disadvantage of these techniques was the final attachment of the two parts that were built separately, which required a considerable skill and expertise to obtain homogeneous gaps. More recent manufacturing techniques build the complete Micromegas as a unit, which results in very robust and homogeneous readout planes that can be scaled to larger surfaces. The two main designs achieved with this manufacturing method are bulk Micromegas [45] and microbulk Micromegas [46].

Bulk technology

The bulk Micromegas [45] technology replaces the electroformed mesh with a woven wire mesh ($\sim$30μm thick) that is very robust and resistant to stretching and handling. Also, the mesh is industrially produced, so it can be purchased inexpensively at big quantities in a variety of materials.

The steps of the fabrication process are shown in figure 2.4. The Micromegas base is a PCB with a copper plane. This base is covered by a photoresist foil that will set the height of the amplification gap. Then, the mask of the pillars is fixed by UV lithography and the woven wire mesh is placed on top. A new layer of photoresist foil is used to cover the mesh, encapsulating it, and the mask of the pillars is fixed again on this new layer. Finally, the readout goes through a chemical bath to remove the not fixed

[1] Electroforming is a metal forming process that forms parts through electrodeposition on a model. Colloidal particles suspended in a liquid medium migrate under the influence of an electric field (electrophoresis) and are deposited onto an electrode.

photoresistive foil, forming in this way the pillars below and above the mesh fixed to the copper substrate.

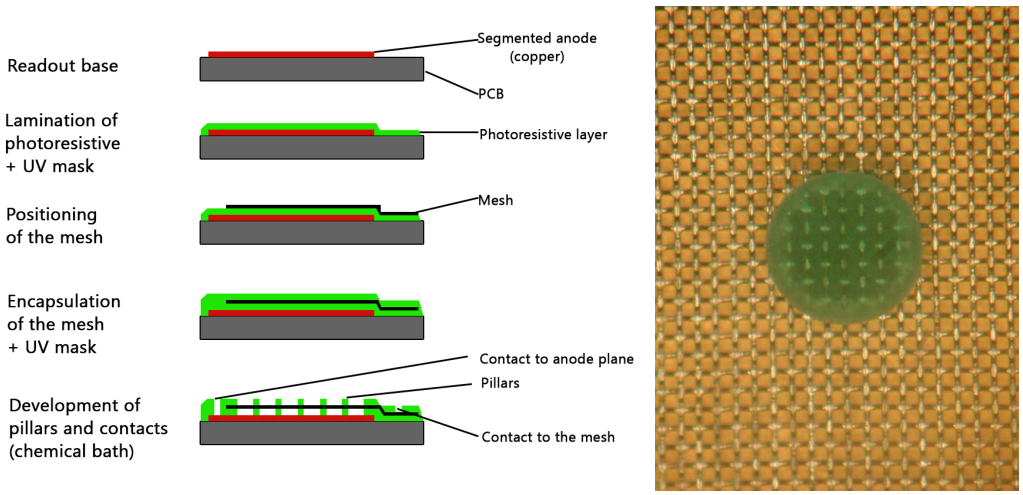

Figure 2.4: (Left) Comprehensive scheme of the fabrication process of a bulk Micromegas. **(Right)** Detail of the copper woven mesh showing one of the pillars.

The amplification gap in bulk detectors ranges typically between 64 μm, 128 μm or 256 μm, depending on the thickness (or the number of layers) of the photoresisitve foil used in the manufacturing process. These detectors provide a very high gain before the spark limit is reached (2×10^4 in Ar + 5% C_4H_{10}), an ion-induced signal risetime of about 100 ns (dependent on the gap size), and energy resolution better than 20% FWHM at 5.9 keV. But the fact that this readouts are built on top of PCB bases makes them non convenient from the radiopurity perspective.

Also, the pillars of about 200-300 μm diameter can be relatively spaced from each other, around 2-4 mm, so the amount of insulator material between the electrodes is minimized. This fact makes the bulk Micromegas to have low capacitance per unit area, what helps to build large areas without a limiting noise or the need to segment the mesh.

Microbulk technology

The microbulk Micromegas [46] technology uses double and single copper-clad-kapton foils to produce the entire readout, both the segmented anode and the mesh, at once. This technique allows a very homogeneous amplification gap, which leads to the best energy resolutions in Micromegas detectors with a relatively high gain. Also, as it is only made out of copper and kapton, high levels of radiopurity can be reached.

Figure 2.5 (left) shows a schematics of the manufacturing process. The base material is a kapton foil 50 μm thick with 5 μm copper layers in both sides (double copper-clad-kapton). The readout pads are constructed by means of photolytography technique, attaching extra single copper-clad-kapton foils to obtain pads at different levels. These foils are etched and different vias are constructed in concordance with the readout pattern.

Then, the mesh grid is made by photochemical etching, creating a holes pattern on the superior copper layer. Finally, the kapton layer is also etched and removed in order to build pillars that avoid dead spaces.

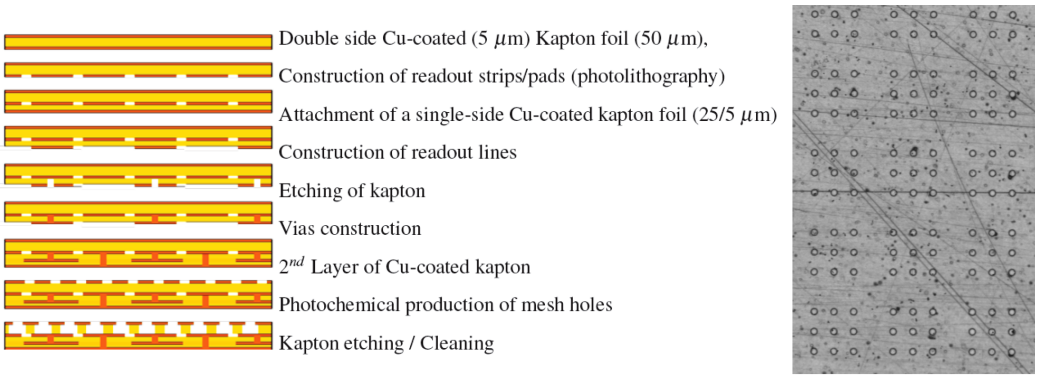

Figure 2.5: **(Left)** Comprehensive scheme of the fabrication process of a microbulk Micromegas. **(Right)** Microscopic detail of the copper mesh.

Through this fabrication technique, the amplification gap that is produced has an homogeneity accuracy of $\sim$1 μm, so the resulting energy resolution is very good for MPGD standards: 11.2% FWHM at 5.9 keV in Ar+5% C_4H_{10} [46], or better than 2% FWHM at 5.5 MeV in Ar+2-5% C_4H_{10} mixtures can be achieved. The gain and energy resolution of microbulk Micromegas in different argon and xenon gas mixtures at different pressures have been extensively studied for example in [19, 20, 47].

Microbulk Micromegas are more fragile than bulk Micromegas to handling and sparks can happen due to their delicate mesh. However, they are more robust against continuous vibrations and tensions, and they are generally more stable.

2.3.2 Micromegas properties

It is important to define the fundamental properties of the Micromegas detectors that are usually used for their experimental characterization. First, the **electron transmission** (also known as *transparency*) is the parameter that measures the fraction of initial electrons that pass from the conversion region to the amplification region through the mesh holes. The electron transmission is highly dependent on the field lines that direct the electrons through the holes and on the geometry of the detector itself. Usually, for a given amplification field, the energy transmission at very high drift fields is low because the field lines tend to finish on the surface of the mesh. As the drift field decreases, the electronic transmission tend to its maximum values, and this tendency follows for a longer or shorter field rate range depending on the type of the Micromegas, what is called the *plateau*. In this range, most of the drift field lines go through the the holes of the mesh and enter the amplification region, so usually, this plateau is searched to be the operational point for the detector. Finally, for very low values of the drift field, the drift velocity of the electrons decreases and the attachment and recombination processes star to become relevant, therefore sharply decreasing the electronic transmission.

Another important parameter of a Micromegas detector is the amplification **gain**, or the multiplication factor of the electrons in the amplification gap. This process was described in section 1.5, and the gain was obtained to be dependent on the distance travelled by the primary electron in the amplification field, d, and on the Townsend coefficient, α, that is electric field dependent. This coefficient has been parametrized in various theoretical models, such as the Rose-Korff model [48],

$$\alpha = PAe^{\frac{-BP}{E}}, \tag{2.1}$$

where P is the pressure of the gas, A and B are empirical parameters of such gas and E is the electric field. Then, the gain from equation 1.25 can be expressed as

$$G = \exp\left(PAe^{\frac{-BPd}{E}}\right) = \exp\left(PAe^{\frac{-BPd}{V}}\right), \tag{2.2}$$

where V is the applied voltage. In order to find a set of parameters that optimise the operational point, this expression can be differentiated as

$$\frac{\partial G}{\partial d} = G\alpha\left(1 - \frac{BPd}{V}\right). \tag{2.3}$$

Therefore, the amplification gap that maximizes the gain is $d_{max} = V/BP$. From this relation it is obtained that the pressure is inversely proportional to the amplification gap, so it is expected that small amplification gaps will be more suitable for operation at higher pressures. A study of Micromegas with different gap distances operated at different pressures can be found in [33]. Experimentally, the gain parameter can be measured provided the total energy deposited and the W factor of the gas are known.

Yet another relevant property of the Micromegas detectors is the **energy resolution**, which is the accuracy in the determination of the energy of a measured event. As it was described along the last chapter, the energy resolution for a gaseous detector is given by equation 1.26. It depends on the energy of the incident particle, E, and the energy required to create an e^--ion pair in the corresponding gas, W, and it is affected by the Fano factor (section 1.3) and the gain fluctuations (section 1.5). In practice, some more corrections are needed: δ_n from the electric noise, and δ from any other issues like spatial inhomogeneities of the gap or fluctuations in pressure or temperature. Then, the experimental energy resolution can be expressed as

$$R(\%FWHM) = 2.35\sqrt{\frac{W}{E}(F+b)} + \delta + \delta_n. \tag{2.4}$$

The energy resolution is correlated with both the electron transmission and the gain. It is optimum for the maximum electron transmission, and it worsens below and above the transmission plateau. Also, the energy resolution is degraded at high gain values close to the spark limit due to the fluctuations, as well as at very low gains, where the electronic noise becomes comparable to the signal size.

The **position resolution** is the accuracy in the determination of the two-dimensional position of an event on the readout. Micromegas show excellent position

resolution due to the high granularity of their readouts and the small avalanche gap. This parameter is however limited by the diffusion during the drift of the primary charges trhough the gas. The position resolution is usually measured as the difference between the centroid measured by the Micromegas and the extrapolation of a reference measurement when irradiated by a perpendicular and collimated beam. Alternatively, it is measured as the difference between two Micromegas situated back-to-back. Position resolutions as good as 36 μm and 24 μm have been achieved with Micromegas of 250 μm and 500 μm pitch respectively in argon-based mixtures [49].

Finally, the **time resolution** is the accuracy in the determination of the temporal dimension of an event. Some tests have been made to estimate the time resolution of the Micromegas detectors, for example in [50], where time resolutions as good as 0.5 ns were achieved.

Part II

Micromegas X-Ray detectors for axion search in IAXO

CHAPTER 3

Axions and Axion-Like particles

Contents

3.1 Introduction

Axions are hypothetical elementary particles of a grown interest in the last years inside the particle physics and cosmology scene. They were postulated by Weinberg and Wilczek in 1978 from the Peccei–Quinn solution to the strong CP problem of Quantum Chromodynamics, and named after a laundry detergent[1] because they *cleaned up* such problem. These particles are very well motivated as they arise as possible explanations or consequences in several Standard Model extensions and furthermore, they are fitting candidates for dark matter particles.

In this chapter, the idea that postulated the existence of the axions is explained, as well as the main properties of these particles, the different theoretical models and the most relevant constrains for their properties from astrophysical and cosmological observations.

[1] Quoting Frank Wilczek talking about axions in [51]: *I named them after a laundry detergent, since they clean up a problem with an axial current.*

Then, a more generic view of the axions and the possibility of them being part or the totality of the dark matter of the Universe is explained, and finally, some of the current experimental techniques to detect them are shown.

3.2 The strong CP problem and axions

A problem: the $U(1)_A$ problem

The strong CP problem arises in the context of the Quantum Chromodynamics theory (QCD), which is an important part of the Standard Model (SM) of particle physics. QCD is a non-abelian gauge field theory that describes the properties of the strong interactions between quarks and gluons, the fundamental particles that form composite hadrons like protons, neutrons, pions, etc. It has a $SU(3)$ symmetry group with a charge called color, that must be conserved. Gluons are the force carriers of QCD, and there are eight types of gluons corresponding to the generators of $SU(3)$.

The QCD Lagrangian has two terms: the first one describes the quark fields and the second one, the gluon self-interactions. In can be written as

$$\mathcal{L}_{QCD} = \sum_n \overline{\psi_n}(i\gamma^\mu D_\mu - m_n)\psi_n - \frac{1}{4}G^a_{\mu\nu}G^{\mu\nu}_a, \tag{3.1}$$

where $G^a_{\mu\nu}$ are the strength tensors of the gluon fields with a color index $a = 1, 2, ..., 8$; ψ_n are the quark fields with the flavour n and the corresponding quark mass, m_n; and $D_\mu = \partial_\mu - igA^a_\mu T^a$ is the covariant derivative, where g is the coupling constant and T^a are the generators of the $SU(3)$ group rotations of the quark fields in the color space.

The QCD Lagrangian is invariant under its symmetry group transformations ($SU(3)$), what corresponds to the color conservation in strong interactions. In the particular limit of vanishing quark masses $m \longrightarrow 0$, the system has an additional global symmetry that can be expressed as $U(N)_V \times U(N)_A$. This symmetry implies that the system is invariant under flavour and chirality transformations. However, only the u and d quark masses are approximately zero with regard to the dynamic scale of the QCD theory ($m_{u,d} \ll \Lambda_{QCD}$). Therefore, QCD can be considered approximately invariant under $U(2)_V \times U(2)_A$:

- $U(2)_V = SU(2)_V \times U(1)_V$, where the associated quantity under $SU(2)_V$ is the isospin, which describes the organization of hadrons in multiplets of similar mass (singlets: Λ_0, doublets: (p, n), triplets: $(\Sigma^+, \Sigma^0, \Sigma^-)$, quartets: $(\Delta^+ +, \Delta^+, \Delta^0, \Delta^-)$, etc.); and on the other hand, $U(1)_V$ is associated with the baryon number. This term is the vectorial part of the global symmetry, and is actually an exact symmetry. The invariance of QCD under the $U(2)_V$ term has been observed experimentally.
- $U(2)_A = SU(2)_A \times U(1)_A$, is the axial term of the global symmetry, and the invariance of QCD under this term has never been observed in nature. It is

understood then that the $U(2)_A$ symmetry is not preserved by the QCD vacuum (ground) state.

When a symmetry that is valid for the Lagrangian is not valid for the vacuum state, it is said that the symmetry is spontaneously broken. If the symmetry is exact, the consequence is the existence of a massless Nambu-Goldstone (NG) boson. But, if the symmetry is only approximate, as it is the addressed case, the consequence is the existence of a massive pseudo-NG boson. The pseudo-NG bosons associated with the breakdown of $SU(2)_A$ are the pion triplet (π^+, π^0, π^-). The problem is that the breakdown of $U(1)_A$ should also have a pseudo-NG boson associated, with an expected mass less than $\sqrt{3}m_\pi$, but there is not such a particle in the hadronic spectrum. This is known as the $U(1)_A$ problem of QCD [52], and it was addressed by S. Weinberg in 1975.

A solution: Θ-vacuum

The solution to this problem came from the realization by tHooft [53, 54] that $U(1)_A$ has a chiral (or axial) anomaly and that the ground state (vacuum) of QCD is non-trivial. In fact, the QCD vacuum has an infinite number of degenerate states which are topologically different. Thus, the correct vacuum configuration of QCD is the superposition of an infinite number of degenerate states (labelled by n), called the Θ-vacuum, that can be written as a function of the parameter Θ:

$$|\Theta\rangle = \sum_n e^{in\Theta}|n\rangle. \tag{3.2}$$

The consequence of this vacuum state is the anomalous breaking of the $U(1)_A$, which is not longer a true symmetry of QCD.

The effect of the Θ-vacuum can be recast in a single non-perturbative term to be added to the QCD Lagrangian

$$\mathcal{L}_\Theta = \Theta \frac{g^2}{32\pi^2} G^a_{\mu\nu}\tilde{G}^{\mu\nu}_a. \tag{3.3}$$

If the electroweak interactions are taken into account, then a second term arises in the theory

$$\mathcal{L}_{weak} = Arg(detM)\frac{g^2}{32\pi^2} G^a_{\mu\nu}\tilde{G}^{\mu\nu}_a, \tag{3.4}$$

where M is the diagonalized quark mass matrix. If an effective $\overline{\Theta} = \Theta + Arg(detM)$ parameter is defined, which takes into account both QCD and electroweak information (quarks acquire their effective masses through the breakdown of the electroweak symmetry), then the resulting additional term to the QCD Lagrangian from equations 3.3 and 3.4 is

$$\mathcal{L}_{\overline{\Theta}} = \mathcal{L}_\Theta + \mathcal{L}_{weak} = \overline{\Theta}\frac{g^2}{32\pi^2} G^a_{\mu\nu}\tilde{G}^{\mu\nu}_a, \tag{3.5}$$

which effectively solves the $U(1)_A$ problem.

Another problem: strong CP problem

However, this solution brings another problem. The additional $\mathcal{L}_{\overline{\Theta}}$ term to the QCD Lagrangian is not invariant under CP transformations, and as a matter of fact, CP violation has never been observed experimentally in QCD.

One of the experimental consequences of the $\mathcal{L}_{\overline{\Theta}}$ term would be the existence of electric dipole moments (EDM) for protons, d_p, and neutrons, d_n. However, they have never been observed for neutrons [55]. The most sensitive measurements of EDMN set a strong experimental bound at $|d_n| < 2.9 \times 10^{-26}\,\mathrm{e\,cm}$ (90% C.L.), which constrains the value of $\overline{\Theta}$ to

$$\overline{\Theta} \lesssim 10^{-10}. \tag{3.6}$$

The smallness of this parameter results unnatural and it implies an extreme fine-tuning of Θ to the value of $Arg(detM)$ for these contributions to cancel with a precision of $\overline{\Theta}$. Additionally, these two contributions are in principle unrelated: one is the angle characterizing the QCD vacuum Θ and the other, the common phase of the matrix of SM quarks, that comes from the Higgs Yukawa couplings, which are known to violate CP. This is what is known as the strong CP problem.

Another solution: axions

An elegant answer to the strong CP problem was proposed by Peccei and Quinn in 1977 [56, 57]. They postulated the extension of the SM with an additional $U(1)$ global chiral symmetry, known as the PQ symmetry $U(1)_{PQ}$, that is spontaneously broken at high scale f_a. And as it was realized by Weinberg and Wilczek [58, 59], this symmetry breakdown implies the existance of a new massive pseudo-NG boson. Here is where the **axions** were introduced.

This new axion field, a, will transform under the new $U(1)_{PQ}$ symmetry as

$$a \xrightarrow{\text{PQ}} a + \alpha f_a, \tag{3.7}$$

and because of the chiral anomaly of this symmetry, the axion will couple to gluons, resulting in the appearance of an extra term in the QCD Lagrangian.

$$\mathcal{L}_a = \frac{a}{f_a}\xi\frac{g^2}{32\pi^2}G^a_{\mu\nu}\tilde{G}^{\mu\nu}_a - \frac{1}{2}\partial_\mu a\partial^\mu a + \mathcal{L}(\partial_\mu a, \psi), \tag{3.8}$$

where the first term is the axion potential energy with ξ a model-dependent constant, the second term is the kinetic energy of the axion field and the third term accounts for all the possible interactions of the axion field with fermions.

Taking into account that both $\mathcal{L}_a$ and $\mathcal{L}_{\overline{\Theta}}$ have been added to the $\mathcal{L}_{QCD}$ so far:

$$\mathcal{L}_a = \left(\frac{a}{f_a}\xi + \overline{\Theta}\right)\frac{g^2}{32\pi^2}G^a_{\mu\nu}\tilde{G}^{\mu\nu}_a - \frac{1}{2}\partial_\mu a\partial^\mu a + \mathcal{L}(\partial_\mu a/f_a, \psi), \tag{3.9}$$

and the effective potential acquired by the axion field can be expressed as

$$V_{eff} \sim cos\left(\overline{\Theta} + \frac{a}{f_a}\xi\right). \tag{3.10}$$

The minimization of this potential with respect to the axion field occurs at the axion field vacuum expectation value $\langle a \rangle$, such as

$$\left\langle \frac{\partial V_{eff}}{\partial a} \right\rangle = 0 \quad \Rightarrow \quad \langle a \rangle = -\frac{f_a}{\xi}\overline{\Theta}. \tag{3.11}$$

In this way, the physical axion field

$$a_{phys} = a + \langle a \rangle, \tag{3.12}$$

absorbs the $\overline{\Theta}$ dependent term and no CP violation occurs, solving the strong CP problem.

Finally, if one expand the axion field around the vacuum expectation value, the axion gets a mass of

$$m_a^2 = \left\langle \frac{\partial^2 V_{eff}}{\partial^2 a} \right\rangle = -\frac{\xi}{f_a}\frac{g^2}{32\pi^2}\frac{\partial}{\partial a}\left\langle G^a_{\mu\nu}\tilde{G}^{\mu\nu}_a \right\rangle\Big|_{\langle a \rangle}, \tag{3.13}$$

which is dependent on the PQ symmetry breaking scale f_a, so *a priori* it is arbitrary.

As it has been seen, the Peccei-Quinn mechanism is the most elegant solution to the strong CP problem and it introduces the possibility of a new massive pseudo-NG boson, the axion. The experimental detection of such a particle would prove this theory.

3.3 Axions properties

Axions arises from the PQ solution of the strong CP problem, so some of their properties are determined by the $U(1)_{PQ}$ symmetry breaking scale f_a. These properties are the axion mass, m_a, and its coupling constant to other particles, g_{ai}:

$$m_a \propto \frac{1}{f_a}, \quad g_{ai} \propto \frac{1}{f_a}. \tag{3.14}$$

In this section, some of the main axion coupling mechanisms with matter will be described, as well as the most relevant axion models.

3.3.1 Axion couplings

From the axion Lagrangian term it is seen that couplings to gluons and photons appear naturally for all theoretical models, but other couplings like coupling to fermions will be model dependent.

Coupling to gluons

Axions couple to gluons as a consequence of the chiral anomaly of the $U(1)_{PQ}$ symmetry, so it is a direct outcome of any axion model and the most generic property of the axions. It is described by the surviving term of the axions Lagrangian (equation 3.9) after the $\overline{\Theta}$ cancellation from the PQ solution,

$$\mathcal{L}_{aG} = \frac{\alpha_s}{8\pi f_a} G^a_{\mu\nu} \tilde{G}^{\mu\nu}_a \, a, \tag{3.15}$$

where α_s is the fine-structure constant.

The coupling of axions with gluons makes that axions can mix with pions, that have the same quantum numbers, and therefore, they can acquire mass depending on the mass and decay constant of the pion, m_π=135 MeV and $f_\pi \simeq$93 MeV, as

$$m_a = \frac{m_\pi f_\pi}{f_a} \sqrt{\frac{z}{(1+z+w)(1+z)}} \simeq 6\, MeV \frac{10^9\, GeV}{f_a}, \tag{3.16}$$

where $z = m_u/m_d = 0.46 \pm 5$ and $w = m_u/m_s = 0.036 \pm 0.0004$ are the quark masses ratios (from [4]).

Coupling to photons

The axions coupling to photons is a very interesting axion property from the experimental perspective. They have two main coupling mechanisms: through the mixing with neutral pions and, if the fermions carry PQ charge and electric charge as well, through the Yukawa coupling to two photons. The axion to photons coupling can be described by the Lagrangian term

$$\mathcal{L}_{a\gamma} = -\frac{g_{a\gamma}}{4} F^a_{\mu\nu} \tilde{F}^{\mu\nu}_a \, a = g_{a\gamma} \overrightarrow{E}\, \overrightarrow{B}\, a, \tag{3.17}$$

where $F_{\mu\nu}$ is the electromagnetic field-strength tensor, $\overrightarrow{E}$ and $\overrightarrow{B}$ are the electric and magnetic fields, a is the axion field, and $g_{a\gamma}$ is the coupling constant, that can be expressed as

$$g_{a\gamma} = \frac{\alpha}{2\pi f_a} \left(\frac{E}{N} - \frac{2(4+z+w)}{3(1+z+w)} \right) = \frac{\alpha}{2\pi f_a} \left(\frac{E}{N} - 1.92 \pm 0.08 \right), \tag{3.18}$$

where α is the fine-structure constant, z and w are again the quark masses ratio, and E/N is a model dependent ratio between the electromagnetic anomaly, E, and the color anomaly, N, of the axial current associated with the axion field. The values that this ratio takes in different models will be addressed later, but generically, E/N can take a broad range of values.

It is seen that photons can oscillate into axions and *vice versa*. This process is known as the Primakoff effect (and the inverse-Primakoff effect), and it turns out very useful for the experimental approaches, because axions can turn into detectable photons in a laboratory magnetic field.

Coupling to fermions

Whether fermions carry PQ charge or not is a model dependent property, so this coupling is not as generic as the gluons or photons ones. The possible interaction of an axion with a fermion f can be expressed as

$$\mathcal{L}_{af} = \frac{g_{af}}{2m_f}(\overline{\psi}_f\,\gamma^\mu\gamma_5\,\psi_f\,\partial_\mu a), \tag{3.19}$$

where ψ_f and m_f are the fermion field an mass, and g_{af} is the axion-fermion coupling constant

$$g_{af} = \frac{C_f m_f}{f_a}, \tag{3.20}$$

where C_f stands for the model-dependent effective PQ charge of the fermion.

Specifically, there are models that consider the **coupling of axions to electrons**. For those which $C_e \neq 0$, the axion-electron coupling occurs at tree-level (e.g. for the DSFZ model), and the axion-electron coupling constant is $g_{ae}^{tree} = \frac{C_e m_e}{f_a} = 0.85\times10^{-10} m_a C_e eV^{-1}$. On the other hand, for those models where $C_e = 0$, the axion-electron coupling can occur through higher order loops corrections, the so-called radioactively induced coupling, with a coupling constant g_{ae}^{rad}. Although this coupling can occur, g_{ae}^{rad} is usually weaker than g_{ae}^{tree}.

In a similar way, some models consider the **coupling of axions to nucleons**. This coupling consists of two components, one derived from the tree-coupling of axions to up and down quarks, and other one from the axion-pion mixing. The coupling constant is $g_{aN} = \frac{C_N m_N}{f_a}$, where C_N is a combination of the masses of the quarks

3.3.2 Axion models

The axion mass is dependent on the $U(1)_{PQ}$ symmetry breaking scale (or decay constant) f_a, so different values of this scale will lead to different massive axions: heavy and strong coupled axions for small f_a values, called *visible* axions, and light and weakly coupled axions for large f_a values, called *invisible* axions.

Visible axions

The original assumption from the Peccei-Quinn solution [56, 57] was that the $U(1)_{PQ}$ symmetry breaking scale is of the same order as the electroweak scale, so $f_a \simeq 250\,\text{GeV}$. This would have been translated to an axion with a mass $\sim$100 keV that should has been detected in reactor and accelerator experiments through the process

$$K^+ \longrightarrow \pi^+\,a. \tag{3.21}$$

However, several experiments have excluded the existence of such axion, setting a strong bound by the non observation of this process [60].

Invisible axions

Since the scale f_a is an arbitrary value, it can be much larger than the electroweak scale, f_{weak}, that was originally proposed. In this way, the coupling of the axion becomes weaker so that it could have eluded all the preliminary searches, it would be *invisible*. These invisible axion models introduce a complex scalar field, ϕ, with a very large vacuum expectation value,

$$\langle \phi \rangle = \frac{f_{PQ}}{\sqrt{2}} \gg f_{weak}. \tag{3.22}$$

There are two groups of invisible axion models depending whether or not they allow the axion-fermion coupling at tree level: the KSVZ and the DFSZ. Figure 3.1 shows the different axion-photon coupling constants allowed by the different models depending on the E/N ratio values (mentioned in section 3.3.1).

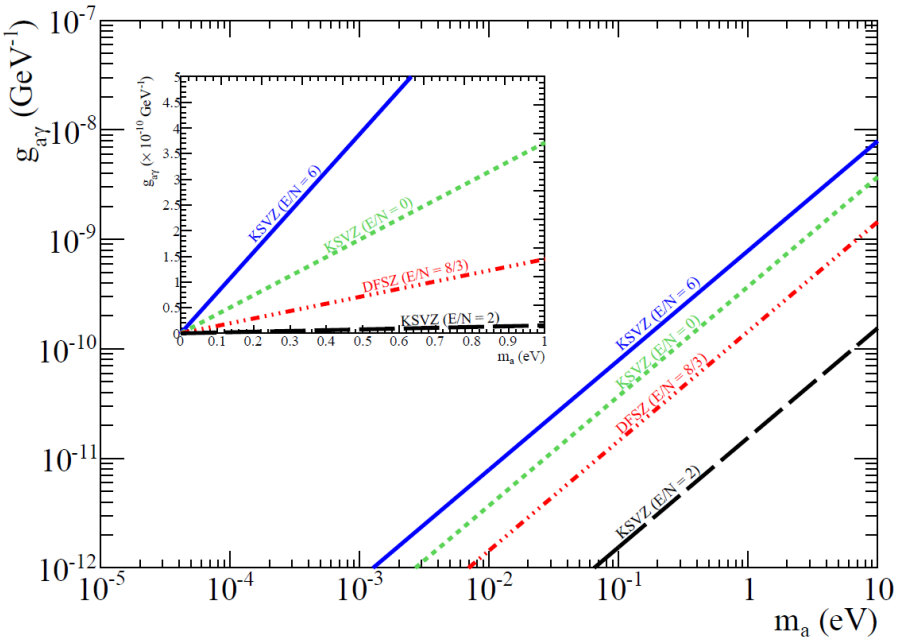

Figure 3.1: Axion-photon coupling constant as a function of the axion mass for invisible axion models. Three lines for the KSVZ model are shown: $E/N = 6$ (solid blue line); $E/N = 0$ (dotted green line) and $E/N = 2$ (dashed black line). The DFSZ model with $E/N = 8/3$ (dashed red line) is also shown.

- **KSVZ model** was proposed by Kim [61], and Shifman, Vainstein and Zakharov [62], and it suggest the existence of new, heavy quarks that carry CP charge, while the usual leptons and quarks do not. This implies that $C_e = 0$, so the axion-electrons coupling is forbidden at tree level, although as it was explained in the previous section, it can already exist a weaker coupling to electrons radiatively induced. This axions are known as *hadronic* axions. On the other hand, hadronic axions do couple with nucleons ($g_{aN} = \frac{C_N m_N}{f_a}$), with a coupling constant different for protons and neutrons.

Different implementations of this model provide different axion properties, expressed in terms of the E/N ratio. The standard KSVZ model generates a neutral quark: $E/N = 0$, although E/N can typically range between 0 and 6. There can be models with $E/N \simeq 2$ [63], that suppress the axion-photon coupling. In that case, the dominant contribution comes from the axions-to-nucleons coupling. Figure 3.1 show some of these dependences.

The main drawback of this model is that there is not a physical motivation for this new generated heavy quark.

- **DSFZ model** was proposed by Dine, Srednicki and Fischler [64], and Zhitnitski [65], and it stands that normal quarks and leptons carry PQ charge, so the existence of a new exotic quark is not required. Therefore, $C_e \neq 0$ and the axion-electrons coupling at tree level will be allowed. In this model, the Higgs field is substituted by two new ones with vacuum expectation values f_1 and f_2, whose interaction with the scalar field ϕ will induce this tree-level coupling of axions with quarks and leptons, and the E/N ratio is fixed to $E/N = 8/3$ (figure 3.1).

3.3.3 Relevant constrains to axion parameters

Axions arise as a consequence of the strong CP problem, so the axion mass m_a and the value of its symmetry breaking scale f_a are theoretically arbitrary. But due to their implication in astrophysics, particle physics and cosmology, axions have been deeply studied and some limits have been found for their properties, mainly from astrophysical considerations [66,67]. Actually, axions could be produced in hot and dense environments such as stars, globular clusters or white dwarfs by Primakoff effect, so they would contribute to the total energy loss of the stars thus shortening their burning process and reducing their lifetime. In this section, some of the most relevant constrains for the axion parameters will be discussed.

- **Solar model:** The emission of axions from the Sun implies an increment of the nuclear burning, and consequently, of the solar temperature distribution. This would lead to an increase in the solar neutrino flux with respect to the standard one without axions [68]. In this way, the axion flux from the Primakoff effect will set a limit to the coupling $g_{a\gamma} \lesssim 0.7 \times 10^{-9}\,\mathrm{GeV}^{-1}$ (labelled as *Sun* in figure 3.2). On the other hand, the Bremsstrahlung process in electron collisions ($e^- + (A,Z) \longrightarrow e^- + (A,Z) + a$) constrains $g_{ae} < 2.5 \times 10^{-11}\,\mathrm{GeV}^{-1}$.

- **Stars from globular clusters:** An astrophysical limit to $g_{a\gamma}$ can be set by the population of low-mass Horizontal Branch (HB) stars and Red Giant Branch (RGB) in globular clusters. These are highly dense spherical collections of stars that orbit a galactic core as a satellite, and whose stars were formed at about the same time. HB stars are the next step in the stellar evolution of the RGB stars, and have helium burning cores with hydrogen shells. The axion emission from the core of these stars would accelerate the loss of energy, therefore reducing their lifetime.

This phenomenon would lead to a reduction of the population of the HR stars with respec to the RGB stars. From this, a limit can be set on $g_{a\gamma} \lesssim 10^{-10}\,\mathrm{GeV}^{-1}$ [66,69]. A more recent study that analizes the dependence of $g_{a\gamma}$ with Helium mass fraction provides another limit, $g_{a\gamma} < 0.66 \times 10^{-10}\,\mathrm{GeV}^{-1}$ [70]. The constrains of this HB stars are shown later in figure 3.2, labelled as *HB*.

Also, knowing that RGB stars have a degenerate[2] helium core, the processes involving axion-electron coupling are supposed to happen more frequently (in DSFZ models). Measurements of the RGB stars luminosity in globular clusters like the M5 [71] set another limit on $g_{ae} < 4.7 \times 10^{-13}\,\mathrm{GeV}^{-1}$.

- **White dwarf cooling:** White dwarfs are the next step of the stelar evolution of a HB star, after it burns out all the helium of its core. These stars fist cool down by neutrino emission, and finally by surface photon emission. The observed white dwarf luminosity is in accordance with the expectation, which eliminates new cooling agents like axions. The cooling speed of some white dwarfs, such as the ZZ Ceti star G117–B15A [72], has been studied and a limit to the axion-electron coupling has been set as $g_{ae} < 1.3 \times 10^{-13}\,\mathrm{GeV}^{-1}$ (95% C.L.). However, the case of the star G117–B15A together with other pulsating WD observations are further interesting because unexpected fast coolings have been observed through their pulsating period, and although some other mechanisms could explain them and set the previous g_{ae} limit, axion emission could be a suitable explanation as well. This will be discussed in section 3.4.2.

- **Existence of Cepheid stars:** Stars between 8-12 $\mathrm{M}_\odot$[3] can be used to set a limit on $g_{a\gamma}$. The energy losses by axion emission from the helium-burning core would shorten the lifetime of these stars and eventually, eliminate the blue loop phase of their evolution[4]. This would contradict observational data, since the blue loops are required for some stars to actually exist, like the Cepheid stars. This fact would limit $g_{a\gamma} \lesssim 0.8 \times 10^{-10}\,\mathrm{GeV}^{-1}$ [73].

- **Supernova 1987 A:** A supernova (SN) is a extremely energetic and luminous stellar explosion that occurs during the last evolutionary stages of very massive stars, that can either collapse to a neutron star or a black hole, or be completely destroyed. In this powerful burst of radiation, axion-nucleon Bremsstrahlung ($N + N \longrightarrow N + N + a$) could be an additional energy loss channel that would accelerate the cooling process and reduce the burst duration, given that the axion-nucleon couplings, g_{aN}, is neither too small, so there would not be any energy loss, or too big, so axions would be trapped in the core. In 1987 SN, a $\sim$10 s burst of neutrinos with a total of 24$\overline{\nu}_e$ was measured by three different observatories (IMB, Kamiokande II and Baksan), which is in agreement with the theoretical expectations, what sets a limit of $g_{ap} \lesssim 10^{-9}$ [67], or equivalently, $m_a < 16\,\mathrm{meV}$

[2]Degenerate matter is a highly dense state of fermionic matter in which particles must occupy high states of kinetic energy to satisfy the Pauli exclusion principle. In astrophysics, it refers to dense stellar objects where gravitational pressure is so extreme that quantum mechanical effects are significant.

[3]$\mathrm{M}_\odot \sim 2 \times 10^{30}$ kg is the mass of the Sun.

[4]A blue loop is a stage in the life of an evolved star where it changes from a cool star to a hotter one before cooling again.

(labeled as *SN1987A* in figure 3.2). However, this limit is uncertain due to the complex computation of the axion flux in a SN. Recent studies have revised some of these uncertainties and as a consequence, have relaxed this limit to $g_{ap} \lesssim 5 \times 10^{-10}$ [74, 75].

Also, if axions had been emited by the SN, they could have transformed to x-rays in the magnetic field of the Milky Way, so a potential γ-ray excess would have been measured in coincidence with the neutrino boost. The absence of this excess can be used to set another limit to the axion-photon coupling, $g_{a\gamma} < 5.3 \times 10^{-12}\,\mathrm{GeV}^{-1}$ (95% C.L.) [76]. This region is shown later in figure 3.2, labeled as *γ-rays*.

3.4 Axion-like particles (ALPs) and dark matter

Beyond the axions it extends a whole category of particles called Axion-Like particles (ALPs), that are also well motivated from different extensions of the SM. They form part of the general group of particles called Weakly Interacting Slim Particles (WISPs), that are invoked in many low energy particle physics scenarios [77]. Although ALPs and axions arise from different extensions of the SM model, they both appear as pseudo Nambu-Goldstone boson of new symmetries broken at high energies, so they share part of their phenomenology: they are light pseudo-scalar particles that weakly couple to two photons [78, 79]. However, there is a fundamental difference: since ALPs are not motivated from QCD, they will not necessarily couple to gluons, and also, their mass, m_A, and coupling constant, $g_{A\gamma}$, will be independent parameters, so the full parameter space shown in figure 3.2 becomes available for ALPs.

ALPs are also motivated from the string theory [80–82]. This is interesting because the region of the ALPs parameter space that can be explored by future experiments is theoretically favoured, as it corresponds to string scales contributing to the natural explanation of several hierarchy problems in the SM. Other important examples of WISPs are hidden photons and minicharged particles [83–85], that appear in extensions of the SM including hidden sectors (sectors that interact with SM particles through interchange of very heavy particles) and show mixing with normal photons. Some more exotic ALPs are the *quintessence* fields [86] or the chameleons [87] related with the Dark Energy (DE) problem.

Last but not least, WISPs are candidates to be the Dark Matter (DM) [88] of the universe, for which a wide range of the ALPs $g_{A\gamma} - m_A$ parameter space could generically contain models with the required DM density. Part of this parameter space is at reach of current and near-future experiments. The fact that axions and ALPs are motivated from such different beyond SM approaches, makes them very appealing for experimental research.

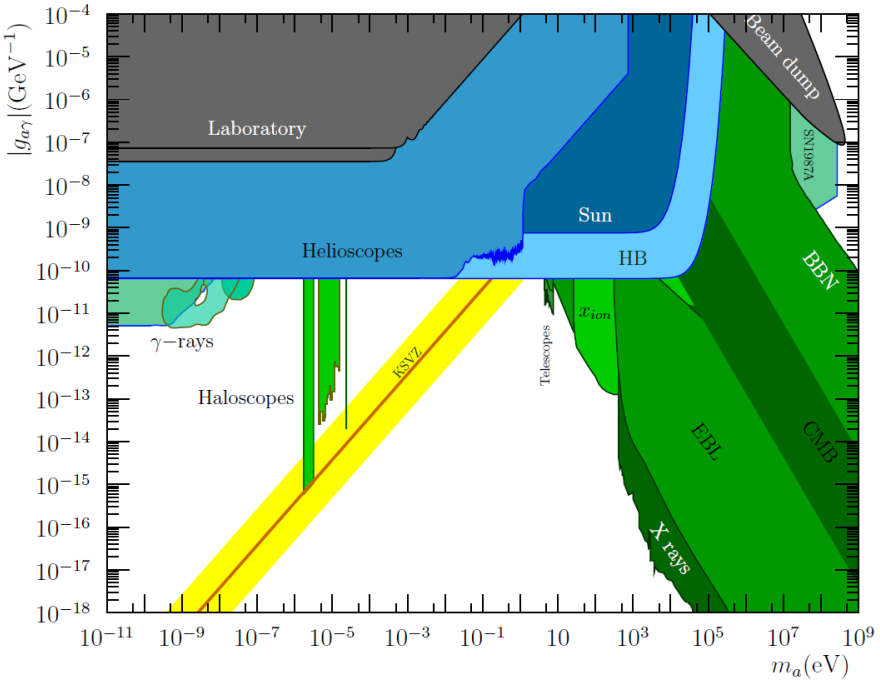

Figure 3.2: Review of the current constrains in the axion and ALP $g_{A\gamma} - m_a$ parameter space. Blue colors represent helioscope experiments (section 3.5.1) or bounds depending on stellar physics (like the solar model or the HB bounds mentioned in section 3.3.3). Green colors stands for haloscope experiments (see section 3.5.2) or cosmological bounds (like the SN1987 and the SN γ-ray explained in section 3.3.3 and the extragalactic background light (EBL) hints explained in section 3.4.2). Black and gray areas represent laboratory experiments (section 3.5.3). Yellow and orange bands correspond to the QCD motivated axion models. Extracted from [89].

3.4.1 Axions and ALPs as dark matter candidates

Dark Matter (DM) was first postulated by F. Zwicky in 1933 [90] from a discrepancy between the velocity of galaxies at the edge of a galaxy cluster and its estimation from the brightness and the number of galaxies: there was needed more mass in the galaxy than the observed one to explain such fast orbits. Since then, several observational evidences of the presence of DM in the universe have been collected, like the rotation curves of spiral galaxies, the gravitational lensing effect or the fluctuations in the Cosmic Microwave Background (CMB). The last results of the Planck Collaboration [91] measures the baryonic density of the Universe to be only $\Omega_b h^2 = 0.02237 \pm 0.00015$ (i.e. 4.2%), while the DM density is $\Omega_{DM} h^2 = 0.1200 \pm 0.0012$ (i.e. 27.2%) and and the DE density is $\Omega_\Lambda h^2 = 0.3107 \pm 0.0082$ (i.e. 68.6%).

The DM can be explained as non-relativistic neutral particles that interact weakly with standard particles and among themselves. And as previously seen, axions and ALPs fulfil these requirements at the same time they arise from different beyond SM theories not DM related, so they are very appealing candidates for the totality or a part of the DM of the universe. However, there exist other DM candidates such as the Weak Interacting Massive Particles (WIMP) that typically appear in supersymmetric extensions of the SM.

But despite they are being searched for in a variety of underground experiments, up to date there is neither any hint of superysmmetry at the LHC or any clear signature for WIMPs in direct detection experiments. Actually, the possibility of a mixed WIMP-axion DM is not excluded.

DM axions could have been formed in the early Universe either thermally or non-thermally. For small enough f_a parameter (i.e. more massive axions with stronger coupling constants), axions could have been produced thermally by collisions of particles in the primordial plasma and they would contribute to the Hot Dark Matter (HDM) of the Universe. Cosmological observations of the CMB from WMAP-7 [92] and Planck [93] constraining the amount of hot dark matter set an upper limit on the axion mass $m_a \lesssim 0.9\,\text{eV}$. The inclusion of other data sets like the matter power spectrum released by the Sloan Digital Sky Survey (SDSS-DR7) and the Hubble parameter measured by the Hubble Space Telescope (HST), constrains the axion mass to ma $m_a \lesssim 0.72\,\text{eV}$ (95% CL).

On the other hand, axions with large f_a parameter would have a weak enough coupling so it would have not thermalized in the early universe. The production mechanism for such non-relativistic axions is called *vacuum-realignment* (and its decay of topological defects), and they would contribute to the Cold Dark Matter (CDM) [94, 95]. In the very early Universe, when the temperature was above the PQ symmetry breaking scale $\sim f_a$, the axion was massless and the axion field assumed an initial value characterized by the misalignment angle $\theta_0 \equiv a_0/f_a \in (-\pi, \pi)$. Then, when the temperature dropped below f_a, the axion field appeared but its initial value was set differently in different causally connected regions. Later, when the Universe cooled down to the the QCD phase transition, the axion potential rose and then, the axion acquired its mass m_a. Finally, the axion field relaxed to its CP conserving minimum, and the oscillations around this minimum represent a population of non-relativistic axions, with a density that depends on the unknown initial value of the axion field before the start of the oscillations. At this point, because a/f_a is an angle variable, discrete domains would naturally form and their borders topological defects would form too. These defects would have soon decayed radiating a large amount of non-relativistic axions which would add up to the realignment population.

Two cosmological scenarios are possible depending whether or not inflation happened after or before the PQ phase transition.

- If inflation happened after the PQ phase transition, the axion field would have been homogenized by inflation, making the value of θ_0 unique. Therefore, the axion CDM density is easily determined because only the realignment mechanism would have contributed to it,

$$\frac{\Omega_a}{\Omega_{DM}} \sim \theta_0^2 F \left(\frac{f_a}{5 \times 10^{11}\, GeV} \right)^{1.184} \simeq \theta_0^2 F \left(\frac{12\,\mu eV}{m_a} \right)^{1.184}, \tag{3.23}$$

  where $F = F(\theta_0, f_a)$ is a correction factor. For typical values of $\theta_0 \sim \mathcal{O}(1)$, $\Omega_A \sim \Omega_{DM}$ for axion mass of around 10-100μeV ($f_a \sim 5 \times 10^{11}$ GeV). In this case, θ_0 has to be small enough so m_a is not too light and therefore, the CDM density would be larger than the value observed experimentally.

- If inflation happened before the PQ phase transition, the value of θ_0 would have been randomly distributed in different casually connected parts of the universe. In this case, it is necessary to average the above result for $\theta_0 \in (-\pi, \pi)$ to obtain an estimation of the DM contribution from vacuum-realignment.

$$\frac{\Omega_a, VR}{\Omega_{DM}} \sim \left(\frac{40\,\mu eV}{m_a}\right)^{1.184} . \tag{3.24}$$

  Then, the effect of the decay of the topological defects needs to be taken into account, but its computation is uncertain (for a more detailed description, refer to [96]). In any case, this scenario would lead to larger preferred values of m_a.

The fact that axions could account for the totality of CDM seem possible. Although the uncertainties prevent to define a specific preferred axion parameter, the *classic axion window* [95] $m_a \sim 10^{-4} - 10^{-6}\,\text{eV}$ is often considered as the preferred m_a range for CDM axions. However, the post-inflationary PQ symetry breaking scenario hints towards axions masses up to $m_a \sim 10^{-1}\,\text{eV}$ [96]. Also, it is worth to mention that the non-thermal production mechanism is not only valid for axions but for all the bosonic WISPs in general, including ALPs.

3.4.2 Hints for axions and ALPs

Several well understood physics phenomena from astrophysics has been used during the years to constrain the axion and ALPs properties. But there are also cases where axions can be invoked as the solution for unexplained astrophysical observations. These are very interesting situations for the axion and ALPs scenario, although usually there are alternative explanations. In this section, two of the main hints for the existence of axions and ALPs will be described: the excessive transparency of the intergalactic medium to very high energy (VHE) photons and the anomalous cooling rate of white dwarfs. Figure 3.3 shows the exclusion range of these hints, as well as the rest of the constrains previously addressed.

Intergalactic transparency to VHE photons

VHE photons ($\gtrsim$100 GeV) that travel long distances through the intergalactic medium can interact with the photons of the extragalactic background light (EBL) via e^+e^- pair production, so in principle, the Universe should be opaque to distant VHE sources such as active galactic nuclei (AGN). Even though collaborations like HESS [98] or Fermi [99] have measured the EBL density, which has been found to agree with the theoretical models, there are some observations [100, 101] that draw attention to the fact that the Universe is too transparent to VHE photons, even for the lowest EBL models. Also, VHE photons correlated with distant AGN sources have been observed by both HESS [102] and MAGIC [103, 104] imaging atmospheric Cherenkov telescopes.

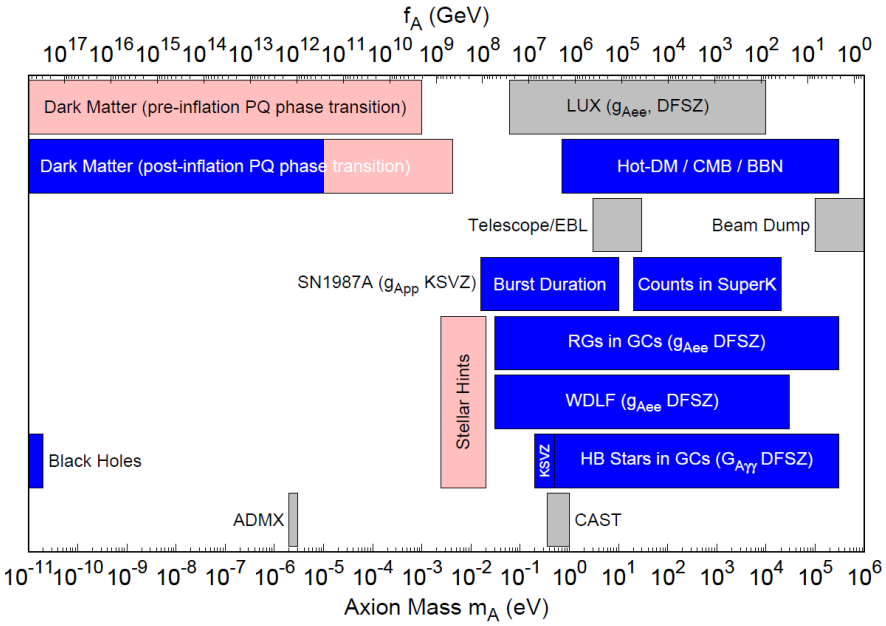

Figure 3.3: Exclusion ranges in the axion masss parameter space. Extracted from [4]. Dark Matter axions are addressed in section 3.4.1; extragalactic background light (EBL), white dwarfs (WD) and globular clusters (GCs) axion hints are explained in section 3.4.2; axion constrains from the SN 1987 and the stellar hints and constrains from RS and HB stars are detailed in section 3.3.3. Also, the CAST [34] and ADMX [97] search ranges are shown (see section 3.5).

These observations could be explained with no need of new physics, but it would require either a too low density of the EBL or a discrepancy in the intensity of the source spectra. Alternatively, these discrepancies can be explained by photon-ALP oscillations of the VHE photons in their way through intergalactic magnetic fields. Since ALPs are very weakly interactive particles, they could travel longer distances than photons, resulting in the current observed transparency of the intergalactic media.

Several authors have invoked ALPs as a solution to the intergalactic transparency discrepancies (e.g. in [100, 101, 105]) and the resulting axion parameters required to effectively explain it agree in very small ALP mass $m_a \lesssim 10^{-7}\,\text{eV}$ and $g_{a\gamma} \sim 10^{-12} - 10^{-10}\,\text{GeV}^{-1}$ [43]. This region is showed in figure 3.2 as the green region superposed with the γ-rays region.

Anomalous cooling of stellar objects

Independent observations of different stellar objects have show deviations, or *cooling anomalies*, from the standard models. The fact that such different stellar systems systematically show an excessive energy loss that is not well understood is remarkable, and also motivating for the search of new physics. An appealing explanation of this anomalous effect would be to assume that light weakly interacting particles, like axions, are being emitted by the stellar core and not being detected.

The original hint to cooling anomalies was that the period observed in the G117-B15A **pulsating White Dwarfs** (WD) [72,106] (mentioned in section 3.3.3), was larger than what it was expected by the standard models. This is known as the rate of period change, and it is proportional to the cooling rate, meaning that the WD was cooling faster than expected. Since then, more abnormal large periods have been observed in pulsating WD like R548 [107], PG 1351+489 [108] and L 19-2 [109]. Such energy loss could be explained by a particle produced in the dense core of the WD which freely escapes carrying energy away. These particles could be axions produced by axion-electron Bremsstrahlung [106,109] with expectations of coupling constant values of $g_{ae} \simeq 5 \times 10^{-3}$ for axion masses of $m_a > 3\,\text{meV}$, for DSFZ axions. This axion region in the parameter space could be within reach of planned experiments like the IAXO observatory [43]. However, this cooling could be due to neutrino physics [110].

Other hints can be found in recent analysis of the Red Giant Branch (RGB) stars in the **globular clusters**. As it was explained in section 3.3.3, RGB stars are the previous step to the Horizontal Branch HB stars. During the RGB evolution, stars become brighter until they reach a tip corresponding to the He ignition in their core. After that, the luminosity decreases and the star moves into the HB stage. Some recent studies of the M5 [71] and the ω-Centauri [111] globular clusters have shown a RGB tip brighter than expected, what means that some additional cooling mechanism is delaying the He ignition, allowing the star to become more brighter before entering the HB phase. Moreover, some other analysis [70] have shown a disagreement between the expected number ratio of HB and RGB stars in the globular cluster, indicating a larger number of RGB stars than predicted. This discrepancy can be interpreted as an anomalous cooling of the HB stars, as explained in section 3.3.3.

Assuming these two anomalies are due to new physics, cooling by axion emission would be a suitable explanation: ALPs coupled to photons and produced via Primakoff effect in the stellar cores of HB stars would accelerate the HB stage [70,112], and also, ALP coupled to electrons and produced through axion-electron Bremsstrahlung or Compton could explain the cooling during the RGB stage [113]. This is usually called the *HB hint*.

Also, another cooling anomaly was observed in the **He-burning core stars** of masses $\sim 10\,\text{M}_\odot$. It comes from the discrepancy between the observation of the number ratio of blue (hot) over red (cold) supergiants (B/R) with the numerical simulations, that predict a larger number [114,115]. This could be explained by an additional cooling channel efficient in the stellar core but not in the H-burning shell. In this scenario, and axions coupled to photons produced via Primakoff effect would fit as such a cooling agent [116]. However an exact prediction of the required additional cooling is currently unavailable.

3.5 Experimental searches for axions and ALPs

The direct detection of an axion or an ALP is unlikely because they interact very weakly with matter. Experiments that search for these particles usually rely on their axion-photon oscillation via Primakoff effect (or inverse Primakoff effect) in the presence of a magnetic field. There are three main experimental approaches for direct axion detection depending on their source of axions: helioscopes look for axions potentially emited by the core of the Sun; haloscopes look for the relic axions that potentially form the dark matter galactic halo; an finally Light-Shining-Through-Wall (LSW) experiments look for axions produced in the laboratory.

In this section, these three main detection techniques and the current experiments that implement them will be reviewed. Finally, some other type of less sensitive searches, or still in a development phase, will be mentioned.

3.5.1 Helioscope experiments

The helioscope technique searches for axions produced at the core of the Sun, since is our closest source of axions formed in stars. It was first proposed by P. Sikivie [117] in 1983 and further developed by K. van Bibber et al. [118] in 1989. This technique consist of directing a powerful magnet towards the sun to allow solar axions to convert to photons inside it. Solar axions reach the Earth with energies of ∼keV, so the converted photons will be in the range of the x-rays. This is why at the other side of the magnet, x-ray detectors are used to measure this excess over the radioactive background that would give the positive axion signal. The basic requirements for a helioscope are therefore a movable and powerful magnet, and low-background x-ray detectors. The enhanced version of the helioscope involves the use of x-ray focusing optics that collects the x-rays produced in the magnet and focus them on a small area of the detector, improving the signal-to-noise ratio. Figure 3.4 shows a conceptual scheme of the helioscope detection technique.

Helioscopes can cover axion masses in a wide range of the parameter space up to the ∼eV scale because the signal is independent of the axion mass. In order to extend the sensitivity towards larger mass values, different buffer gases at certain pressures can be used in the axion-photon conversion region. Further information about the helioscope technique will be given in chapter 4.

The first helioscope was implemented in the Brookhaven National Laboratory in 1992 [119] with a static magnet, a conversion volume of variable pressure gas and a xenon proportional chamber as x-ray detector. This experiment excluded $g_{a\gamma} < 3.6\times10^{-9}\,\mathrm{GeV}^{-1}$ for $m_a < 0.03\,\mathrm{eV}$ and $g_{a\gamma} < 7.7\times10^{-9}\,\mathrm{GeV}^{-1}$ for m_a in the 0.03-0.11 eV range (95% C.L.). Later in 1998, the second generation Tokyo Axion Helioscope (SUMICO) used a superconducting magnet on a tracking mount that allowed to follow the Sun trajectory. They reported an exclusion limit of $g_{a\gamma} < 6.0\times10^{-10}\,\mathrm{GeV}^{-1}$ for $m_a < 0.3\,\mathrm{eV}$ [120, 121].

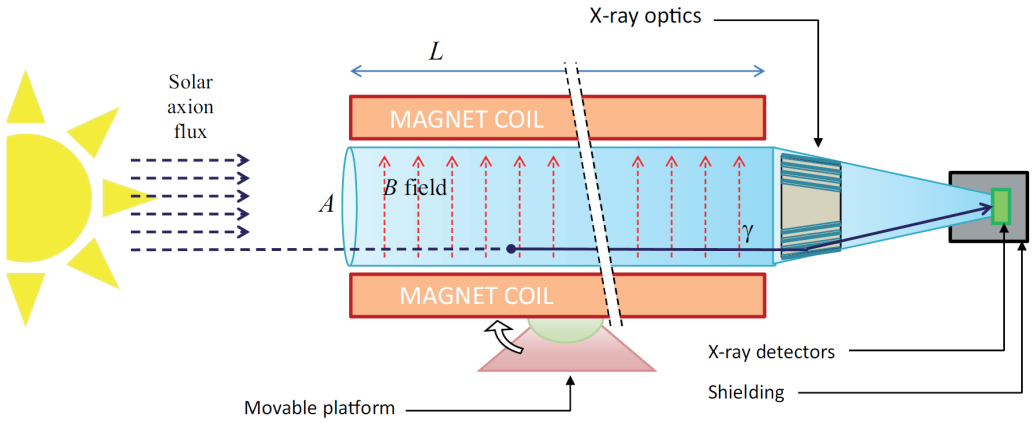

Figure 3.4: Conceptual scheme of the CAST-IAXO enhanced axion helioscope. Solar axions are converted into photons by the transverse magnetic field inside the bore of a powerful magnet. Then, they are focused by some x-ray optics to the surface of a low-background x-ray detector, producing a detectable signal.

The third and latest axion helioscope that has been commissioned is the CERN Axion Solar Telescope (CAST) [122], that uses a 9.3 m long, 9 T decommissioed LHC dipole magnet on a tracking mount and ultra-low background x-ray detectors. This experiment started taking data in 2003 and has gone over different phases with various gas buffers to study different m_a ranges up to 1.17 eV, surpasing the astrophysical constrain imposed by HB stars. It also implemented x-ray focusing optics in some of their lines to enhance the signal-to-noise ratio. A more detailed description of the CAST experiment and the most relevant results will be given later in section 4.2.4, because it is important for the motivation and the *lore* of this work. To close this section, the last result of the CAST experiment, that is also a pathfinder for the proposed fourth generation IAXO helioscope [43], set the limit of $g_{a\gamma} < 0.66 \times 10^{-10}\,\mathrm{GeV}^{-1}$ for $m_a < 0.02\,\mathrm{eV}$ [34].

3.5.2 Haloscope experiments

The haloscope technique aims to detect CDM axions that could potentially form the galactic halo. It was first proposed also by P. Sikivie [117] in 1983, and it relies on the conversion of axions into photons in the presence of a magnetic field inside of resonant cavity. If the resonant frequency of the cavity matches the frequency of the produced photon, which is related to the mass of the axion, the rate will be significantly enhanced, and an excess in the power of the cavity would give the positive axion signal. Figure 3.5 shows an scheme of the ADMX haloscope.

These experiments have mechanisms to tune the resonant frequency of the cavities to aim for different axion masses. One of the most representative haloscope experiments is the ADMX [97], with a 1 m long, 0.5 m diameter, 8 T superconducting solenoid magnet, which has achieved sensitivity to QCD axions (KSVZ) over the m_a mass range 1.9-3.3 μeV, assuming that axions saturate the local DM density [123]. A new improved phase of

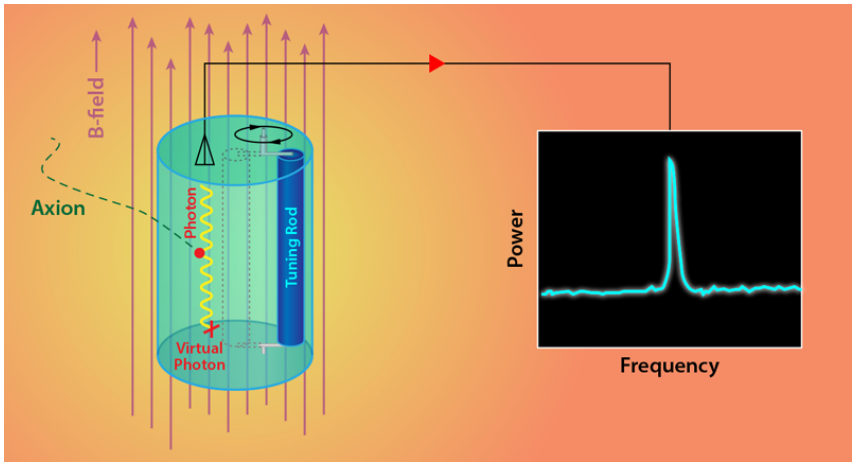

Figure 3.5: Scheme of the ADMX haloscope [123]. The resonant frequency of a cavity is shifted by moving rods placed inside it. If the resonant frequency of the cavity matches the frequency of photons coupled to axions, the rate of axion-photon conversion is significantly enhanced, generating power in the cavity.

ADMX [97] that has implemented near quantum-limited SQUID[5] amplifiers also excludes KSVZ DM axions with masses between 3.3-3.53 μeV.

Other recent experiment is the HAYSTAC haloscope [124], that exclude axion models with $g_{a\gamma} \gtrsim 2 \times 10^{-14}\,\mathrm{GeV}^{-1}$ over the axion mass range of 23.55-24.0 μeV. Finally, the ORGAN experiment [125] is designed to probe axions in the mass range of 60-210 μeV. In a pathfinding run, it has set a limit of $g_{a\gamma} < 2 \times 10^{-12}\,\mathrm{GeV}^{-1}$ at $m_a \sim 110\,\mu$eV.

3.5.3 LSW experiments

The LSW [126] experimental technique aims to detect axions produced in the laboratory, and they are based on the simple idea of an intense laser beam going through an intense magnetic field so the photons can transform into axions. Then, an absorbent surface (a *wall*) is placed in the path of the beam, so axions can pass through but the light is blocked. After the wall, another strong magnetic field would allow the axions to transform again into photons, and therefore be detected. A conceptual scheme of this technique is shown in figure 3.6.

One advantage of the LSW experiments is that they are less model-dependent because they do not rely on cosmological or astronomical assumptions. On the other hand, their sensitivity is penalized due to the fact that the axion-photon conversion has to happen twice. The conversion probability is $\sim (1/4)(g_{a\gamma}BL)^2$ where B is the intensity of the magnetic field and L is the length of the magnet. Some strategies to boost the sensitivity of these experiments could be to use more intense and long magnets, but even though, the parameter space at reach is well above the bounds set by astronomical observations or helioscopes. The most restrictive limits from these types of experiments

[5]Superconducting QUantum Interference Device.

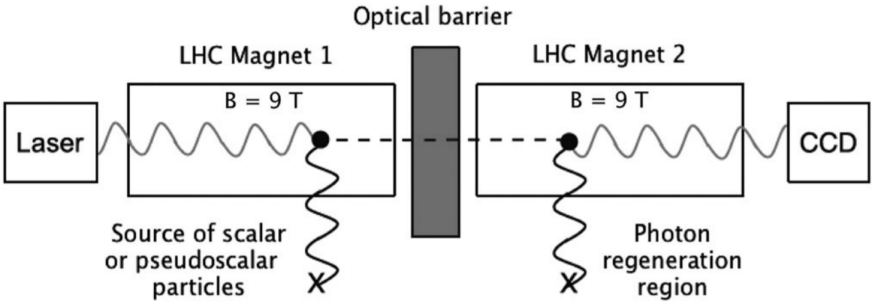

Figure 3.6: Principle of a LSW experiment (from the OSQAR experiment [127]). Photons can transform to axions in the initial magnetic field, pass through the opaque wall, and convert back to photons in the final magnetic field, creating a detectable signal.

come from the ALPS-I experiment, that set a limit of $g_{a\gamma} < 6.5\times10^{-8}\,\mathrm{Gev}^{-1}$ [128] for axion masses of $m_a \lesssim 1\,\mathrm{meV}$, and the OSQAR experiment, with a limit of $g_{a\gamma} < 3.5\times10^{-8}\,\mathrm{Gev}^{-1}$ [127] for axion masses of $m_a \lesssim 0.3\,\mathrm{meV}$.

A new way of enhancing this detection technique that is being studied and implemented is by the introduction of optical resonator cavities that may open unexplored regions of the parameter space. In this scheme, both the production and detection magnets are within Fabry-Perot optical cavities and actively locked in frequency. The experiments ALPS-II is based on this concept and aims to an improvement of 10^3 of $g_{a\gamma}$ in the year 2020 [129].

3.5.4 Other techniques

In addition to the three main techniques, there are other searches that have given limits to the axion coupling constants, but usually as a secondary result from experiments that investigate other fields.

One example are the **laser polarization experiments**, that use another approach to detect axions in a LSW experiment. It is based on the idea that if axions generate in the magnetic field from a photon beam, the polarization state of the beam will change. As the laser propagates through the first magnetic field, the component of the electric field of the beam that is parallel to the magnetic field will be reduced due to the production of axions, resulting in a rotation of the polarization vector (known as *dichromism*). Some experiments that are exploiting this technique are the BFRT [130] at the Brookhaven National Laboratory or the PVLAS [131] at the Legnaro National Laboratory.

Also, the **Bragg scattering** technique is based on the solar axion-photon conversion in the Coulomb field of the nuclei in the crystal lattice of crystalline detectors, more comonly used to detect WIMPs. This idea was originally proposed by E. A. Paschos and K. Zioutas [132], and it states that the conversion occurs when the angle of the incident axion fulfils the Bragg condition with the plane of the crystal. On this line, results have been reported from experiments such as SOLAX [133], DAMA [134], COSME [135],

CDMS [136] and EDELWEISS [137].

Some other experiments search for axions via more specific phenomenology, such as the axioelectric effect ($A + e + Z \longrightarrow e + Z$) that incident solar axions are supposed to produce when interacting with crystals (e.g. in [138–140]), or the axion-emitting nuclear transitions (e.g. in [141, 142]). Also, the Cosmic Axion Spin Precession Experiment (CASPEr) [143] will search for experimental signatures of the energy shift oscillations (with a frequency m_a) produced by the coupling of ALPs with gluons and fermions.

CHAPTER 4

IAXO: the International AXion Observatory

Contents

4.1 Introduction

The International Axion Observatory (IAXO) is a fourth generation axion helioscope that aims to reach sensitivities to the axion-photon coupling, $g_{a\gamma}$, of more than one order of magnitude higher with respect to the current best limits, with real potential of discovery.

This chapter is dedicated to the helioscope technique and the probability of detection, as well as the basic layout and the figure of merit. Then, the CAST experiment will be explained, as it has been a strong pillar for the IAXO helioscope design. After that, the main subsystems of the IAXO proposal will be explained, as well as the BabyIAXO helioscope as an early stage of IAXO. Finally, the physics potential of both helioscopes and their expected sensibilities to axion coupling to photons and electrons will be addressed.

4.2 Helioscope technique

Helioscopes are experiments that search for axions and ALPs emmited by the Sun. They are very well motivated because the axion emission by the solar core is a robust prediction that involves well known solar physics, as well as the model-independent conversion of plasma photons into axions, the Primakoff effect. Therefore, they do not rely on the assumption of axions forming the dark matter of the universe. Moreover, solar axions have energies of ∼keV, and if they reach a strong laboratory magnetic field, they can convert back into photons in the x-ray energy range, producing a detectable signal.

In this section, the solar axion flux as well as the expected photon flux from axion conversion will be explained. Then, the main experimental parameters that somehow affect the sensitivity to the axion couplings and the definition of the figure of merit of an enhanced axion helioscope will be addressed. The final section will be dedicated to the CERN Axion Solar Telescope (CAST), the most sensitive axion helioscope up to date.

4.2.1 Axion emission from the Sun

Axions can be produced in the hot thermal plasma of the core of the stars by several mechanisms. The most relevant production channel is the Primakoff conversion of plasma photons into axions because it is model-independent. If non-hadronic axion models are considered (DSFZ), then other processes like the axio-Bremsstrahlung, axio-Compton scattering and Atomic axio-recombination and deexcitation (or BCA reactions) [144, 145] can occur. Figure 4.1 shows the axion flux spctra at Earth by each of these mechanisms, as well as a Feynman diagram to illustrate them.

Even though the contributions from non-hadronic axions interacting with electrons can be greater than the contribution from the Primakoff effect, usually in helioscopes only the $a\gamma$ component is considered. The main reasons behind this choice are, first, that it maintains the generality only relying on model-independent phenomenology; also, it is conservative to consider only those processes at the source that are later used for the detection; furthermore, it covers a larger fraction of ALPs; and finally, astrophysical limits on g_{ae} are quite restrictive and the values at reach for helioscopes are generally disfavoured, although this could change with the IAXO experiment (more about this in section 4.5). Therefore, the results obtained by helioscopes are especially relevant for hadronic axions that do not couple to electrons at tree level, so that the Primakoff process is expected to be dominant.

In the core of the stars, the production of axions via Primakoff effect occurs when a plasma photon interacts with the Coulomb electromagnetic field of electrons and nuclei (described by equation 3.17). The solar plasma is considered non-relativistic because the temperature $T \ll m_e$, so the recoil effects of the electrons or nuclei can be neglected, and therefore, the energy of the initial photon and the produced axion will be the same, $E_\gamma = E_a = E$. The transition rate of a photon producing an axion of the same energy by

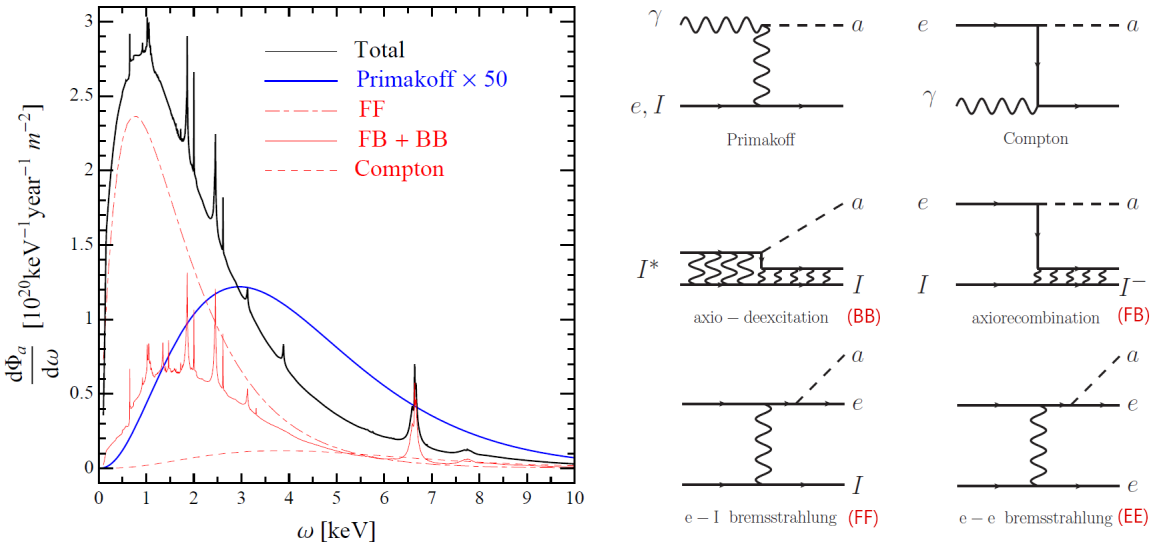

Figure 4.1: (Left) Solar axion flux spectra at Earth by different production mechanisms. Red lines represent individual contributions from mechanisms based on axion-electron coupling for $g_{ae} = 10^{-13}\,\mathrm{GeV}^{-1}$: Atomic recombination and deexcitation (FB+BB, solid), Bremsstrahlung (FF, dot-dashed) and Compton (dashed); the black line is the total contribution from mechanisms based on axion-electron coupling; and the blue line is the Primakoff flux from the axion-photon coupling for $g_{a\gamma} = 10^{-12}\,\mathrm{GeV}^{-1}$ (scaled up by a factor 50 to make it visible). **(Right)** Feynman diagrams of the reactions responsible for the solar axion flux in non-hadronic axion models (DSFZ). Figures adapted from [144].

Primakoff effect in the stellar plasma is [146]

$$R_{\gamma\to a} = \frac{g_{a\gamma}^2 T \kappa_s^2}{32\pi}\left[\left(1+\frac{\kappa_s^2}{4E^2}\right) ln\left(1+\frac{4E^2}{\kappa_s^2}\right)-1\right], \tag{4.1}$$

where κ_s^2 is a parameter called the Deybe-Huckel screening scale, that is a measure of the net electrostatic effect of a charge carrier in a plasma and how far its electrostatic effect persists. Beyond this scale, the axion production via Primakoff effect is significantly reduced. It depends in the plasma composition and its temperature.

The total axion flux at Earth can be obtained by combining the transition rate $R_{\gamma\to a}$ with the Bose-Einstein distribution of the thermal photons in the solar plasma, $(e^{E/T}-1)$, and then, integrating over the Sun volume and the photon energies. The complete calculations can be found in [147]. Using the solar model of Bahcall and Pinsonneault [148, 149], the axion flux at Earth, Φ_a, and the axion luminosity of the Sun, L_a, are found to be

$$\Phi_a = g_{10}^2 3.75\times 10^{11}\, cm^{-2}\, s^{-1}, \tag{4.2}$$
$$L_a = g_{10}^2 1.85\times 10^{-3}\, L_\odot, \tag{4.3}$$

where $g_{10} = g_{a\gamma}\times 10^{10}\, GeV^{-1}$ and $L_\odot$[1] is the photon luminosity of the Sun. The mean axion energy of the distribution is $\langle E\rangle = 4.20\,\mathrm{keV}$, and the most expected axion energy is $E_a = 3\,\mathrm{keV}$.

[1] $L_\odot = 3.8418\times 10^{33}\,\mathrm{erg\,s^{-1}}$, from [149]

An analytical approximation to the solar axion flux spectrum was found in [147] with a fit accuracy better than ∼1% in the interval 1-11 keV,

$$\frac{d\Phi_a}{dE_a} = 6.02 \times 10^{10} g_{10}^2 E_a^{2.481} e^{-E_a/1.205}\, cm^{-2}\, s^{-1}\, keV^{-1}. \tag{4.4}$$

4.2.2 Axion detection in a helioscope

Once the axions produced in the Sun reach the Earth and enter into the helioscope magnet, they must convert into photons in order to produce a measurable signal. Since the transformed photon will have the same energy than the former axion, E_a, the positive signal will be an excess over the x-ray background of the detector in the energy range of the axion flux spectrum. This energy region is what is known as Region of Interest (RoI).

The probability of an axion to convert into a photon, $P_{a\to\gamma}$, while going through a transverse and homogeneous magnetic field B (calculated in [118]) is

$$P_{a\to\gamma} = \left(\frac{g_{a\gamma}B}{2}\right)^2 \mathcal{F}(q, L), \tag{4.5}$$

where L is the length of the magnetic field, $g_{a\gamma}$ is the axion-photon coupling constant and $\mathcal{F}(q, L)$ is a term that accounts for the coherence of the process.

It is noted that the transition rate is maximum when the waves of the former axion and the produced photon are in phase, i.e. they are coherent along the detection volume. But since the axion is not massless, this coherence will be lost after a certain distance. A solution would be to fill the conversion region, in this case the cold-bore of the magnet, with an appropriate medium, in this case a buffer gas, to give the photons an effective mass m_γ that can be tuned to match the former axion mass, m_a.

This coherence term depends of the size of the conversion region, i.e the length of the magnet L; the axion-photon momentum transfer q; and the *damping*, Γ, that is the inverse photon absorption length in the specific medium, and can be expressed as [118]

$$\mathcal{F}(q, L) = \frac{1}{q^2 + \Gamma^2/4}\left[1 + e^{-\Gamma L} - 2e^{-\Gamma L/2}\cos(qL)\right], \tag{4.6}$$

where

$$q = \left|\frac{(m_\gamma^2 - m_a^2)}{2E_a}\right|, \tag{4.7}$$

and $m_\gamma = \sqrt{4\pi\alpha n_e/m_e}$, where n_e is the number density of electrons and m_e is the electron mass.

Therefore, there will be two detection strategies: to use a low-absorption buffer gas, or vacuum, and assure a coherent conversion for small axion masses in a wide range, or to fill the medium with a higher-absorption buffer gas and fulfil coherence for axions with bigger but more specific masses.

In the case of a helioscope operating in vacuum ($\Gamma = 0$ and $m_\gamma = 0$), the conversion probability can be expressed as

$$P_{a\to\gamma} = \left(\frac{g_{a\gamma}}{2}\right)^2 B^2 L^2 \left(\frac{2[1-\cos(qL)]}{(qL)^2}\right), \tag{4.8}$$

where the condition to preserve the coherence is that $qL \ll 1$. Considering the scales of the current helioscopes, in the case of a magnet length of $L \sim 10\,\mathrm{m}$, the coherence condition is fulfilled for axion masses up to $m_a \sim 10^{-2}\,\mathrm{eV}$.

In order to extend the sensitivity of the helioscope to higher axion masses, a buffer gas is required with the specific density and pressure to make the converted photons to acquire a mass such that $q = 0$, restoring the coherence of the process. This method allows tuning m_γ by changing the buffer gas conditions and therefore, to use the helioscope to explore different regions of the axion parameter space.

The final step after the axion-photon conversion is to estimate the expected number of photons to be detected by the x-ray detectors. A differential flux of photons, Φ_γ, can be obtained by

$$\frac{d\Phi_\gamma}{dE} = \frac{d\Phi_a}{dE} P_{a\to\gamma}, \tag{4.9}$$

and it is usually expressed by means of the specific length and the magnetic field of the magnet of the helioscope. As an example, the CAST expected photon flux for the 9.26 m and 9 T magnet would be [147]

$$\frac{d\Phi_\gamma}{dE} = 0.088\, g_{10}^4 E^{2.481} e^{-E/1.205} \left(\frac{L}{9.26\,m}\right)^2 \left(\frac{B}{9\,T}\right)^2 cm^{-2}\, s^{-1}\, keV^{-1}. \tag{4.10}$$

Finally, the expected number of photons in the x-ray detector N_γ is

$$N_\gamma = \int \frac{d\Phi_\gamma}{dE} A\, \epsilon\, t\, dE, \tag{4.11}$$

where A is the cross section area of the magnet bore, t is the data taking real time and ϵ is the detection efficiency. This efficiency depends of several parameters related to the different detection steps, and will be addressed in the next section.

4.2.3 Figure of merit

A big effort has been put during the last years to fully understand the dependence of the sensitivity to the axion couplings with each of the experimental parameters of a helioscope. This knowledge has lead to the definition of the basic layout of an enhanced axion helioscope [150], which involves a dedicated magnet with enlarged cross sectional area, where x-ray focusing optics are equipped together with low-background x-ray detectors. A conceptual scheme of this design is shown in figure 4.2.

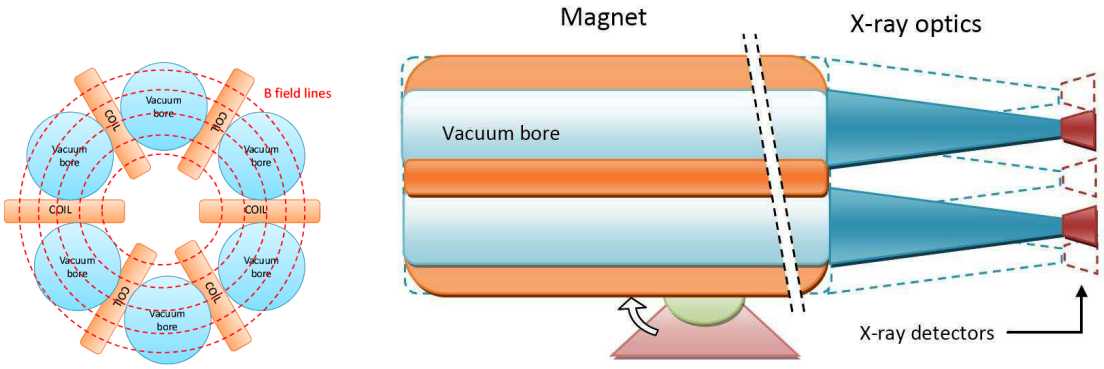

Figure 4.2: Basic design of an enhanced axion helioscope [150]. In this example, a toroidal magnet with six bores and coils is shown. At the end of each bore there are focusing x-ray optics and detectors attached. **(Left)** Cross section of the magnet with the six bores and coils and a representation of the magnetic field lines. **(Right)** Longitudinal section of the helioscope.

As seen in the previous section, the axion signal counts will come from the number of photons detected by the x-ray detectors, N_γ, that can be expressed as:

$$N_\gamma \propto B^2\, L^2\, A\, \epsilon\, t\, \times g^4 \equiv N^*\, \times g^4, \tag{4.12}$$

where B and L are the magnetic field and length of the magnet, A is the cross sectional area of the bores, and ϵ is the efficiency, that can be factorized as

$$\epsilon = \epsilon_d\, \epsilon_o\, \epsilon_t, \tag{4.13}$$

where ϵ_d is the efficiency of the detectors, ϵ_o is the focusing efficiency of the optics, assuming that such optics cover the entire cross sectional area, and ϵ_t is the fraction of measuring time when the magnet is pointing the Sun, known as the data-taking efficiency.

When the magnet is not pointing to the Sun, the data recorded is considered *background data*. This is also important because it gives the baseline over which the axion signal should be found. The number of background counts, N_b, can be parametrized as

$$N_b = b\, a\, \epsilon_t\, t, \tag{4.14}$$

where b is the normalized background of the detector in area and time units, a is the spot area where all the signals from the magnet will be focused by the optics and t is the total time of the data taking.

Therefore, and assuming that the measurement is dominated by the background ($N_b > N_\gamma$), and also that the exposure of the experiment is enough to be in the Gaussian regime (i.e. $N_b \gtrsim 10$, so the standard deviation on the expected background counts is $\sigma_{N_b} = \sqrt{N_b}$), then the discovery potential of the experiment depends on the ratio $N_\gamma/\sqrt{N_b}$. Taking into account equation 4.12, the sensitivity on the corresponding axion coupling (to photons or, if possible, to electrons), can be expressed as

$$g^{-4} \sim \left(\frac{N*}{\sqrt{N_b}}\right). \tag{4.15}$$

This expression can be used to define the *figure of merit* (FOM), f, which is a useful way to express the *merit*, or value, of the different parameters for the total sensitivity of the experiment.

In conclussion, the FOM of an enhanced helioscope can be written as

$$f \equiv \frac{N^*}{\sqrt{N_b}} = f_M \, f_{DO} \, f_T, \tag{4.16}$$

where each factor is chosen to show the contributions from the different experimental steps: the influence of the Magnet parameters in the axion-photon conversion, f_M; the effect of the Detectors and Optics in the photons collection and measurement, f_{DO}; and the effective exposure time of the experiment, f_T:

$$f_M = B^2 \, L^2 \, A, \quad f_{DO} = \frac{\epsilon_d \, \epsilon_o}{\sqrt{b \, a}}, \quad f_T = \sqrt{\epsilon_t \, t}. \tag{4.17}$$

From this FOM, it is clear that the parameters of the magnet are important for the sensitivity of an enhanced axion helioscope, for which a large and potent magnet with bores that have big cross sections is favoured. Secondly, highly efficient x-ray optics that focus the signal to a very small spot on the readout surface of a highly efficient ultra-low background detector are both required. And finally, although it has less impact on the sensitivity than the other parameters, a system that allows the movement of the magnet to assure the longest tracking time is also important.

4.2.4 CAST: The CERN Axion Solar Telescope

The CERN Axion Solar Telescope (CAST) experiment has been the most sensitive axion helioscope up to date. It was proposed in 1999 by K. Zioutas et al. [122], commissioned between 2000-2003 at the building SR8 at CERN and started its physics research program in 2003. From then on, it has been operating with different detectors, searching mainly for solar axions. Figure 4.3 shows a picture and a scheme of the CAST experiment.

The CAST layout

CAST uses one of the decommissioned superconducting dipole magnet of the LHC that provides a magnetic field up to 9 T for the solar axions to convert into photons. This magnet is 9.26 m long and it is composed by two straight magnetic bores with an aperture of 14.5 cm^2 each. They can be operated in their superconductive regime at a nominal temperature of 1.8 K thanks to a cooling system. A vacuum system allow to isolate the cold-bores and maximize the x-ray transmission through them. These bores are also prepared to be filled with different buffer gases and therefore, extend the axion search towards higher axion masses, as it was explained in section 4.2.2. This gas system was used to operate the experiment with ^{3}He and ^{4}He at different pressures.

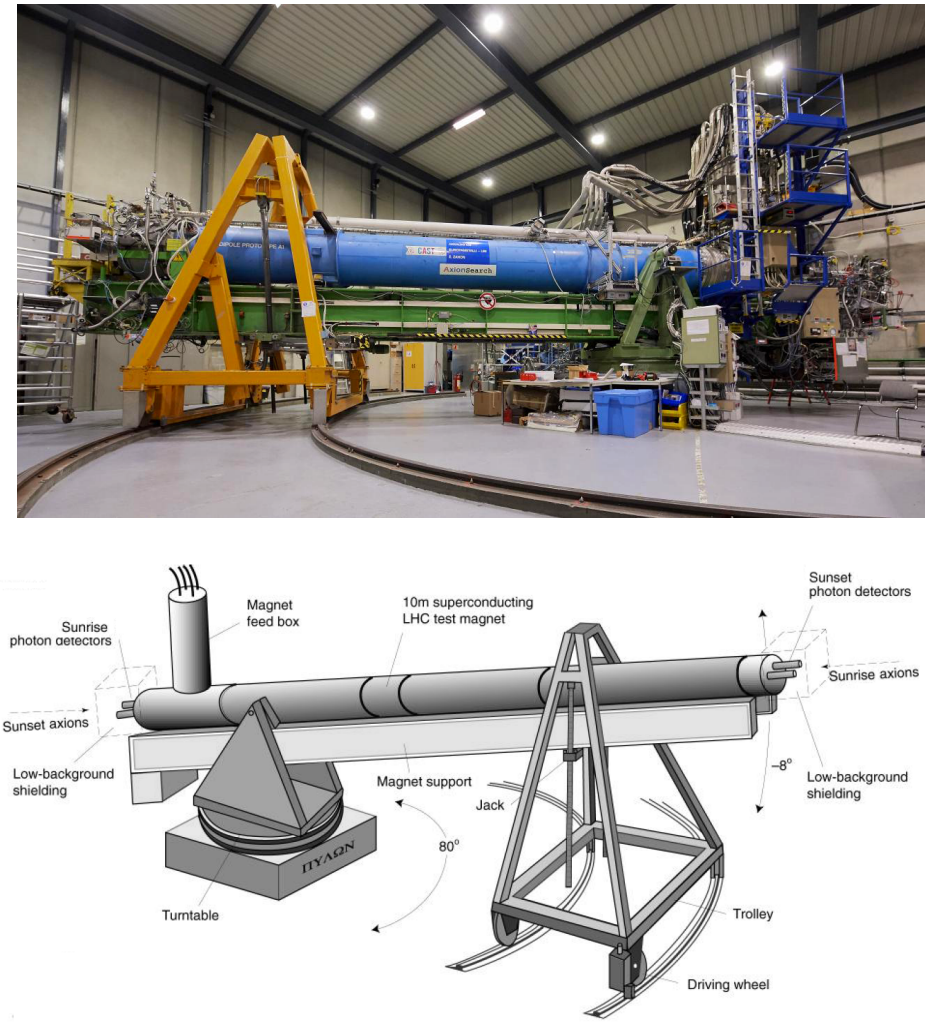

Figure 4.3: (Top) The CERN Axion Solar Telescope. **(Bottom)** A scheme of the main components of CAST. A LHC superconducting test magnet is mounted over a movable structure that allows it to track the Sun during sunrise and sunset. At the ends of the bores of the magnet, four x-ray detectors are attached, two of them with x-ray focusing devices to focus the signal produced in the magnet.

The magnet is sitting on top of a rotating platform that enables a vertical movement of [-8,8]° and an azimuthal movement of 80°, which allowed the magnet to track the Sun during ∼1.5 hours, twice per day, at sunrise and sunset ($\epsilon_t \sim 0.12$). The pointing accuracy of the system is monitored to be below 10% of the solar radius.

The two bore magnet allows the implementation of four detectors at the same time, two at each end of the magnet. The sides are named after the period of the day when the detectors are taking tracking data: sunrise (SR) and sunset (SS) lines (and detectors). During non-tracking time, the detectors are calibrated and background data is collected. Along the years, different types of x-ray detectors with low background and high efficiency for the CAST RoI, [2,7] keV, have been used in the experiment. The main detectors that have contributed to the axion research in CAST are:

- **A pn-Junction Charge Coupled Device (pn-CCD)** [151], installed at the beginning of the experiment at one of the sunrise lines until 2014. This detector was a fully depleted silicon pn-CCD detector with a sensitive surface of 30×9.6 mm divided in pixels of 150 μm side. It was operated together with an x-ray focusing device and the spot generated over the surface had only a diameter of ∼19 pixels. This allowed the detector to measure signal at the center of the surface and background at the edges simultaneously. If no excess in the number of counts was found in the solar axion spot area with respect to the rest of the surface, the result was an upper limit of $g_{a\gamma}$.

  This detector had an efficiency $\epsilon_d \gtrsim 95\%$ and background levels of $(8.00 \pm 0.07) \times 10^{-5}$ counts keV^{-1} cm^{-2} s^{-1} in the [1,7] keV energy range and the total area of the readout. Some studies of the pn-CCD background showed that the dominant componen was coming from external gammas [152].

- **A TPC with a multiwire proportional counter (MWPC) readout plane** [153], also installed at the beginning of the experiment, that extended over both bores of the sunset side. This gaseous detector was taking data until 2008 with a mixture of Ar+CH_4 (95/5)% at 1 bar, and it had a 15×30 cm^2 readout surface with a 10 cm drift conversion volume. The readout had two planes of wires with 48 wires in the anode plane and 68 wires in the cathode plane that were set perpendicularly to the anode ones. Also, two 5 μm thick aluminized Mylar[2] foils glued on metallic grid structures acted as the differential windows to separate the gas of the TPC from the vacuum of the magnet bore.

  This detector also had some passive shielding to reduce the background: it was covered by a 25 mm thick copper box and also, by a layer of lead to block the environmental gamma radiation. A 22.5 cm thick polyethylene layer was used to thermalize neutrons and then, a cadmium layer was placed to absorb them. Also, a muon active veto was installed at the top of the detector to reject background from cosmic sources. The radiopurity of the materials was taken into account in the design of the detector, and the topological information provided by the MWPC readout allowed to develop offline background rejection algorithms. These techniques to reduce the radioactive background of a detector will be further explained in chapter 5. Overall, this TPC achieved a background level of the order of 4×10^{-5} counts keV^{-1} cm^{-2} s^{-1} in the CAST RoI with an efficiency of $\epsilon_d \sim 100\%$ for x-rays.

- **Various microbulk Micromegas detectors (MM)**, installed at both sunrise and sunset lines in 2008. Two MM replaced the former MWPC detector at the sunset side, and another MM was installed at the last free sunrise line. They are based in the Microbluk technique and were designed with radiopure materials. Their readouts have typically amplification gaps of 50 μm and sensitive areas of 60×60 mm^2, divided

[2]Mylar is a polyester film (biaxially-oriented polyethylene terephthalate or BoPET) made from stretched polyethylene terephthalate (PET) that can be aluminized by evaporating a thin film of metal onto it to reduce its permeability. It is commonly used in CAST to build x-ray windows because it is a stable material with high tensile strength, it is mostly transparent to x-rays in the RoI and also, it is radiopure [154].

in square pads of 400 μm. The pads are interconnected in x and y directions (strips) with a pitch of 500-550 μm, depending on the MM model. They worked inside of gaseous TPCs with 3 cm drift volumes filled with Ar+C_4H_{10} (98/2)% at 1.4 bar.

These detectors went through some changes and improvements along with the Micromegas technology development. Different passive and active shielding techniques were implemented over the years, and they resulted in the lowest background detectors of the CAST experiment. The evolution of the background of the different Micromegas detectors in CAST will be described in section 5.4.1. The lowest background mark registered in the CAST experiment corresponds to the sunrise Micromegas line in the vacuum revisit period in 2014 (see table 4.1). An x-ray focusing device was installed in this line for this data taking campaign, and its combination with a state-of-the-art microbulk Micromegas detector resulted in a background of $(1.0 \pm 0.2) \times 10^{-6}$ counts keV^{-1} cm^{-2} s^{-1} in the CAST RoI and the spot area [155].

- **An integrated Micromegas with a silicon sensor (InGrid)**, installed in 2014 in the sunrise line with the first x-ray telescope, replacing the pn-CCD. This detector integrates a Micromegas gas amplification structure with a silicon readout chip anode produced by wafer postprocessing technique [156]. A mesh (or grid) is suspended over the wafer anode by insulating pillars creating an amplification gap of 50 μm. This manufacturing technique produces very uniform gaps, what makes this detector to have superior energy resolution than a conventional Micromegas. Furthermore, each mesh hole is precisely aligned to the pixels below them. All these features result into a readout with very low energy thresholds that provides detailed topological information of the event.

  The InGrid is operated in a 3 cm drift gaseous TPC with a mixture of Ar+C_4H_{10} (97.7/2.3)% at 1 bar, and a Mylar differential window separates the gas volume from the vacuum line. The readout of the InGrid that operates in CAST is a Timepix ASIC [157] with a surface of 1.4×1.4 cm^2 that is divided in pixels of 55 μm side. This detector shows a good energy resolution and efficiency in the CAST RoI and it registers a background of the order of $\sim 10^{-5}$ counts keV^{-1} cm^{-2} s^{-1} [158].

Finally, two of the magnet bores are instrumented with x-ray optics that focus the expected signal in a few mm^2 area on the detector surface, enhancing the signal-to-background ratio and increasing the identification potential [159]. The first x-ray optic was implemented in 2003 for the pn-CCD line and it is a Wolter I type mirror system, that is actually a spare module of the ABRIXAS satellite mission [160]. This mirror system consist of *nested* radial reflection surfaces with decreasing radius, and will be explained in more detail in section 4.3.2. In 2014, another detection line was equipped with a Wolter I x-ray optics, but in this case, the telescope was fabricated with the CAST experiment requirements and optimised for axion detection. It was implemented in the sunrise Micromegas detector line, what is considered the IAXO pathfinder [155], and was operating in vacuum mode until 2015. The results of this last phase of CAST are very relevant for the IAXO experiment, and are further explained in section 5.4.2.

Year	Phase	Mass range (eV)	g_{10} (GeV^{-1}) (95% C.L.)
2003-2004	Phase I - vacuum	$\lesssim$0.02	1.16 [161]
2006-2007	Phase II - ^{4}He	0.002 - 0.39	2.17 [162]
2008-2011	Phase II - ^{3}He	0.39 - 0.64	2.27 [163]
2008-2011	Phase II - ^{3}He	0.64 - 1.17	3.3 [164]
2012	Phase II - ^{4}He	0.39 - 0.42	1.47 [165]
2013-2015	Vacuum revisit	$\lesssim$0.02	0.66 [34]

Table 4.1: Main results from the CAST axion research program since the beginning of the experiment up to 2015, when the last Micromegas detector was dismantled.

The CAST axion research program

The CAST axion research program started in 2003 and it has gone through different phases with different detectors and buffer gases. The main results of the experiment are upper limits to the axion coupling constant, $g_{a\gamma}$, because thus far, no positive axion signal has been recorded. Table 4.1 shows the axion coupling limits for the different axion mass ranges that have been prospected with the CAST helioscope. Also, figure 4.4 shows the exclusion plot in the $g_{a\gamma} - m_a$ parameter space from the CAST results.

Phase I refers to the first year of data taking with vacuum in the cold-bores of the magnet. During this phase, axion masses up to $m_a \lesssim 0.02\,\text{eV}$ were probed, and a limit to the axion-photon coupling constant was set to $g_{a\gamma} < 1.16 \times 10^{-10}\,\text{GeV}^{-1}$ (95% C.L.), which is comparable to the stellar energy-loss arguments and more restrictive than any previous experiment over an extensive range of axion masses.

Then, during Phase II, the magnet bores were filled first with ^{4}He to increase the axion mass range. The strategy was to increase the gas density (i.e. the pressure) in steps, to change the gas photon absorption (as it was explained in section 4.2.2). During this data taking, axion masses of $0.002 < m_a < 0.39\,\text{eV}$ were probed in 160 pressure steps, and a limit was set to the axion-photon coupling of $g_{a\gamma} < 2.17 \times 10^{-10}\,\text{GeV}^{-1}$ (95% C.L.). The following data taking campaigns used ^{3}He as the buffer gas because it condensates at higher pressures than the ^{4}He, so higher axion mass ranges could be explored. Two campaigns were carried out with this gas, the first one explored the axion mass range of $0.39 < m_a < 0.64\,\text{eV}$ in 252 density steps, setting a limit of in the axion coupling of $g_{a\gamma} < 2.27 \times 10^{-10}\,\text{GeV}^{-1}$ (95% C.L.); and the second campaign explored the axion mass range of $0.64 < m_a < 1.17\,\text{eV}$ in 452 density steps, what resulted in a limit of $g_{a\gamma} < 3.3 \times 10^{-10}\,\text{GeV}^{-1}$ (95% C.L.). To finish this Phase II of the program, in 2012 the bores were filled again with ^{4}He, to revisit the highest part of the reachable mass range with upgraded and more sensible detectors. An axion mass range of $0.39 < m_a < 0.42\,\text{eV}$ was explored and again, the absence of a positive signal over the background set an upper limit in the axion coupling of $g_{a\gamma} < 1.47 \times 10^{-10}\,\text{GeV}^{-1}$.

The last data taking campaign in the CAST axion research program was performed

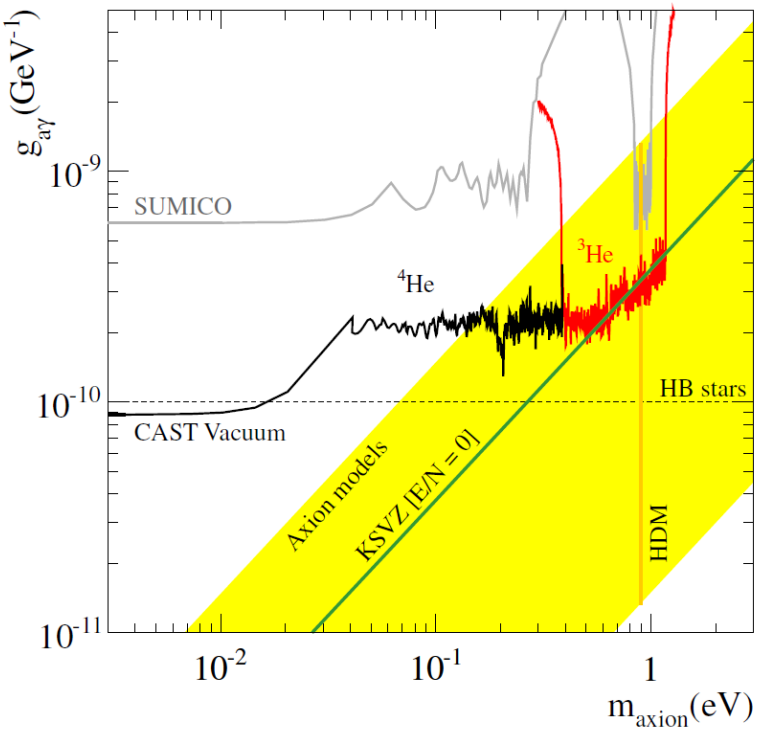

Figure 4.4: Exclusion plot in the $g_{a\gamma}$-m$_a$ parameter space from the CAST results in the different phases: vacuum, ^{4}He and ^{3}He. The constrains from SUMICO [120, 121] are also shown, as well as the astrophysical constrains of horizontal branch (HB) stars and of Hot Dark Matter (HDM). The yellow band represents the QCD axion models, and the green line represents the KSVZ model with $E/N = 0$. Figure from [164].

with the previously mentioned IAXO Pathfinder setup: an ultra-low background microbulk Micromegas working together with a focusing x-ray telescope. The improved detection performance justified the revisit of the vacuum phase, which correspond to axion masses of $m_a \lesssim 0.02\,\text{eV}$. From this last campaign, the most restrictive limit for the axion-photon coupling was obtained: $g_{a\gamma} < 0.66 \times 10^{-10}\,\text{GeV}^{-1}$ (95% C.L.).

Overall, the third generation CAST helioscope was a big improvement from the previous generations, probed the physical potential of axion helioscopes over its 15 years of axion research program and set the pillars for the basic layout of an enhanced fourth generation helioscope.

4.3 The IAXO proposal

The International Axion Observatory (IAXO) [43, 150] is a proposed 4th-generation helioscope with the main goal of searching for axions and ALPs emitted by the core of the Sun via Primakoff Effect. The expected sensitivity of IAXO for the axion-photon coupling constant is $g_{a\gamma} \sim 10^{-12}\,\text{GeV}^{-1}$ for a wide range of axion masses up to $m_a \lesssim 0.25\,\text{eV}$. This translates into a factor ∼20 better than the CAST sensitivity, and into 4-5 orders of

magnitude more sensitive in terms of signal-to-background.

With this sensitivity, IAXO will be able to enter into completely unexplored axions and ALPs parameter space, having potential for discovery. If no positive signal is found, it will firmly exclude a big region of such parameter space. And of course, in case of axion discovery, it would be a groundbreaking result for particle physics.

IAXO is designed following the basic layout of an enhanced axion helioscope. A conceptual design is shown in figure 4.5. It will feature a large superconductive 8-coil toroidal magnet optimized for axion search. All the magnet aperture will be equipped with x-ray optics that will focus the axion conversion photons flux into a $\sim 0.2\,\mathrm{cm}^2$ spot on the readout surface of ultra-low background x-ray detectors. Also, the magnet will be built into a movable structure that will allow solar tracking for $\sim$12 hours each day.

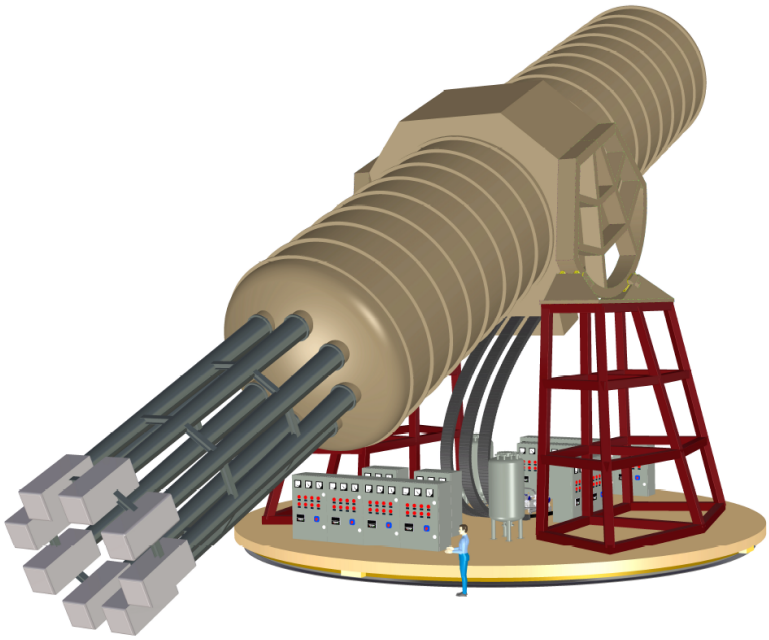

Figure 4.5: Conceptual design of the IAXO enhanced helioscope. A large superconductive magnet will track the sun to allow axion-photon conversion in the magnetic bores. X-ray optics will focus the photon flux into a small area, or spot, on the surface of ultra-low background x-ray detectors.

In this section, the three main subsystems of the IAXO enhanced helioscope will be described: the superconductive magnet, the x-ray focusing optics and finally, the ultra-low background x-ray detectors.

4.3.1 Superconductive magnet

The FOM study has shown that the parameters of the magnet have a really big impact in the sensitivity of the helioscope. It is clear that a dedicated magnet specifically manufactured for axion searches is necessary, with a design that maximizes the magnet

FOM, $f_M = B^2L^2A$. Remembering from equation 4.17, B and L are the magnetic field intensity and the length of the magnet respectively, and A is the aperture, or cross section, of the bores that is covered by x-ray focusing optics.

From the current available technology, a cost-wise option would be to use NbTi superconductor technology, that provides peak magnetic fields up to $B = 5 - 6\,\mathrm{T}$. And since the length of the magnet is limited by technical manufacturing (and cost) reasons, the only parameter that can be considerably enlarged, in comparison with previous generation helioscopes like CAST, is the aperture of the bores. For that, the magnet design proposal is a toroidal geometry with eight racetrack coils of 1 m in width and 21 m in length, wich makes a magnet of 5.2 m in diameter and 25 m in length. It is designed to allow a peak magnetic field of 5.4 T with a total stored energy of 500 MJ and an operational current of 12.3 kA.

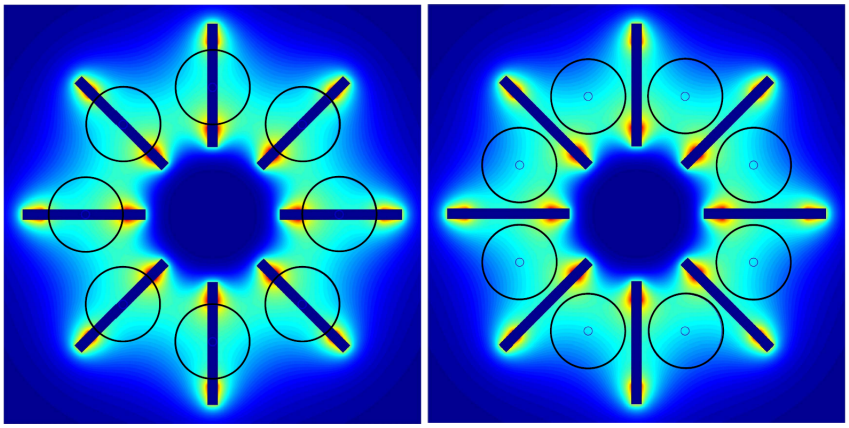

Figure 4.6: Representation of the two considered scenarios of the alignment of the telescopes (circles) with the magnet coils (rectangles). **(Left)** *Field dominated* scenario, where the telescopes are placed behind the coils. **(Right)** *Area dominated* scenario, where the telescopes are placed between the coils.

To obtain the value of f_M for the IAXO magnet, a length of $L = 20\,\mathrm{m}$ is considered, and the B is integrated over the open area that is covered by the x-ray optics. Two possible scenarios are considered in regard to the optics placement with respect to the magnet, and they are shown in figure 4.6. The first scenario, or *field dominated* scenario (figure 4.6, left), would be to place them behind the racetrack coils in order to align them to the areas where the magnetic field is higher. The second scenario, or *area dominated* scenario (figure 4.6, right), would consist of placing the optics aligned with the bores, and therefore to take advantage of the entire aperture while the magnetic field is not as high. An optimization study was made and showed that the area dominated alignment was favoured to maximize the f_M.

A scheme of the section of the magnet is shown in figure 4.7. It was designed at CERN following well known and proven engineering solutions from the ATLAS toroids. The total mass of the magnet is estimated to be ∼250 tons. An inner cylindrical support holds the weight and magnetic forces of the eight coils, helped by Al5083 keystone elements for both gravitational and magnetic loads support. The total cold mass consist of eight coils of ∼130 tons operating at a nominal temperature of 4.5 K. They are embedded in

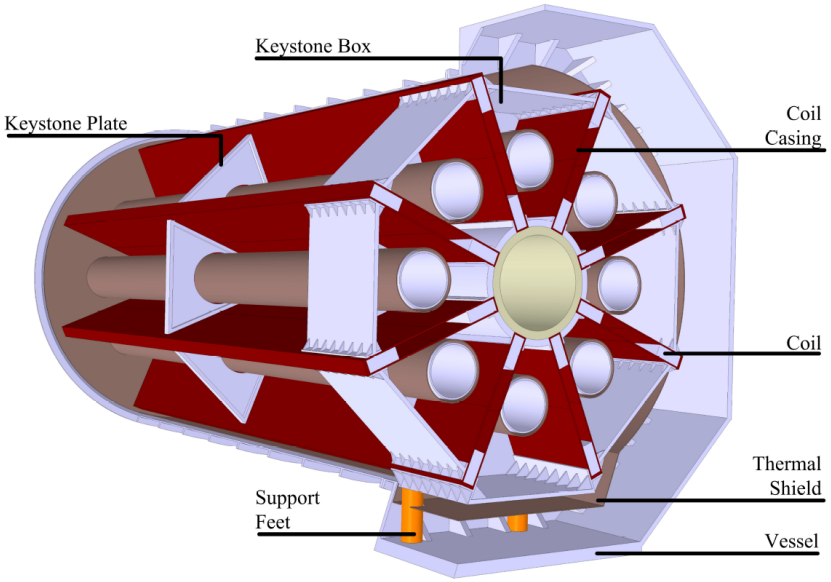

Figure 4.7: Section of the IAXO cryostat. The cold mass (coils) is supported by a central cylinder and embedded in Al5083 alloy casings. The open bores are placed between the coils, closer to the central cylinder to maximize the magnetic field inside them. A thermal shield surrounds the cold mass, and a vacuum vessel isolates it from the exterior.

Al5083 alloy casings which are attached to the inner support cylinder. The purpose of these casings is to minimize the possible coil deflection caused by the magnetic forces. Then, eight cylindrical open bores are placed between the coils, as close to the inner part of the coils as possible in order to maximize the f_M.

The conductor that forms the coils have 40 strands of NbTi/Cu Rutherford cable with 1-3 mm of diameter, following the techniques used in ATLAS or CMS magnets at CERN [166]. This Rutherford type superconducting element provides high performance and high current densities. An Al-based doped stabilizer is used in order to protect the magnet from quench[3] and also, to improve the stability of the superconductor.

The coils are cooled down by a conductive circuit that is attached to the coil casings. These pipes circulate a flow of sub-cooled liquid helium at supercritical pressure, which is able to cool the coils to a temperature of 4.5 K. A thermal shield surrounds the cold mass, and it is also cooled by a flow of helium gas between 40 and 80 K. This is a well known and low-cost technology proven by the ATLAS toroids.

All the system is enclosed in an Al5083 vacuum vessel that is designed to be as light and thin as possible, while being able to hold the atmospheric pressure difference and the gravitational load. The complete system will be supported by the cryostat central

[3] A quench occurs when a rise in temperature triggers a sudden loss of superconductivity of the coils of the magnet. When the coils are in superconducting state, they present zero resistance, so if the coil temperature rises and the superconductivity state is lost, the coils suddenly develop a finite resistance. This can make that the high currents that circulate through the coil create a rise in the temperature causing an explosive boil-off of liquid helium.

post placed at its center of mass, where an altitude-over-azimuth mount configuration will support and rotate the magnet. This type of mounts are broadly used for large telescopes, and it will allow a vertical inclination of $\pm 25^{\circ}$ and a 365° horizontal rotation independently. This mobility is required in order to increase the data-taking efficiency, ϵ_t, so the magnet will be able to track the sun as long as possible.

Finally, other systems such as quench protection circuits, to avoid damages due to rises of temperature in the coils, are also considered. Quench detector circuits are placed along the coils of the magnet, and when a temperature increase is detected, a series of heaters ensure a fast and uniform heat propagation while the current is discharged through a dump-resistor.

4.3.2 X-ray optic telescope

The x-ray optics are another important element of an enhanced helioscope that allow focusing the possible x-ray signal produced by axion conversion in the magnet bores to a small spot on the detector's readout. This feature enables the use of smaller detectors with lower radioactive backgrounds. The IAXO *pathfinder* setup in CAST has proven this concept with an x-ray telescope from the NASA's NuSTAR mission [167], and very good results in terms of signal-to-background ratio have been obtained [155]. The baseline technology for the IAXO x-ray optics will follow that used in the IAXO *pathfinder*: segmented, slumped glass Wolter I optics with multilayer W/B_4C coated mirrors in 124 nested layers (or shells). Figure 4.8 shows the x-ray optics design for IAXO.

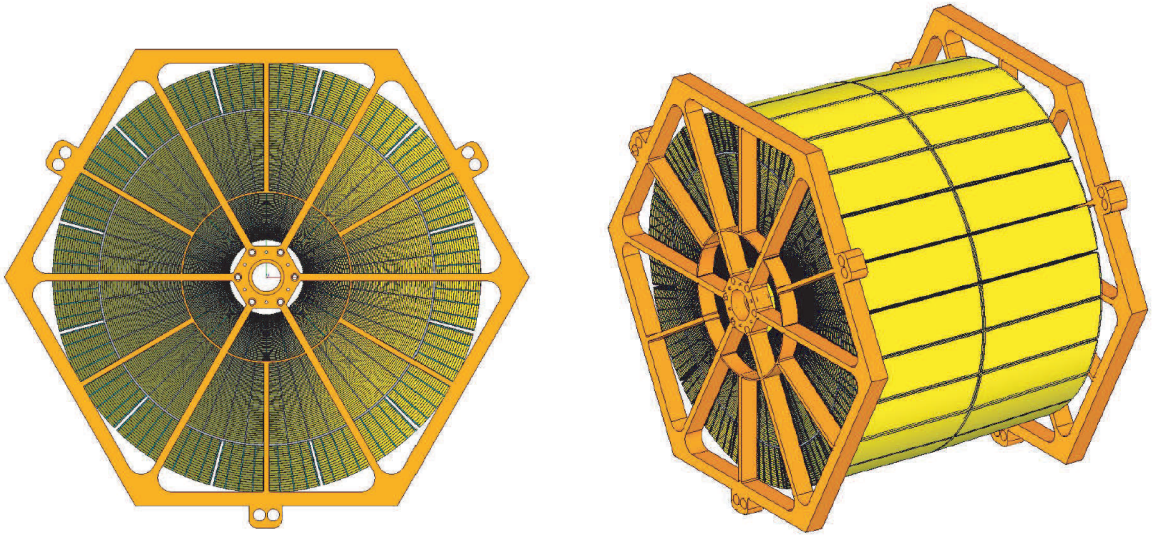

Figure 4.8: Frontal and isometric views of the IAXO x-ray optics. The thousands of mirror segments are shown, as well as the hexagonal *spider* structure designed to attach the optics to the magnet bores.

The main concept of these type of focusing optics is shown in figure 4.9. Basically,

the photons produced by conversion in the bore magnetic field will have the same direction than the former axions, so they will reach the reflective mirrors of the optics with a very small grazing angle[4], α. Each photon will be reflected twice, and due to the geometry of the optics, all of them will be focused to the same small spot.

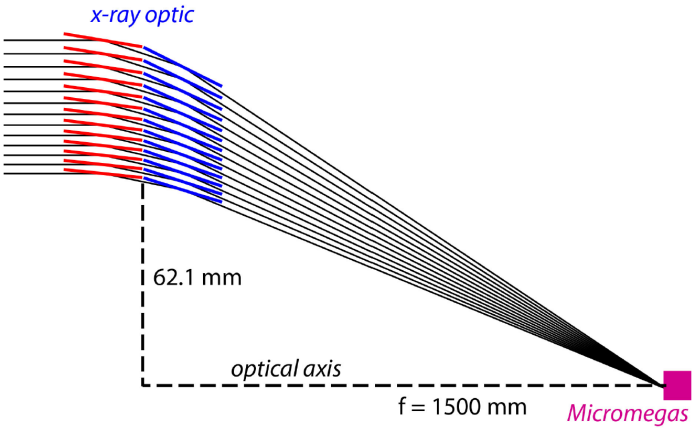

Figure 4.9: Conceptual scheme of the cross-section of a segmented glass focusing optic. The measurements correspond to the CAST pathfinder setup. Black lines represent photons that reach the optics from the magnet bore. Each photon is reflected twice and they are finally focused to a small region on the detector (Micromegas) readout plane.

The performance of the x-ray optics can be described by three parameters: the Point Spread Function (PSF), which is the shape of the focused spot; the throughput (ϵ_o), that is the amount of incident photons that result focused to the corresponding spot; and the Field-Of-View (FOV), which is the extent up to which the optic device can properly focus off-axis x-rays. Taking into account that the area of the spot, a, grows quadratically with the focal length, f, (i.e. $a \propto f^2$), the focal length of the optics should be short in order to obtain a small spot. However, the reflectivity of the individual mirrors of the optics increases with small grazing angles. This angle is inversely proportional to the focal length, $f \propto \alpha^{-1}$, so the highest throughput will be achieved for long focal lengths. Moreover, the dependence of the ϵ_o, FOV and PSF parameters with the energy of the incident photon, E_i, and α is complex, so the optimization of the x-ray optics is non trivial.

A thorough study of the optics parameters in regard to the detector efficiency and the axion spectrum was made [43] in order to optimize the FOM, f_{DO}, previously discussed in equation 4.17. A concept was introduced that accounts for the *detected axion flux* (DAF), which is defined as the energy-dependent axion flux (described in equation 4.4) multiplied by the optics throughput, ϵ_o, and the detector efficiency $\epsilon_d(E)$. Figure 4.10 shows the dependence of the DAF with the spot size and the focal length. From this study, the optimal figure of merit was found for a focal lenth of $f = 5\,\mathrm{m}$.

This type of x-ray optics have many advantages to be considered for IAXO. First, it is a well known technology that has been developed by members of the IAXO

[4]The grazing angle is the angle between the incident direction of the x-ray and the surface of the reflective mirror. This term is commonly used when the incident beam is almost parallel to the reflective surface.

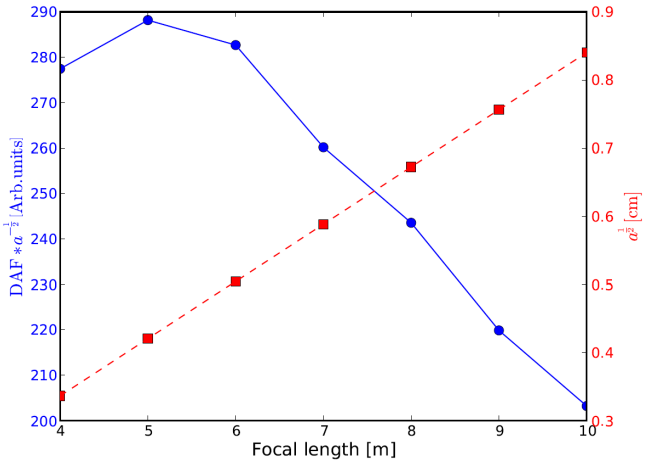

Figure 4.10: (Left axis) The figure of merit $DAF \times a^{-1/2}$ versus the focal length, f. **(Right axis)** The focal spot size $a^{1/2}$ versus the focal length f. The optimal FOM is found at $f = 5\,\mathrm{m}$.

collaboration, in the context of NuSTAR. Also, this approach facilitates the deposition of single-layer or multi-layer reflective coatings that ultimately enhances the throughput and allows optimizing the spectral response of the optics. In addition, the manufacturing process is mature and one of the least expensive available. Finally, although other optic technologies may have better imaging capabilities, the IAXO solar observation needs are very modest, only requiring to focus the central 3 arcminute core of the Sun.

4.3.3 Ultra-Low background x-ray detectors

The baseline technology for the IAXO low background x-ray detectors are small gaseous TPCs with a pixelated microbulk Micromegas readout and a thin window to allow the entrance of the x-rays to the gas chamber. As previously seen, these detectors have proven to show a suitable performance for axion searches in helioscopes and also, to develop very low levels of background, so they are perfect candidates to meet the IAXO requirements.

The design of the Micromegas detectors for IAXO is very similar to that used in the IAXO *pathfinder* setup in CAST (see section 5.4.2). Figure 4.11 (left) shows a conceptual scheme of the working principle of the TPC adapted to this particular scenario: x-rays from axion conversion would enter to the gas chamber through a thin window which acts as the cathode of the TPC. This window holds the gas of the detector and withstand the pressure difference between the gas and the vacuum pipe that connects with the optics. Also, it has to be x-ray transparent so it does not worsen the detection efficiency. Mylar foils have commonly been used for this purpose in several CAST detectors, supported by a copper structure (the *strongback*). Then, the drift distance of the TPC is chosen to be long enough to efficiently stop x-rays within the axion spectrum. From CAST experience, it is known that a 3 cm long drift at ∼1.5 bar with an argon penning mixture suits the needs. Finally, at the anode of the TPC it is placed a microbulk Micromegas readout, which faces the window, and that is located at the focal point of the x-ray optics.

A 3D representation of the Micromegas detector design is shown in Figure 4.11 (right). The TPC chamber is closed at the top by the window cathode (*strongback*), that connects directly to the interface pipe that will be attached to the optics. At the bottom, the chamber is closed by the copper substrate (*raquette*) of the Micromegas readout. All the pieces are made out of radiopure copper (Cu-ETP), and the inner side of the chamber and pipe is covered in a thin layer of radiopure PTFE to prevent the possible fluorescences of the copper. This same design has been used in this work for the commissioning of the IAXO-D0 prototype (that will be introduced in section 4.4.2), so a detailed technical description can be found later in chapter 8.

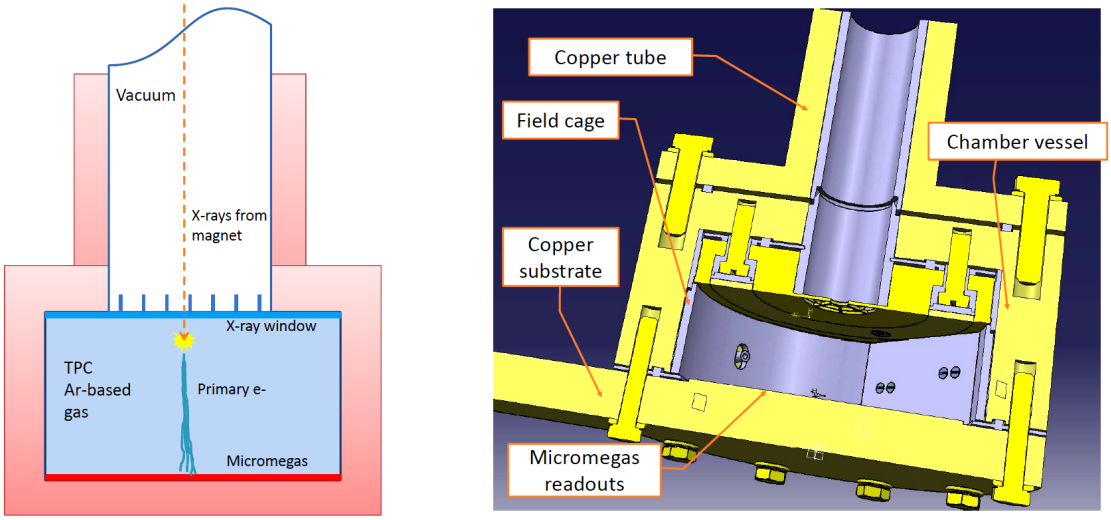

Figure 4.11: (Left) Conceptual scheme of a TPC gaseous detector with a microbulk Micromegas readout adapted for axion searches in a helioscope. A gas-tight x-ray transparent window holds the gas of the chamber and allows the entrance of the x-rays from the vacuum pipe. The drift volume is selected specifically to stop the x-rays within the energy RoI. **(Right)** Design of a IAXO detector prototype.

Also, all the known low-background techniques learnt from the CAST experience and from independent bench tests will be considered in order to reduce the radioactive background of the IAXO detectors. This topic will be addressed in detail in chapter 5 because it is a very important point for the development of this *thesis* work. In a nutshell, to obtain the lowest possible background, the detector need to be built with very radiopure materials. Some screening programs have been done in the context of the CAST and TREX [168, 169] projects, in order to measure the rates of the radioactive contaminants of all the materials involved in the detector's design. Also, passive shielding, like a surrounding layer of dense and high-Z materials (lead), and active shielding, like cosmic vetoes, can avoid the interaction of external radiation in the detector, or identify it to be able to offline discard background. Furthermore, a small granularity of the detector readout combined with offline analysis and rejection algorithms can help to obtain the topological information of the events that interact inside the TPC and therefore, reject the non x-ray-like signals.

Other advantages of microbulk Micromegas detectors that make them appealing for IAXO are that they provide high time stability, as well as good spatial and energy

resolutions. Moreover, their consolidated manufacture technique makes them very robust and relative cost-effective, and also, the patterning of the anode plane is very flexible, so different patterns can be build for different needs.

Finally, even though Micromegas are the baseline technology for the IAXO detectors, the experiment has been conceived as a generic infrastructure for axions and ALPs physics, with potential for additional detector technologies and search strategies. Currently within the IAXO Collaboration, a R&D of alternative detection techniques with excellent energy resolution, energy thresholds and efficiency, and also, with the possibility of using radiopure materials to decrease their backgrounds, is ongoing. Some of the technologies that are being considered are listed below.

- **GridPix** detectors [170], developed by the groups in Bonn and Siegen, which can reach energy thresholds of 300 eV and background levels of $\sim 10^{-5}$ counts keV^{-1} cm^{-2} s^{-1}.
- **Metallic Magnetic Calorimeters (MMC)** dispersive detectors [171, 172], developed by the Heidelberg group, that present quantum efficiencies of 99% for x-rays at 6 keV, energy resolutions of 1.6 eV (FWHM) and backgrounds of $\sim 10^{-5}$ counts keV^{-1} cm^{-2} s^{-1} between 6 and 10 keV.
- **Neutron Transmutation Doped (NTD) detectors** [173, 174] instrumented thin Ge bolometers can be considered due to their low noise and high energy resolution (0.2-0.4 keV FWHM for 5.9 keV x-rays of ^{5}5Fe). Backgrounds of $\sim 10^{-6}$ counts keV^{-1} cm^{-2} s^{-1} have been achieved underground with these detectors.
- **Transition-Edge Sensors (TES)** based detectors [175, 176], that allow very flexible designs and the possibility of being fabricated with radiopure materials. They are already being operated in several dark matter experiments requiring very low background like CRESST or CDMS.

4.4 The BabyIAXO experiment

The BabyIAXO[5] [177] helioscope has been conceived as a first experimental stage towards IAXO. The main objectives for this experiment are to act as a technological prototype of IAXO, but also, to produce relevant physical outcome. Additionally, further opportunities of improvement of some of the baseline experimental parameters are expected from the experience of builing and operating BabyIAXO, allowing the enhancement of the final IAXO design.

BabyIAXO follows the layout of an enhanced 4th generation helioscope: a two parallel coils magnet with two parallel 70 cm diameter bores will be used to track the

[5] *BabyIAXO* was proposed at the 7th IAXO collaboration meeting in 2017 at DESY, Hamburg, when the IAXO collaboration was formally constituted. The name was chosen to address the fact that this first *baby* helioscope will hopefully *grow* into the full size IAXO.

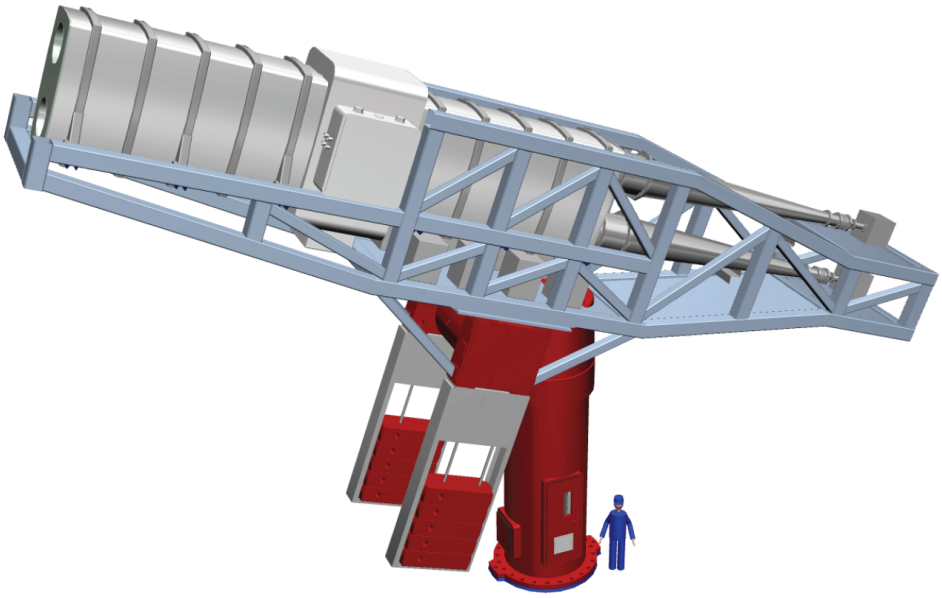

Figure 4.12: Scheme of the full BabyIAXO helioscope. The two bores magnet allows two detection lines with x-ray focusing optics and ultra-low background x-ray detectors at the end of each line. The external shielding of the x-ray detectors are shown. All the system is sustained by a support frame. Both detection lines are represented with the same length (corresponding to the 7.5 m focal length of the XMM optics), but in reality, one of them will be shorter (5 m focal length of the custom optics).

Sun, and x-ray Wolter I focusing optics will be attached to the end of the bores. They will focus the signal to the readout planes of ultra-low background microbulk Micromegas detectors. Figure 4.12 shows a conceptual design of the BabyIAXO helioscope. A more detailed description of the setup will be given later in section 4.4.1.

As it happened for IAXO, several additional/alternative detection technologies are being developed for BabyIAXO. Most of these technologies present higher backgrounds than Micromegas detectors, but on the other hand, they outperform them in terms of energy threshold or resolution. Ideally, IAXO and BabyIAXO could host an selection of different detection techniques to combine the FOM and the robustness of different detectors with different systematics. And even though the baseline for discovery are Micromegas detectors, in case of an actual discovery, the focus of the experiment would change from *discovery* detectors (lower backgrounds) to *high-precision measurement* detectors (high spatial and energy resolutions). Furthermore, if a discovery happens in the BabyIAXO stage, then IAXO, that has a signal-to-noise ratio $\sim 10^{-2}$ times larger than BabyIAXO, could be equipped from the beginning with high-precision detectors to enhance the physics capabilities.

BabyIAXO will not only be a prototype for all the IAXO subsystems, but also a preparatory exercise for the infrastructure, a test of the long-term stability of the systems and a platform to create and develop resources such as software and analysis tools, collaboration structure and data taking protocols. As it will be seen later in section 4.5.1, the physics prospects for BabyIAXO are computed assuming two data taking campaigns

of ∼1.5-2 years each, in the same fashion as CAST: one with vacuum and the other, with a buffer gas, to recover the coherence at higher axion masses.

4.4.1 BabyIAXO enhanced helioscope

The basic layout of the enhanced BabyIAXO helioscope has three main subsystems: the magnet, the x-ray optics and the x-ray detectors. The aim of the experiment design is to maximize the FOMs of the three of them (see equations 4.17), while considering state-of-the-art and well known technologies and also, the lowest cost-efficiency rate.

BabyIAXO magnet

The main goal for the magnet FOM of BabyIAXO is to be at least 10 times higher than the CAST one (i.e. $f_M \gtrsim 200\,\mathrm{T}^{-2}\,\mathrm{m}^{-4}$). To achieve that, a so called *common coil design* has been proposed, with two flat racetrack coils of 10 m length. The conductor consists of a Rutherford superconducting cable with 8 strands of NbTi/Cu, co-extruded with a pure aluminium stabilizer matrix. The common coil design was chosen due to its simplicity and cost efficient manufacturing process.

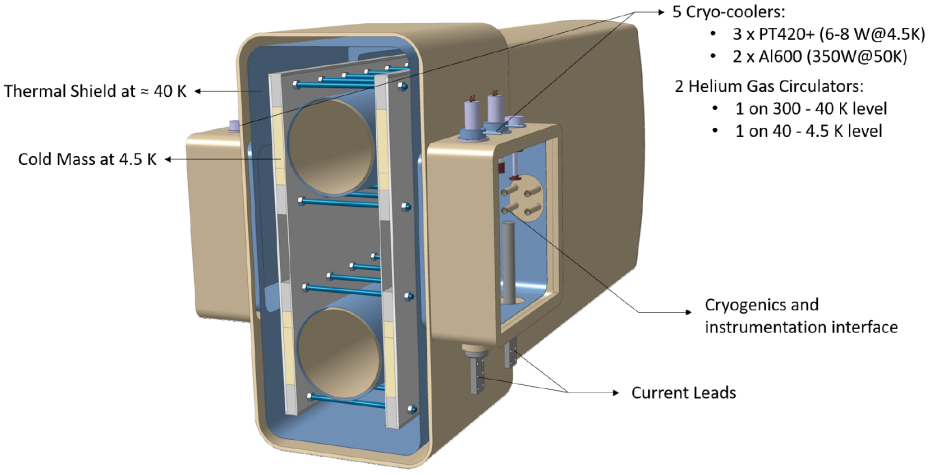

Figure 4.13: Scheme of the cross-section of the BabyIAXO magnet cryostat. Two vertical racetrack coils form the cold mass of the magnet and allow the placement of two bore tubes in between. They are enclosed by a thermal shield. Some of the cryogenics facilities are shown.

A scheme of the BabyIAXO cryostat design is shwon in figure 4.13, where the two 10 m long coil windings are placed in vertical position, constituting the cold mass of the magnet. A 0.8 m separation between the coils allows locating two 0.7 m-diameter magnet bore tubes, one on top of the other. This configuration allows an easy layout for supports and a good magnetic field in the bores. These two bores are closed on one side by two flanges, and on the other side, special gate valves need to be installed to separate the internal volume of the bores from and the x-ray optics. And also, vacuum

pumps and a gas system will allow to operate in both vacuum and buffer gas scenarios to reach coherence at higher axion masses. The nominal operating current of the winding is 9.8 kA at a peak magnetic field of 3.2 T, which corresponds to a 56 A mm^{-2} average current density in the windings.

Finally, the cryostat of BabyIAXO consists of a Al5083-O alloy rectangular box with a thermal shield operated at 45 K. This thermal shield will hold less than 4 W of heat load on the cold mass, which will be operated at 4.2 K. The cryogenics for the cryostat are based on a *dry* cooling system with cryocoolers, which is a simple and rather low cost system compared to cryogenic liquids. This design also counts with all the security measures considered for IAXO, such as the quench protection.

Regarding the structural concept, the magnet, optics and detectors are assembled together and installed on a non-magnetic stainless steel support frame. A central post transfers the loads between the cold mass and a supporting base. The system allows a vertical inclination of $\pm 25^\circ$ for the cryostat, and the base will be able to rotate 365°, therefore optimizing the tracking efficiency. Taking into account the cryostat, the optics and the detectors, a total length of 20 m, is obtained.

With all these considerations, two magnet FOM, $f_M = B^2 L^2 A$, have been obtained with different estimates of the magnetic field, B: 1) integrating the distribution of the magnetic field over the space of the two bores in 2D and assuming it constant along L, and 2) integrating altogether in 3D. The FOMs obtained for each case are

$$f_M(2D) = 326\,\mathrm{T}^2\,\mathrm{m}^4, \tag{4.18}$$

$$f_M(3D) = 232\,\mathrm{T}^2\,\mathrm{m}^4, \tag{4.19}$$

where the 3D calculation is lower because the magnetic field decreases from the center of the magnet towards the ends. But even the lower value of the f_M fulfil the BabyIAXO initial requirement in regard to CAST.

BabyIAXO x-ray optics

The design of the magnet of BabyIAXO allows the placement of two x-ray optics at the end of the two bores. The x-ray focusing optics need to cover completely the 0.7 m-diameter section of the bores in order to maximize the magnet FOM in terms of aperture. The baseline approach for BabyIAXO is to cover one of the bores with a new custom-designed optic with a similar performance than the ones required for IAXO. The other bore would be covered with a spare optic module of the X-ray Multimirror Mission (XMM) Newton [178], from the European Space Agency (ESA). In terms of the optics FOM, $f_O = \frac{\epsilon_o}{\sqrt{a}}$, the most important parameters of the optics will be the throughput (ϵ_o) and the PSF, that determines the spot area (a).

- **Custom x-ray telescope:** The design of the custom x-ray telescope for BabyIAXO needs to be as close as possible in terms of dimensions and performance to the IAXO

x-ray optics, but without forgetting that BabyIAXO is also a learning and testing facility. Therefore, the same segmented-glass approach was chosen for building this telescope, but two different techniques will be explored together. The inner part of the optic (with inner radius of r_i=5 cm and outer radius of r_o=20 cm) will be built by the same hot-slumped, multilayer-coated glass technique that was already used in the NuSTAR telescope, and that is the baseline technology for the IAXO optics. On the other hand, the outer part of the telescope (r_i=20 cm, r_o=35 cm) will be built using cold-slumped glass [179]. A scheme of this design is shown in figure 4.14 (left). This telescope will be able to focus the parallel beam of photons from axion conversion in the magnet bores to a $a \sim 0.2\,\mathrm{cm}^2$ spot on the detector readout.

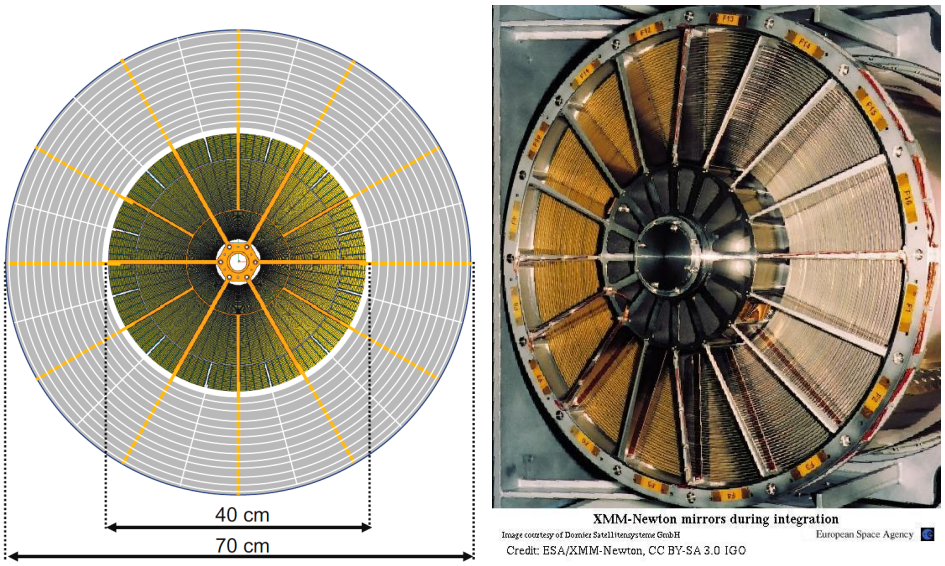

Figure 4.14: (Left) BabyIAXO optics design, including the hexagonal *spider* structure that will be used to mount it to the magnet bores. The inner part is designed with the hot-slumped glass technique (the same optics as the ones from IAXO in figure 4.8), while the outer part is designed with the cold-slumped glass technique. **(Right)** The XMM-Newton mirror module on the backside of the XMM-Newton service module. One spider carrying a full set of 58 flight mirror shells is visible. Image courtesy of Dornier Satellitensysteme GmbH and ESA (ESA/XMM-Newton, CC BY-SA 3.0 IGO).

- **XMM spare telescope:** An already existing 35 cm-radius spare telescope from the XMM Newton mission will cover the other magnetic bore of BabyIAXO. It consists of 58 Wolter I grazing-incidence mirrors, where the gold-coated shells are nested in a co-axial and co-focal configuration. A real image of one of these optics used for the XMM Newton mission is shown in figure 4.14 (right).

  Although this telescope has a focal length of 7.5 m, which is slightly larger than the nominal focal length for the IAXO baseline optics (5 m) and it is heavier than the custom IAXO optics, it can be successfully implemented in BabyIAXO. Also, due to the longer focal length, the focal spot area for the XMM telescope is expected to be $a \sim 0.3 - 0.7\,\mathrm{cm}^2$, which is slightly larger than the spot of the custom optics. But overall, in terms of performance, the XMM telescope fulfil the IAXO requirements despite not being an optimized optics for axion searches.

The BabyIAXO optics will be placed inside independent vacuum vessels attached to the magnet lines with a gate valve and a flexible bellow that will allow some movement for alignment purposes. At their other side, the optics will connect to the detector placed in the focal plane by means of an interface pipe and another gate valve. An x-ray source at the opposite end of the telescope can be used to monitor the focal spot stability. In addition, a laser alignment system need to be implemented in order to align both optics in the BabyIAXO setup.

BabyIAXO x-ray detectors

The baseline technology for the BabyIAXO detectors is the same than that for IAXO: small gaseous TPCs with radiopure pixelated microbulk Micromegas readouts, as well as active and passive shielding along with other low background techniques. In principle, the same design described in section 4.3.3 is proposed because it has already been proven in the CAST experiment and several other bench tests. However, the BabyIAXO detectors will include some upgrades to test their effect in terms of background reduction, b, and efficiency improvement, ϵ_d, aiming to enhance the IAXO FOM, $f_D = \frac{\epsilon_d}{\sqrt{b}}$.

A more detailed description of the background understanding of these detectors and the corresponding techniques to reduce it will be given in chapter 5. In this section, the main detector upgrades that are being exploresd for the BabyIAXO detectors in regards to the IAXO *pathfinder* design will be addressed.

- **Active shielding:** An efficient cosmic veto shielding has proven to effectively reduce the radioactive background of Micromegas detectors with. A full 4π solid angle coverage with a 99% muon tagging would allow such detectors to reach backgrounds at the order of $\sim 10^{-7}\,\mathrm{counts\,keV^{-1}\,cm^{-2}\,s^{-1}}$.

  Different technological options are being considered for this purpose. Plastic scintillators have been the go-to for CAST muon vetoes, and new customized-geometry ones are being prepared by the Institute for Nuclear Research (INR) group, in Moscow, for their testing in the IAXO-D0 prototype. Also, an alterative approach is being developed at the Johannes Gutenberg University, in Mainz, based on large bulk Micromegas detectors ($100\times50\,\mathrm{cm^2}$). This system can be very useful for characterization purposes and also, for simulation models of background data validation.

- **Passive shielding:** The current passive shielding design consists of a 20 cm thick lead layer completely surrounding the detector to reduce external gamma radiation. Nonetheless, some weak spots exist at the points where the detector connects with the optics or the electronics. Some improvements would include further shielding the pipe towards the magnet, or to implement a lead slab above the upper cosmic veto to tag high-energy gamma events. These implementations require additional simulations and background modelling studies.

- **Ultra thin x-ray windows:** Micromegas and the first GridPix detectors in CAST were equipped with x-ray windows made out of 2-4 μm thick foils supported by metallic *strongbacks*. Their purpose was to maintain the difference of pressure between the TPC gas volume and the vacuum line while being transparent to x-rays in the energy RoI. The main issue is that the detector's threshold is mostly determined by the transmission of the window, which quickly drops for energies below 1.5 keV. Also, the leak tightness of such windows is not very good.

Figure 4.15: A 300 nm silicon nitride window under 1.5 bar pressure for the second GridPix detector in CAST. Developed at the University of Bonn.

Some alternatives are being developed at the University of Bonn. These new windows consist of a silicon *strongback* covered with a silicon nitride membrane about a hundred nm tick [180] with improved transmissions below 1.5 keV, and sizes as big as 14 mm diameter (shown in figure 4.15). These windows have been used and proved at the second GridPix detector in CAST, surviving a pressure difference of 1.5 bar with a leak tightness better than 8×10^8 mbar l s^{-1}. Further improvements will be made towards thinner membranes, potentially larger areas and better *strongback* designs.

- **TPC active gas:** Typically in CAST, Micromegas detectors operated with a mixture of Ar+C_4H_{10} (∼98/2)% at an overpressure of ∼ 1.5 bar. However, argon based mixtures can be problematic due to the *escape peak* at 3 keV, that lays at the middle of the energy RoI, and also, due to the contribution of the β^- decay of the ^{3}9Ar isotope, as it will be seen in section 5.2.6.

  To solve these problems, xenon based mixtures have been proposed. Xenon offers higher stopping power to x-rays than argon, so it can be operated at lower pressures while obtaining similar detection efficiency. For BabyIAXO, mixtures of Xe+C_4H_{10} at 0.5 bar are being tested. Working at lower pressures would reduce the mechanical stress on the x-ray window, so thinner windows could be considered, with its consequent improvement in the detection efficiency and the reduction of the energy threshold.

- **Data acquisition and electronics:** The high granularity readouts of the Micromegas detectors provide rich topological information of the events that interact in the target gas of the TPC. To take full advantage of such information, suitable readout electronics are needed. Current state-of-the-art electronics allow digitalizing

full temporal waveforms of a large number of channels. Taking into account that the Micromegas readouts proposed for IAXO and BabyIAXO have small areas and number of strips, and also, low expected acquisition rates, these electronics perfectly fulfil their requirements. However, it is important to reduce the electronic noise as much as possible in order to low the energy threshold of the detector.

The current technology proposed for BabyIAXO, that has already been implemented in the IAXO-D0 prototype, are the AGET [181] chips. This technology provides autotrigger capabilities for each individual channel, which allows reducing the energy thresholds below 1 keV. The specific design for the AGET-based electronics for the BabyIAXO detectors are based on a modular and flexible general purpose readout system for gaseous detectors, designed at IRFU CEA Saclay. A conceptual design of these electronics cards is shown in figure 4.16. The 240 channels of the Micromegas readout are split and connected to four Front-End Cards (FEC) with four AGET chips. The output of the four FECs is connected to the Back-End Board (BEC), which digitalizes the signal and communicates with a remote DAQ PC. If needed, the BEC can receive a global clocking and external triggering from a Trigger and Clock Module (TCM).

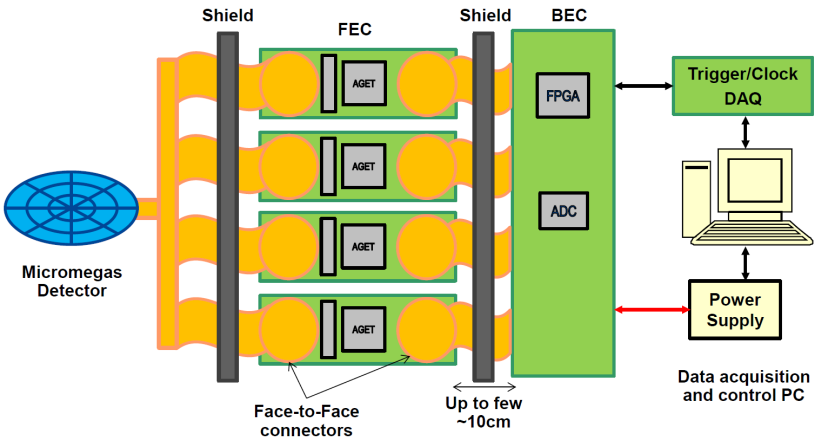

Figure 4.16: Conceptual scheme of the radiopure AGET-based electronics readout designed for the BabyIAXO detectors.

Some effort is being done among the IAXO Collaboration in order to explore the possibility of building *radiopure* electronics by using kapton as the base of the board and replacing the most radioactive components, such as capacitors, resistors, diodes for the spark protection circuit and the AGET coupling capacitors. This would allow placing the FEC closer to the detector, thus reducing the electric noise and reducing the energy threshold. In parallel, simulation studies are being carried out to study the effects of such electronics on the detector background [182].

The last proposed improvement is the use of face-to-face kapton PCB connectors, without solder or intermediate connector pieces. They have been developed and tested in the University of Zaragoza in the context of previous low-background Micromegas applications [183].

Finally, figure 4.17 shows the implementation of the detectors in the BabyIAXO

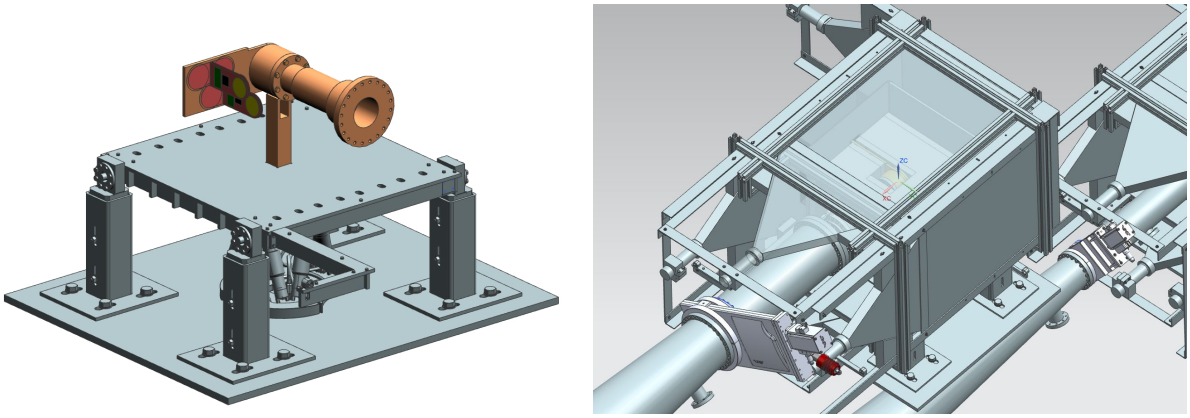

Figure 4.17: (Left) Detector chamber and shielding structure base plate positioning. The new version of the AGET electronics is shown. **(Right)** BabyIAXO Micromegas detector with a proposed $\sim 4\pi$ cosmic veto positioning. The ^{55}Fe source assembly, the bellow and gate valve at the vacuum line are also shown.

detection line. An independent platform will sustain the detector chamber and the shielding structure whole system. A calibration system will be installed between the optics and the detector for detector calibration purposes, with a ^{55}Fe retractile source. Also, a bellow will allow some movement to ease the alignment process, and a pneumatic gate valve will be installed for safety reasons.

4.4.2 IAXO-D0 prototype

IAXO-D0 is a IAXO and BabyIAXO detector prototype that has been commissioned at the University of Zaragoza during 2016-2018. The main purpose of this prototype is to recreate the already known stable performance and good energy resolution and threshold of the baseline technology of the IAXO detectors, and also, to implement the new strategies proposed for BabyIAXO in order to push the results even further.

For these purposes, a spare IAXO *pathfinder* detector was shipped from CERN to the University of Zaragoza. A complete 20 cm thick passive lead shielding was built and a new gas system was commissioned. This system allows the operation with argon and xenon, with recirculating and recovery options. Also, the new Feminos-AGET electronic cards were implemented outside of the shielding, along with a new acquisition and analysis software. Figure 4.18 shows pictures of the commissioning period and the IAXO-D0 setup.

The commissioning and first data taking campaign, as well as the data analysis and background study of IAXO-D0 is one of the main goals of this *thesis* work. A more detailed description of IAXO-D0 will be done in chapter 8, and the experimental background study will be presented in chapter 9. Also, a IAXO-D0 background model has been developed in the context of this work, and will be explained in chapters 6 and 7.

Some more implementations are planned in the near future. A cosmic veto system

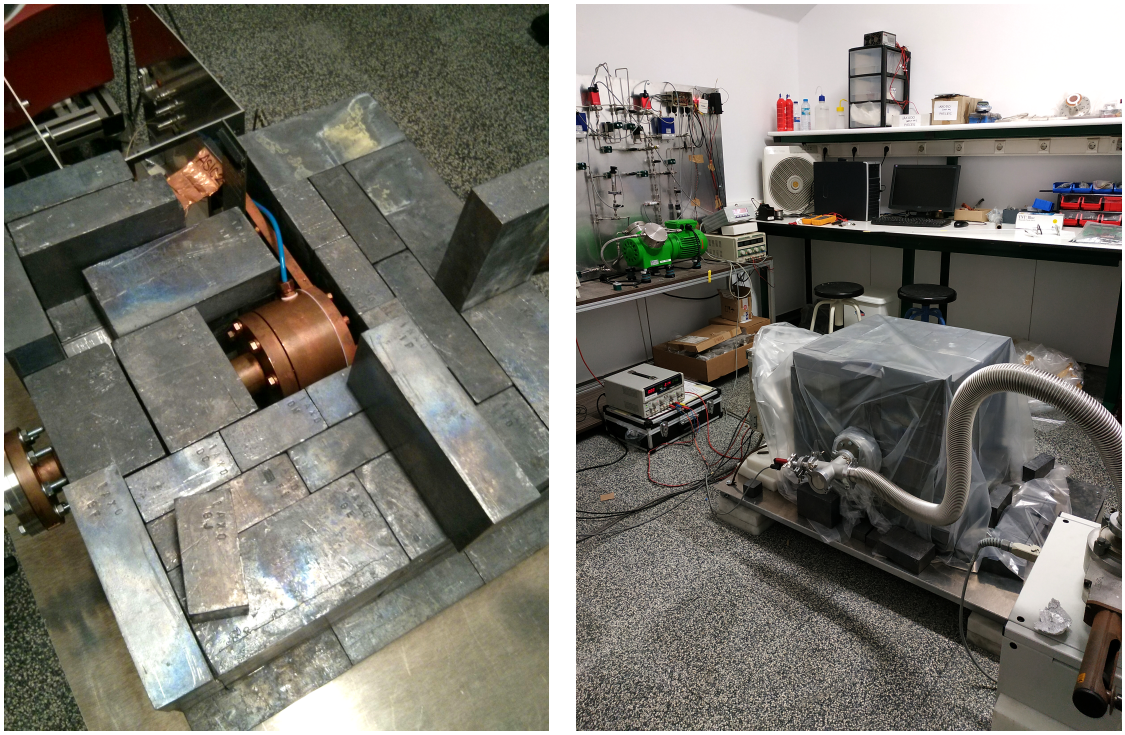

Figure 4.18: (Left) Picture of the commissioning process of the IAXO-D0 prototype. The detector chamber is positioned inside the lead bricks shielding. The vacuum pipe and the electronic connections are visible, as well as the gas tube. **(Right)** Picture of the IAXO-D0 prototype commissioned at the TREX laboratory, at the University of Zaragoza. The gas system, the passive lead shielding and the vacuum pipe and pump are visible.

will be soon installed and a first version of a customized-geometry plastic-scintillator muon veto system is under preparation, featuring a cube of $65\times65\,\mathrm{cm}^2$. in collaboration with the Institute for Nuclear Research (INR) in Moscow, and should be ready before the end of 2019. This will most likely allow IAXO-D0 to reach levels of background of the order of $\sim 10^{-7}\,\mathrm{counts\,keV^{-1}\,cm^{-2}\,s^{-1}}$.

4.5 Physics potential

The main physics goal of IAXO and BabyIAXO is the search for solar axions and ALPs emitted from the core of the Sun via Primakoff effect, with an axion-photon coupling $g_{a\gamma}$. But these experiments will also be able to probe the axion-electron coupling, g_{ae}, parameter space for the first time with realistic sensitivities for the BCA axion-electron spectrum. Furthermore, IAXO will also test models of other proposed particles at the low energy frontier of particle physics, such as hidden photons or chameleons. And the fact that it is able to implement new detectors such as microwave cavities or antennas, will allow to search for relic axions as well.

In this section, the expected sensitivity of IAXO (and BabyIAXO) to solar axions

Parameter	Units	CAST-I	IAXO (nominal)	IAXO+ (enhanced)
B	T	9	2.5	2.5
L	m	9.26	20	20
A	m^2	2×0.0015	2.3	2.3
f^*_M		1	300	300
b	$\frac{10^{-5}\,c}{keV\,cm^2\,s}$	∼4	5×10^{-3}	$\times 10^{-3}$
ϵ_d	1	0.5-0.9	0.7	0.8
ϵ_o	1	0.3	0.5	0.7
a	cm^2	0.15	8×0.2	8×0.15
f^*_{DO}		1	17	60
ϵ_t	1	0.12	0.5	0.5
t	year	∼1	3	3
f^*_T		1	3.5	3.5
f^*		**1**	2×10^4	6×10^4

Table 4.2: Estimated values of the relevant parameters of the IAXO FOM [43] compared to the ones from the first CAST vacuum phase [147]: $f^* = f/f_{CAST}$.

and ALPs will be shown, and a summary of the main physics cases that these experiments will have potential to probe, will be explained.

4.5.1 Expected sensitivity to solar axions and ALPS

To obtain the IAXO expected sensitivity to solar axions, an estimation of the FOM is required. The main experimental parameters that affect the FOM of an enhanced helioscope (equations 4.17) are listed in table 4.2 for the specific case of the IAXO proposal. Two scenarios are considered: a *nominal scenario* with more conservative and already achievable parameters, and an *enhanced scenario*, also called IAXO+, that could be potentially implemented after the experience of BabyIAXO. The way the figure of merit is factorized allows quantifying the improvements from each of the helioscope subsystems. This estimation of the enhanced FOM leads to an increment of the sensitivity up to $\sim 10^{4-5}$ times better than the fist CAST vacuum result [147] i.e. more than one order of magnitude of improvement in the $g_{a\gamma}$.

Also, an estimation of the exposure of the experiment is also required. For that, two runs have been assumed (table 4.3) in the same fashion as CAST: Run-I will consist of 3 years of effective data taking with vacuum in the magnet bores, which will determine the sensitivity for axion masses below $m_a \lesssim 0.01\,\text{eV}$. On the other hand, Run-II will use ^{4}He buffer gas inside the magnet bores with density continuously changed from 0 to 1 bar, that will allow axion-photon coherence above $m_a \gtrsim 0.01\,\text{eV}$. Overall, this program would allow IAXO to reach axion masses of ∼0.25 eV. A similar exercise was carried out to obtain the sensitivity of BabyIAXO, supposing also two data taking campaigns, one in vacuum and one with buffer gas, during an effective exposure period of 1.5 year for each of them. More details about the sensitivity calculations can be found in [96].

		Run I	Run II
Total duration		∼4 years	∼4 years
Effective data taking duration		3 years	3 years
Effective exposure		9540 hours	9540 hours
Gas density	^{4}He at room temperature	0 bar	variable from 0-1 bar
	In terms of axion mass	0 eV	0-0.25 eV

Table 4.3: Proposed IAXO runs and exposure that were used to compute the sensitivity curves.

With these considerations, the sensitivities of IAXO and BabyIAXO to axion-photon coupling are shown in figure 4.19, where the area of the $g_{a\gamma} - m_a$ parameters space to be explored is represented. Both the *nominal scenario* (labelled as IAXO) and the *enhanced scenario* (labelled as IAXO+) are shown, as well as the CAST limit for the sake of comparison. IAXO will be ∼15-20 times more sensitive than CAST in terms of the axion-photon coupling constant, reaching values of $g_{a\gamma} \sim 5 \times 10^{-12}\,\mathrm{GeV}^{-1}$ for $m_a \lesssim 0.01\,\mathrm{eV}$, and around $g_{a\gamma} \sim 10^{-11}\,\mathrm{GeV}^{-1}$ for $m_a \lesssim 0.25\,\mathrm{eV}$. This translates into ∼5 orders of magnitude more sensitive than CAST in terms of signal intensity. And even though BabyIAXO will not reach such sensitivity values, it will suppose a big improvement in regard to CAST, which will allow probing new areas of the parameter space. The estimated axion-photon coupling sensitivity for BabyIAXO will be $g_{a\gamma} \sim 1.5\times10^{-11}\,\mathrm{GeV}^{-1}$ for $m_a \lesssim 0.02\,\mathrm{eV}$.

From figure 4.19 it is seen that IAXO will deeply enter into completely unexplored axion and ALP parameter space, even reaching the QCD axion phase space that has not be explored yet. Also, axions are good candidates to hot DM for higher m_a areas ($m_a \sim 0.1 - 1\,\mathrm{eV}$). And even masses below $m_a \lesssim 10^{-7}\,\mathrm{eV}$ are interesting, since ALPs at such areas are invoked to explain anomalies in light propagation over astronomical distances.

In regard to the axion-electron coupling g_{ae}, IAXO and BabyIAXO will be sensible also to non-hadronic axions produced in the Sun core by BCA reactions. As it was shown in figure 4.1, the flux of solar axions produced by BCA processes is in the range of 0.5-2 keV and can be up to 100 times larger than the Primakoff axion flux. If the threshold prospects of IAXO optics and detectors are reached, the axion-electron coupling parameter space could be probed.

Figure 4.20 shows the parameter space for axion-electron coupling with the estimated sensitivities for IAXO and IAXO+, assuming that the Primakoff emission from the Sun is subdominant, so the axion solar flux is caused only by BCA processes. The expected signal depends of $g_{ae}g_{a\gamma}$, accounting for the production process in the Sun and the detection process in the helioscope. In this parameter space, in case of no positive signal, IAXO would set a limit of $g_{ae}g_{a\gamma} < 2.5 \times 10^{-25}\,\mathrm{GeV}^{-1}$ (95% CL) for axion masses $m_a \lesssim 10\,\mathrm{meV}$. This implies a sensitivity more than two orders of magnitude better than similar analysis performed with CAST data [145].

With this $g_{ae}g_{a\gamma}$ sensitivity, IAXO would be able for the first time to reach relevant

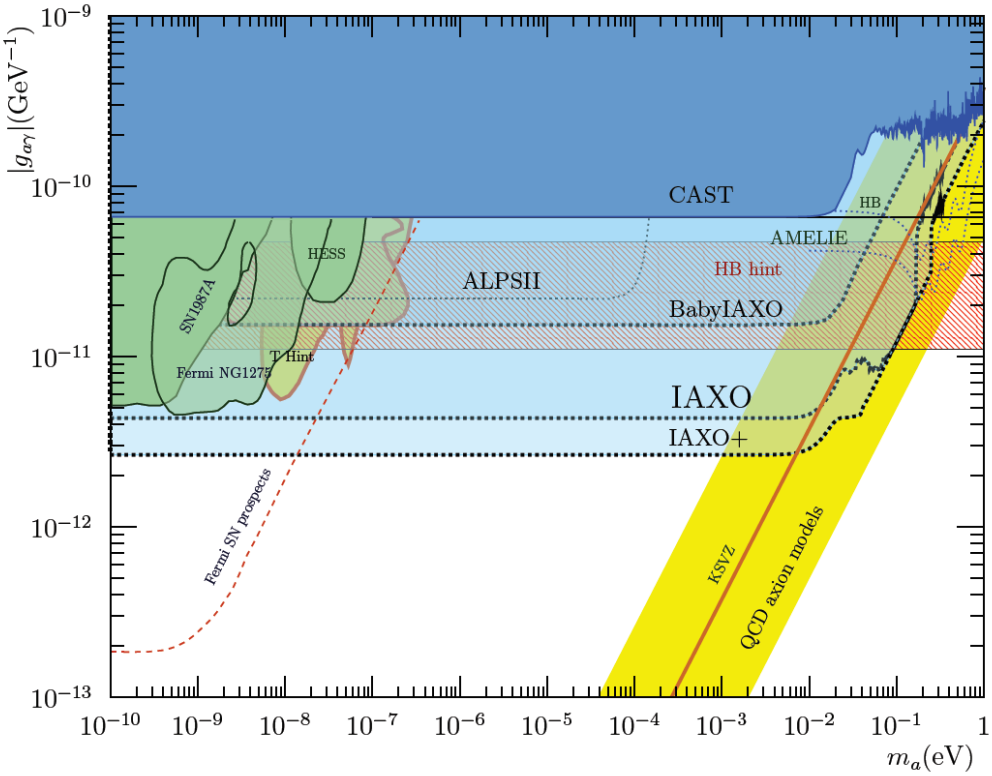

Figure 4.19: Sensitivity of CAST and sensitivity prospects for IAXO, IAXO+ and BabyIAXO in the $g_{a\gamma} - m_a$ parameter space. Some of the axion and ALPs hints explained in chapter 3 are shown. The yellow band shows the QCD axion model preferred region. Plot and further information in [89].

areas of the parameter space not previously excluded and relevant for the WD cooling hint. Also, it would allow to probe relevant QCD axion models at mass values of $m_a \gtrsim 3\,\mathrm{meV}$ that may be hinted by anomalous astrophysical observations.

4.5.2 Summary of physics potential

In chapter 3, some of the main cosmological and astrophysical hints for axions have been addressed. In this section, the most important physics potential cases that IAXO will be able to probe (and BabyIAXO to a lower extent), will be sumarized. For a more detailed explanation of the theoretical, cosmological and astrophysical motivation of the search for axions in the IAXO reachable parameter space, see reference [96].

- **Axion-photon coupling:** Both IAXO and BabyIAXO will enter into unexplored $g_{a\gamma} - m_a$ parameter space, pushing the current astrophysical bounds more than one order of magnitude. At high m_a, it will be able to explore realistic QCD axion models in the meV to eV mass band. This region is very interesting because it is where several cosmological (DM), astrophysical and theoretical (strong CP problem) motivations overlap.

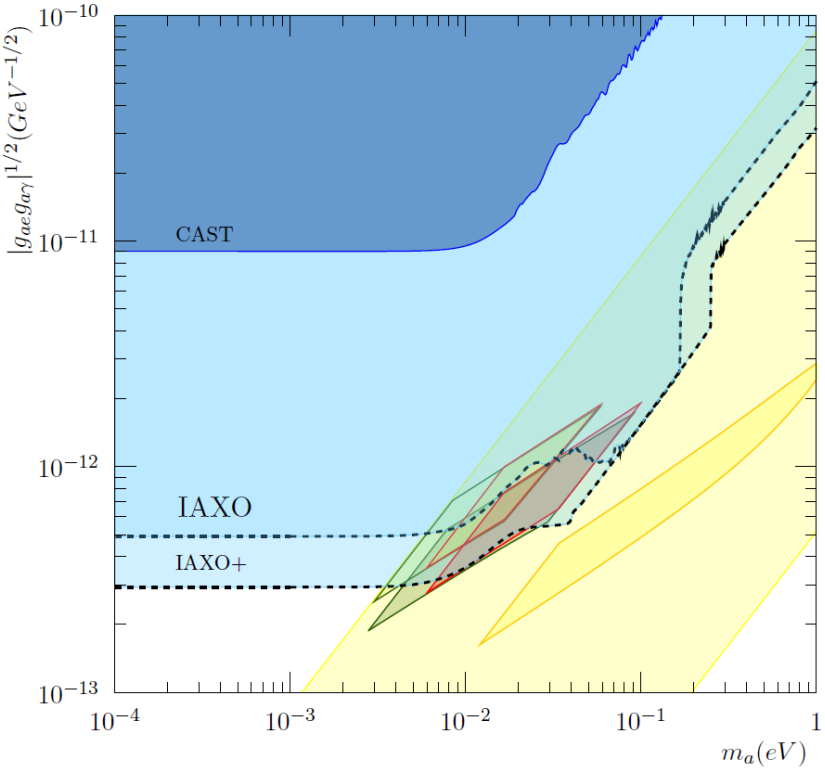

Figure 4.20: Sensitivity of IAXO to solar axions produced by BCA processes in the $|g_{ae}g_{a\gamma}|^{1/2} - m_a$ parameter space. The yellow band corresponds to the QCD axion models and the different color diamond-shaped regions correspond to particular QCD axion models that are able to explain anomalous stellar cooling observations (see section 3.4.2). Sensitivities are estimated for detector and optic thresholds of 0.5 keV. Plot and further information in [96].

- **Very High Energy (VHE) photons:** The Universe being more transparent to VHE photons than it should, was explained in section 3.4.2. Photons from distant emitters like active galactic nuclei (AGN) should not reach such long distances due to their non-negligible probability to interact with photons of the extragalactic background light (EBL). However, there are observations of such far sources [100–104] that present a universe too transparent for VHE photons. To solve this discrepancy, photon-ALP oscillations triggered by cosmic magnetic fields are suggested [100, 101, 105]. ALPs can travel unimpeded through the intergalactic medium, so this would imply an increase of the effective mean free path of VHE photons. The required mass for such ALPs is $m_a \sim 10\,\text{neV}$, and the coupling constant, $g_{a\gamma} \sim 10^{-11}\,\text{GeV}^{-1}$. IAXO would be sensitive to this entire parameter region. On the other hand, BabyIAXO would probe a large fraction of it.

- **Anomalous cooling:** The cooling anomalies were addressed in section 3.4.2. There are independent observations of diverse stellar objects that have shown an abnormal high energy loss that is not well understood by the current stellar models. This cooling anomalies have been observed studying the period change and the luminosity funcion of white dwarfs (WD) [72, 106–109], the luminosity of the tip of the red giant stars branch (RGB) [71, 111], the number ratio of horizontal branch (HB)

stars over the RGB stars in globular clusters [70], the ratio of blue and red (B/R) he-burning supergiants [114–116], and also neutron stars [184, 185]. This extra cooling could be explained by the emission of light and weakly interacting axions or ALPs produced in the stellar core, with couplings of $g_{ae} \sim 10^{-13}\,\mathrm{GeV}^{-1}$ for some of them, and $g_{a\gamma} \sim 10^{-11}\,\mathrm{GeV}^{-1}$ for others. Moreover, there are some QCD axion models that feature these couplings and that are able to explain collectively all anomalies [186, 187], and correspond to $m_a \sim 10\,\mathrm{meV}$. And at lower masses, the hinted $g_{a\gamma}$ overlaps with the parameters required to explain the VHE transparency hints. Such regions of the parameter space could actually be probed by IAXO.

- **ALPs as cold dark matter (CDM) candidates:** Another relevant feature of axions and ALPs is that they are very compelling candidates to Cold Dark Matter (CDM). As it was explained in section 3.4.1, the relic axion density varies depending on the mass of the axion and on whether the PQ symmetry breaks spontaneously before or after inflation. There is a broad range of compatible axion masses with the correct relix density, including values above the meV scale for the QCD axion. It was also seen that production of cold axions via the vacuum-realignment mechanism requires $m_a \sim 10^{-5}\,\mathrm{eV}$. And if the PQ symmetry is restored after inflation, then the effect of the decay of the topological defects need to be taken into account, and relatively large axion masses would be featured. IAXO would be able to probe all these parameter space regions.

- **Relic axions:** The resulting relic axion density for all non-thermal production mechanisms is approximately inversely proportional to the axion mass, $\rho_a \sim m_a^{-1}$. This implies that, if axions are only a fraction of the DM, the corresponding m_a will be larger. Since these mechanisms are generic to several ALP models, then a large section of the IAXO parameter space will contain ALP models with adequate DM density [88]. Therefore, IAXO would be sensible to axion models that could be part of the DM of the Universe even though it does not rely on axions being DM to detect them.

- **Dark radiation:** Axions and ALPs could also be produced from thermal processes or from decays of heavy particles. Current cosmological observations suggest the presence of Dark Radiation [188], which is a cosmological relic of relativistic particles with very weak interactions with the standard model, that could be in the form of axions or ALPs. Their abundance can be detectable by forthcoming cosmic microwave background (CMB) experiments like [189]. These ALPs would couple to photons with a coupling constant that would probably be in the IAXO reachable range [190].

- **Inflation:** ALPs have masses protected by large radiative corrections, so they could be used as candidates for the inflaton field. The slow-roll of such inflaton in a potential is what would have driven primordial inflation. A recent scenario (called *ALP miracle*) showed that an ALP with approximate parameters of $m_a \sim 0.01-1\,\mathrm{eV}$ and $g_{a\gamma} \sim 10^{-11} - 10^{-10}\,\mathrm{GeV}^{-1}$ could be responsible for cosmic inflation, and also, form the DM of the Universe [191, 192].

Finally, an important remark is that IAXO sensitivity goals only depend on the axion emission by the Sun, which is a solid prediction of most axion models. IAXO does not rely on the hypothesis of the axions or ALPs being the DM of the Universe. So, in case of non-detection, IAXO will provide a robust exclusion of the corresponding regions of the parameter space.

IAXO aims to be a generic infrastructure for axions and ALPs physics with potential for additional search strategies. Although the main detection strategy relies on Micromegas detectors for solar axions, it will be possible to implement haloscope-like setups to search for DM axions. On the other hand, BabyIAXO will be able to probe a relevant region of yet unexplored parameter space, and a discovery is not excluded.

CHAPTER 5

Low-background Micromegas for axion detection.

Contents

5.1 Introduction

In axion direct search experiments, as in any rare event searches, a deep understanding of the background of the detector is mandatory in order to reduce it. The best background level ever achieved for a Micromegas detector at surface is $(1.0 \pm 0.2) \times 10^{-6}$ counts keV^{-1} cm^{-2} s^{-1}, and corresponds to the last data taking period in CAST [34].

In this chapter, the principal sources of background for the Micromegas detectors designed for CAST and IAXO will be explained. Then, all the techniques and improvements developed to control and reduce the background of these detectors during the CAST experience and also, in test bench studies at the University of Zaragoza and the Canfranc Underground Laboratory (LSC), will be described. Finally, the last and most

optimized detector setup, the *IAXO pathfinder* and its recent results will be presented.

5.2 Principal sources of background

The principal sources of background for the Micromegas detectors in the context of the IAXO experiment are: cosmic rays (muons and neutrons), cosmic and environmental gammas, intrinsic radioactivity of the detector components, target gas and shielding, radioactivity neutrons, and cosmogenic activation of the detector materials. All these radiations can produce secondary or fluorescence emissions that can reach the detector active volume and produce a fake axion-like event.

5.2.1 Cosmic muons

Cosmic muons produce an important number of the background events in Micromegas setups installed at sea level. They can cross the entire detector shielding and directly ionize the gas. But also, they can interact in the shielding and produce secondary fluorescences in the innermost part of the detector, populating the low energy part of the spectrum.

In the context of the CAST experiment, test bench studies have been made [193] in order to quantify the effect of cosmic muons to the Micromegas background level, both at the University of Zaragoza and at the Canfranc Underground Laboratory (LSC), where the cosmic muon flux is a factor of $\sim 10^5$ lower than the flux at surface [194].

The direct comparison between the background levels measured underground and at surface by detectors with equivalent shielding configurations suggests a muon contribution around $10^{-6}\,\mathrm{counts\,keV^{-1}\,cm^{-2}\,s^{-1}}$ in the 2-7 keV range (RoI of CAST). The background energy spectra measured by the test bench setups are shown in figure 5.1 for comparison's sake.

5.2.2 External gammas

The background of the first generations of CAST Micromegas detectors was dominated by the external gamma radiation. This radiation can be originated by the intrinsic radioactivity of the materials of the walls of the room, the magnet or other facilities of the experiment around the detector. It is mainly produced from the decay of the ^{238}U and the ^{232}Th isotopes. But it can also come from different cosmic sources, such as supernovae or pulsars, or it can be produced as secondary cosmic rays in the Earth's atmosphere.

A big effort has been done in order to quantify and reduce this contribution: setups with different shielding designs were used to measure and study the detectors background,

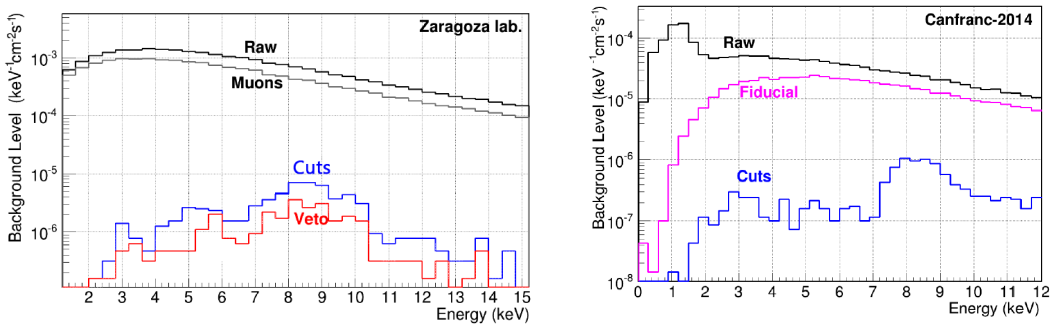

Figure 5.1: Background energy spectra measured by CAST-like Micromegas detector setups during the bench test studies (plots adapted from [14]): **(Left)** at the University of Zaragoza. The estimation of the cosmic muons contribution to the background is indicated in the plot. The blue line (cuts) is the background after the discrimination process (further explained in section 5.3.3). The red line (veto) is the background after removal of muon-vetoed events (further explained in section 5.3.2). The mean background level at surface is $(1.5\pm0.1)\times10^{-6}$ counts keV^{-1} cm^{-2} s^{-1} in the 2–7 keV range. **(Right)** at the LSC, where the raw background is one order of magnitude lower. The pink line (fiducial) is the background from a smaller circular area at the center of the readout (radius of 21.5 cm), where the axion signal is expected to be found. The blue line (cuts) is the background after the discrimination process. The mean background level underground is $(1.5\pm0.1)\times10^{-7}$ counts keV^{-1} cm^{-2} s^{-1} in the 2–7 keV range.

and also simulation toolings were developed to estimate it. Finally, the external gamma radiation was quantified to contribute about $\sim 1.5 \times 10^{-6}$ counts keV^{-1} cm^{-2} s^{-1} int he 2-7 keV range [193].

The simulated spectrum is shown in figure 5.2. The spectrum shape gives useful information about the fluorescence peaks produced by the remaining gammas reaching the innermost copper parts of the detector, or by gammas interacting with the stainless steel pipe that connects the detector to the magnet. This estimation is corroborated by the experimental tests performed in CAST, as well as by the bench tests mentioned in the previous section, with the same setups at surface and underground.

5.2.3 Intrinsic radioactivity of the detector materials

The intrinsic radioactivity from the materials of the detector components as well as the shielding, the magnet and other elements of the experiment site, is another inevitable source of background. One of the main concerns in the design of IAXO detectors is to choose very radiopure materials to build not only the readout, but also the chamber, the pipe, all the mechanical components and even the innermost shielding. Radioactive isotopes like ^{238}U and ^{232}Th are present in all the materials, and they usually represent the biggest part of the radiation background. Also, some materials present not negligible levels of ^{40}K activity that can populate the low part of the energy spectrum.

Several radioassay campaigns have been done to measure the radioactivity of the

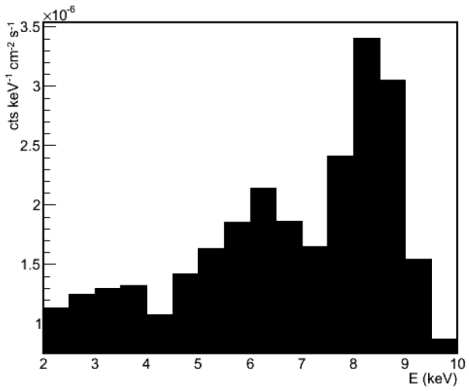

Figure 5.2: Simulated background spectrum of a CAST-like Micromegas detector induced by external gamma flux [43]. The cumulation of events in the 5-7 keV region are due to the fluorescence in the stainless steel pipe used in this specific setup, and the 8 keV peak is generated by the copper fluorescence.

materials involved in the construction of ultra-low background detectors in the context of CAST and TREX projects [154, 168, 195]. These material screening programs are mainly based on germanium gamma-ray spectrometry carried out in the Canfranc Underground Laboratory (LSC). Most of the germanium measurements were made using a ∼1 kg ultra-low background detector of the University of Zaragoza (Ge Paquito) operated at the LSC [196, 197]. With this technique, activities of different sub-series in the natural chains of ^{238}U, ^{232}Th and ^{235}U are evaluated, as well as common primordial, cosmogenic or anthropogenic radionuclides like ^{40}K, ^{60}Co and ^{137}Cs.

Other complementary techniques for the screening programs that are not operated at the LSC are Glow Discharge Mass Spectrometry (GDMS), performed by Evans Analytical Group, in France, that provided concentrations of U, Th and K; and Inductively Coupled Plasma Mass Spectrometry (ICPMS) analysis carried out at the Laboratori Nazionali del Gran Sasso (LNGS), in Italy, that quantified the U and Th concentrations of some materials.

Also, taking advantage of the *foil* format of some material samples, such as the Micromegas readouts, very sensitive measurements were made by the BiPo-3 detector [198] in the LSC. This detector has been developed by the SuperNEMO collaboration and it is able to measure levels of a few μBq kg^{-1} of ^{208}Tl and ^{214}Bi radioactivity in samples below 200 μm thick.

This exhaustive study of the materials allowed improving the design of the Micromegas detectors by replacing the most radioactive parts of the setup and therefore, decreasing the background. Some of the changes and improvements that lead to this reduction are explained later in section 5.3.1. With the last design of the IAXO pathfinder detector, the contribution of the radioactivity of its components was estimated to be $\sim 2 \times 10^{-7}$ counts keV^{-1} cm^{-2} s^{-1}. This level was experimentally obtained [193] at the LSC in a setup with special shielding, where both gamma and cosmic rays were reduced to negligible levels.

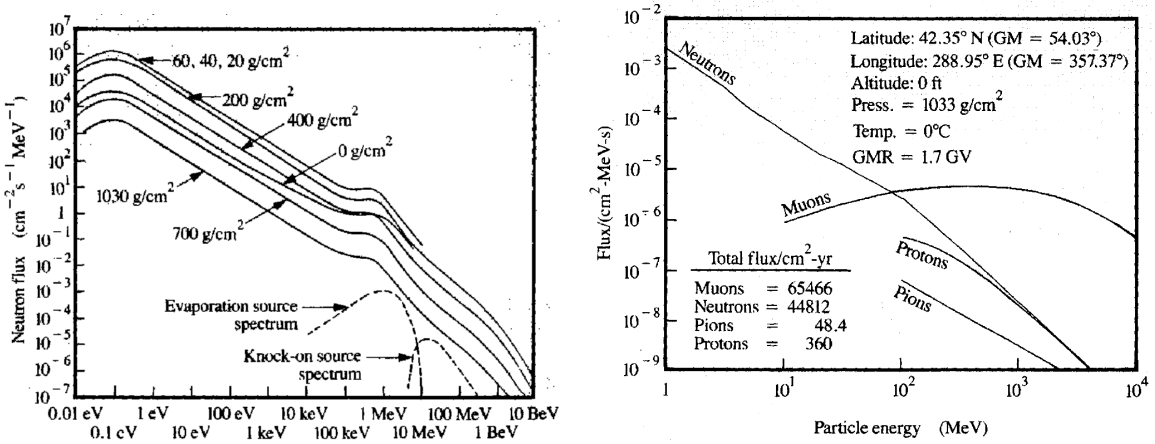

Figure 5.3: (Left) Neutron flux for different altitudes. This plot shows the flux of neutrons as a function of altitude up to outer space. The g/cm^2 indicates the thickness of the atmosphere. The lowest curve, labelled 1030 g/cm^2 is for sea-level neutrons. The curve labelled 700 g/cm^2 is for an altitude of about two miles. The two dashed lines indicate the special nuclear reactions which cause the bumps in the flux curves from 1-100 MeV. **(Right)** Theoretical flux of cosmic rays at sea level. Figures from [199].

5.2.4 Neutrons

Neutrons can also contribute to the background because they can penetrate most materials much deeper than charged particles. Their main interaction mechanisms are scattering, spallation or neutron capture, releasing other detectable particles such as gammas or electrons, or even breaking nuclei into activated isotopes.

The main expected background contribution would come from cosmic neutrons produced by high energetic cosmic rays when they reach the Earth's atmosphere. These primary cosmic rays collide with gas molecules, mainly oxygen and nitrogen, and disintegrate their nuclei through inelastic nuclear reactions. The result is the emission of protons, neutrons and α-particles among others. The energy spectrum expected from this contribution at sea level is shown in figure 5.3.

Another possible source of background caused by neutrons can be the ^{238}U and ^{232}Th contamination of the materials of the detector. The radioactive chains of these two elements (mostly in the case of the ^{238}U) produce neutrons due to spontaneous fission and (α, n) reactions. This will produce the well known evaporation source spectrum for fission neutrons, as shown also in figure 5.3. The (α,n) spectrum is slightly different and depends of the surrounding materials, but for our purposes, the evaporation spectrum has been considered for both contributions.

Through the CAST experience with Micromegas detectors, the contribution to the background caused by neutrons had always been estimated to be negligible. The amount of ^{238}U and ^{232}Th found in the materials of the detector components is very small because radiopurity of the materials is always a priority. But the contribution from the cosmic

neutrons has never been properly simulated or verified. It will be seen later on this work that this assumption is not straightforward and that the contribution from cosmic neutrons needs to be reconsidered for the detector background.

5.2.5 Cosmogenic activation of copper

Activation is a process by which radioactivity is induced into materials by letting them interact with other radiation. The production of radioactive isotopes by exposure to cosmic rays at sea level is a known issue, and in the context of low-background experimental conditions, these long-lived radioactive impurities in the materials of the detector may be even more important than residual contamination from primordial radionuclides.

The main contribution to our background from cosmogenic activation would come from the copper, which is the material chosen to build most of the parts of the detector. Due to the fact that they operate at surface and they were never stored underground to prevent them from cosmogenic activation, this contribution has to be taken into account.

A summary of the mean contributions expected from cosmogenic activation of copper [200] is shown in in table 5.1. Among these isotopes, ^{46}Sc, ^{59}Fe and ^{60}Co decay through a β^- process, thus producing electrons that could interact in the gas.

	^{46}Sc	^{48}V	^{54}Mn	^{59}Fe	^{56}Co	^{57}Co	^{58}Co	^{60}Co
Half-life	83.787 d	15.9735 d	312.19 d	44.494 d	77.236 d	271.82 d	70.85 d	5.2711 y
Measurement [201]	2.18±0.74	4.5±1.6	8.85±0.86	18.7±4.9	9.5±1.2	74±17	67.9±3.7	86.4±7.8
MENDL+YIELDX [202]	2.7		27.7	4.9	20.0	74.1	123.0	55.4
GEANT4 [203]	1.2		12.3	8.8	10.3	67.2	57.3	64.6
ACTIVIA [203]	4.1		30.0	10.5	20.1	77.5	138.1	66.1

Table 5.1: Production rates (in kg^{-1} d^{-1}) at sea level for isotopes induced in natural copper following measurements from [201]; calculations from [202] using the Medium Energy Nuclear Data Library (MENDL [204]) and the YIELDX routine [205]; and from [203] using GEANT4 [206] and ACTIVIA [207] software.

Some measurements of exposed radiopure copper bricks were done in the Canfranc Underground Laboratory with a HPGe detector [208], concluding that the maximum time for copper storage above ground to maintain a negligible ^{60}Co content is about 6 weeks. Since the IAXO experiment will be running at surface, the copper parts of the detector will soon reach saturation activity, so the ^{60}Co has to be taken into account for the background study.

5.2.6 Radioactivity from the active gas

During their working time in CAST, the Micromegas detectors operated with a mixture of argon and isobutane as the quencher gas. These mixtures of a noble gas with a

small amount of an organic molecular gas provide suitable conditions for a good detector performance, improving the drift velocity and reducing the diffusion of the charge.

One down side of the use of an argon based mixture is the presence of the natural β^- emitting isotope ^{39}Ar of the Ar gas produced by cosmic ray induced nuclear reactions, with an endpoint energy of 565 keV and half-life of 269 years [209]. This is a source of background because the decay takes place in the active volume itself, so it will produce detectable signals. Measurements of the specific activity of ^{39}Ar in natural liquid argon result in $1.01 + 0.02(stat) \pm 0.08(syst)\,\mathrm{Bq\,kg^{-1}}$ of natural Ar [210]. Although only a ∼2% of those decays would release energies below 10 keV and the mass of gas in the IAXO Micromegas detector is rather small (∼ 0.36 g), the background contribution was estimated to be $< 5 \times 10^{-8}\,\mathrm{counts\,keV^{-1}\,cm^{-2}\,s^{-1}}$ [14].

Also, tritium (^{3}H) is a radioactive isotope that can be cosmogenically induced in argon, contributing as a relevant background source due to its decay properties: it is a pure beta emitter with transition energy of 18.591 keV and a long half-life of 12.312 years. Following the shape of its beta spectrum, 85% of the emitted electrons are in the range from 1 to 10 keV. There is no experimental information of tritium production in argon, but the production rate has been estimated [211] at sea level to be $(146 \pm 31)\,\mathrm{kg^{-1}\,d^{-1}}$.

Alternatively, xenon based gas mixtures are also being considered because they present similar characteristics as drift gases for TPCs than the argon based mixtures, and the activity of the radioisotopes that are produced have lower activities [200].

5.3 Low background techniques

The microbulk Micromegas detection concept exploit many strategies developed for background reduction, not only from the CAST experience, but from the entire TREX project context, since low background techniques are common to any other rare event search experiment. First, it is important to design the detectors with radiopure materials to reduce the intrinsic background. Then, shielding techniques can prevent the external radiation to reach the detector. And finally, offline event discrimination methods allow identifying signal-like events and rejecting those compatible with background events.

5.3.1 Radiopurity

A significant effort has been made to study and measure the intrinsic radioactivity of the materials of the detector components, as it is an inevitable source of background. Table 5.2 shows the principal measurements that contribute to the IAXO detectors and shielding radioactive background, and that will be used for the background model. A more complete table of radioactivity values with measurements for specific connectors, cables, etc. can be found in [154].

Material	Supplier	Geometry part	Method	Unit	^{238}U	^{226}Ra	^{232}Th	^{228}Th	^{235}U	^{40}K	^{60}Co	^{137}Cs
Pb	Mifer	Shielding	GDMS	mBq/kg	0.33		0.10			1.2		
ETP Cu	Sanmetal	Chamber and pipe	GDMS	mBq/kg	<0.062		<0.020					
ETP Cu	Luvata	Raquette	GDMS	mBq/kg	<0.012		<0.0041			0.061		
Microbulk MM	CAST	Readout	Ge Paquito	μBq/cm^2	26±14		<9.3		<14	57±25	<3.1	
Kapton-Cu foil	CERN	Readout	Ge Paquito	μBq/cm^2	<11		<4.6		<3.1	<7.7	<1.6	
Teflon	Sanmetal	Chamber inner shielding	ICPMS	mBq/kg	<0.062		<0.041					
Mylar	Goodfellow	Xray window	Ge Paquito	μBq/cm^2	<29	<0.59	<0.80	<0.36	<0.29	<3.3	<0.18	<0.21
Kapton-Cu PCB	LabCircuits	Field shaper	Ge Paquito	μBq/cm^2	<42	<1.3	<1.1	<0.66	<0.41	<4.0	<0.24	<0.28

Table 5.2: Activities measured for samples analyzed in the radiopurity assessment program carried out for IAXO and TREX-DM [154]. Values reported for ^{238}U and ^{232}Th correspond to the upper part of the chains and those of ^{226}Ra and ^{228}Th give activities of the lower parts. Reported errors correspond to 1σ uncertainties and upper limits are evaluated at 95% C.L. for germanium measurements. The different methods of radioactivity measurements are: Ge Paquito, a ∼1 kg germanium gamma-ray ultra-low background detector of the University of Zaragoza operated underground at the LSC; GDMS, measurements based on Glow Discharge Mass Spectrometry by Evans Analytical Group in France; ICPMS, measurements by Inductively Coupled Plasma Mass Spectrometry (ICPMS), carried out at the Laboratori Nazionali del Gran Sasso (LNGS) [212].

The microbulk Micromegas readout is made out of kapton foils doubly clad with copper, materials that turned out very radiopure. Both the raw foils and fully built readouts have been measured and their activity values were suitable for the background levels required for IAXO.

Another detector part that has a high impact on the background is the Micromegas chamber. Previous versions of Micromegas based detectors in CAST had Plexiglas chambers, which is an intrinsically radiopure material. In the last data taking campaign in CAST [193], a new design was tested with a chamber made out of electro-formed copper[1]. This material is not only highly radiopure, but it also acts as the innermost passive shielding of the detector. More about this will be discussed later.

The strongback and the differential window are another source of background. The previous aluminium versions with non negligible contributions of ^{238}U and ^{232}Th were replaced by electro-formed copper cathodes with aluminized Mylar differential windows.

Moreover, all the components that are designed to be inside the lead shielding (i.e. screws, gaskets, etc.) are made out of radiopure copper or PTFE (Polytetrafluoroethylene or Teflon). Even the field shaper was designed and printed on a kapton circuit and covered by a PTFE coating to avoid copper fluorescence. Another improvement was to implement the high voltage connections in the detector printed board, which allows having all the signal and HV connections at the outside of the lead shielding.

5.3.2 Active and passive shielding

Shielding techniques have proven to be very effective in reducing external sources of background. Two main techniques are broadly used in rare event searches: active shielding, that detects external radiation and correlates it with the events produced in the detector, and passive shielding, that uses high-Z materials so the external gamma radiation loses all its energy before it can reach the detector.

Active shielding

Helioscopes like CAST and IAXO operate on surface and their detectors are totally exposed to cosmic rays. This is why active shielding like cosmic vetoes becomes a very important part in the background rejection process. From the different CAST stages and shielding upgrades, it has been proven that an efficient use of cosmic vetoes can efficiently reduce the background level in the [2-7] keV energy range.

In the CAST context, cosmic vetoes have always consisted on large plastic scintillators coupled to a low-noise photomultiplier. A picture of two cosmic vetoes is

[1] Electroforming is a metal forming process that forms parts through electrodeposition on a model. Electroformed metal is extremely pure, with superior properties over wrought metal due to its refined crystal structure. This process also prevents the contamination of the metal from the manufacture.

shown in figure 5.4 (right). When an ionizing particle crosses the plastic, scintillation light is emitted and reflected in the scintillator walls. Then, a light guide collects the scintillation light towards a photomultiplier, where a photocathode generates photoelectrons from the incoming scintillating photons. The photoelectrons are amplified by the successive dynodes and finally, a fast (∼ns) electronic signal is generated. The plastic scintillator thickness is selected to allow the cosmic particles to release more energy than any radioactivity gamma, which grants that vetoes are rejecting events coming from cosmic radiation.

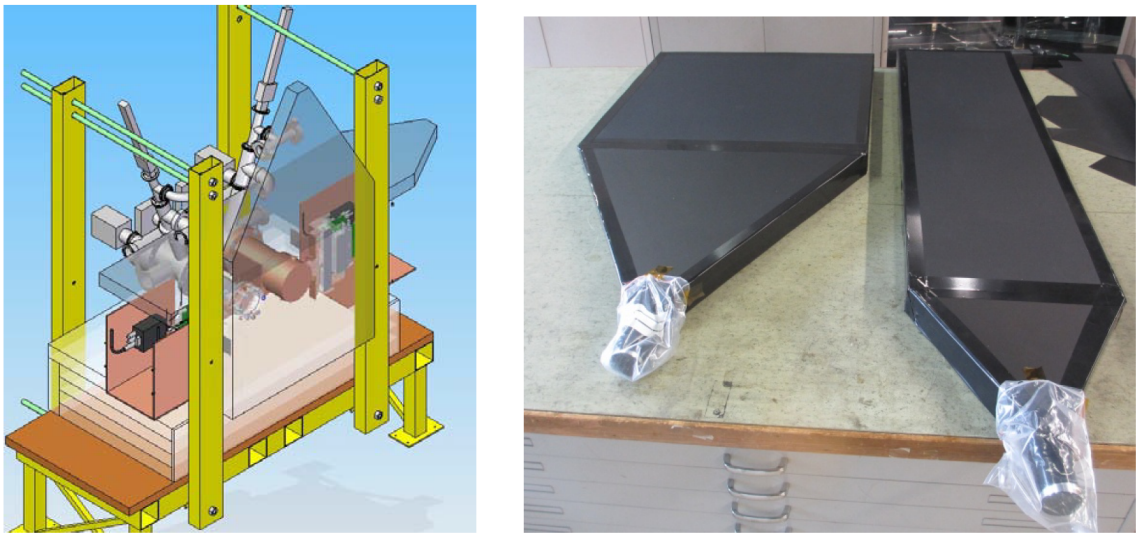

Figure 5.4: (Left) Schematics of the vetoes placement for the CAST2013-M18 detector setup. Two plastic scintillator vetoes granted a geometrical coverage of a ∼95% for cosmic muons. **(Right)** Picture of the plastic scintillator vetoes (black plates) attached to the photomultipliers, that are protected with plastic bags.

Table 5.3 shows background levels of different CAST-Micromegas detector setups with increasing amount of cosmic veto geometrical efficiency. The CAST2012-M18 setup consisted of one scintillator veto on top of the CAST detector, and it produced a reduction of ∼ 22% in the background level. Then, a higher efficiency system based on two plastic scintillators was tested in the University of Zaragoza (CAST-M10) and then fully implemented at CAST (CAST2013-M18), further reducing the background in a ∼ 46%. A comprehensive scheme of the placement of the vetoes at the CAST site is shown in figure 5.4 (left).

Setup	Geometrical efficiency (%)	Bkg. [2–7] keV Before veto cut	Bkg. [2–7] keV After veto cut	Reduction (%)
CAST2012-M18	44	1.66± 0.05	1.29± 0.05	22± 3
CAST-M10	75	1.60± 0.12	0.82± 0.08	48± 5
CAST2013-M18	95	1.23± 0.10	0.66± 0.07	46± 6

Table 5.3: Background levels obtained by different CAST-Micromegas setups with similar shielding and the effect of the muon vetoes rejection [213]. Final background levels are expressed in units of 10^{-6} counts $\mathrm{keV}^{-1}\,\mathrm{cm}^{-2}\,\mathrm{s}^{-1}$ and statistical errors given as 1σ.

Figure 5.5 shows the background energy spectra of the CAST-M10 and the CAST2013-M18 detectors before (blue) and after (red) the application of the veto cut. The reduction in background level represents an improvement of a factor 2 with respect to the 2012 Micromegas, and this reduction is visible at the ∼8 keV copper fluorescence peak and the corresponding escape peak at ∼5 keV, and also at the x-ray peak of argon at at ∼3 keV.

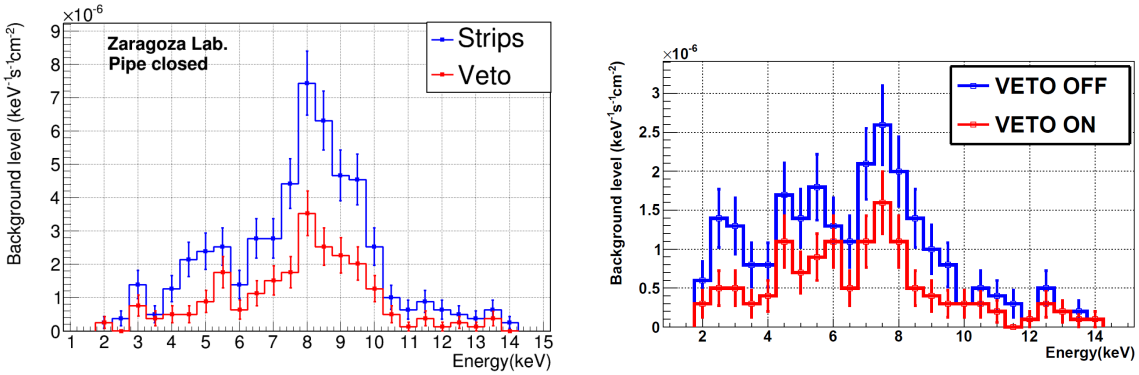

Figure 5.5: (Left) Background energy spectra of the CAST-M10 setup at the University of Zaragoza, with two muon vetoes [14]. **(Right)** Background energy spectra of the CAST2013-M18 setup at the CAST site, at CERN, with two muon vetoes [213]. In both figures, the blue line is the background spectrum after the offline discrimination analysis; and the red line is the background spectrum after the offline discrimination analysis and the vetoes rejection.

This was the first time that a background level below $\sim 10^{-6}$ counts keV^{-1} cm^{-2} s^{-1} was reached at CAST, which supposed an important milestone for the experiment. This has been taken into account for the IAXO shielding design, where active vetoes will cover a solid angle of $\sim 4\pi$ for cosmic radiation.

Passive shielding

The passive shielding is a low background technique which consist in blocking the gamma radiation from the environment or the outer parts of the detector passively, using extra layers around the detector or the properties of the materials involved in the detector fabrication themselves.

The passive shielding for the CAST detectors has always had similar designs, using layers of high-Z materials with different thicknesses, so the inner layers acts as passive shielding from the possible radiation of the exterior ones. The most external layer is made out of lead with a $\sim 4\pi$ coverage, which grants the absorption of any cosmic gamma or environmental gamma that could reach the detector from the outside. There are however some *weak spots* in this layer, for example, where the interface pipe comes out and connects with the telescope, or at the side where the electronic and signal connections between the detector and the electronic hardware are done.

Then, the chamber, the pipe and all the detector components are made out of radiopure copper, that blocks the possible radiation from the lead. Finally, the inner

side of the chamber and the pipe is covered by layer of PTFE that absorbs the copper fluorescences.

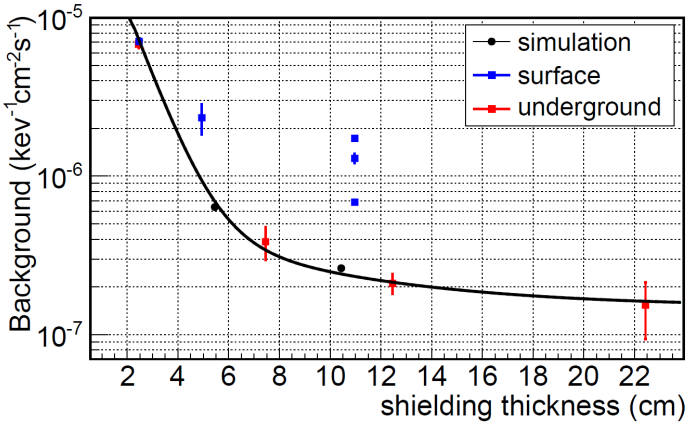

Figure 5.6: Comparison between experimental background levels obtained at surface and underground for CAST detectors shielded with different lead thickness. Black circles and their corresponding fit represent the Monte Carlo prediction from the environmental gamma flux over an intrinsic radioactivity level [193].

Several studies at the LSC and at surface have been done with different passive shielding configurations. An advantage of operating underground is that the effect from cosmic radiation can be neglected and the external gamma becomes the main background contribution. Figure 5.6 shows the comparison between different measurements of CAST-Micromegas backgrounds with different shieldings. From these studies it was proved that a layer of 20 cm of lead properly reduced the gamma background contribution to a negligible level. In the same plot, the two first points from surface background correspond to a CAST detector during the 2012 data taking campaign, and the three measurements at surface correspond, from highest to lowest level, to Micromegas setups with 11 cm thick lead shielding and no muon veto, ∼44% ∼75% efficient geometric coverage respectively.

5.3.3 Event discrimination

Finally, another technique to reach a very low radioactive background is to identify and characterize the axion-like signal events and reject every other event that does not fit with such signal characterization. For this purpose, a readout that can provide a quality topological information of the signals is required, as well as hardware that is able to process as much information as possible, and finally, an offline software discrimination process that is able to recognise signal events and reject background.

Readout patterning

The topological information from the ionization processes inside the TPC is useful in order to identify what physical process caused it. For example, a photoelectric process

caused by an x-ray event will leave a unique energy deposit in the gas that, after drifting through the TPC, will leave a small and symmetrical print on the readout. On the other hand, a muon that passes through the gas will leave a long track of ionization that will leave a long and non-symmetrical print on the readout.

To obtain a quality information from the topology of the events produced in the gas of the TPC, the readout needs to be patterned with high granularity, and microbulk Micromegas readout planes fulfil this requirement. Since their first application in CAST, the manufacturing process of this type of detectors has been refined and consolidated, and several pattern concepts can be produced. A systematic study during the years on the microbulk Micromegas mesh and pixelated anode has been done, leading to the optimization of the different parameters of the detector structure, such as the mesh pattern and thickness, the shape and size of the holes, the anode layout and the pitch of the strips. In the context of the CAST project, stripped readout planes with a pitch of $\sim$500 μm have been used during many years, showing an excellent performance in terms of pattern recognition.

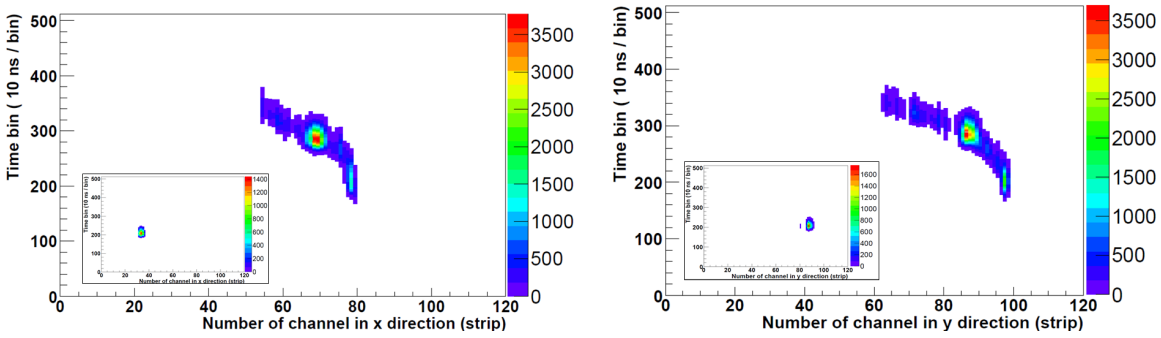

Figure 5.7: The xz (left) and yz (right) view of an electron acquired in a background run by the CAST-M10 detector in the [2-7] keV energy range, using the AFTER-based electronic cards [214]. For comparison, the embedded figures show the same views for a typical ^{55}Fe calibration x-ray event. [193]

Figure 5.7 shows two examples of different processes registered in the TPC of a CAST-Micromegas detector, highlighting the quality 3D topological information that a microbulk Micromegas can provide. The charge collection of each event is projected in spatial (x and y strips) and temporal direction (time bin). The bigger plot shows the charge deposit from a background event, presenting an extended track with a δ-ray at the center and a small energy deposit at the end. The inset plots show the same projections for an x-ray event, where the charge deposit is smaller, point-like and symmetric. This level of detail in the topological information can be used with the proper software in order to efficiently discriminate background events.

Hardware discrimination

In order to take advantage of the topological information that the readout provides, specific front-end electronics and acquisition system are needed to process the analogical

data and not loose any important information.

Previous Micromegas setups in CAST used Gassiplex-based electronics [215], with the limitation that only the integrated charge was stored. Newer designs started using the improved front-end AFTER [214], developed at CEA/Saclay, with the main advantage being that every strip pulse can be digitized with its independent temporal information. This provides a potentially large improvement in the event discrimination process, adding extra topological information, which translates in lower backgrounds. Some studies were made in the context of the CAST experiment and the upgrade of the electronic cards lead to a background reduction of a ∼25%. Table 5.4 shows the background values of two different Micromegas setups, being CAST-M10 the bench test at the University of Zaragoza and CAST2012-M18/CAST2013-M18 the detectors at CAST site.

Setup	Electronic card	Run time (hours)	Background [2-7] keV ($\mathrm{kev^{-1}\,cm^{-2}\,s^{-1}}$)
CAST-M10	Gassiplex	303.1	2.07±0.19
CAST-M10	AFTER	303.1	1.60±0.12
CAST2012-M18	Gassiplex	2265.5	1.66±0.05
CAST2013-M18∗	AFTER	445.9	1.23±0.10

Table 5.4: Comparison of the background levels obtained in the [2-7] keV range between Gassiplex and AFTER electronics for two different setups [213]. Statistical errors given as 1σ. (∗) measured with Al cathode, rest of measurements using a Cu one.

For the new IAXO detectors, a further upgrade is being tested with the new front-end AGET [181] based electronics, also developed at the CEA/Saclay. This chip offers self-trigger capabilities on every channel, so no external triggers need to be used. This can translate in a lower energy threshold. Other rare event search experiments are using this AGET based electronics like TREX-DM [35] for WIMPs, or PANDAX-III [36] for neutrinoless beta decay with satisfactory results. A more detailed description about these chips will be given later in section 8.2.4.

Software discrimination

Finally, software algorithms allow us to process the detailed topological information obtained by the patterned readout in order to discriminate x-ray signal events from other background events. Typically in CAST, the raw background in the energy region of [2,7] keV can be reduced by a factor of about $\sim 10^3$ only by the offline discrimination analysis, as it is shown in figure 5.8.

For the IAXO project, a new framework, called REST [216], is being developed in order to unify all the software needs of the experiment, from data acquisition and storage to analysis, simulation and background discrimination. It includes all the experience learnt from the CAST analysis in terms of background rejection in a new modular framework that will allow its general use and improvement in the long run. More about REST will be explained in the next sections, as it has been the main software used for this work.

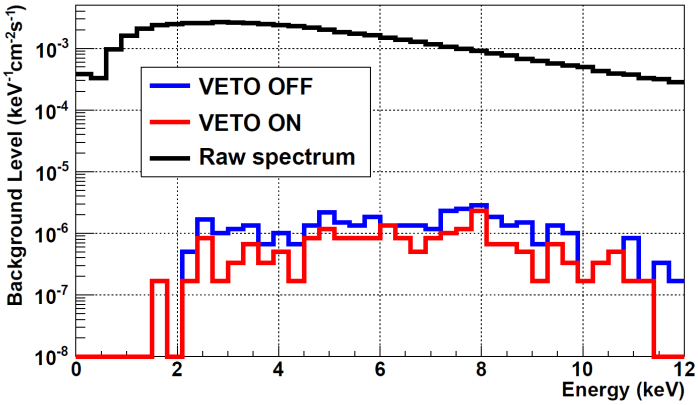

Figure 5.8: Background energy spectra of the CAST2013-M18 detector installed on the sunset side of the CAST magnet. Black line represent the raw background and red and blue lines represent the background after the discrimination analysis, with and without the veto cuts respectively.

5.4 State of the art

For the most part, the development and utilization of Micromegas detectors for solar axion searches have happened in the context of the CAST experiment. From the very first Micromegas detector installed in 2003, lots of improvements to the detector itself and the setup have been tested and proved, improving the background and the signal-to-noise ratio of the experiment. These improvements lead to the last data taking setup in 2014, with an ultra-low background microbulk Micromegas detector coupled with an x-ray focusing telescope, what is known as the *IAXO pathfinder*.

In this section, the background evolution of the different Micromegas detectors of the CAST experiment is presented, as well as its last and best results, which correspond to the IAXO pathfinder data taking campaigns.

5.4.1 Background evolution in CAST

The thorough study and the consequent upgrades of the Micromegas detectors at CAST have lead to a background reduction of about two orders of magnitude since the beginning of the experiment.

The evolution of the background level of the Micromegas detectors at CAST is shown in figure 5.9. The first detectors were installed in 2003, and the black circles correspond to in-situ background measurements in CAST. During 2007, the detectors were shielded and bulk and microbulk technologies were implemented, which resulted in a background reduction of a factor of 4.5 for the data taken the following years (the other black dots). Blue, green and purple squares represent the levels of the sunset detectors during the 2012, 2013 and 2014 data-taking campaigns, each pair of points representing

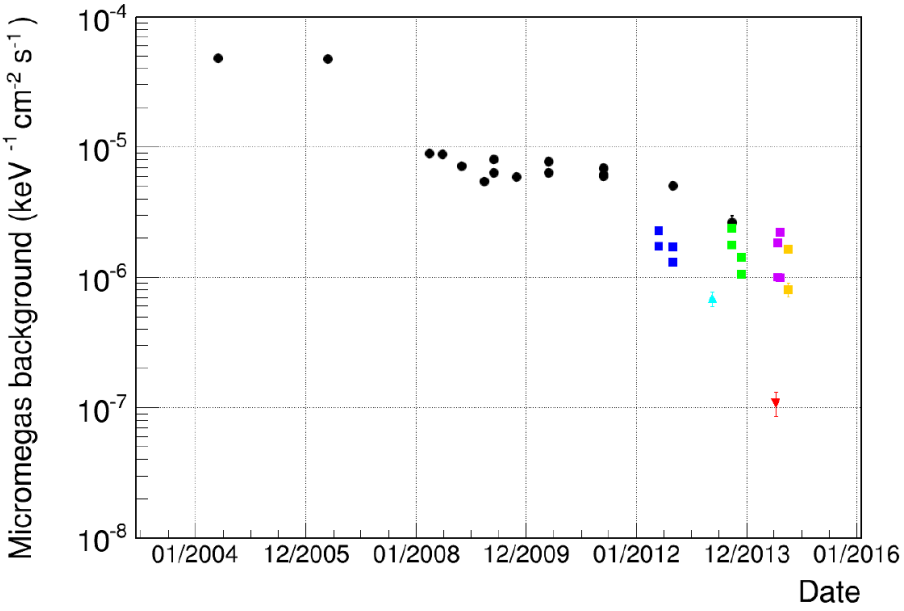

Figure 5.9: Evolution of the background level in the Micromegas detectors of CAST. Different bullets represent modifications and improvements in the experimental setup that lead to background level reductions [14]. Black circles correspond to in-situ measurements in CAST with different levels of shielding; blue, green, purple and yellow squares represent the levels of the sunset detectors; cyan triangle is the level obtained in a bench test at TREX Zaragoza laboratory; and the red triangle is the level obtained in the ultimate setup at LSC.

the level before and after the application of the veto cut. Yellow squares are the levels obtained after the sunrise upgrade in 2014 before and after the application of the veto cut. Finally, the cyan triangle is the level obtained in a bench test at TREX Zaragoza laboratory, and the red triangle is the level obtained in the ultimate setup at LSC.

The evolution of the background spectra of the CAST detectors is shown in figure 5.10. The improvements in active and passive shielding, detector design, hardware and event rejection algorithms have led to a background reduction of almost two orders of magnitude in the range of interest for axion detection.

As a final note, CAST-Micomegas detectors achieved their ever lowest background level during the bench test campaign in the LSC in 2013, with a background level of $(1.5 \pm 0.1) \times 10^{-7}$ counts keV^{-1} cm^{-2} s^{-1}in the 2–7 keV range. The energy spectrum as well as the background level during that data taking campaign are shown in figure 5.11. This value is 5–6 times lower than the lowest level obtained at surface in the CAST site.

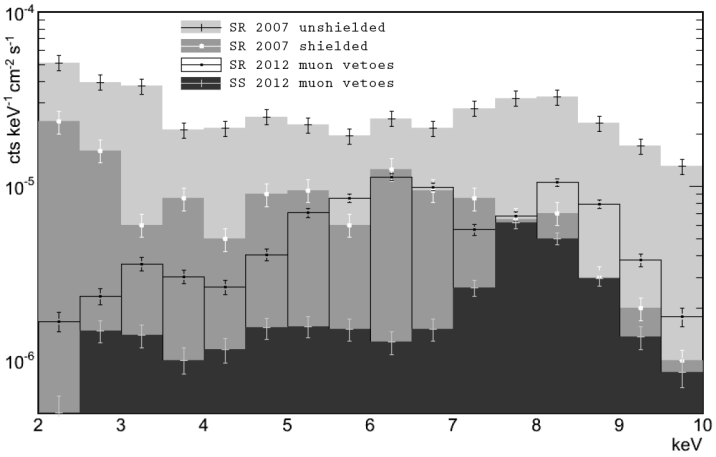

Figure 5.10: Evolution of the CAST Micromegas background spectra from 2007 to 2012 [43]. The shielding improvements are listed in the plot.

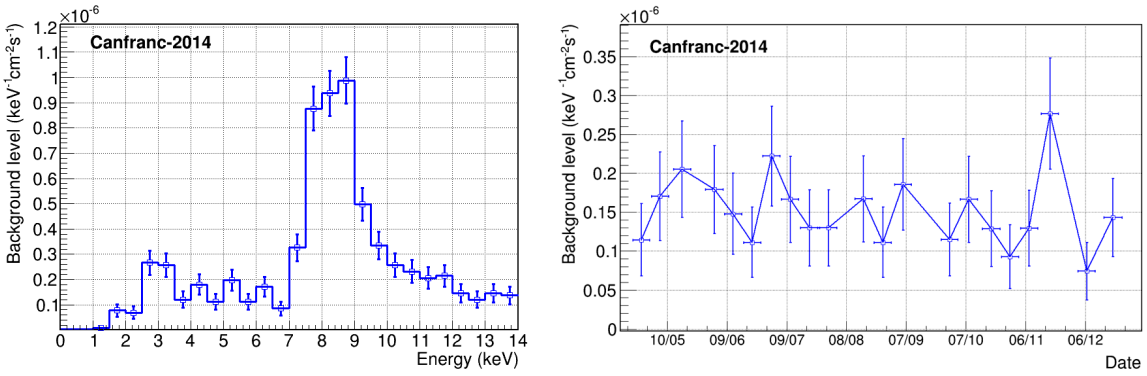

Figure 5.11: **(Left)** Background energy spectrum measured by a CAST-Micromegas detector at the LSC. [14]. The spectrum is dominated by the 8 keV copper fluorescence. **(Right)** Background rate evolution over the ∼8 months of data taking.

5.4.2 IAXO pathfinder: CAST Micromegas + XRT system

For the 2014 CAST data taking campaign, one of the Micromegas setups was upgraded by coupling an X-ray focusing telescope[2] (XRT) that allowed to focus the potential axion signal to the center of the detector readout. This was the first time an X-ray optic specifically built for axion research operated in a helioscope together with an ultra-low background detector (XRT-MM). A detailed view of the setup is shown in figure 5.12.

This upgrade came along with a new detector design fulfilling almost all the requirements discussed previously: all the detector components were built with radiopure materials (copper, kapton and PTFE); a printed board was used to leave all the high voltage and signal connections outside of the shielding; the focusing x-ray optics allowed to reduce the aperture of the pipe to half of the previous diameter; the external lead shielding was enlarged and one muon veto was installed at the top of the shielding. The

[2]Designed and built by Lawrence Livermore National Laboratory (LLNL), Technical University of Denmark (DTU) and the University of Columbia.

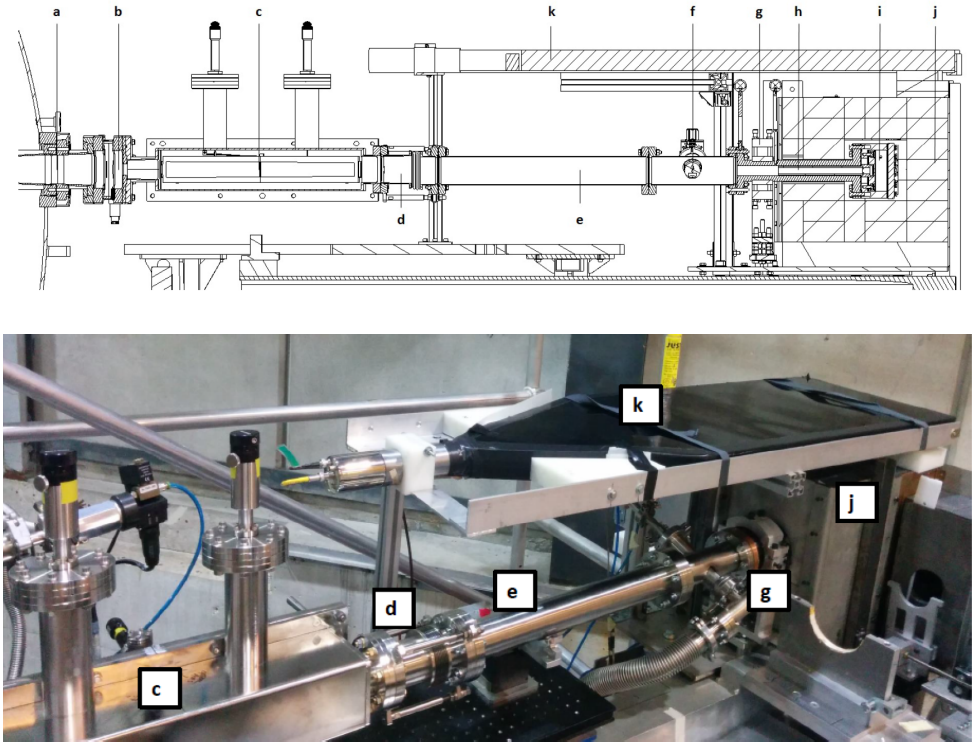

Figure 5.12: (Up) Scheme of the XRT-MM setup and **(Bottom)** picture of the actual setup installed at the end of one of the CAST magnet bores. The different parts shown are (a) a gate valve to isolate the detector line from the magnet, (b) a 4 μm Mylar differential window to protect the magnet cold bore vacuum, (c) the Wolter I x-ray optic to focus the axion signal, (d) a bellow to align the detector with the optic, (e) a stainless steel interface tube to place the detector at the correct optic focal distance, (f) a calibration system composed of an actuator with a ^{55}Fe source, (g) a precision stage that is part of the optics alignment system, (h) a copper interface tube that is screwed to the detector chamber and also forms part of the passive shielding, (i) the Micromegas detector, (j) the passive lead shielding and (k) a cosmic veto.

front-end electronics were also upgraded to the AFTER chip based technology and a new acquisition software was developed.

A new Micromegas readout was manufactured with the same specifications of the IAXO detector design: 120 strips per axis with a pitch of 500 μm in an active area of 60×60 mm^2. This resulted in the detector with the better performance working at CAST with 13% of FWHM in the 5.9 keV peak and with an excellent spatial resolution and homogeneity of the grain in the active area as well [155] (see figure 5.13).

The XRT-MM system took data during 2014 and 2015 for a total of ∼290 hours of axion-sensitive conditions (when the magnet was tracking the Sun) and ∼5500 hours of background. Table 5.5 summarizes the data sets taken with this setup [34]. The measured count rates shown are obtained after processing raw data from the Micromegas detectors with offline algorithms based on topological information of the event to keep only signal-like events, i.e. x-ray-like events [193]. This event filtering analysis can improve the raw background level at low energy in a factor ∼100, while the signal efficiency stays at 60-

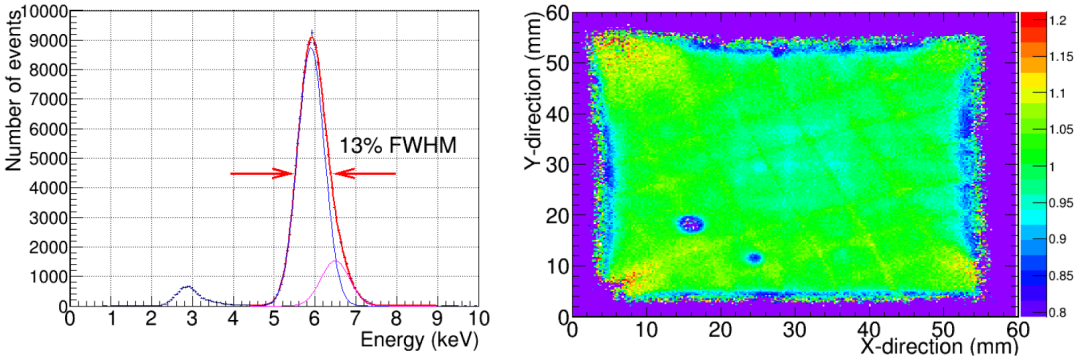

Figure 5.13: (Left) An on-site ^{55}Fe calibration of the new Micromegas detector, where the mean peak has been fit to two Gaussian functions (blue and magenta lines) corresponding to the K_α (5.9 keV) and K_β (6.4 keV) lines. **(Right)** Gain uniformity of the detector readout. The axion signal area shows 100%-95% values for the detector gain (green-light blue).

70%, which adds to the rejection factor of ∼2 of the anti-coincidence condition of the muon vetoes signal. Finally, the considered energy range of interest (RoI) is the band of 2-7 keV that contains most of the expected signal spectrum. The low energy limit is set to be well above the ∼1 keV energy threshold of the Micromegas detector, and the high energy limit prevents the contamination of the ∼8 keV Cu fluorescence peak that inevitable comes from the copper parts of the detector.

Data set	Year	Tracking exposure (h)	Background exposure (h)	Measured count rates ($\pm1\sigma$ error) (10^{-6} keV^{-1} cm^{-2} s^{-1})	
				Tracking	Background
K	2014	69.8	1379.4	0 counts	0.25±0.05 counts
L	2015	220.4	4125.4	3 counts	0.75±0.15 counts

Table 5.5: Tracking and background exposure, as well as the integrated 2-7 keV measured count rate for the two data sets taken with the XRT-MM setup at CAST [34]. Background levels are expressed in units of total counts in the spot area (95% signal-enclosing).

The background spectra of both data sets are shown in figure 5.14, where the ∼3 keV Ar and ∼8 keV Cu fluorescence peaks are clearly observed. These background events are most likely coming from cosmic secondaries that are not properly tagged due to the fact that the veto coverage was not complete, and also from remaining environmental gammas that reach the detector from the weak shielding areas such as the magnet pipe aperture or the electronics connection.

Finally, figure 5.15 shows the 2D distribution of the detected events with the XRT-MM detector, both for background and tracking data of the K and L data sets. The level of background is estimated with the events inside the expected signal area (spot) during non-tracking periods. Normalized to the ∼290 hours of tracking data, the expected background value is only 1.02±0.22 (2.13±0.47) counts in the 95% (99%) signal-enclosing focal spot region, where errors indicate 1-σ intervals [34]. The tracking data reveals 3 (4) observed counts inside such regions, with energies of 3.05, 2.94, 2.86 and 2.56 keV.

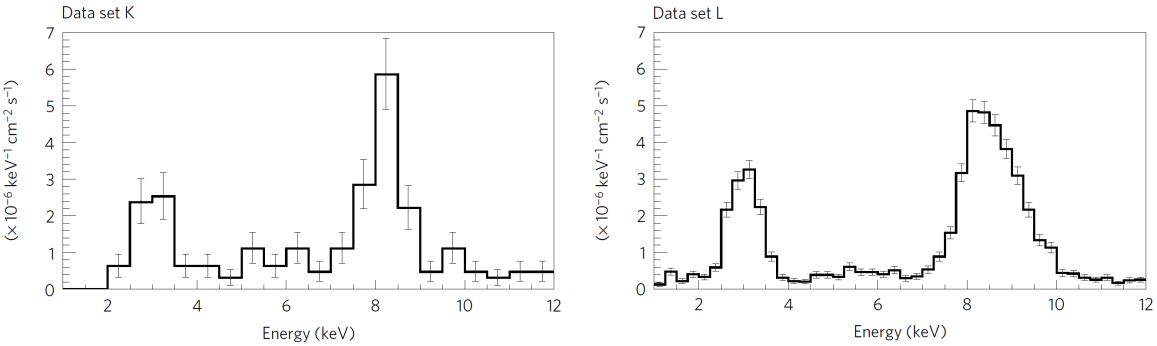

Figure 5.14: Measured count rate spectrum of background data from the XRT-MM detector (K and L sets). Data from all the detector area are included to increase the statistics of the spectra. The error bars correspond to the 1-σ statistical fluctuation of each bin content following Poissonian statistics.

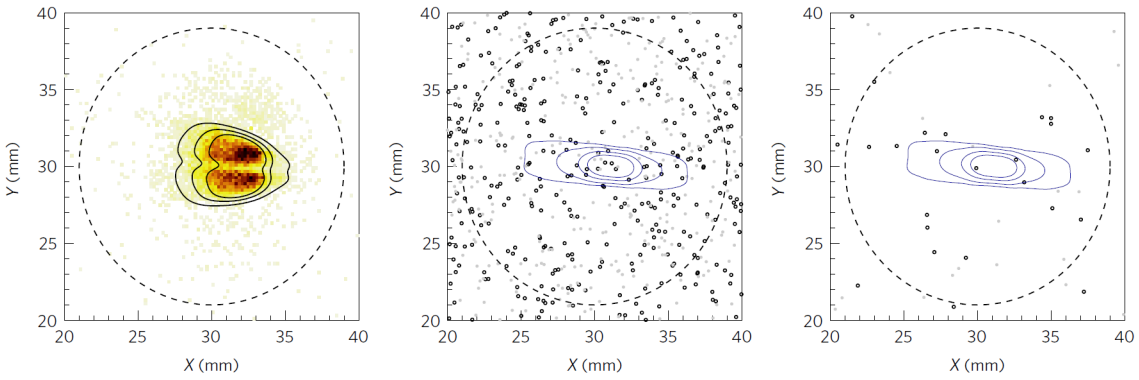

Figure 5.15: 2D hitmap of events detected in the XRT-MM detector in **(Left)** a typical on site telescope calibration run, for which an x-ray source is placed ∼12 m away of the detector, at the other side of the magnet. The contours represent the 95%, 85% and 68% signal-encircling regions from ray-trace simulations; **(Middle)** the total background data and **(Right)** the total tracking data of both of K and L data sets. In these two hitmaps, grey full circles represent events that pass all the detector cuts but are rejected because they are in coincidence with the cosmic vetoes, and black open circles represent final counts. Closed contours indicate the 99%, 95%, 85% and 68% signal-encircling regions from ray-trace simulations. The large circle represents the region of detector exposed to daily energy calibration. Results from [34].

CHAPTER 6

Simulations for IAXO-D0 with REST software

Contents

6.1 Introduction

One of the features proposed for the IAXO experiment has been the implementation of a new software that unifies all the individual analysis that previously existed in a *one for all* framework. It has been conceived to follow a collaborative work methodology so it can be used for all the different tasks required in the experiment. The philosophy behind the development of the software is to program generically, consistently and to properly document the code, so other people can learn what is already done and do not repeat work.

In this chapter, a description of this software will be presented, as well as the work that has been done to implement the geometry, readout and gas mixture of the IAXO-D0 prototype. Finally two simulation studies have been carried out to start understanding the expected behaviour of the prototype: a simulation of the efficiency of the detector and a simulation of a typical ^{109}Cd calibration.

6.2 REST Software description

Software for Rare Event Searches with TPCs, or REST [217], is a software that arises from the need to unify common codes for simulation and data processing within the GIFNA[1] group. It is an initiative from the University of Zaragoza and is being developed with the experience gained by the group during the last years while working in many TPC-based experiments, such as CAST or TREXDM. Recently, REST was proposed to be the official software framework for the IAXO project.

In the following section, a complete description of the REST software will be given, from the main classes that forms the framework to the specific packages to perform the simulations, the type of information that can be extracted from the REST based analysis and the tools that allow plotting specific information and applying event discrimination methods.

6.2.1 REST concept: one for all

REST provides a common and collaborative framework for acquisition, storage, simulation, treatment and analysis of data taken with gaseous TPCs, allowing direct comparison between data and simulations. It grants access to detailed topology information of the events in order to develop the advanced analysis tools and discrimination algorithms that rare event searches experiments require.

REST is based on ROOT[2] [218], which means that data access capabilities of ROOT are automatically inherited. Other third party software are accessed in a transparent way via packages, like GEANT4 [206, 219, 220] for the simulation of particle transport and interactions, or Garfield++ [221] for the computation of electron swarm properties in the gas.

A very important and useful feature of this framework is that it establishes a common procedure and format to define input information, via configuration (*.rml*) files. This way, there is no need for the user of modifying the code as all the information can be given to the software through these configuration files.

In a nutshell, REST can be reduced to four different type of classes that interact with each other (see figure 6.1).

- A **run** class of the type *TRestRun*. TRestRun is the central class that manages all the event data and metadata. We call a *run* to any launch of REST with the aim to perform any possible operation involving event data (as input, output or

[1] Grupo de Física Nuclear y Astropartículas, University of Zaragoza.

[2] ROOT is a modular scientific software framework. It provides all the functionalities needed to deal with big data processing, statistical analysis, visualisation and storage. It is mainly written in C++ but integrated with other languages such as Python and R.

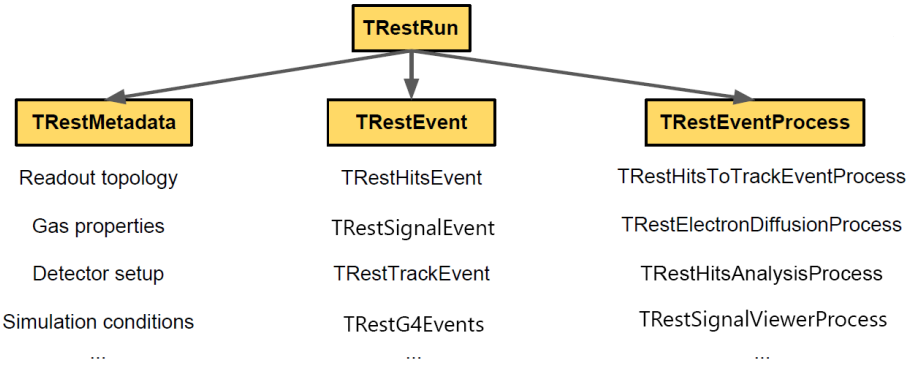

Figure 6.1: Scheme of the four types of classes that form REST and different examples of each one.

both). This can be the launch of a simulation that will generate an output event, a transformation between different types of event data, an analysis to obtain useful information from a certain event, etc. All the files generated by a run will have a pre-defined structure in the form of root trees (Ttree): one tree containing the objects of the REST event data class and another tree that contains the analysis information if any analysis was performed. Also, metadata objects are stored in the root file with collateral information on how the event data were generated.

- An **event holder** class derived from the virtual class *TRestEvent*. REST provides classes for every possible representation of a TPC event, from hit simulations to pulse data. This TRestEvents are holders that contain a collection of events of the same type. For example, a TRestSignalEvent will contain a certain number of signal pulses, and all the information about them will be stored in the corresponding root tree. A deeper description of the event classes available in REST will be provided next in this section.

- A **metadata** class derived from the virtual class *TRestMetadata*. We call *metadata* to all the additional information of the event data related with how the events were generated and all the initial conditions, like the geometry, the readout, the gas of the TPC, the acquisition configuration, etc. It is also referred to all the information related with the processes the event data have gone through. These metadata are stored via TRestRun into the root files, and they are conserved in future operations on the files. This way, every root file contains all the information needed to track back how the event data in the file was generated. The metadata classes can read input values from configuration *rml* files.

- A **process** class derived from the virtual class *TRestEventProcess* (which is derived from TRestMetadata). A *process* is an operation that acts on an input event of a specific type and creates an output event that can be the same type than the input event or a different one. For example, a TRestSignalAnalysisProcess process will read a file with signal type events and perform a series of operations with the information of the events, finally creating another signal type output file with information about the height of the pulse, the integral, the number of pulses, etc.

Another example could be TRestSignalToHitsProcess, that will read a signal type event and transform it into a hit type event. More about the specific processes used in this work will be discussed later on this section. Finally, the TRestRun is in charge of chain more than one process that the user may define in the configuration file, providing all the metadata information in case it is needed.

REST events

The most general event that REST offers is a **TRestHitsEvent**, because it can be produced both from acquired or simulated data. It is a TRestEvent that contains TRestHits. A *hit* is a deposit of energy defined by five parameters: a three-dimensional position, the energy and a temporal mark. The TRestHitsEvent stores information such as the number of hits it contains or the total energy deposited by all the hits of such event. A TRestHitsEvent is the result of transforming another input TRestEvent type (a TRestG4Event, from simulation, a TRestSignalEvent, from data, or another TRestHitsEvent) into TRestHits.

If the input TRestEvent comes from acquired data, we talk about TRestRawSignalEvent and TRestSignalEvent. A **TRestRawSignalEvent** is a TRestEvent that contains TRestRawSignals. A *raw signal* is a pulse from one of the strips of the detector readout, so it is defined only by one coordinate, where the data of the pulse is stored. Then, these TRestRawSignalEvents have to be transformed into TRestSignalEvents by a REST process that gives physical meaning to the digitalized pulses stored in the TRestRawSignals. A **TRestSignalEvent** is a TRestEvent that contains TRestSignals. These *signals* are defined by two coordinates as they have information of the charge and the relative time of the pulses. More about how TRestEvents are used for actual data taking will be further explained in chapter 9.

On the other hand, if the input TRestEvent is obtained in a GEANT4 simulation, it will be a **TRestG4Event**, which contains *G4 tracks*, formed by *G4 hits*. More details about how GEANT4 is integrated in REST will be discussed later in this section. Briefly, every time a simulated initial particle interacts with the geometry of the detector and creates a secondary emission, this is stored as a **TRestG4Track**. And all the energy deposits within this track are stored as **TRestG4Hits**, which inherits from TRestHits. The number and position of the hits depends on the GEANT4 step defined by the user.

Finally, once we have a TRestHitsEvent, it can be transformed into a **TRestTrackEvent**. It is a TRestEvent that contains TRestTracks. A *track* is a Tobject formed by a certain number of TRestHits that are closer to each other than a specific length. A TRestTrackEvent will contain all the information of the individual TRestHits that form it, as well as the total energy, the total number of hits, etc. This is very useful for the development of discrimination algorithms because it allows to know the topology of the events and, therefore, to distinguish one-single track events, which are more likely to be x-ray events rather than background.

REST processes

REST offers a broad number of different processes for simulations, data treatment and analysis. The individual processes that are relevant for this work will be described below. REST processes can be organised into three types: those that transform a TRestEvent of a specific type into another type; those that take a certain TRestEvent type data and apply transformations while keeping the same type of TRestEvent; and *analysis* processes, that operate with the information of a certain TRestEvent type and obtain physical relevant information, what we call *observables*. REST also defines a *processes.rml* configuration file where all the parameters that each process may require can be easily set by the user.

All the main TRestEvent types have processes to transform them into another. Since there are more types of TRestEvents, only those processes used in this work will be described here: from data or simulations to tracks.

- **TRestG4toHitsProcess**, from TRestG4Event to TRestHitsEvent. Every simulated deposit of energy, or TRestG4Hit, has its own (x,y,z) position, energy and time, so it is directly transformed into a TRestHit.

- **TRestFEMINOSToSignalProcess**, transforms the raw acquisition data from the FEMINOS electronic card format to a suitable REST input format for its use in the framework: TRestRawSignalEvent.

- **TRestSignalToHitsProcess**, from TRestSignalEvent to TRestHitsEvent. The x or y positions of the hit are given by the strip of the readout triggered on each case. The z position is calculated using the relative time of the signal within the signal event, the sampling time of the acquisition and the drift velocity according to the gas mixture, pressure and drift field. Finally, the energy of the hit is related to the height of the signal pulse.

- **TRestHitsToTrackProcess**, from TRestHitsEvent to TRestTrackEvent. This process goes through all the hits of the TRestHitsEvent and checks if they are closer than a certain distance defined by the user in the configuration file. If they are, they will form part of the same TRestTrack. Then, the position of the track will be defined as the mean value of the positions of every hit weighted by their energy. The energy of the track is the sum of the individual energy of every hit.

The second type of processes worth mentioning are the analysis processes. These processes are used to obtain physical information about the events, by means of observables. There are functions defined in the analysis processes that read or calculate parameters of a specific TRestEvent using the information stored in the event itself. Each specific TRestEvent has its own TRestAnalysisProcess. A brief description of the processes is given below, and a more detailed explanation about the observables will be done later on this section.

- **TRestGeant4AnalysisProcess** analyses a TRestG4Event. It calculates the energy deposited by every event in all the active volumes defined in the configuration files, as well as the mean position of the events in all the volumes. It also gives information about the physical processes behind any GEANT4 track, such as photoelectric or Compton scattering.

- **TRestRawSignalAnalysisProcess** reads a TRestRawSignalEvent as the input and it both generates observables and also computes the temporal coordinate for every signal, giving a TRestSignalEvent as the output. This is an example of how versatile REST is, since the user can customize every process as needed. This analysis process calculates observables like the integral of the signal, the baseline and its fluctuation, the rise time, the number of strips triggered, etc.

- **TRestHitsAnalysisProcess** obtains information from a TRestHitsEvent about the hit's energy, position and the shape of its print on the readout. It is a very important step in the background discrimination process because hits caused by x-rays can be characterised by some of these observables. Another useful feature of this process is that it allows the user to define a fiducial volume. A set of observables are defined related to this fiducial volume, giving information about the events that registered any energy inside, such as their mean position, distance to the fiducial volume's walls, etc.

- **TRestTrackAnalysisProcess** generates observables from TRestTrackEvents such as the number of tracks of each event, their energy, the lenghth of the tracks or the track with maximum energy of the event. It is also very useful in the discrimination process, because it benefits from the shape and the number of tracks to discriminate x-ray events from background events.

Finally, other general processes are used in the REST work flow. There exist processes like **TRestRawSignalViewerProcess** or **TRestSignalViewerProcess** that allow the user to open a viewer and see how the acquired data signals look like, allowing some preview configuration settings to filter certain aspects of the signal. Also, very useful processes for acquired signal events are **TRestSignalZeroSuppresionProcess**, to erase all the non-physical data stored in the acquisition, lightening the files and hastening further analysis. Also, **TResetSignalChannelActivityProcess**, to obtain channel activity histograms in order to check if the readout is behaving properly or if there is any bad strip.

TRestElectronDiffusionProcess modifies the punctual energy deposits from simulated data to emulate the effect of the diffusion of the gas. It performs a gaussian spreading for every hit in both longitudinal and transversal directions, using the diffusion coefficients for the particular gas mixture and pressure. Also for simulated events, when a very small step is used in the simulation process, the resulting event can have a very big amount of energy deposits, which makes further analysis very slow and also very heavy data files. To solve this, we count with processes like **TRestHitsReductionProcess**, that merges hits if they are closer to each other than a specific distance.

6.2.2 Simulation package: restG4 and GEANT4

The simulations of particle interactions in the REST framework are performed by means of the restG4 package, which implements a GEANT4 code. GEANT4 [206, 219, 220] is a modular object-oriented toolkit implemented in C++ language that provides all the functionalities for simulating the passage of particles through matter. It includes all aspects of the simulation process: the implementation of the geometry of the system and the materials definitions; the properties of the fundamental particles and the physics processes involved in particle interactions; the generation of primary particles and the tracking of the secondary particles through materials and external electromagnetic fields; the response of sensitive detector components; the generation and storage of event data and finally, the visualization of the detector and particle trajectories.

Conceptually, at the beginning of a GEANT4 simulation processing, an event contains primary particles. These particles are transported through the materials step by step with a tolerance that allows significant performance but that preserves the required tracking precision. A step is a *delta* that can be configured by the user and that provides information about what happened to the particle during this *delta*, for example, the energy lost in the step or the time spent by the step, as well as the volume where it happened or the type of interactions produced. Finally, GEANT4 implements the tracking, that stores all this information in order, so it can be followed.

In this software, the physics models that handle the interactions of particles with matter are drawn from many databases and sources, acting as a repository of particle interactions. It includes many physics processes such as electromagnetic, hadronic and optical processes, and also a large set of particles, materials and elements over a wide energy range starting from 250 eV, perfect for low-energy physics simulations.

Following the same philosophy from REST, the restG4 package allows the user to define and specify all the simulation conditions trough REST metadata configuration files (*rml*). Finally, restG4 will launch and perform the simulation using the conditions specified in the configuration file, and will create a ROOT file using the classes structure of REST libraries.

Working with restG4

In order to use restG4 as a simulation tool inside REST, two input files are required: a GDML file describing the geometry of the detector, and a *rml* file defining the simulation conditions.

The **geometry** is implemented using Geometry Description Markup Language (GDML) [222]. It is a specialized XML-based language designed as an application-independent format for describing geometries of detectors. It allows the definition of complex solid volumes which can be added, subtracted or intersected from one another. Loops can be used in order to create several volumes with similar characteristics. Then,

the materials needed can be defined by their element or by creating mixtures of elements or previously defined materials, and are assigned to the solid elements of the geometry, creating physical volumes. These volumes can be positioned and rotated, allowing the creation of rather complex geometries to work with.

The **simulation conditions** are specified in a configuration *rml* file. This file is divided in sections, each one being related to a unique TRestMetadata class:

- A *globals* section for the REST global variables used by all the framework. In this section we set information as the path where the output data files will be stored or the paths to different needed files, like the gas files.

- A *run* section that will be used for any further REST task. In this section we define generic information for the run, like the initial number of primaries to be launched by the simulation, and *runTag*, a tag that is written inside the output file name as a useful simulation identifier.

- A *restG4* section that contains all the information required for the simulation itself. There are two specific subsections for this purpose: the generator and the storage.

  The *generator* subsection describes the source, i.e. which initial particles will be launched by the simulation, their initial energy and their angular distribution; and also the origin of this source. Any number of sources can be chosen inside the generator section, each of them defined by the type of the particle, energy and angular distribution. A large variety of particles or isotopes can be chosen because it uses GEANT4 information. Also, different energy distributions can be used for the primary particles: mono-energetic, uniform energy distribution within a range or a user defined spectrum from an external ROOT file. The same can be applied for the angular distribution, having choices as isotropic, a flux in a certain direction or a user defined angular distribution from an external ROOT file. Finally, the origin of the source can be a point, a virtual surface or volume, or even a volume from the detector's geometry.

  The *storage* subsection describes which information from the simulation we want to save by the use of sensitive and active volumes. These volumes can be any physical volume from the geometry file. The *sensitive volume* acts as a trigger: only if an event produces an energy deposit in the sensitive volume, the event will be stored. Generally, the sensitive volume is set to be the gas of the TPC chamber. Furthermore, several *active volumes* can be specified to store the energy deposits occurred inside these volumes, providing it left any energy deposit in the sensitive volume as well. Finally, we can define the *energy range* we are interested on. Only events that produced an energy deposit in the sensitive volume within this range will be stored.

- Finally, a *physics list* section allows us to implement the physical processes and also cuts for track lengths or energies of certain particles. GEANT4 supports three types of physics lists: 1) electromagnetic physics list, that manages the electromagnetic interactions of leptons, photons, hadrons and ions; 2) decay physics

list for radioactive isotopes; 3) and hadron physics list, that manages cross-sections and final state or isotope production models.

6.2.3 Analysis observables

The analysis *observables* contain physical information obtained from the different types of events once they have been processed by an analysis process. They are stored in the analysis tree of the event, and they are conserved even when the same event is processed by many different analysis. These observables do not only provide information of the events but also allow us to apply cuts on them, which will be the main tool for the background discrimination. In this subsection, the main observables from each relevant analysis process will be listed.

G4 analysis observables:

The observables obtained with the TRestG4AnalysisProcess give information about the specific interactions in the simulations. They are very useful to understand the physical processes that follows each primary particle and how they interact with different parts of the geometry. The most significant ones are listed below.

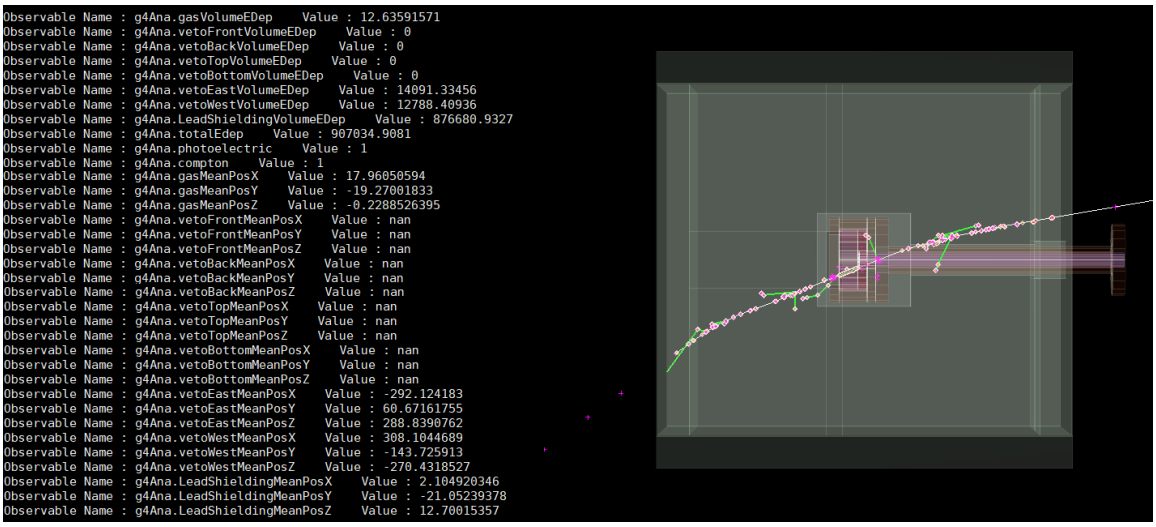

Figure 6.2: Example of a TRestG4Event with some of its corresponding observables from the IAXO-D0 background simulations. The image and the information were obtained with one of the REST visualizers, in this case, for TRestG4Events. This example corresponds to a cosmic muon crossing the setup, passing through the east and west vetoes, the lead shielding, some of the copper parts of the detector and interacting in the target gas. A further explanation of the detector geometry will be given later on this chapter.

- **Total energy deposited in a specific volume:** it stores the energy deposited by the event in all the geometry volumes specified in the configuration file.

- **Interaction types occurred in a specific volume:** these observables indicate the type of interactions occurred once the primary event has interacted with the geometry. It specifies if a photoelectric interaction, a compton interaction, etc. has been produced in a specific volume.

- **Track information in a specific volume:** these observables counts the different physical tracks produced in a specific volume, such as alpha tracks, gamma tracks, neutron tracks, etc.

- **Mean position in a specific volume:** mean x, y an z positions of the G4 event weighted with the energy of each G4 hit in a specific volume of the geometry.

Signal analysis observables:

The observables from the TRestSignalAnalysisProcess allow us to characterize the signal pulses. They give information about the shape of the pulse and the average values of certain properties of the signals that form each TRestSignalEvent. Here are listed the most significant ones. Other observables can be defined as ratios or differences between them.

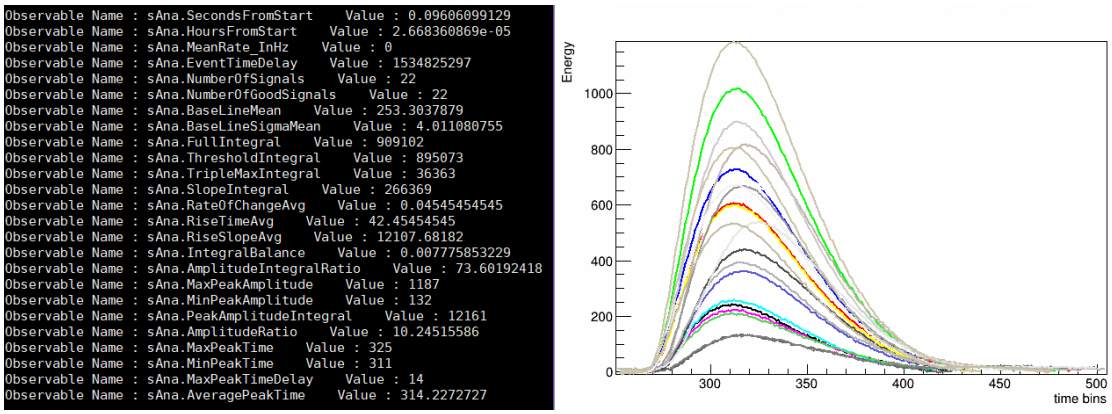

Figure 6.3: Example of a TRestSignalEvent with its corresponding observables from the TRestSignalAnalysisProcess. This example corresponds to a 22 keV event from a IAXO-D0 ^{109}Cd calibration, and it was obtained by the corresponding REST visualizer.

- **Time from start:** the time stamp of every event. It gives information about the stability of the data taking over time. It is a useful observable to localize and exclude bad data due to sporadic noise from external sources.

- **Number of signals:** number of triggered strips.

- **Number of good signals:** number of signals with voltage above a certain threshold set by the user in the configuration file.

- **Base line:** mean value of the strips voltage when no signal is induced. The window range taken in order to calculate the base line average can be set by the user. In our case, the range used is [20,200] bins.

- **Base line fluctuation:** the standard deviation of the baseline level.

- **Rise time:** the time between the point where the signal passes the threshold set and the maximum amplitude of the peak.

- **Full integral:** the pulse area between two points set by the user. This full integral takes the total pulse height for each point, regardless the baseline.

- **Threshold integral:** the pulse area between two points set by the user and over the threshold. This is a more accurate observable for the integral of the pulse, since it takes only the area of the pulse over the user set threshold and the baseline.

- **Peak amplitude integral:** integral where only the height of the bin corresponding to the peak amplitude is taken into account. It is used to obtain an energy spectrum with the same counts than signals measured on that run.

- **Maximum and minimum peak amplitude:** the amplitude of the highest and lowest signal of the signal event.

- **Maximum and minimum peak time:** the time bin of the peak of the signal with higher and lower amplitude of the signal event.

Hits analysis observables:

The observables from the hits analysis give information about the average position, shape and energy of the hit events. There are also observables related to the virtual fiducial volumes, that allow us to introduce spatial cuts to the hit events. This is specially useful in order to study a certain region of the detector or to remove border effects.

Due to the different ways of defining a TRestHitsEvent if we start from a TRestSignalevent or a TRestG4Event, there will be observables that only make sense for one of those cases. A TRestHitsEvent that comes from a G4 simulation will contain hits with three-dimensional very precise positions, whether a TRestHitsEvent that comes from acquired data will contain TRestHits with two-dimensional positions (xz or yz). This happens because each TRestHit results from the transformation of a TRestSignal, that contains information of the data acquired by one strip. The strip number is translated into distance by the TRestSignalToHitsProcess using a decoding, resulting in rather x-TRestHits or y-TRestHits.

Here are listed the most significant ones, but as happened with the signal observables, others are defined as ratios or differences between them:

- **Energy** $E = \sum_i E_i$**:** this observable is the sum of the energy of every single hit that forms the hit event. They also exist the **x energy** and **y energy** observables, that are the sum of the energy for those hits that come from the x or y strips.

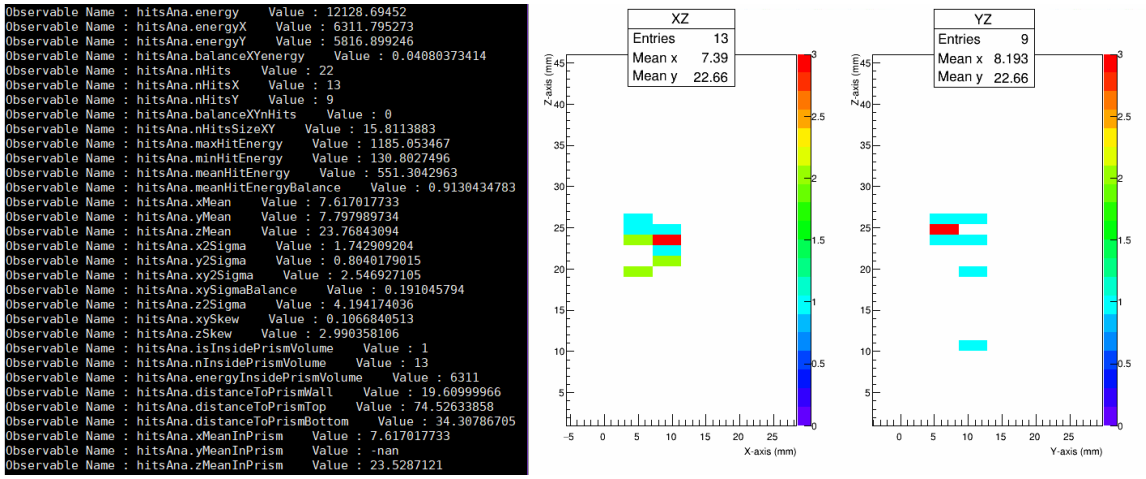

Figure 6.4: Example of a TRestHitsEvent with its corresponding observables from the TRestHitAnalysisProcess. This example corresponds to a 22 keV event from a IAXO-D0 ^{109}Cd calibration, and it was obtained by the corresponding REST visualizer.

- **xy energy balance** $\frac{E_x - E_y}{E_x + E_y}$ **:** balance between the energy deposited on the x and y strips.

- **Number of hits:** the total number of hits of the hit event. They also exist the **number of x hits** and **number of y hits**, associated to x or y strips.

- **Maximum and minimum energy hit:** the energy of the hit of maximum and minimum energy.

- **Mean position** $(\overline{x}, \overline{y}, \overline{z})$**:** the weighted mean position of the TRestHitsEvent.

$$\overline{x} = \frac{1}{E}\sum_i x_i\, E_i; \quad \overline{y} = \frac{1}{E}\sum_i y_i\, E_i \quad \text{and} \quad \overline{z} = \frac{1}{E}\sum_i z_i\, E_i \tag{6.1}$$

- **Hit size** σ_{xy}^2 **and** σ_z^2**:** these observables are the variance of the energy distribution of the hit event and give information about the xy and temporal distribution of the event. They are defined as follows:

$$\sigma_{xy}^2 = \frac{1}{E}\sum_i \left[E_i(\overline{x} - x_i)^2 + E_i(\overline{y} - y_i)^2\right] \quad \text{and} \quad \sigma_z^2 = \frac{1}{E}\sum_i E_i(\overline{z} - z_i)^2, \tag{6.2}$$

- **xy sigma balance** $\frac{\sigma_x - \sigma_y}{\sigma_x + \sigma_y}$**:** balance between the variance of the energy distribution of the hit on each x and y directions. This observable gives information about the distribution of the energy deposits on the readout.

- **Skewness** γ_{xy} **and** γ_z**:** the third standardized moment of the energy distribution inside the TRestHitsEvent. This observable measures the asymmetry of the hit event, and is defined as follows:

$$\gamma_{xy} = \frac{1}{E\sigma_{xy}^3}\sum_i \left[E_i(\overline{x} - x_i)^3 + E_i(\overline{y} - y_i)^3\right] \quad \text{and} \quad \gamma_z = \frac{1}{E\sigma_z^3}\sum_i E_i(\overline{z} - z_i)^3 \tag{6.3}$$

- **Fiducial prism or cylinder:** observables related with the virtual fiducial volumes that can be defined in the hit analysis:
  - Whether or not the TRestHitsEvent is inside the fiducial volume.
  - Number of TRestHitsEvents inside the fiducial volume.
  - Energy of the TRestHitsEvents inside of the fiducial volume.
  - Distance to the wall of the fiducial volume of the closest hit of each TRestHitsEvent.
  - Distance to the top and the bottom of the fiducial volume of the closest hit of the TRestHitsEvent. It can only be applied to simulated events.
  - Mean position of the TRestHitsEvent inside the fiducial volume.

Tracks analysis observables:

Finally, the observables from the TRestTrackAnalysisProcess give information about the number of tracks or the length and energy of the tracks in the TRestTrackEvents. Here are listed the most significant ones:

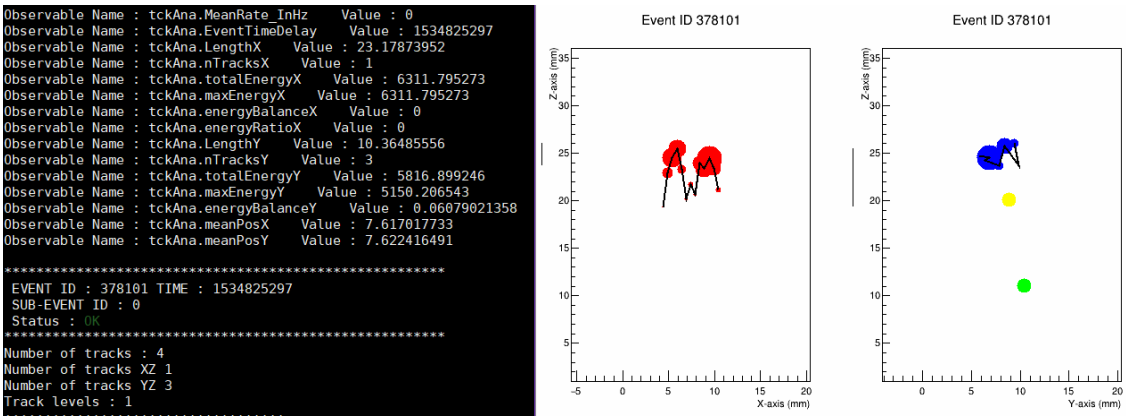

Figure 6.5: Example of a TRestTrackEvent with its corresponding observables from the track analysis process. This example corresponds to a 22 keV event from a IAXO-D0 ^{109}Cd calibration, and it was obtained by the corresponding REST visualizer.

- **Number of tracks:** the number of tracks that form part of the TRestTrackEvent. For track events that come from real data, there exist also observables for the number of x or y tracks.
- **Total energy** ($E = \sum_i E_i$)**:** sum of the energy of every track in the TRestTrackEvent. For tracks that come from signal events, there exist the E_x and E_y observables, that are the sum of the energy of the tracks from the x and y strips individually.
- **Energy of the most energetic track** (E^{max}): this observable is the energy of the most energetic track of the TRestTrackEvent. There are also E_x^{max} and E_y^{max}

observables, that are the energy of the most energetic track of the TRestTrackEvent from the x and y strips individually.

- **Energy balance:** the balance between the total energy of the track event and the track with maximum energy of the track event. This observable can be used to identify track events where most of the energy is deposited in one of the tracks. It is defined as follows:

$$Balance_x = \frac{E_x - E_x^{max}}{E_x + E_x^{max}} \quad \text{and} \quad Balance_y = \frac{E_y - E_y^{max}}{E_y + E_y^{max}} \tag{6.4}$$

These observables will be referenced along this work because they are the main tool used to understand, characterize and identify events from data and simulations. They are the central concept of the new discrimination method for the background rejection.

6.2.4 Plots and discrimination cuts

REST implements a tool to plot the observables of the event files using the ROOT graphic options. Following the framework philosophy, all the specifications of the plots can be easily set by the user using a *rml* configuration file. This file gives a lot of freedom to plot whatever information we need. It allows us to use as many input files as needed, and a parameter is required in order to specify if the observables from the different files will be compared or added.

The configuration file also allows to define several plots. The size and the layout of the canvas can be specified. Each of the individual plots will ask for a name and title, the labels for the axis and the observables to be ploted, with their range and the number of bins. If only one observable is set, the resulting plot will be a histogram. With this tool, two and three dimensional plots can be defined.

The most interesting part of the plot tool is the definition of the **selection cuts** on the observables. These cuts are conditions that can be imposed to the plotting tool so it will only plot the events from the event file that satisfies that condition. For example, we could be interested in plotting the energy of the events with only one track, or of the events that interact only at the central surface of the readout (figure 6.6).

In the configuration file, global and individual cuts can be defined. The general cuts will be applied to all the plots of the canvas. But also, individual cuts can be set in the different plots for more detailed information.

6.3 IAXO-D0 geometry implementation

The first stage of this work was the IAXO-D0 implementation in REST. This involved the creation of the geometry of the complete setup, the detector itself as well as the

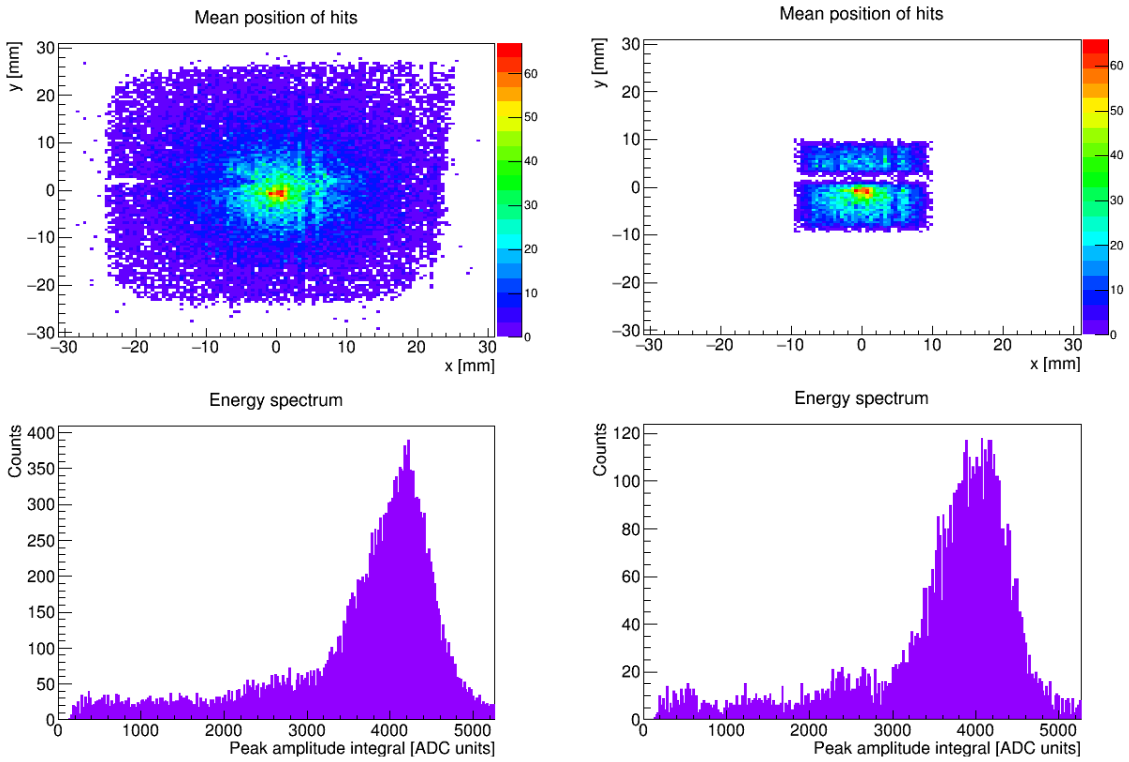

Figure 6.6: (Up) Hitmaps (xy mean position of the hits) of a IAXO-D0 ^{109}Cd calibration. **(Down)** Energy spectra of a IAXO-D0 ^{109}Cd calibration in ADC units. **(Left)** Plots with no xy-fiducial cuts. **(Right)** Plots with a fiducial cut, where only the events in a $10\times10\,\mathrm{mm}^2$ area at the center of the readout are selected.

surrounding shielding, and the definition of all the materials using the GDML tools that REST provides. It was also needed to define the structure of the detector readout as accurately as possible in order to take advantage of its high granularity. Finally, another step has been to generate all the gas mixtures with all their transport properties.

6.3.1 Geometry

Following the GDML approach, a geometry was produced to replicate the IAXO-D0 detector and shielding as accurately as possible. Although, some aspects of the real setup have been simplified when they were considered to have little or no impact on the background, such as the copper screws, the exact shape and details of the teflon gaskets, etc.

Some views of the geometry of the chamber are shown in figure 6.7. The detector chamber is a copper cylinder with an inner radius of 50 mm, a height of 45 mm and a thickness of 18.8 mm. It sits on a circular piece attached to a rectangular one, which both together form the raquette. On top of the circular part of the raquette it is placed a 40 μm coat of kapton, and on top of that, a 5 μm copper squared readout with 60 mm long sides. A 2 mm thick teflon cylinder covers the internal side of the copper chamber. The

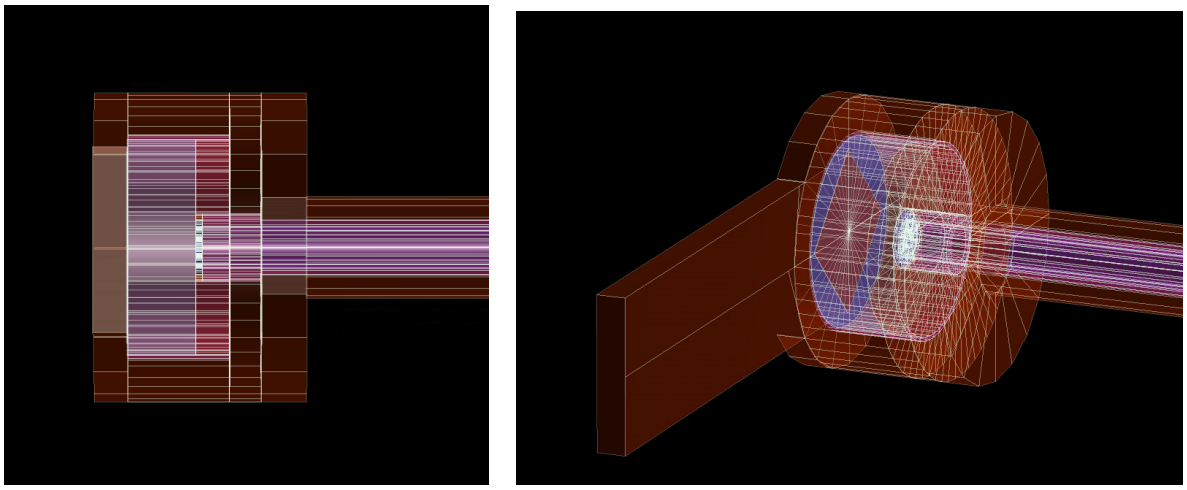

Figure 6.7: Simulated detector geometry. The orange volumes are the copper parts (pipe, raquette, chamber, cathode...); the grey volume is the target gas; the pink volumes correspond to the kapton pieces (inner cover of the tube and chamber), and finally the blue volume is the kapton external cover of the readout.

copper cathode closes the upper part of the chamber, leaving an internal gas cylindrical volume of 30 mm of height and a radius of 48 mm. To ensure the tightness of the gas chamber, another copper piece closes the chamber and it is attached to the flange of the pipe. The pipe has an internal radio of 12.5 mm and lengthens all the way to the outside of the shielding. Its inner side is covered by a teflon cylinder of 3 mm thick. The volume left inside of the pipe is defined to be vacuum.

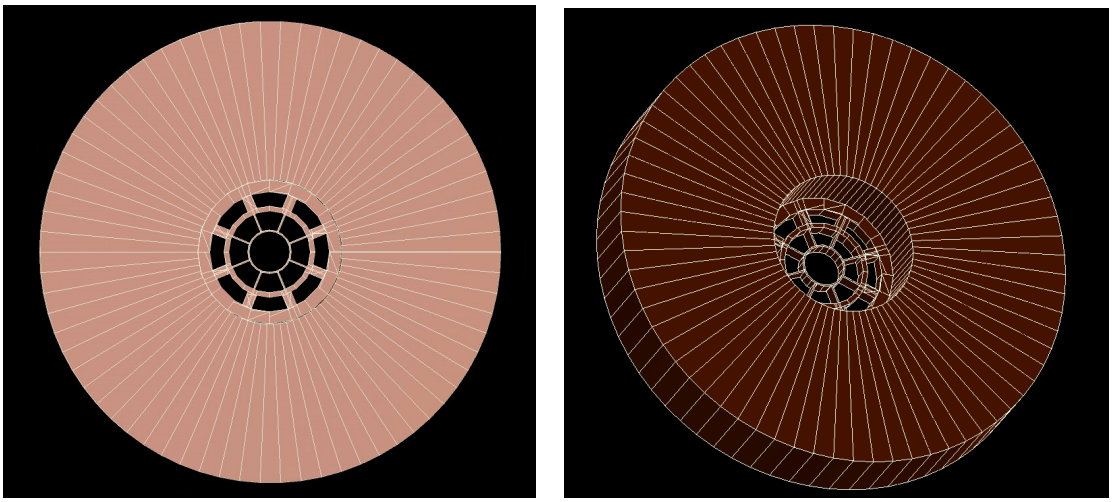

Figure 6.8: Detailed simulated spider cathode, using GDML description and ROOT visualization tools.

A detailed view of the copper spider-web cathode is shown in figure 6.8. It consists of three concentric cylinders joined by eight radii, leaving a central circular hole with a radius of 4.25 mm. The cathode has a thickness of 3 mm and it has attached a 4 μm layer of Mylar to act as the detector window. Also, a cylindrical piece of teflon is placed on

top of the spider-web cathode, allowing a better attachment to the pipe and also covering part of the cathode itself, leaving a smaller open space.

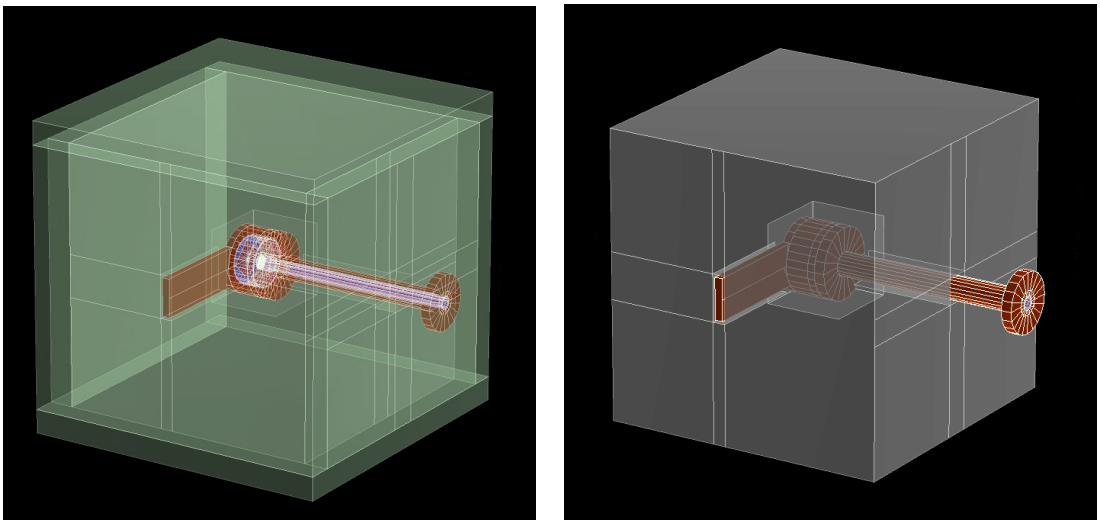

Figure 6.9: (Left) Complete geometry of IAXO-D0 with the detector inside the lead volume (grey) and all the six idealized cosmic vetoes around it (green). **(Right)** Geometry of IAXO-D0 without the cosmic vetoes, for a better understanding of the lead shielding.

The detector chamber is placed in the middle of the lead shielding, as it is shown in figure 6.9. It consist of a solid lead cube with 550 mm long sides, and a cubic air hole inside for the chamber to fit in. It also has holes for the raquette and the pipe to go through. Finally, on all the six sides of the lead shielding, a squared plastic scintillator is placed to act as cosmic vetoes. They are long enough to cover completely the lead shielding and have a thickness of 50 mm.

6.3.2 Readout

In REST there are a set of classes all related to the readout generation and implementation, derived from TRestMetadata. The readout class defines methods to stablish a relation between the hits inside the TPC and the signals obtained by the acquisition electronics.

Any readout can be defined in a *rml* file, allowing the user to generate and implement different readouts without modifying the code. The most elementary component is a **pixel** (TRestReadoutPixel). All the pixel features like the geometrical description, origin, position, orientation an size can be specified. A certain number of pixels will construct a readout **channel** (TrestReadoutChannel). This is the equivalent to the Micromegas strips: when a pixel is activated, the corresponding channel will be activated as well. A set of channels will define a readout **module** (TRestReadoutModule). The module geometrical description, position, orientation an size can be specified. Also, it will contain a vector of channels with the definition of the readout channels existing in the module. Several of this modules can be placed at the same readout **plane**

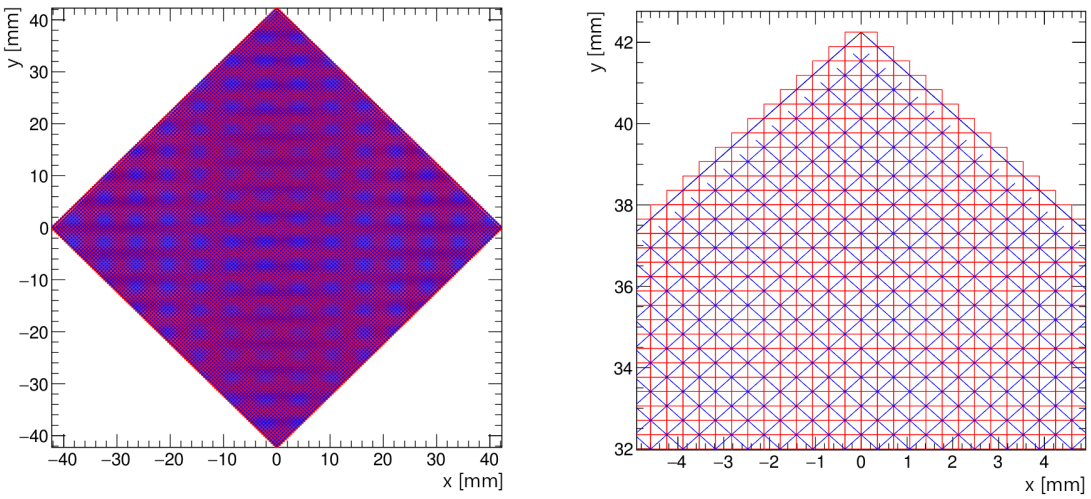

Figure 6.10: Simulation of the readout of the IAXO-D0 Micromegas detector.

(TRestReadoutPlane). The properties of the plane have to be specified as well, including the geometrical description, plane position, orientation, and the cathode position. Finally, one or several planes will form the **readout** (TrestReadout).

For the IAXO-D0 readout implementation, a single plane and single module REST readout has been created. It is a squared readout with 60 mm sides, and it is rotated 45 degrees to match the experimental configuration. It has 120 strips per side separated by a pitch of 500 μm. Each pixel is a square with sides of $\sqrt{5}\,\mu$m. Special attention has been put to match the border strips, because in the IAXO-D0 readout, the border pixels are triangular shaped.

A very important part of the readout is the decoding, i.e. the relation between the channel number imposed to every signal by the acquisition electronic card and the REST readout channel. This relation can be implemented in the readout definition by means of an external decoding file. REST allows to specify different decoding files for the different modules of the readout. A detailed effort was also done to create the decoding file taking into account the channels given by the AGET electronic card. This way, the same readout can be used to analyse both the simulations and the laboratory data.

6.3.3 Gas mixtures

REST provides a TRestMetadata class, named TRestGas, that allows us to generate and implement any gas mixture and its electron drift properties, such as drift velocity, diffusion, Townsend coefficients, etc. TRestGas uses a CERN's software called Magboltz [16] to generate gas files. Magboltz is a code that computes drift gas properties by numerically integrating the Boltzmann transport equation. Once these gas files are generated, REST can easily access to all the drift properties of a certain gas mixture

at a specific pressure, temperature or electric drift field.

One of the first steps for the IAXO-D0 implementation in REST has been to generate the gas files needed, that are

- **Ar+iC4H10 (98%-2%) at 1.4 bar** is the gas mixture that was typically used in the last years for the CAST Micromegas detectors, and was also the target gas used for the first data taking campaign in IAXO-D0.
- **Xe+iC4H10 (98%-2% and 99%-1%) at 0.5 bar** are the mixtures proposed for the IAXO Micromegas detectors and therefore, it is required a proper study and test of these gas mixtures. As it was mentioned in chapter 4, Xenon has a bigger ionization cross section [223], which allows to reduce the pressure of the chamber while obtaining a similar efficiency than Argon based mixtures. The reduction of the gas pressure is an advantage in order to go towards thinner differential windows to reduce the energy threshold.

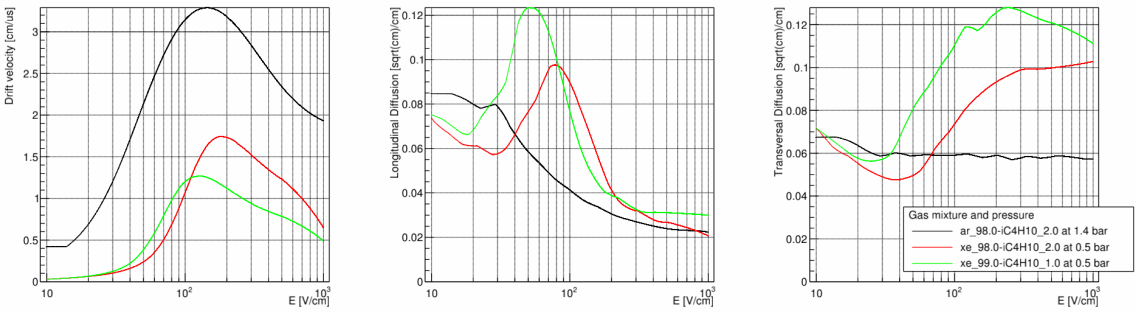

Figure 6.11: Properties of the gas mixtures studied for IAXO detectors, obtained using REST and Magboltz. Black line is the Argon and Isobutane (98%-2%) mixture at 1.4 bar; red line is the Xenon and Isobutane (98%-2%) mixture at 0.5 bar and green line is the Xenon and Isobutane (99%-1%) mixture at 0.5 bar.

Figure 6.11 shows the drift velocity and longitudinal and transversal diffusion coefficients of these three mixtures as a function of the drift field of the chamber. For the IAXO-D0 prototype, the drift fields will be of the order of ∼100 V/cm. As a general conclusion, for such values of drift field, higher drift velocity and also smaller diffusion coefficients will be reached in the argon based mixture than in the xenon based mixtures.

6.4 IAXO-D0 preliminary studies with REST

Once the IAXO-D0 setup has been fully implemented in REST, some preliminary studies have been made in parallel of the prototype commissioning in order to start comprehending what to expect from the experimental setup. In this context, a simulation of the efficiency of the detector has been carried out for the gas mixtures and the energy range of interest,

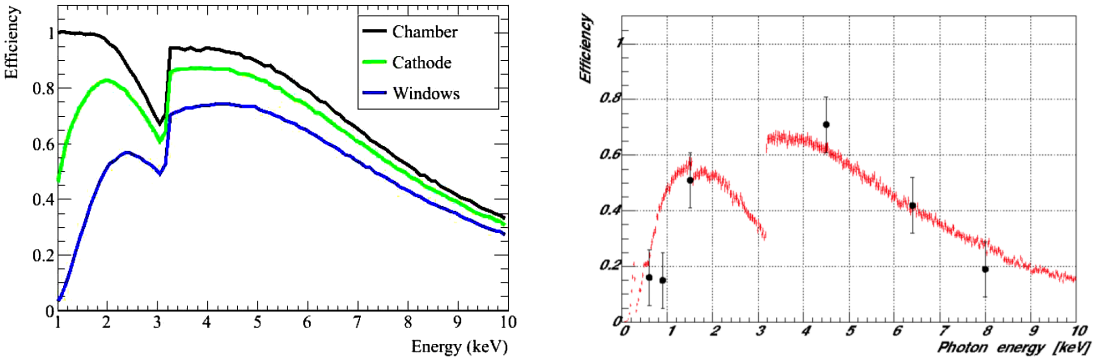

Figure 6.12: (Left) GEANT4 simulation of the quantum efficiency of the 2011 CAST Micromegas detector with Ar+iC4H10 (98%-2%) at 1.4 bar. Different efficiency losses are shown: considering only the *chamber* (or gas) efficiency (black line), adding the strongback cathode (green line) and also, the differential and cold windows (blue line) [224]. **(Right)** Simulated detector efficiency with the experimental points measured at PANTER for the 2003 CAST Micromegas detector with Ar+iC4H10 (95%-5%) at 1 bar [225].

and also a simulation of a ^{109}Cd calibration, which has been the radioactive source used for the daily calibrations during the data taking.

6.4.1 IAXO-D0 efficiency

The efficiency of the detector is the probability of a signal event, i.e. an x-ray coming from the magnet's bore with an energy in our RoI, being registered in the detector. In IAXO, this efficiency depends on many aspects, beginning with the photon having to go through the windows and strongbacks that separate the magnet from the x-ray telescope (cold-window), the x-ray telescope from the detector's pipe (differential window) and then, the pipe from the TPC gas chamber (detector window). The distance from the cold-bore to the detector does not affect the photons because the pipe is under vacuum. But when the photon reaches the gas volume, the actual percentage of photons that reaches the gas and converts into charge carriers, or the quantum efficiency, has to be taken into account.

In the context of the CAST detectors, measurements [159,225,226] and simulations [14,21,224] have been done in order to quantify the efficiency of the Micromegas detector in the energy RoI (figure 6.12). These efficiency studies were performed considering the previous configurations of CAST detectors, featuring different cathode strongbacks, materials of the chamber parts, different options of polypropylene and aluminized-polypropylene windows and different proportions of Ar+iC4H10 for the gas target. Simulations are more recent, but measurements of the detector efficiency require the use of specialized x-ray facilities like PANTER[3], so the available information is not completely updated.

For a proper study of the IAXO detectors, new simulations have been done

[3]PANTER x-ray test facility. Max Planck Institute for extraterrestrial Physics (Munich).

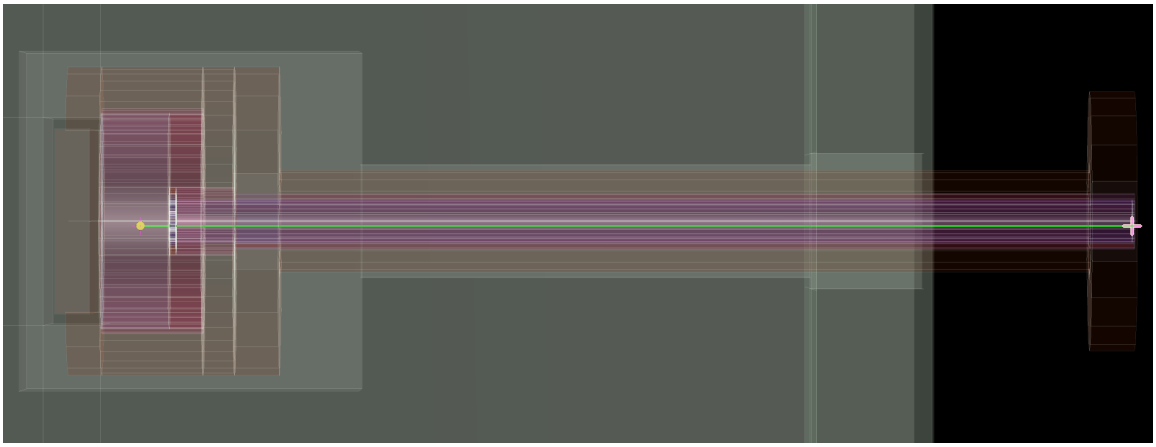

Figure 6.13: Example of a simulation of a 3 keV x-ray event from the virtual source at the beginning of the pipe. The pink cross marks where the x-ray was produced, the green line is the path of the x-ray trough the vacuum of the pipe and the yellow dot is the energy deposition of the x-ray in the gas.

implementing the new elements of the detector geometry: the copper strongback with spider-web design and the 4 μm Mylar window. Also, the possibility of using xenon instead of argon as the active gas has to be taken into account, so new simulations of the detector efficiency with xenon were needed.

Simulations and methodology

The objective of this study has been to compute the efficiency of IAXO-D0 for both Ar+iC4H10 and Xe+iC4H10. This is why only the detector window has been implemented in the geometry, and the focusing feature of the x-ray telescope has not been taken into account.

A new REST geometry has been created for this purpose with a virtual volume at the beginning of the pipe, shaped as a flat disc with the internal diameter of the pipe and a few μm of thickness. The primary x-rays have been configured to have their origin uniformly distributed in the virtual source and their angular direction parallel to the pipe towards the detector.

The REST simulations have been configured to launch monochromatic x-rays as primary events, 10^6 x-rays per emission line, in the IAXO energy RoI with 0.1 keV spacing. These simulations have been performed for both Ar+iC4H10 (98%-2%) at 1.4 mbar (CAST conditions) and Xe+iC4H10 (98%-2% and 99%-1%) at 0.5 mbar. An example of one of these simulations is shown in figure 6.13.

The quantum efficiency has been calculated as the ratio between the number of the primary x-rays and the number of the simulated events that have been registered in our detector after they have travelled along the pipe, passed through the window and interacted with the target gas.

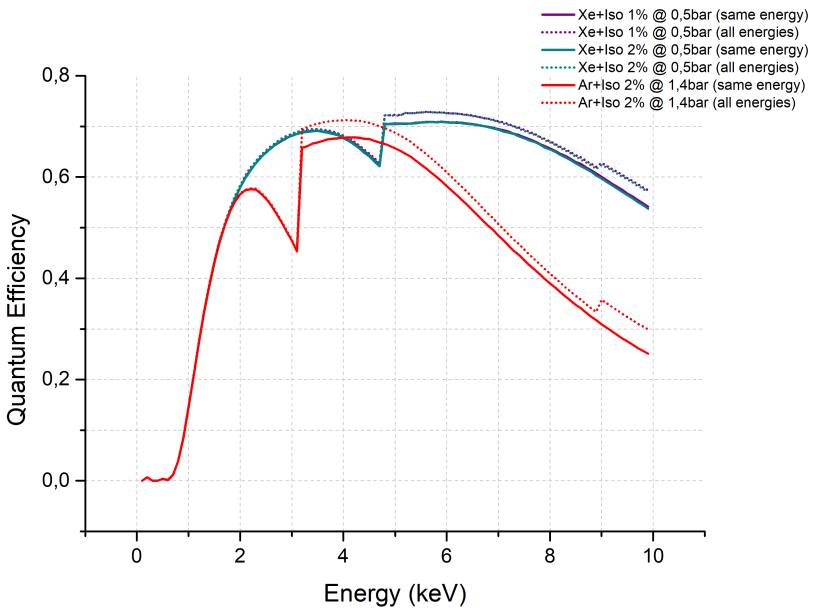

Figure 6.14: IAXO-D0 quantum efficiency. Only the detector window was considered. Three mixtures of gas were simulated: Ar+iC4H10 (98%-2%) at 1.4 mbar and Xe+iC4H10 (98%-2% and 99%-1%) at 0.5 mbar. Dotted lines correspond to the scenario where all the final events were considered while solid lines correspond to the scenario where only the final events with the same energy than the initial x-ray were considered. Note that both Xe based mixtures overlap.

Results for Argon and Xenon

Once the x-ray simulations for the energy range of interest had been carried out, the corresponding root files containing the TRestG4Events have been processed using different processes of TRestEvent conversion and analysis to obtain TRestTrackEvents with all the observables. The resulting curves of the quantum efficiency simulations for IAXO-D0 are shown in figure 6.14 for the three gas mixtures studied. We see that using xenon based mixture allows us to go down to lower pressures while obtaining the same quantum efficiency.

In order to define the number of events detected, two scenarios have been considered: 1) including all of the events that interacted inside the gas, despite of their energy up to 10 keV (labelled as *all energies*); 2) considering only the events that interacted in the gas with the same energy as they were launched (labelled *same energy*). The second scenario is a theoretical one in order to know precisely the percentage of x-rays that do not lose any energy in their journey from the entrance of the pipe to the gas volume itself. But experimentally, the second scenario is more likely, since we are not able to identify the source of each energy deposit.

The argon based mixture shows a decrease of efficiency for x-rays with energy of 2-3.2 keV because of the absorption of the argon atoms at 2.9 and 3.1 keV. This is not ideal because the expected solar axion spectrum peaks around 3 keV. On the other hand, the

xenon based mixture shows a less pronounced decrease of efficiency around 4-4.7 keV due to the absorption of the xenon atoms at a 4.1, 4.4 and 4.7 keV, but overall, the efficiency remains higher for all the IAXO RoI. This makes this mixture more suitable for the active gas of the detector.

There is also a decrease of efficiency at 8.9 keV but only for the *all energy* curves. This is due to the copper absorption, and is only visible for those cases where also the fluorescence events caused by the walls of the chamber are taken into account.

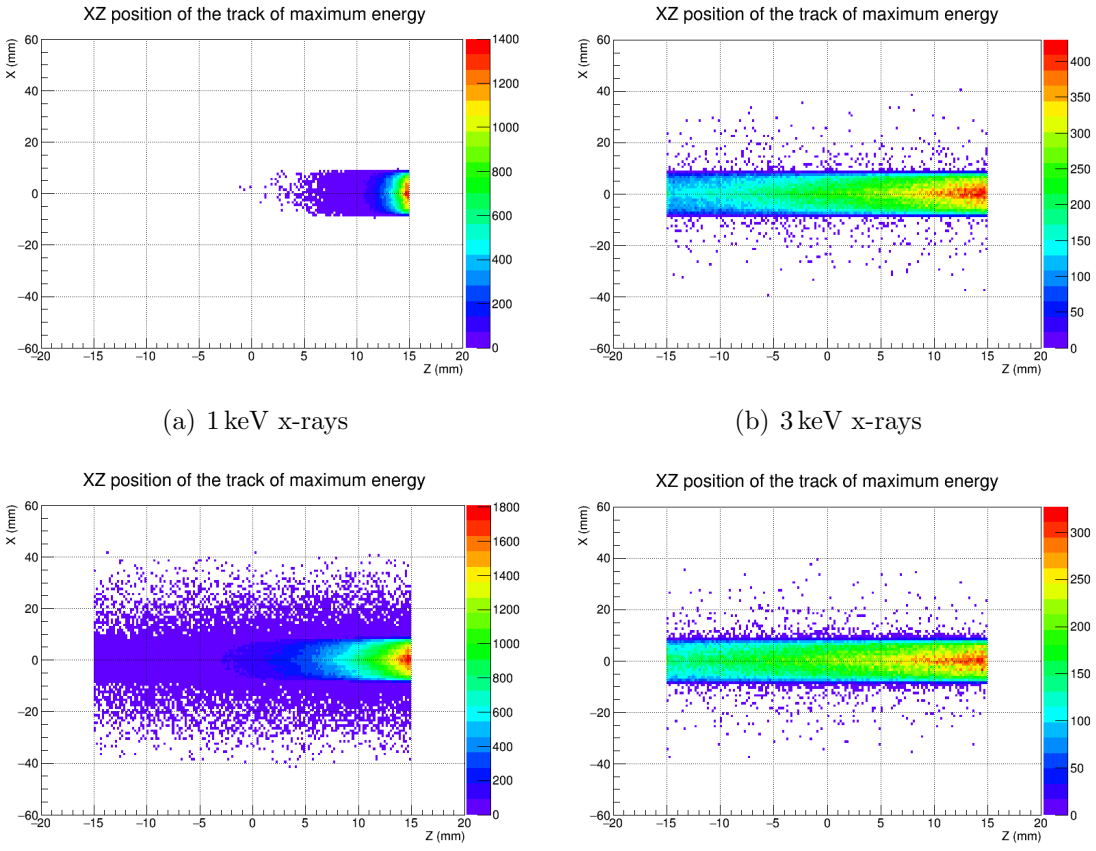

(a) 1 keV x-rays

(b) 3 keV x-rays

(c) 4 keV x-rays

(d) 8 keV x-rays

Figure 6.15: XZ mean position of the track with maximum energy of the events produced by different x-ray lines in Ar+iC4H10 (98%-2%) at 1.4 mbar. The detector window is placed at z=15 mm and the gas volume extends between z=[-15,15] mm and x=[-48,48] mm.

We can also use these simulations to see the effect of the diffusion of the gas and the penetration of the different x-rays inside the chamber depending on their energy. Figure 6.15 shows the xz mean positions of the main track of each event for different x-ray lines in Ar+iC4H10 (98%-2%) at 1.4 mbar. We observe higher penetration for higher x-ray energies. Also, at 4 keV, a higher dispersion of the events is obtained due to the absorption and corresponding emission from the argon atoms of the gas.

Finally, in figure 6.16, xy and xz mean position plots are shown for argon and xenon based mixtures for the same 3 keV x-ray line. We observe that for the argon-based

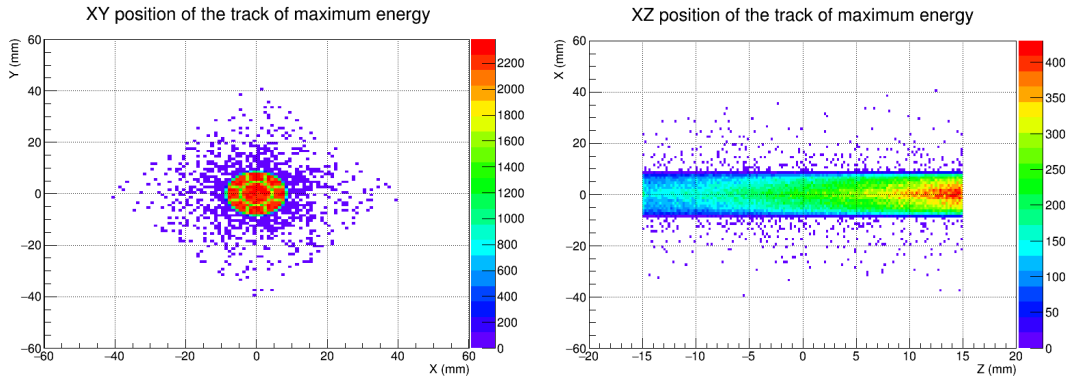

(a) Ar+iC4H10 (98%-2%) at 1.4 mbar.

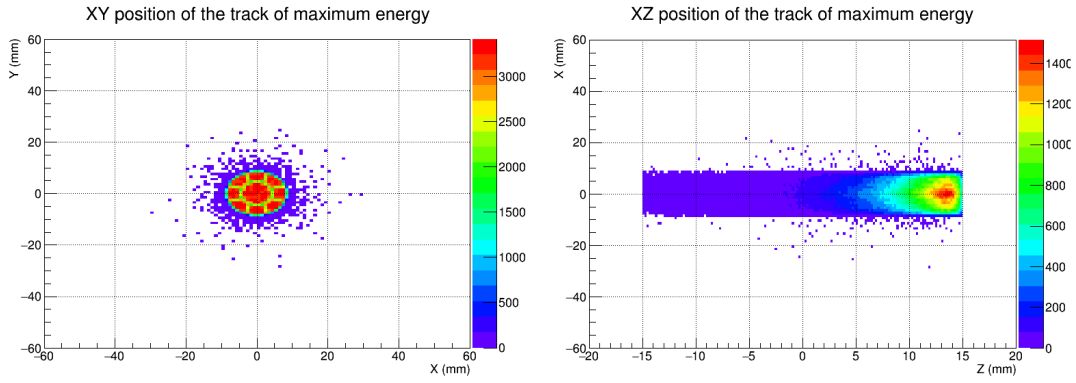

(b) Xe+iC4H10 (99%-1%) at 0.5 mbar.

Figure 6.16: XY and XZ mean position of the track with maximum energy of the events produced by the same x-ray line (3 keV) in Ar+iC4H10 (98%-2%) at 1.4 mbar and in Xe+iC4H10 (99%-1%) at 0.5 mbar. The detector window is placed at z=15 mm with a detection area between x,y=[-48,48] mm and the gas volume extends between z=[-15,15] mm.

mixture, the 3 keV x-rays penetrate deeper in the gas volume, whereas for the xenon-based mixture, almost all the x-rays interact as soon as they enter the chamber, at the top part of the drift volume. This is due to the argon K-edge at 3.2 keV, as it was previously explained in section 1.3.3. Basically, when an argon atom is excited with an energy higher than the binding energy of the K-shell electrons, it will be able to produce either a fluorescence in the x-ray range, or an Auger electron of 3.2 keV. These processes will further ionize the gas, producing a chain reaction that can penetrate deeper in the gas volume. Eventually, this x-ray fluorescence can escape from the gas without interacting, what will produce an *escape peak* in the final spectrum.

Also, the x-rays in the argon-based mixture are more dispersed on the surface of the readout, while the x-rays in the xenon-based mixture are concentrated at the middle of the readout. This can be explained again by the absorption of the argon at 3 keV and the consequent emission of x-ray fluorescences that can travel in the gas and interact farther. These effects can favour the use of xenon over argon, because xy-fiducial cuts can be more restrictive. Also, having all the x-rays interacting at a similar z position will translate in a better definition of the size of the x-ray-like events that come from the pipe,

and therefore a better definition of the background discriminants.

6.4.2 Simulation of a ^{109}Cd calibration

The simulation of a calibration run can give useful information in order to understand the experimental spectra taken in IAXO-D0. The previous CAST Micromegas detectors used to be calibrated with a ^{55}Fe source, which emits a 5.9 keV x-ray. This has changed for IAXO-D0, because the aperture of the pipe has been reduced, so the standard ^{55}Fe source does not fit inside. The calibration source for IAXO-D0 is a ^{109}Cd, that emits a 21.9 keV x-ray (see table 6.1).

X-rays from ^{109}Cd (462.6 d 4)		
E (keV)	I (%)	Assignment
2.984	4.5 7	Ag $L_{\alpha 1}$
3.151	2.6 4	Ag $L_{\beta 2}$
21.990	29.5 11	Ag $K_{\alpha 2}$
22.163	55.7 20	Ag $K_{\alpha 1}$
24.912	4.76 17	Ag $K_{\beta 3}$
24.943	9.2 3	Ag $K_{\beta 1}$
25.455	2.30 8	Ag $K_{\beta 2}$

Table 6.1: Principal emissions of ^{109}Cd [209] (with I(%)>1).

To fully understand the ^{109}Cd spectrum measured with the IAXO-D0 Micromegas detector, a ^{109}Cd calibration simulation has been performed using a special geometry, shown in figure 6.17. An aluminium 2 mm-radius-sphere has been simulated inside the pipe and close to the cathode as the source holder.

The simulation has consisted in 2.22×10^7 initial events of the ^{109}Cd isotope from the aluminium sphere volume. Considering a source of 1μCi, it would correspond to a 10 minutes calibration. The resulting spectrum is shown in Figure 6.18. The peaks are very narrow because the spectrum is taken directly from the information of the TRestG4Events to perfectly understand all the contributions. Then, in order to obtain an spectrum directly comparable with the experimental data, we would need to convolute it taking into account the resolution of the detector. The main peaks we expect are the x-rays from the ^{109}Cd source, at 25.4, 24.9, 22.2 and 21.9 keV. The corresponding escape peaks in argon of these x-rays are situated at 22.2, 21.9, 19.3 and 19.1 keV. Then, at 8.9 and 7.9 keV we have the x-ray emission from the copper parts of the detector. And again, at 5.9 and 5.0 keV we have the escape peaks from the copper x-rays in argon. Finally, at the very beginning of the spectrum, at 1.4 keV a small peak appears due to the x-rays from the aluminium source holder.

Once the simulation has been performed, the usual REST analysis that has been used in this work for processing simulations, and that will be fully detailed in the next chapter, has been applied. TRestG4Events are processed and then transformed into

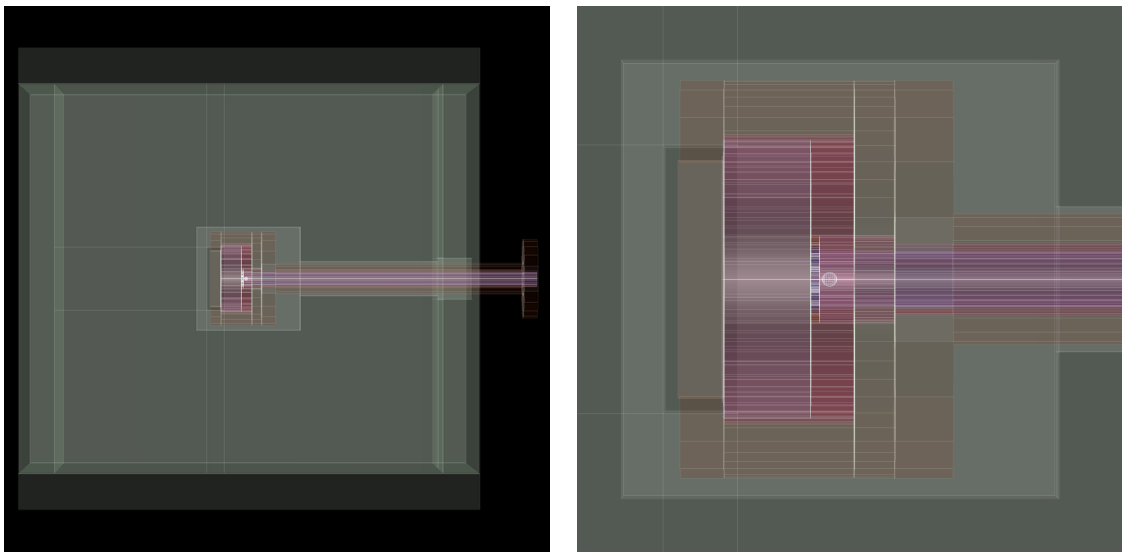

Figure 6.17: IAXO-D0 geometry modified for the simulation of a ^{109}Cd calibration. An aluminium sphere is placed in the pipe, near to the window of the chamber, and the ^{109}Cd isotopes are produced inside.

TRestHitsEvents, that are also analysed to obtain the observables, and finally grouped to form TRestTrackEvents, with their corresponding analysis. Figure 6.19 shows two examples of a one-single track event and a two tracks event produced by a 22 keV x-ray from the ^{109}Cd source.

Finally, an external ROOT script has been used to produce a realistic energy spectrum. A convolution of the simulated energy spectrum from figure 6.18 has been performed taking into account the best energy resolution obtained for the IAXO-D0 detector in this first data taking campaign (more in chapter 8): 18% at the 8 keV peak and 12% at the 22 keV peak. The results are shown in figure 6.20.

Once the energy resolution has been applied, most of the information of the individual sharp peaks is lost, resulting in a spectrum with wider peaks. In the first spectrum at lower energies, the 8 keV peak is clearly differentiated from the 5 keV peak, and some structure can be seen at lower energies. On the other hand, in the second spectrum up to 40 keV, the 8 and 5 keV peaks are merged, resulting in a higher peak with a bump. The structure at low energy is hardly appreciated, and the 19, 22 and 25 keV peaks are merged in one where some structure is visible.

Later in chapters 8 and 9 some experimental ^{109}Cd spectra will be shown and properly explained, but for the sake of completeness, figure 6.21 shows a comparison between the simulated (left) and the experimental (right) ^{109}Cd calibration energy spectra. Some detail has been lost with the convolution that is actually detected in experimental data, like the difference between the double peak at 19 and 22 keV, and also the 25 keV tail. But overall, the REST simulation seem to properly predict the experimental calibration spectrum.

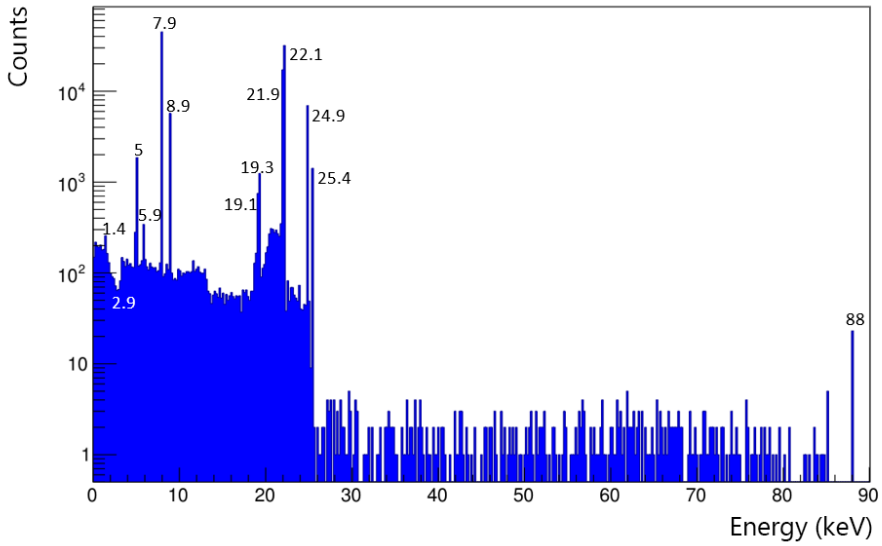

Figure 6.18: Energy spectrum of the C109 calibration simulation. The numbers on the plot indicate the energy (keV) of every peak.

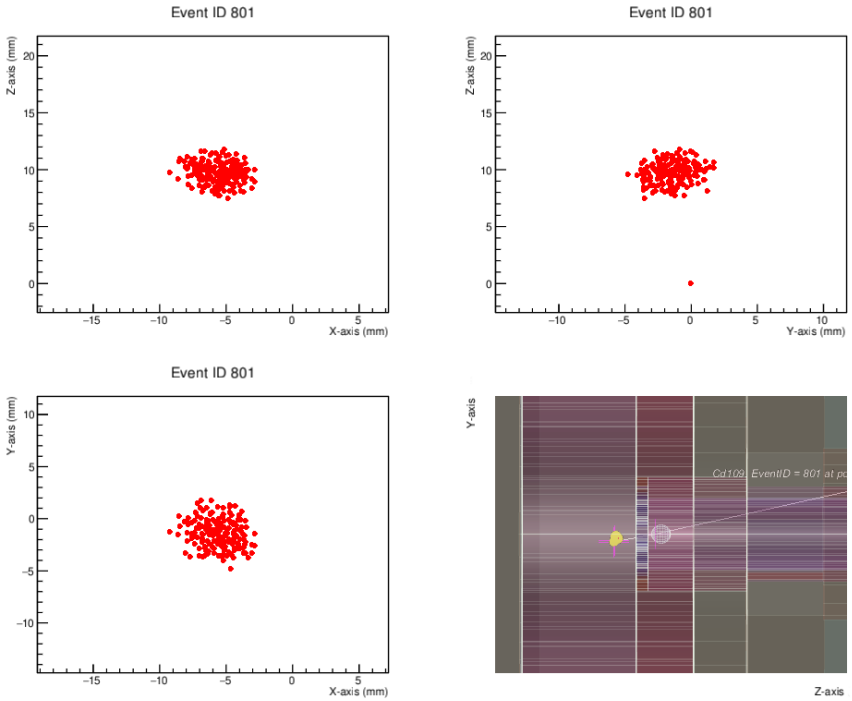

(a) One-track event: 22 keV x-ray

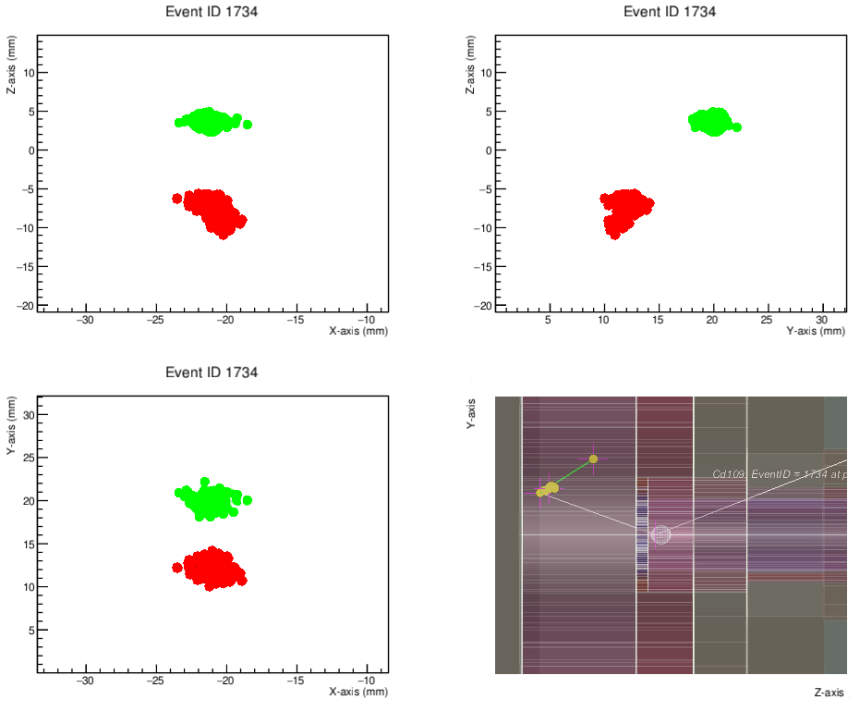

(b) Two-track event: 22 keV x-ray + 2.9 keV x-ray

Figure 6.19: Examples of one-single track and two tracks events from the ^{109}Cd calibration simulation. Xz, yz and xy views of the TRestHitsEvent are shown and also a 3D visualization of the corresponding TRestG4Event.

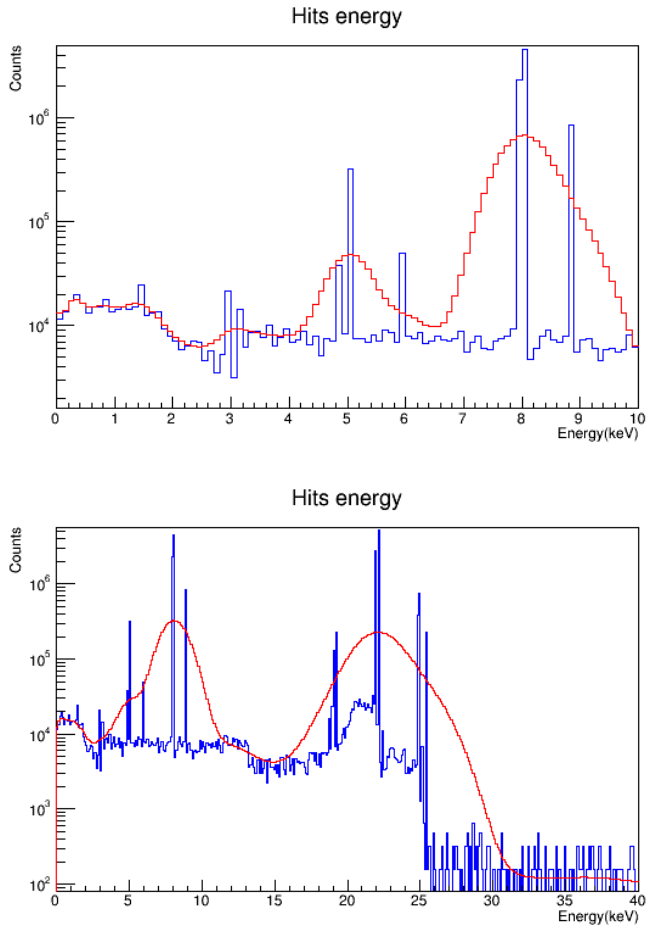

Figure 6.20: Energy spectrum of the 10 minutes equivalent ^{109}Cd calibration simulation: raw (blue line) and including resolution (red line). The energy resolution used was **(Top)** 18% at the 8 keV peak for the [0,10] keV spectrum and **(Bottom)** 12% at the 22 keV peak for the [0,40] keV spectrum.

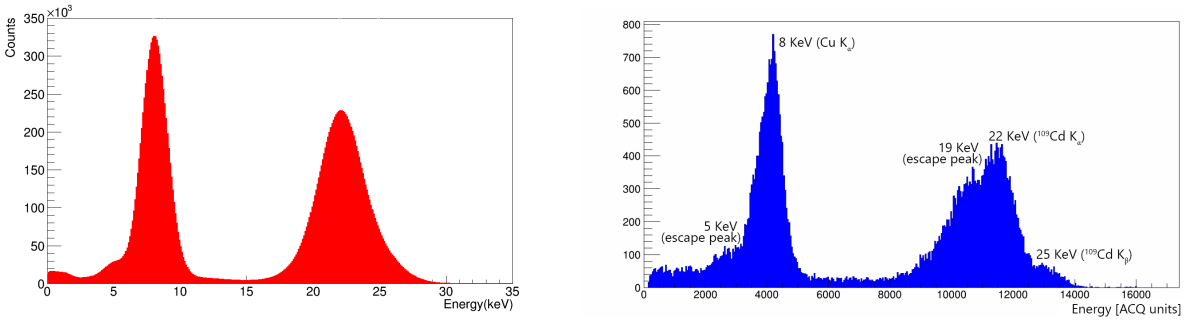

Figure 6.21: **(Left)** Simulated ^{109}Cd calibration spectrum convoluted with a resolution of 12% at 22 keV. **(Right)** Experimental ^{109}Cd calibration spectrum acquired with the IAXO-D0 prototype. Energy is expressed in ADC arbitrary units but the energy of the main peaks is labelled on the plot.

CHAPTER 7

Simulation of IAXO-D0 background model

Contents

7.1 Introduction

One of the key points in rare event searches experiments is a deep understanding of the radioactive background of the detectors. For IAXO, the expected signal is an x-ray excess over the background at energies around 3-4 keV, so an intensive study of the radioactive background of the detector, its shielding and the external sources for energies below 10 keV is important. In this context, the simulation of the IAXO-D0 background model can be very useful to understand the different contributions to the radioactive background in the IAXO Micromegas detectors. Also, having the simulated background model will be helpful in order to understand the experimental data from the IAXO-D0 prototype.

In this chapter, the simulation and analysis general methodology with REST software will be explained, as well as the criteria followed to define the background discrimination parameters. Then, a detailed description of the simulation process of each

known background source will be given, paying special attention to the characteristics of the events produced by each of them. Finally, the discrimination cuts will be described and the background model results will be shown and explained in detail.

7.2 Simulation and analysis methodology

As it was justified in the previous section, REST sofware has been used to simulate the background contributions, analyse them in order to perform the necessary transformations and obtain the corresponding observables, and finally apply the discrimination criteria to obtain the background level. Also, an x-ray calibration has been simulated in order to understand the x-ray events and use this knowledge to define the background discrimination cuts.

7.2.1 General procedure

The first step of the process has been to produce a significant number of simulated events for every known background source of the detector. As described in Chapter 6, the IAXO-D0 geometry has been implemented together with the readout and the gas files. Every background source has been simulated individually using the restG4 package, considering specific initial conditions for each of them in order to be as realistic as possible. A detailed description of this part of the process will be given later on this chapter.

The second step has been to use REST processes to transform the raw TRestG4Events into diffused TRestHitsEvents, and then group them into TRestTrackEvents with observables from the three stages. The processes and work-flow used for the analysis are shown in figure 7.1.

1. **TRestGeant4AnalysisProcess** to obtain information about the energy deposited into each of the detector volumes, the mean position of the energy deposits and the physical properties of the interactions.
2. **TRestG4toHitsProcess** to transform TRestG4Events into TRestHitsEvents.
3. **TRestElectronDiffusionProcess** to simulate the effect of the gas diffusion to every hit. The longitudinal and transversal diffusion coefficients and the drift velocity are read from the gas files for the particular gas conditions of each simulation.
4. **TRestHitsReductionProcess** to reduce the number of hits resulting from the simulations. Using a small step in simulations is an advantage because we can obtain very detailed information about the events at the G4 stage. But since the last goal of this model is to be comparable to the data measurements, some level of hit reduction has to be made. Specifically, we set the minimum distance between

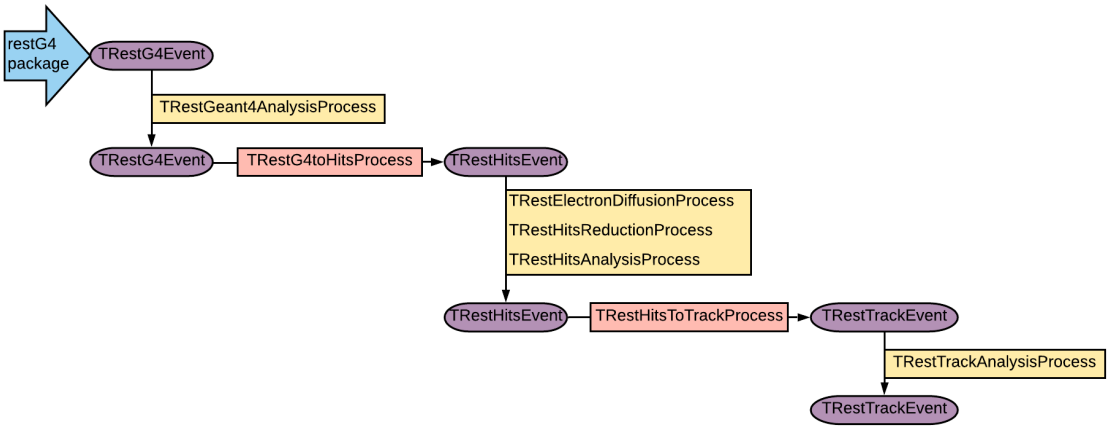

Figure 7.1: Diagram of the REST analysis steps for the simulation data. The purple ovals represent the different event types, the red rectangles are the processes that transform one event type into another, and the yellow rectangles are the processes that performs transformations or calculate the observables for each type of event.

hits to be the pitch of the readout, this is, the minimum distance that we are able to measure with the IAXO-D0 Micromegas detector.

5. **TRestHitsAnalysisProcess** to obtain all the observables related to the energy, position and shape of the hit. The most relevant ones result to be the $\sigma^2_{x,y}$ and σ^2_z, that give information about the size of the event; and the balance between σ_x and σ_y and the skewness, about the symmetry of the event.

   Also, a fiducial volume is defined in this process to be able to apply spatial cuts in the readout plane. Taking into account that the readout is squared, a fiducial volume is defined as a prism with a squared base with the same dimensions as the readout ($60\times60\,\mathrm{mm}^2$) and the same height of the gas volume (30 mm). An observable can be defined related to the distance of the hits to the walls of the fiducial prism. Such observable will allow, for example, selecting only the events that interact at the center of the readout. The *distance to wall*, d_w, is defined as the distance of the closest TRestHit of the TRestHitEvent to the walls of the fiducial prism. This way, we can be sure that the entire event will be contained inside the area of interest when we apply the fiducial cuts.

   The reason behind choosing a fiducial prism rather than a fiducial cylinder was to be consistent with the data analysis: the hits from the simulations are defined by a three-dimensional (x,y,z) position, so in principle, both fiducial volumes could work in order to apply spatial cuts. There are arguments to use a fiducial cylinder like the differential window being circular. But hits from experimental data will be defined by a bi-dimensional (x,z) or (y,z) position coming from the strip triggered by each signal. If we want to apply the same cuts both for data and simulations, we are restricted to a prism.

6. **TRestHitsToTrackProcess** to identify the tracks from each TRestHitsEvent. The definition of a track from previous CAST analysis with similar detectors (previously called cluster) is: a set of consecutive active strips larger than 2 and smaller than 30,

with the possibility of having up to two consecutive non-active strips in between. The pitch of IAXO-D0 readout is 0.5 mm, so, to be consistent with the previous CAST analysis, we set a minimum distance between hits of 2 mm to be considered two different tracks.

7. **TRestTrackAnalysisProcess** to obtain all the observables related with the energy, position and shape of the tracks. The most relevant ones will be the number of tracks and the energy of the most energetic track.

Once all the analysis have been performed, the following step has been to apply the discrimination cuts in order to discard all the non x-ray like events. For that, a simulation of an x-ray calibration has been carried out and its observables have been studied in order to characterize the x-ray events.

After all the discrimination cuts have been applied, the following step has been to calculate the contribution to the total background in the RoI [0-10] keV of each component in the CAST standard background units (counts $\mathrm{keV}^{-1}\,\mathrm{cm}^{-2}\,\mathrm{s}^{-1}$). An external C++/root script has been used in order to obtain the normalized energy spectrum of every contribution. For each of them, a renormalization constant, k, is calculated for the energy RoI, ΔE, taking into account its corresponding flux or activity, A, the number of initial events, n_i, the origin surface or volume where they are generated from, w, and the considered readout surface, s,

$$k = \frac{A\,w}{\Delta E\,n_i}. \tag{7.1}$$

Finally, the energy histogram (b) is rescaled and the numerical contribution (b') with its statistical error is calculated.

$$b' = \int_0^{10} k\,b(E)\,dE \quad \pm k\sqrt{b} \tag{7.2}$$

All the simulations and the analysis of the background components have been computed using the 4 nuclei cluster of the GIFNA group (*sultan*) with a total of 10 processors, and also the supercomputer of the Centro de Supercomputación de Aragón (CESAR), *Cierzo*[1] with 2080 processing cores.

7.2.2 X-rays characterization

In order to properly identify x-rays from background using REST processes, it is important to characterize them via their observables. For this purpose, simulations of x-rays between 1 and 10 keV have been carried out with an increasing difference of 0.1 keV between them.

[1]The author thankfully acknowledges the resources from the supercomputer *Cierzo*, HPC infrastructure of the Centro de Supercomputación de Aragón (CESAR), technical expertise and assistance provided by BIFI (Universidad de Zaragoza) http://cesar.unizar.es.

Each simulation consisted in 10^5 initial x-rays launched from the inner section of the tube at its external end. The expected solar axion spectrum peaks at 3 keV, and extends from 1 keV up to 6-7 keV.

Some examples of events produced by 3 keV x-rays are shown in figure 7.2. This type of plots will be used to describe the spatial distribution of the charge of the events. The dots represent each TRestHit of the TRestHitsEvent and its size is related with the energy of the TRestHit. The same coloured TRestHit are part of the same TRestTrack, so multiple colours represent a multiple track event. Finally, there is also a three dimensional representation of the TRestG4Event for illustrative purposes. In these figures, the initial event is represented by a white line, the electrons produced in the interactions by a pink cross and the energy deposits in the different volumes by a yellow circle. In other examples where gammas are also produced in the interactions, they are represented by green lines.

The topological analysis shows that most of the events produced by x-rays have one or two tracks. The size of the event depends on the Z position where the x-ray interacts with the gas: the closer the distance to the cathode, the higher the diffusion and, therefore, the wider the event in Z or in XY.

The observables used to describe the x-rays are related to the number of tracks and the shape of the events: size ($\sigma^2_{x,y}$ and σ^2_z) and symmetry (the balance between σ_x and σ_y and the skewness). In figure 7.3 these observables are shown for some of the x-ray simulations. For clearness purposes, only nine of them are plotted, from 1 to 9 keV with a difference of 1 keV between them. From these observables we reach the following conclusions:

- The 1 keV events penetrate only ∼5 mm, so they will be highly affected by the diffusion of the gas and therefore, they are the biggest ones, with higher values of $\sigma^2_{x,y}$ and σ^2_z. The rest of the x-rays penetrate deeper in the chamber before they interact, so the events are smaller, up to $\sigma^2_{x,y} \sim 2.5$ mm and $\sigma^2_z \sim 0.5$ mm.

- In terms of symmetry of the events, the balance between σ_x and σ_y for all of the x-rays present a Gaussian-like behaviour around 0, what means that their shape in X and Y direction are comparable in scale, which is produced by the round-like shape of the events. This is also shown by the skewness, that present a Gaussian-like behaviour around 0, which means that there is not a preferred direction for the energy deposit. Finally, the *distance to wall* observable indicates that almost all the events on the readout are distributed in a centred square of ∼13 mm×13 mm.

- In terms of the number of tracks, almost all the events have only 1 track, but there are some of them that have 2 tracks. Typically in the CAST analysis, the x-rays were defined as single track events or alternatively, as events where the dominant track carries at least the 85% of the total energy.

  To prove this definition, the observable that indicates the energy of the most energetic track of the event (E^{max}) was used to study the x-ray simulations. In figure 7.4 (left) it is shown the relation between the total energy of the events and

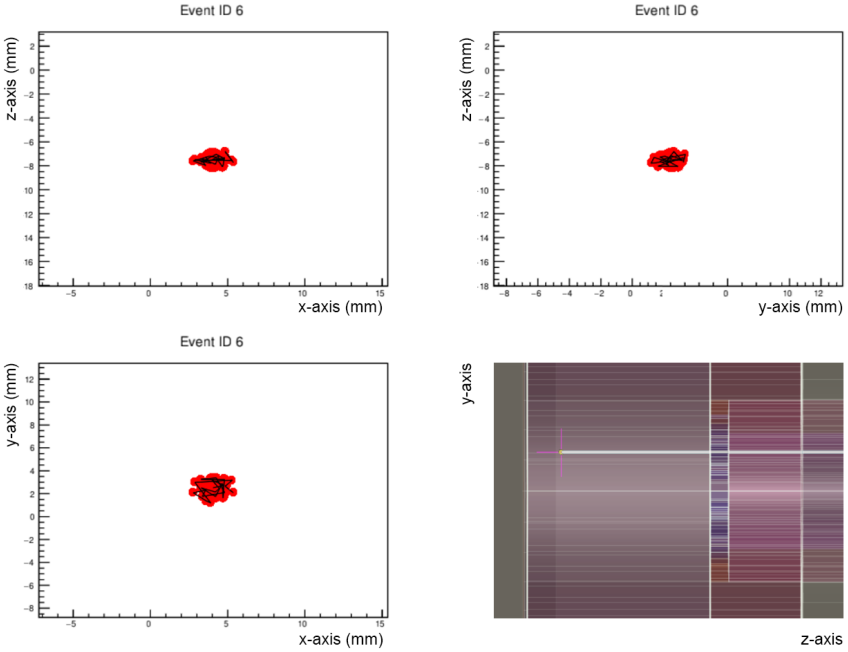

(a) One-track of 3 keV.

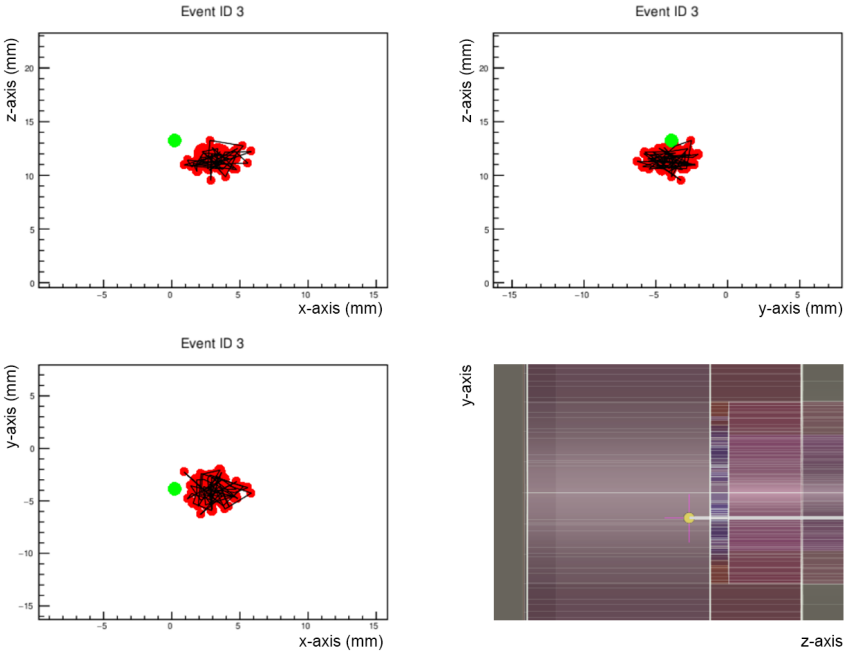

(b) Two tracks of 2.973 keV and 0.027 keV.

Figure 7.2: Examples of one and two tracks events from the 3 keV x-ray simulation launched from the beginning of the pipe. XZ, YZ and XY views of the TRestHitEvents are shown and also a 3D visualization of the corresponding TRestG4Event.

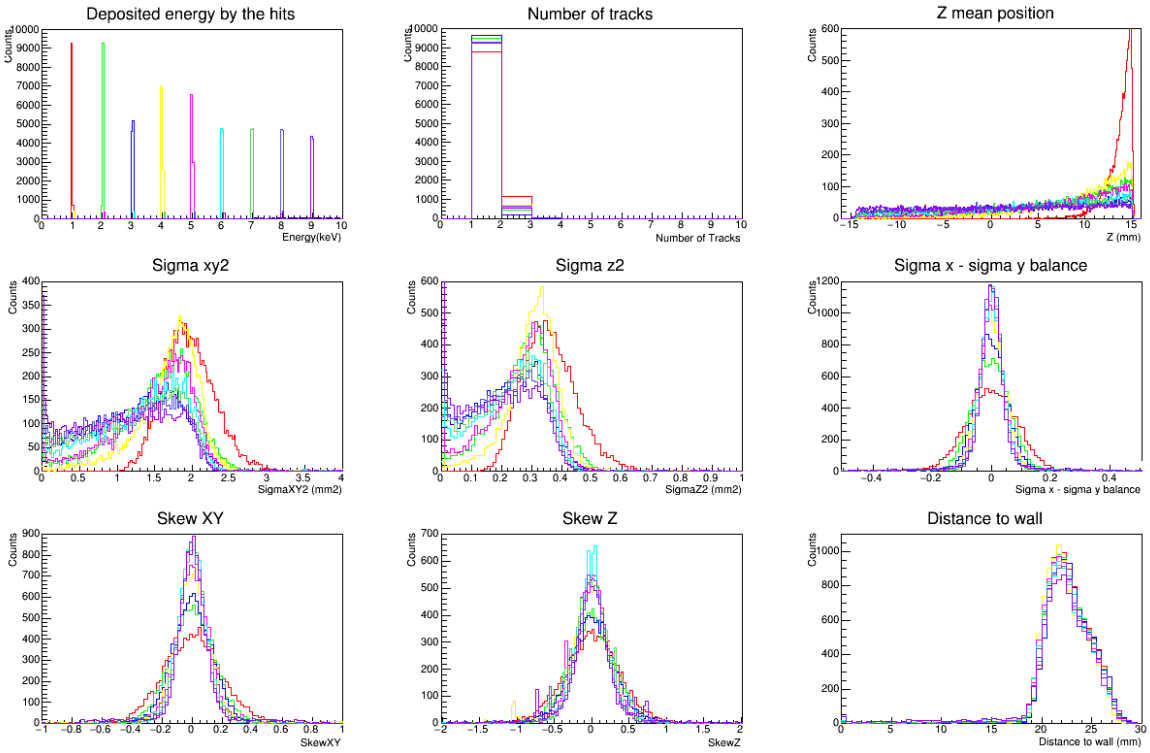

Figure 7.3: Characterization observables for 10^4 initial x-rays simulations of 1-9keV. From the top left corner: energy deposited by the events in keV units; number of tracks; mean Z position in mm; XY extension of the event ($\sigma^2_{x,y}$) in mm^2; extension of the event in Z (σ^2_z) in mm^2; balance between σ_x and σ_y; XY skewness ($\gamma_{x,y}$); skewness in Z direction (γ_z).

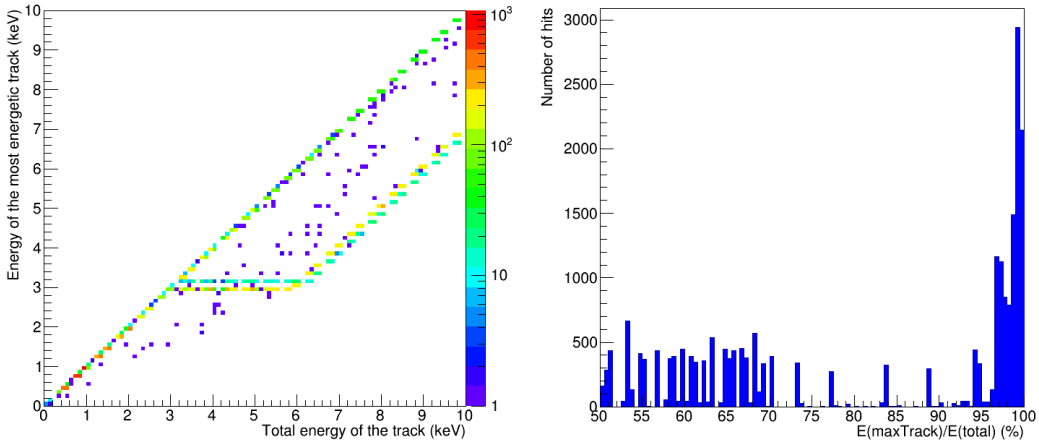

Figure 7.4: **(Left)** Relation between the total energy of the two tracks events and the energy of the most energetic track of these events for the x-ray simulations between 0-10 keV. **(Right)** Percentual ratio between the energy of the most energetic track, $E_{maxTrack}$, and the total energy of the two track event E_{total}.

the energy of the most energetic track for the events with two tracks. Up to 3 keV, the maximum track contains almost all the energy of the entire event. From 3 to 6 keV we can see that this tendency continues, although some of the events have a most energetic track of 3 keV, corresponding with the fluorescence of the argon. From 6 keV onwards, there are two track events with its most energetic track of E_γ-3 keV. Also, figure 7.4 (right) shows the percentage ratio between the energy of the most energetic track and the total energy of the event. Quantitatively, considering all the 0.5-9.8 keV range, almost 50% of the events have a $E_{maxTrack}/E_{total}$ ratio below 85%. But if we consider only an energy range closer to the axion spectrum, like 1.5-6.0 keV, the events with $E_{maxTrack}/E_{total}$ ratio below 85% is reduced to 39%.

With these results, restricting the definition of the x-rays of interest to events where the dominant track carries at least the 85% of the total charge may be too optimistic. On the other hand, the events with 2 tracks represent barely a 6% of the total, so they may not be representative enough to even consider them in the background model.

This x-ray characterization has been used to define the discrimination cuts that have been applied for each background contribution in order to estimate the final background level of IAXO-D0. A detailed description of the cuts and their efficiency will be given later in this chapter (section 7.4.1).

7.3 Background components simulations

In this section, all the contributions simulated for the background model are described. This work was divided in two parts: external background contribution from cosmic and environmental sources and intrinsic background contribution from the radioactivity of the detector components. In table 7.1 a list of all the simulations performed for the external sources is shown. The simulations of the intrinsic radioactivity of the detector were performed by Cristina Margalejo Blasco as a part of her master thesis [227] (table 7.2), and have been revised on this work.

7.3.1 Cosmic Muons

Cosmic muons are a very significant source of background for rare-event search experiments operating at surface. Previous surface and underground background tests with CAST detectors yielded to a final muon contribution of around 10^{-6} counts keV^{-1} cm^{-2} s^{-1} in the 2–7 keV range [14]. Furthermore, a proper coverage with vetoes has been proven both by simulations and experimental setups to lower this contribution in a factor of $\sim$2. Since the objective for the IAXO-D0 detector is to reach the 10^{-7} counts keV^{-1} cm^{-2} s^{-1} level required for IAXO, a very careful study of the cosmic muons contribution has to be made. For this purpose, a 100 hours equivalent set of

Contribution	Number of simulations	Total initial events	Flux/rate	Real time (h)
Cosmic μ	200	7.2×10^8	$125\,m^{-2}\,s^{-1}$ [228]	100
Cosmic γ [1-10] MeV	16	2.304×10^9	$4.18\times10^{-2}\,cm^{-2}\,s^{-1}$ [228]	95.6
Cosmic γ [10-100] MeV	16	1.152×10^9	$2.09\times10^{-2}\,cm^{-2}\,s^{-1}$ [228]	95.6
Cosmic γ [0.1,100] GeV	72	1.6×10^4	$2.70\times10^{-3}\,cm^{-2}\,s^{-1}$ [228]	11.85
Cosmic n [10-1000] MeV	16	2.7648×10^8	$50\,m^{-2}\,s^{-1}$ [199]	96
Cosmic n [1,10] GeV	4	1.3824×10^5	$0.1\,m^{-2}\,s^{-1}$ [199]	96
Environmental γ (^{238}U and ^{232}Th)	10	10^{10}	$0.5\,cm^{-2}\,s^{-1}$ [21]	176.8
Radiogenic neutrons	2	1.1^6	$4.32\times10^{-10}\,kg^{-1}\,s^{-1}$ [154]	3.8×10^8
^{39}Ar from gas	2	2×10^5	1.01 Bq kg^{-1} [210]	1.51×10^5

Table 7.1: Simulations computed for the external background contributions. Further information about the flux and rates considered can be found in the text.

Detector component	^{60}Co	^{40}K	^{232}Th	^{238}U	^{39}Ar	^{210}Pb
Copper cathode	2.0×10^6	3.0×10^6	1.0×10^6	6.0×10^5	-	-
Copper strongback pattern	1.0×10^6	4.0×10^5	2.0×10^5	1.0×10^5	-	-
Copper chamber	5.0×10^6	4.0×10^7	2.5×10^6	3.5×10^6	-	-
Copper chamber top flange	1.0×10^7	1.1×10^8	1.0×10^7	1.1×10^7	-	-
Copper pipe	5.0×10^7	7.8×10^8	5.5×10^7	6.5×10^7	-	-
Copper raquette	5.0×10^6	1.2×10^7	2.6×10^6	4.0×10^6	-	-
Micromegas readout	1.0×10^6	1.2×10^7	6.0×10^5	5.0×10^5	-	-
Gas	-	-	-	-	1.0×10^4	-
Kapton from the readout	-	1.2×10^5	4.0×10^4	2.5×10^4	-	-
Lead shielding	-	9.8×10^9	1.3×10^9	2.4×10^9	-	5.1×10^9*
PTFE chamber inner cover	-	1.0×10^6	1.1×10^5	1.0×10^6	-	-
PTFE pipe inner cover	-	1.0×10^8	2.5×10^7	1.8×10^7	-	-
PTFE cathode inner cover	-	3.5×10^6	1.0×10^8	6.0×10^5	-	-
Mylar window	1.0×10^4	2.0×10^4	2.0×10^4	1.0×10^4	-	-

Table 7.2: Simulations computed for the intrinsic background contribution of the detector, by Cristina Margalejo Blasco [227]. Here are shown the total initial events of each radioactive contamination of every geometry part of IAXO-D0. $*$ Assuming self-shielding of the lead for the 46.5 keV photons, the ^{210}Pb isotope has been simulated only from the inner half of the shielding due to computational restrictions.

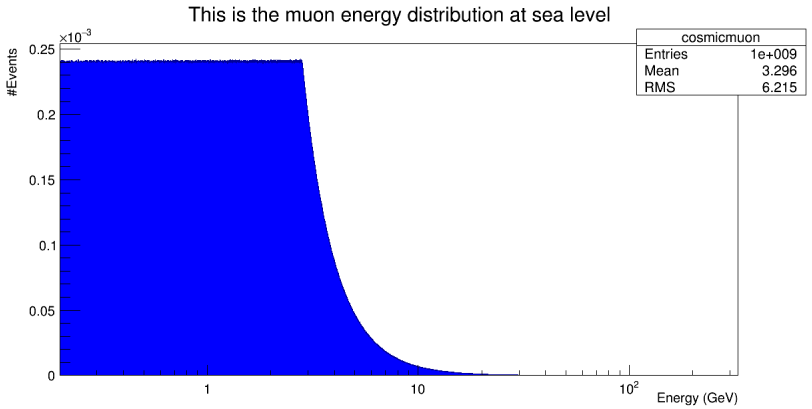

Figure 7.5: Energy distribution of muons at sea level, from 0.2 to 328 GeV [228]

simulations have been performed. The initial events have been launched from a $4\times4\,m^2$ squared virtual wall situated 1 cm over the detector. This size has been chosen in order to maximize the solid angle and the simulations efficiency at the same time.

The energy distribution that has been used for the initial events is shown in Figure 7.5, which corresponds to the sea level muon distribution [228]. The considered flux is $125\mu\,m^{-2}\,s^{-1}$ and the angular distribution as a function of the zenith angle, θ, is $\sim cos^2\theta$ [229]. A total of 200 simulations with 3.6×10^6 initial muons each have been computed, which correspond to a real simulated exposure time of 100 hours.

A simulated muon TRestG4Event is shown in Figure 7.6. The initial muon (white line) goes through the veto where it leaves part of its energy (yellow circles). Then it crosses the entire shielding, depositing energy on its way and creating electrons (pink crosses) that ionize the medium and produce gamma emission (green lines). We can also see how the muon interacts with the copper when it reaches the exterior of the chamber. Finally, it pass trough the gas volume, where the step between energy deposits is smaller to obtain a more detailed topological information of the events. This event will be saved in the TRestG4Event output of the simulation.

Figure 7.7 shows examples of the most common scenario of an event produced by a muon. We will have a linear energy deposit following the path of the muon as it crosses the gas volume, as shown in figure 7.7 (top). This distinctive shape is easy to reject with the observables of the event. But sometimes, the muon can mimic a x-ray like event shape if it hits the gas volume perpendicularly to the readout plane. An example o this is shown in figure 7.7 (bottom), where a small and symmetrical energy deposit of ~1.6 keV is produced my a muon.

The observables of interest that describe the events produced by muons are shown in figure 7.8. The energy spectrum is more populated at low energies, agreeing with the energy loss expected for muons going through the IAXO-D0 argon gas volume, and most of the events have one or two tracks. Their 2D print on the readout can be very large, but most of them are smaller than $10\,mm^2$ and $1\,mm^2$ in the z direction. A very significant observable is the balance between σ_x and σ_y, defined as $\frac{\sigma_x-\sigma_y}{\sigma_x+\sigma_y}$, where we can

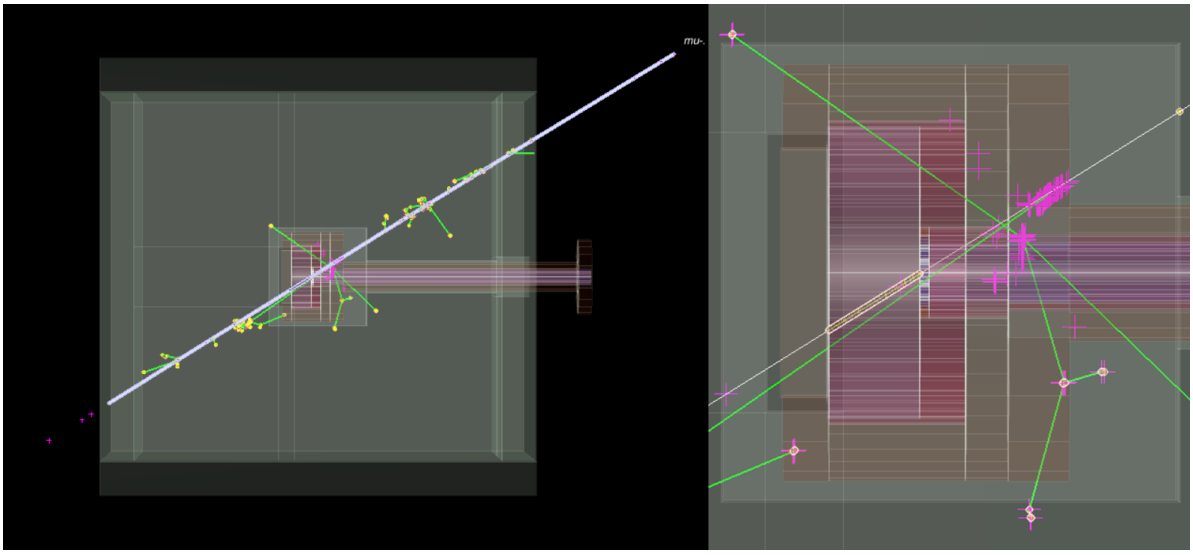

Figure 7.6: An example of a TRestG4Event produced by a muon that deposits energy at the target gas. The white line is the muon path as it goes through the shielding. The pink crosses are the electrons produced by the ionization of the muon and the yellow circles are the energy deposits in the different materials. The green lines represent the gammas produced in the interactions.

observe a tendency to negative values. This means that most of the events are larger in the y direction. Taking into account the geometry and the position of the readout plane, we obtain that the majority of the events are produced by horizontal muons, which is an expectable result. Another significant observable is the distance to the walls of the fiducial volume. We observe that almost all the events produced by muons leave energy deposits very close to the external sides of the readout. Finally, the skewness present a sharp peak-like distribution around zero, which might seem contradictory because muons does not leave symmetrical energy deposits. This is due to the fact that the skewness is a statistical parameter that indicates how a distribution deviates from its mean value. So, since the GEANT4 simulations have been performed with very small steps, the energy left by the muon through the gas at each step is approximately the same, and both the skewness and the standard deviation are energy-weighted observables, the value of the skewness in the end will be ~ 0.

The background contribution of the cosmic muons simulations before the discrimination analysis is applied is shown in figure 7.9, where the background with units of counts $\mathrm{keV}^{-1}\,\mathrm{cm}^{-2}\,\mathrm{s}^{-1}$ is plotted for the energy in the IAXO RoI. The background produced by cosmic muons in IAXO-D0 previously to the analysis discrimination process will therefore be $(7.23 \pm 0.02) \times 10^{-4}$ counts $\mathrm{keV}^{-1}\,\mathrm{cm}^{-2}\,\mathrm{s}^{-1}$ considering all the readout surface. Previous Montecarlo simulations estimated the raw contribution of cosmic muons to the background level of CAST Micromegas detectors between $10^{-3} - 10^{-4}$ counts $\mathrm{keV}^{-1}\,\mathrm{cm}^{-2}\,\mathrm{s}^{-1}$ [14], which is compatible with the new results obtained for IAXO-D0.

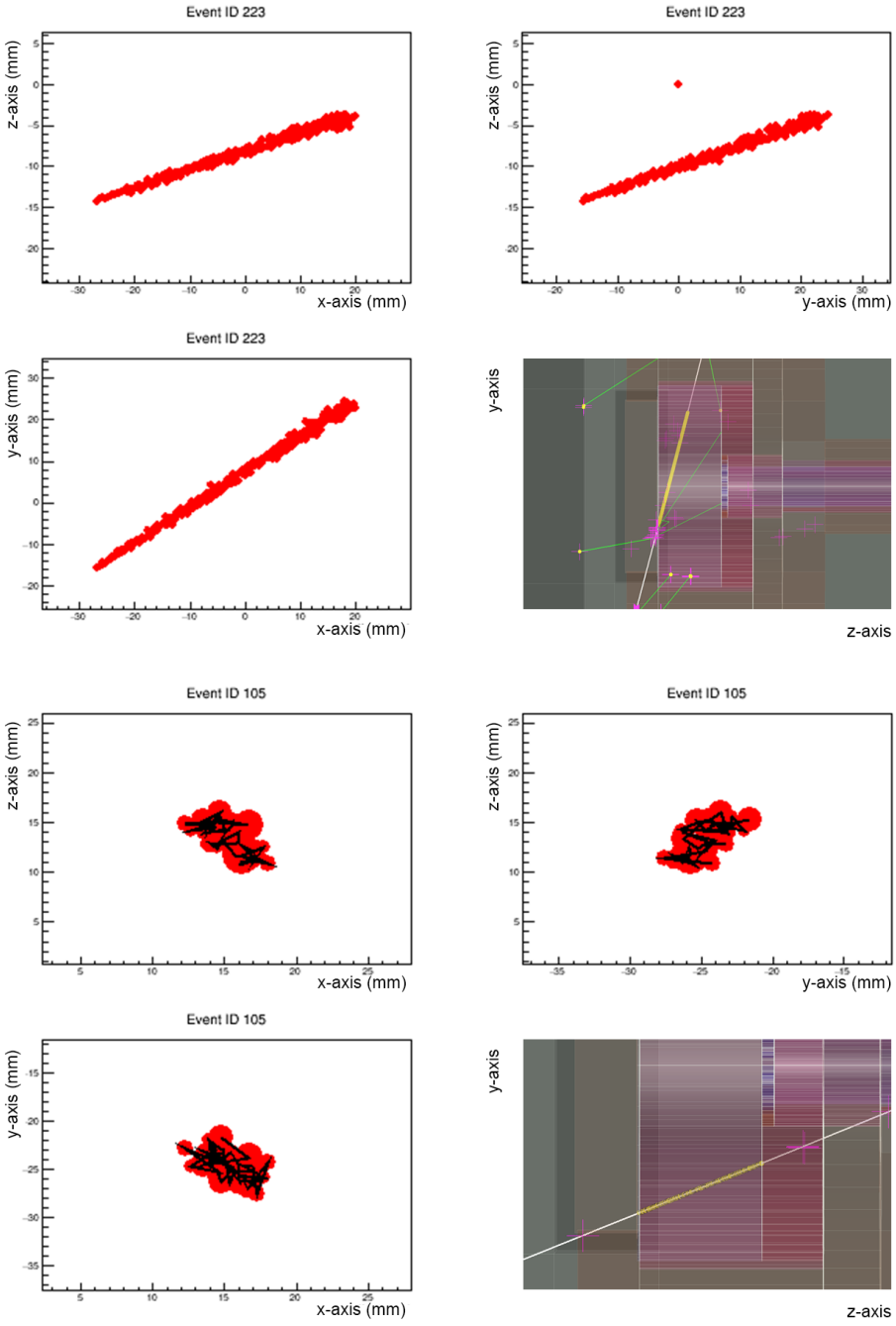

Figure 7.7: Examples of one single track events produced by a muon in the target gas: **(Top)** 21.5 keV event induced by a muon that crosses the gas chamber diagonally. **(Bottom)** 1.6 keV event induced by a muon that crosses the gas chamber perpendicularly to the readout plane.

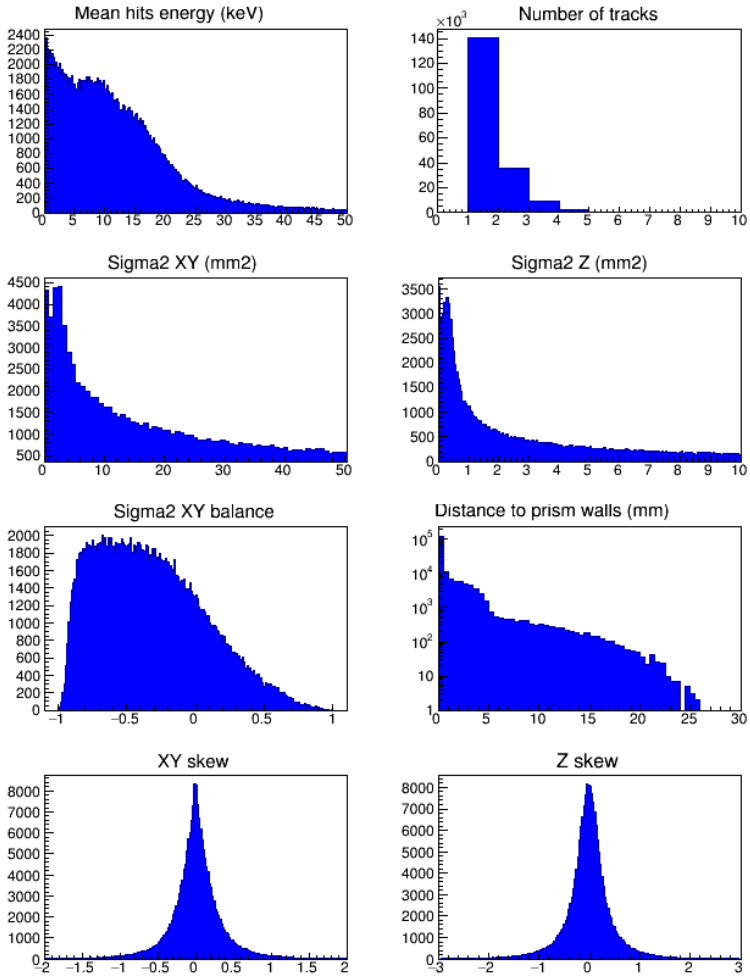

Figure 7.8: Cosmic muons characterization observables. Y axis represents the number of events for all the plots, and each x axis is labelled at the top for clearness, referencing the units if the observable is not dimensionless. The observables shown are the energy, the number of tracks, $\sigma^2_{x,y}$ and σ^2_z, the balance between σ_x and σ_y, the distance to the fiducial volume, γ_{xy} and γ_z, and they are defined in the section 6.2.

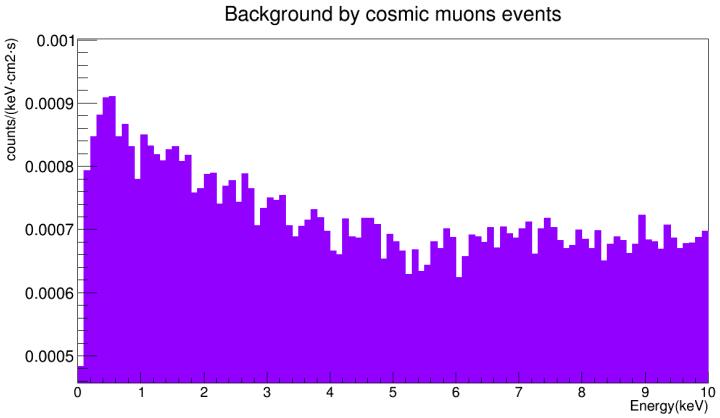

Figure 7.9: Total contribution to the background in the [0,10] keV RoI produced by cosmic muons before the discrimination process.

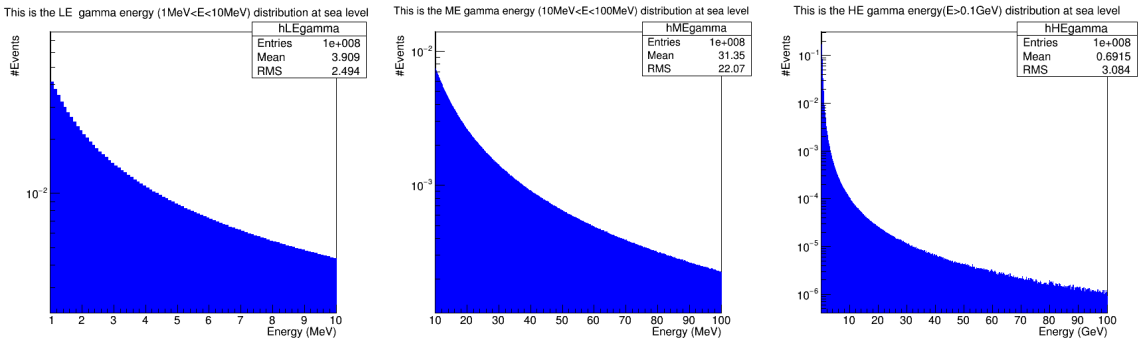

Figure 7.10: Energy distribution of gammas of low, medium and high energy at sea level, from 0.2 to 328 GeV [228].

7.3.2 Cosmic gammas

Gamma rays are a product of a variety of processes and secondary particles that are produced by the cosmic radiation in interaction processes with atmospheric nuclei. This can be a source of background for a surface experiment. Lower energy gammas will most likely deposit all their energy in the external shielding before reaching the detector inside, but high energy gammas could actually have an impact on the background.

Several simulations have been made for cosmic gamma rays following the same procedure used for cosmic muons. The initial events have also been launched from a squared virtual wall situated 1 cm over the shielding. For the less energetic gammas, the virtual wall has been $4{\times}4\,\mathrm{m}^2$, but in the case of the most energetic ones, the sides of the plane have been 1 m long. This size has been chosen smaller for these simulations because the high energy gammas are very ionizing and they produce big showers of electrons and other gammas inside the shielding, and therefore they slow the computation of the simulations. A balance between computational time and solid angle was necessary in order to perform these high energetic cosmic gamma simulations.

In Figure 7.10 the three energy distributions for low, medium an high energy gamma rays at sea level [228] are shown. Both electrons and positrons should follow similar distributions. And the angular distribution for cosmics as a function of the zenith angle θ is again $\sim cos^2\theta$ [229]. Each of the gamma fluxes has been normalized by the solid angle estimated for both virtual wall generators.

- Low energy gammas distribution, from 1 to 10 MeV and a flux of $8 \times 10^{-3}\,\mathrm{cm}^{-2}\,\mathrm{s}^{-1}\,\mathrm{sr}^{-1}$.
- Medium energy gammas distribution, from 10 to 100 MeV and a flux of $4 \times 10^{-3}\,\mathrm{cm}^{-2}\,\mathrm{s}^{-1}\,\mathrm{sr}^{-1}$.
- High energy gammas distribution, from 0.1 to 100 GeV and a flux of $1 \times 10^{-3}\,\mathrm{cm}^{-2}\,\mathrm{s}^{-1}\,\mathrm{sr}^{-1}$.

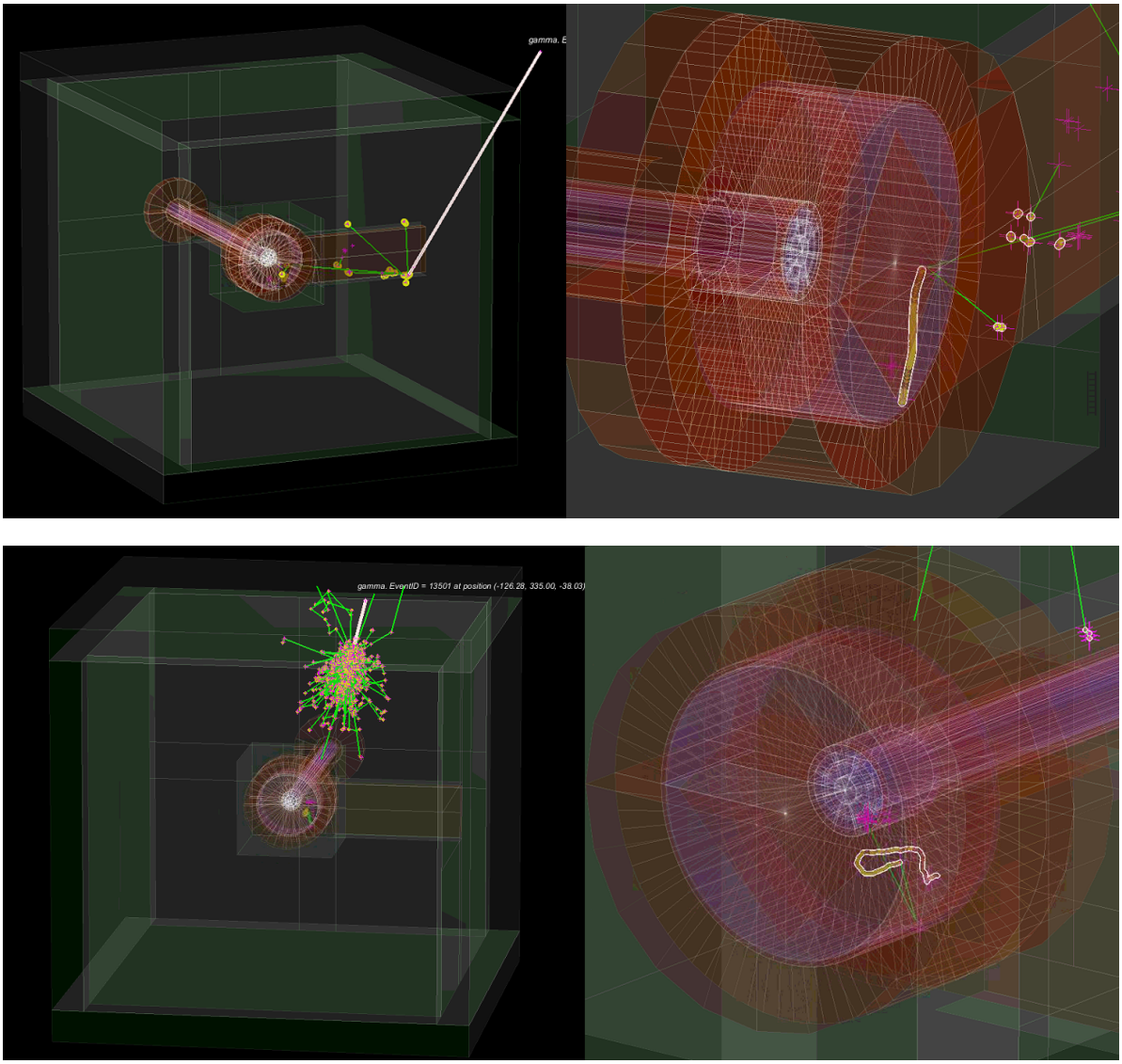

Figure 7.11: Examples of TRestG4Events produced by cosmic gammas that deposit energy at the target gas. The white line is the initial gamma path. The pink crosses are the electrons produced from ionization process and the yellow circles are the energy deposits in the different materials. The green lines represent the gammas produced in the interactions. **(Top)** TRestG4Event from a 57 MeV cosmic gamma that left a one-single track event in the gas with a detected energy of 4.3 keV. **(Bottom)** TRestG4Event from a 3.6 GeV cosmic gamma that left a one-single track event in the gas with a detected energy of 13.7 keV.

Two simulated G4 events produced by cosmic gammas are shown in figure 7.11. The top example corresponds to a 57 MeV cosmic gamma (medium energy) that left a one-single track event in the gas with a detected energy of 4.3 keV. The white line is the initial gamma, that interacts in the inner hole of the lead shielding for the copper raquette. An electron is produced that, though ionization and bremsstrahlung, produces secondary gammas that further ionize the atoms of the lead shielding and copper detector parts. One of these secondary gammas reaches the active gas and produces the primary electron that is finally detected. On the other hand, the bottom example corresponds to a 3.6 GeV cosmic gamma that left a one-single track event in the gas with a detected energy of 13.7 keV. In this example it is shown the big ionization shower that the high energetic gamma produces as it interacts with the lead atoms. As it happened with the other example, one of these secondary gammas will finally reach the gas and produce a detectable electron.

The total equivalent time simulated for cosmic gammas has been 95.6 hours for both low and medium energetic gammas, and only 11.85 hours for high energetic ones due to the very long computational time that took these last simulations. The raw contribution to the IAXO-D0 background from events produced by cosmic gammas is $(5.9 \pm 1.7) \times 10^{-7}$ counts keV^{-1} cm^{-2} s^{-1}, and the major part comes from the high energetic gammas, which they alone contribute with $(4.3 \pm 1.7) \times 10^{-7}$ counts keV^{-1} cm^{-2} s^{-1}. The errors are big due to the small statistics, but further work is planned in restG4 package in order to reduce computational time.

7.3.3 Environmental gammas

Gamma radiation can be produced by the intrinsic radioactivity of the materials of the walls of the room. This radiation can interact with the different parts of the detector or the shielding and produce a secondary charged particle that eventually can reach the active gas volume. The external pasive shielding should in principle absorb all the energy from this radiation, as previous studies with the CAST detectors have shown [14, 21]. This study is aiming to prove this affirmation to be right also for IAXO-D0.

In order to simulate the environmental gamma contribution, the initial events have been launched from the inside of a virtual sphere that contained the entire detector and shielding. The energy distributions used for these simulations are shown in Figure 7.12. They have been obtained by a full chain decay simulation of ^{232}Th and ^{238}U launched uniformly inside a concrete wall. Then the gammas coming out the wall have been counted and its energy filled inside the corresponding histograms. The angular distribution used has been the resulting one from the gamma flux simulated, being $\theta = 0$ the direction normal to the surface.

The environmental gamma flux considered is 0.5 cm^{-2} s^{-1}, which was obtained from CAST in situ measurements, evaluating the main natural radioactive chains intensity in secular equilibrium [21]. A total of 10^{10} initial events have been launched for each isotope, what makes an equivalent time of 176,8 hours of gamma background. As expected, almost

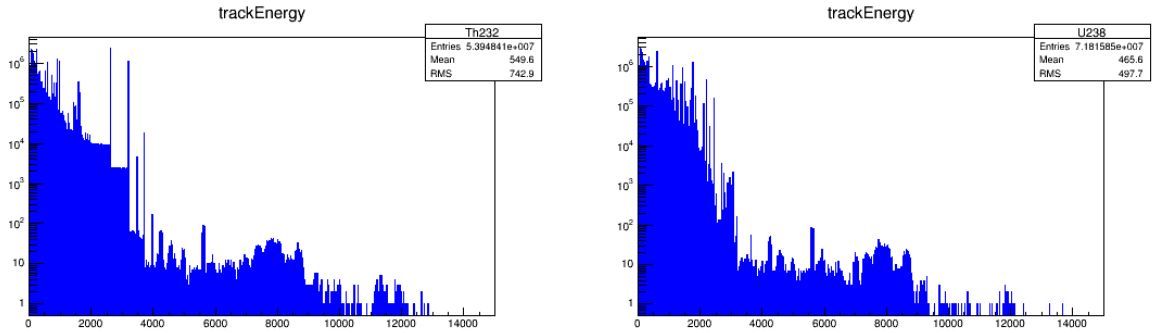

Figure 7.12: Energy distribution of the gammas resulting from the simulation of the ^{232}Th **(Left)** and ^{238}U **(Right)** full chain decays inside a concrete wall. The total number of counts inside the energy distributions corresponds to a simulation of 20×10^6 events in a concrete mass of 17664 tonnes.

all the initial gammas have been absorbed by the shielding and have not reached the active gas volume. Two examples of events produced by environmental gammas are shown in figure 7.13. Despite the few statistics, all the events collected show long and non-symmetrical charge deposits that are very easily distinguishable from the x-ray events.

The resulting background contribution from the combination of all the simulated environmental gammas before applying the discrimination processes is $(2.46 \pm 0.73) \times 10^{-7}$ counts keV^{-1} cm^{-2} s^{-1}. Only 5 events from all the initially simulated reached the active gas, so the result is expressed for a confidence level of 95% [4]. This background level is one order of magnitude lower than the external gamma contribution quantified for CAST-Micromegas detectors [21, 43], which was $\sim 1.5 \times 10^{-6}$ counts keV^{-1} cm^{-2} s^{-1} int he 2-7 keV range. This result corroborates that a thicker passive shielding is effective in order to reduce the external gamma contribution to the background.

7.3.4 Cosmic neutrons

Cosmic neutrons are secondary particles resulting from interactions of cosmic rays with nuclei of air constituents. They contribute also to the background because they penetrate deeper in the materials than the charged particles and IAXO do not have any shielding specifically focused to stop neutrons. Interacting with the nuclei of the shielding and detector chamber materials by neutron scattering or capture, a gamma or other charged particle can be produced and start an ionization process in the gas. Neutrons can also interact with the atoms in the gas itself producing a nuclear recoil that would induce a detectable signal.

For the simulations, the same configuration as for the muons has been used: a virtual 4×4 m^2 squared wall placed 1 cm over the shielding. Two normalized energy distributions have been used [199] for low and high energy cosmic neutrons. They are shown in figure 7.14 and they follow the Ziegler formula [199].

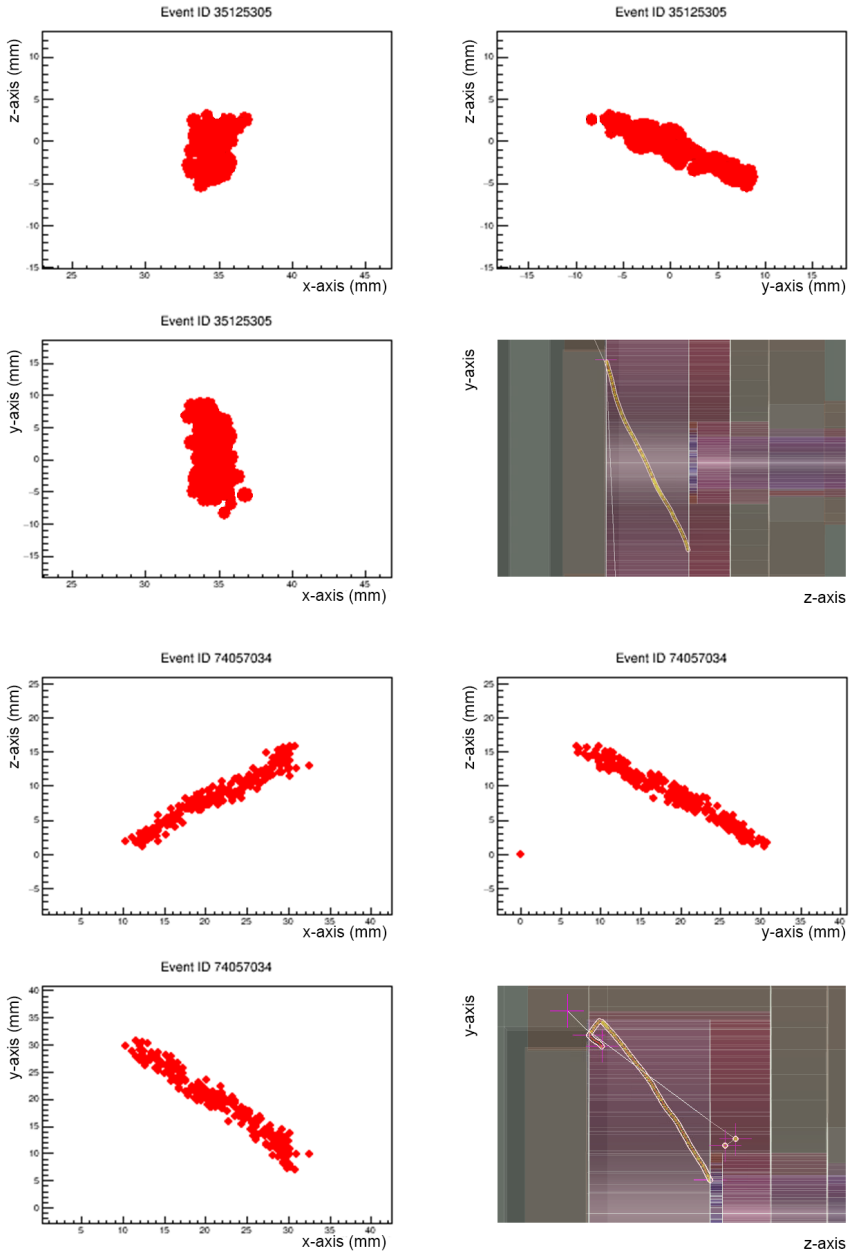

Figure 7.13: Examples of one single track events produced by an environmental gamma in the target gas: **(Top)** 3.09 keV event produced by a resulting electron from the interaction of an external gamma (^{232}Th) with the lead shielding. **(Bottom)** 7.47 keV event induced by a resulting electron from the interaction of an external gamma (^{238}U) with the copper cathode.

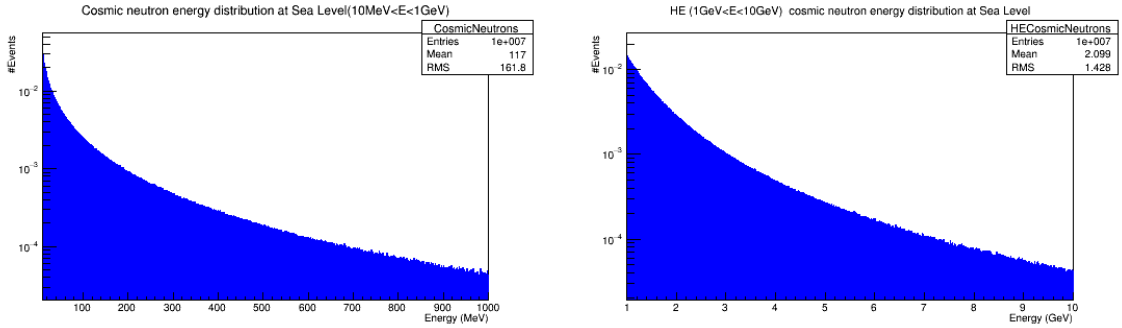

Figure 7.14: Energy distribution of atmospheric neutrons at sea level for two energy ranges: [10, 1000] MeV **(Right)** and [1, 10] GeV **(Left)** [199].

- Low energy neutrons distribution from 10 to 1000 MeV, and a flux of $50\,\mathrm{m}^{-2}\,\mathrm{s}^{-1}$.
- High energy neutrons distribution from 1 to 10 GeV, and a flux of $0.1\,\mathrm{m}^{-2}\,\mathrm{s}^{-1}$.

In this case, the angular distribution as a function of the zenith angle θ has been considered to be $\sim cos^2\theta$, the same one that has been used for cosmic muons and gammas [199, 228].

A total of 2.7648×10^8 initial low energy neutrons and 1.3824×10^5 initial high energy neutrons have been simulated, what corresponds to a equivalent time of 96h. Figure 7.15 shows two examples of the most common scenarios produced by cosmic neutrons interactions. In the top one, a neutron suffers a scattering inside the gas and leaves energy in the process, producing a nuclear recoil. In the bottom one, a neutron capture produces a gamma that reaches the gas and produces some ionization.

The events produced by cosmic neutrons are at the low part of the energy spectrum, as it is shown in the characterization observables of figure 7.16. Most of the events have less than $\sim$20 keV, one-single track and have small values of $\sigma^2_{x,y}$ and σ^2_z, which would be compatible with x-ray events. The most significant observable to discriminate these background events is again the distance to the fiducial prism wall, which indicates that most of the events are due to interactions in the walls of the chamber and therefore, they occur near to the border of the readout.

In order to estimate the background contribution from cosmic neutrons, the quenching factor for the nuclear recoils need to be considered. The energy of an incident neutron that interacts with matter via elastic scattering is shared between atomic motion and electronic excitation. Only the latest part can be used as ionization signal. The nuclear quenching factor is the ratio between the energy given to the electronic excitation and the total energy.

As the quenching factor for gaseous argon has not been measured, a conservative parametrization was calculated [35, 230] as

$$Q(E_R) = \frac{g(E_R)}{1 + g(ER)} \tag{7.3}$$

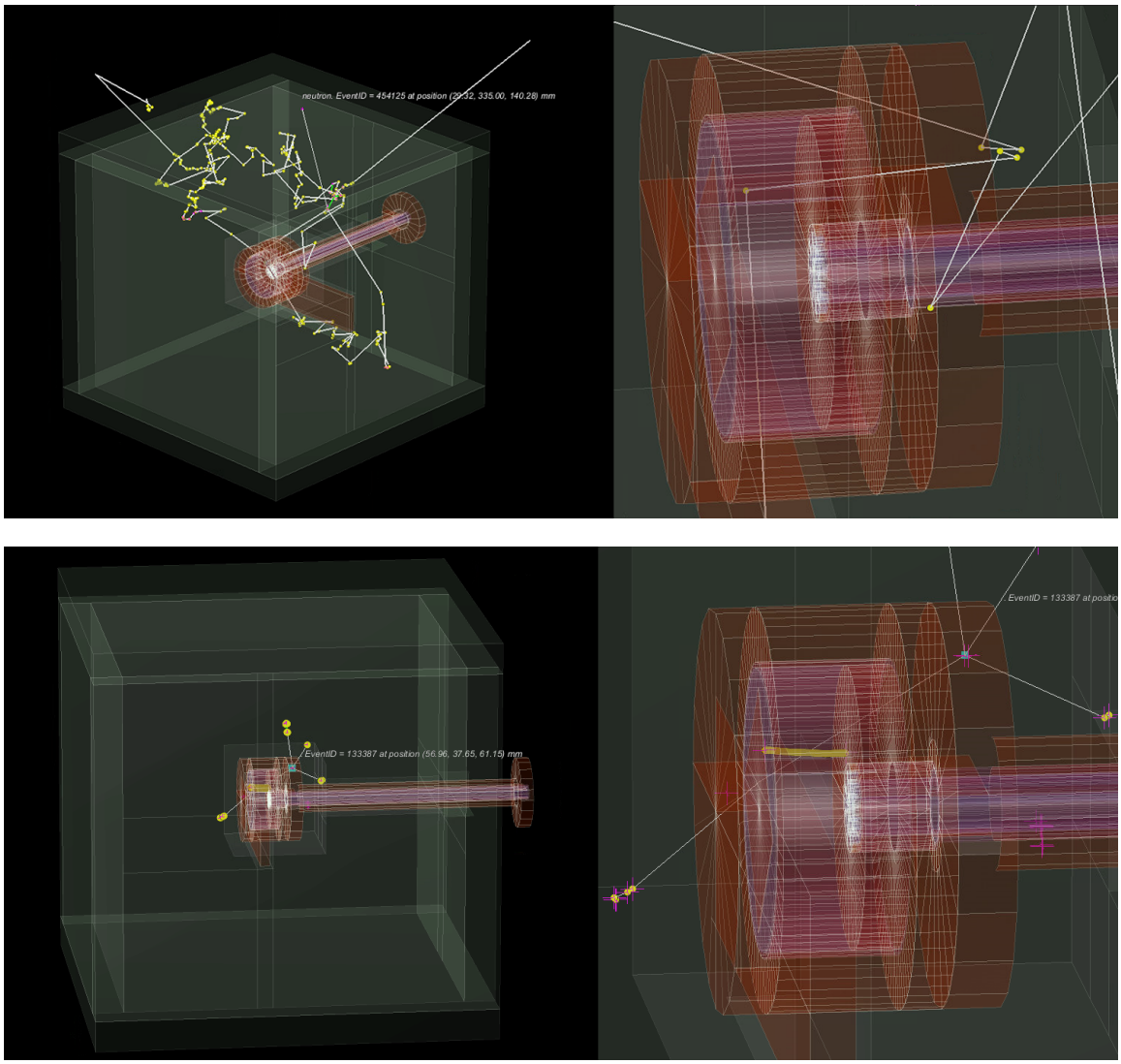

Figure 7.15: Examples of typical TRestG4Events produced by an initial cosmic neutrons. **(Top)** A neutron (white line) reaches the gas and produces an elastic scattering, leaving a small amount of energy in the process (yellow dot). **(Bottom)** This event is the result of a neutron capture, that produces an excited ^{64}Cu isotope (blue square) and some gammas (white lines). One of these gammas reaches the gas and ionize it, producing a detectable signal (yellow dots).

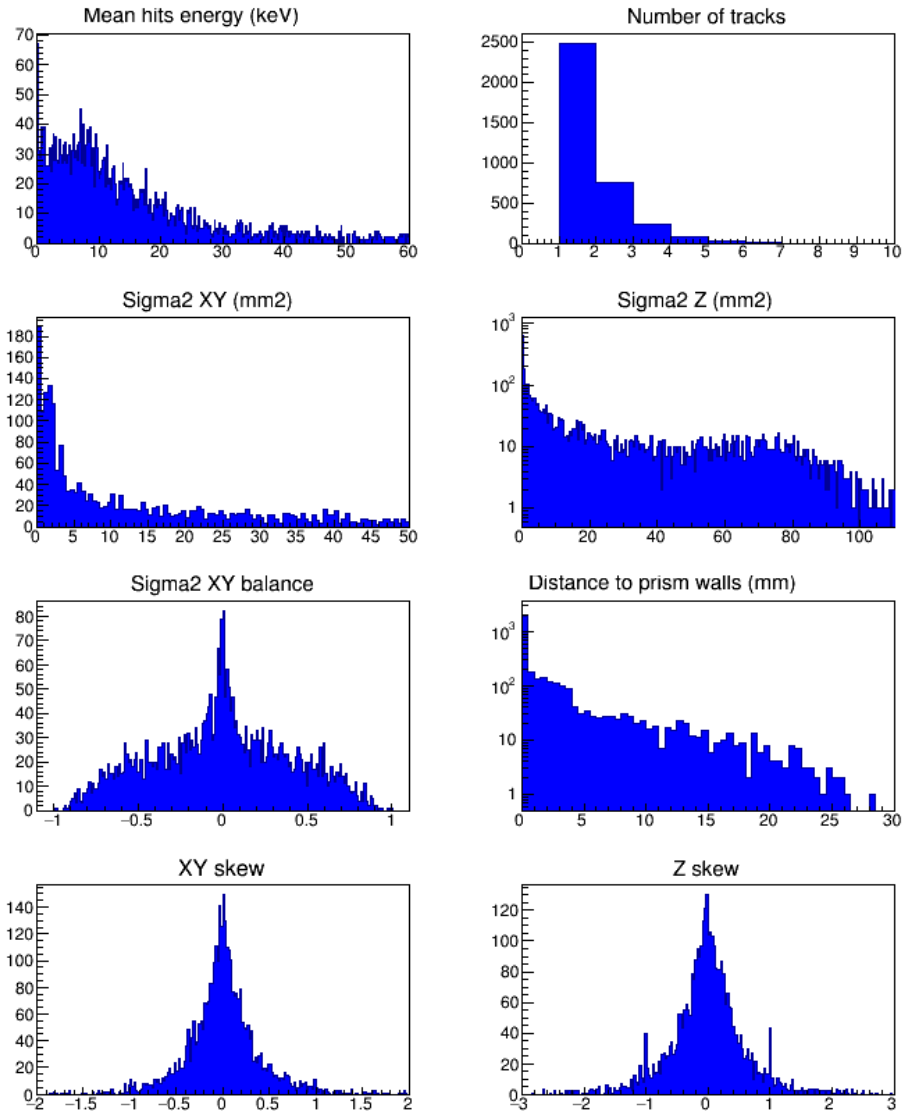

Figure 7.16: Cosmic neutrons characterization observables. These plots correspond to the [10, 1000] MeV range simulations, a total of 2×10^7 initial neutrons and 84.87 equivalent exposure hours. The observables shown are the energy, the number of tracks, $\sigma^2_{x,y}$ and σ^2_z, the balance between σ_x and σ_y, the distance to the fiducial volume, γ_{xy} and γ_z, and they are defined in the section 6.2. Y axis represents the number of events for all the plots, and each x axis is labelled at the top for clearness, referencing the units if the observable is not dimensionless.

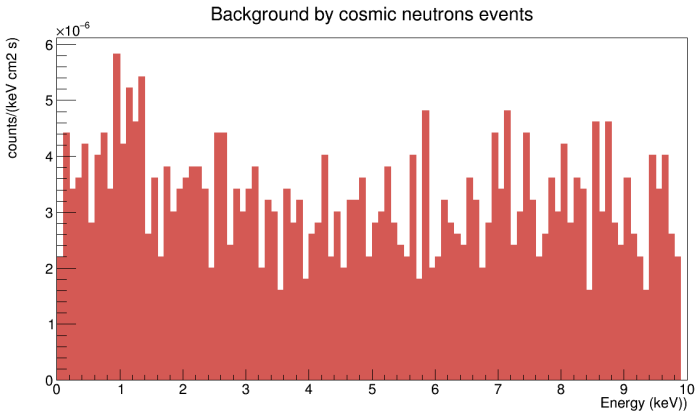

Figure 7.17: Total contribution to the background produced by cosmic neutrons before the discrimination process. Both low and high energy simulations were taken into account, and the quenching factor was applied to the nuclear recoils.

where E_R is the event energy and the function $g(E_R)$ is parametrized in terms of the atom number (Z) and mass (A) as

$$g(E_R) \simeq 0.66 \left(\frac{Z^{5/18}}{A^{1/2}} \right) E_R^{1/6}(keV) \tag{7.4}$$

Natural gaseous argon contains a 99.6% of $^{40}_{18}$Ar, so the quenching factor for the superior limit of the IAXO energy RoI is $g(10\,keV) = 0.34$. This means that events from nuclear recoils up to ∼30 keV need to be considered for the background contribution.

Finally, the raw contribution to the IAXO-D0 background produced by the cosmic neutrons in the IAXO energy RoI is shown in figure 7.17. The results from the two initial energy distributions for low and high energy neutrons have been combined and the quenching factor for the events produced by nuclear recoils has also been applied, leading to a background of $(1.22 \pm 0.03) \times 10^{-5}$ counts keV^{-1} cm^{-2} s^{-1} before the discrimination analysis. This value is high taking into account the IAXO background goal, but as it was already mentioned, the contribution to the background due to cosmic neutrons has never been properly simulated or studied in the CAST-Micromegas context.

7.3.5 Radiogenic neutrons

Another contribution to the detector background can be caused by radiogenic neutrons. They are produced by (α,n) reactions, following the α decays of the radioactive chains from the spontaneous fission of the ^{238}U contamination that is present in the components of the detector or the shielding. This contribution should be minimum because of the high radiopurity of the materials of the detector. For the simulations, a normalized evaporation spectrum of the neutrons produced in the fission of the ^{238}U contamination has been used to estimate the possible contribution to the background from the lead shielding, which is

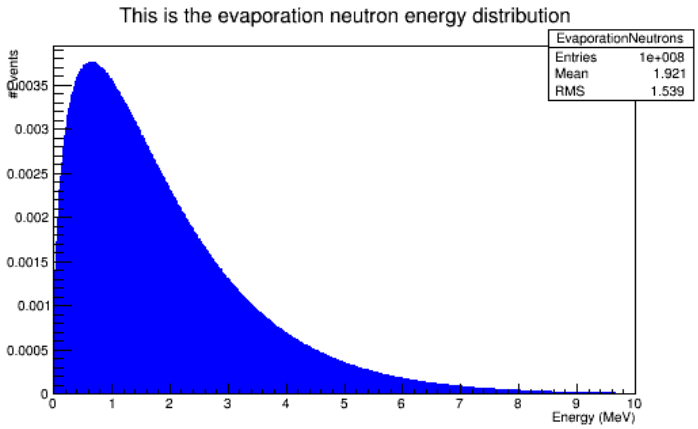

Figure 7.18: Energy distribution of the evaporation neutrons coming from ^{238}U radioactivity of nearby materials and walls.

the biggest mass of material next to the detector. It is shown in Figure 7.18, and it covers evaporation neutrons from 0 to 10 GeV.

The estimation of the neutrons rate has been made considering the ^{238}U contamination of the lead shielding, 0.33 mBq/kg [154] (table 5.2), the number of neutrons produced per fission process, (2.4±0.2), and the number of fissions per decay, $(5.45\pm0.04)\times10^{-7}$ [231]. The rate of radiogenic neutrons production from the lead shielding (1.84×10^{3} kg) is therefore $(4.32\pm0.36)\times10^{-10}\,\mathrm{kg^{-1}\,s^{-1}}$. A total of 1.1×10^{6} initial events have been launched from the shielding, what corresponds to a total of $\sim 4.4\times10^{4}$ years. Note that the neutrons produced in (α,n) reactions from the radioactive chains have not been taken into account.

The events produced by radiogenic neutrons are similar to those produced by cosmic neutrons. Most of them are produced by the nuclear recoils in the gas due to neutron elastic scattering or by secondary gammas produced in other neutron interactions with the chamber or shielding atoms.

Considering the quenching factor for the nuclear recoils, the contribution to the total IAXO-D0 background from radiogenic neutrons in the IAXO energy RoI is $(7.0\ \pm\ 1.1)\times10^{-14}\,\mathrm{counts\,keV^{-1}\,cm^{-2}\,s^{-1}}$ even before the discrimination analysis. This contribution is several orders of magnitude below the IAXO background goal, so it can be considered negligible.

7.3.6 Detector components radioactivity

The radiopurity of the materials that form the components of the Micromegas detector is a very important point that is always present in the design process, specially for the parts that are in direct contact with the active gas. Exhaustive studies of the radioactivity from the materials used to build the CAST-Micromegas detectors have been done mostly in the facilities of Canfranc Underground Laboratory, giving precise values and upper limits

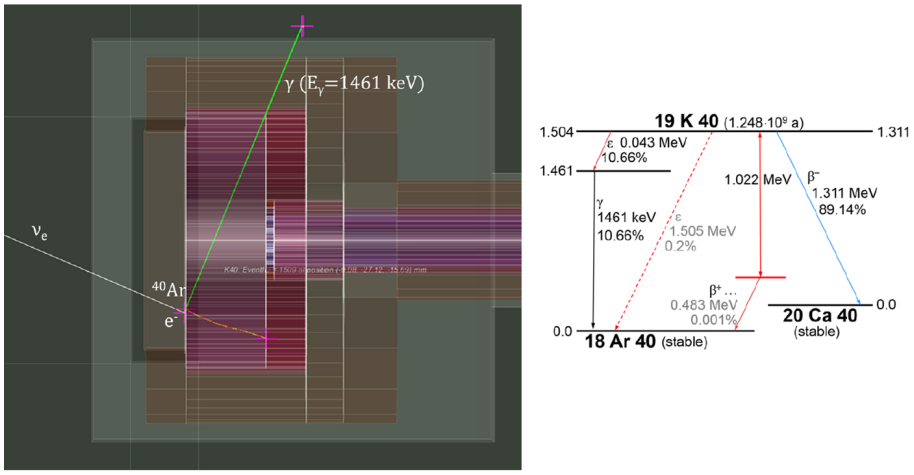

Figure 7.19: (Left) Simulation of an event produced by a ^{40}K disintegration from the copper of the Micromegas readout. As a result, an ^{40}Ar isotope is produced, as well as a ν_e (white line) that escapes from the shielding, and a γ (green line) that interacts in the shielding. As a consequence of the γ emission, an e^- is generated, which interacts in the gas and produces energy deposits, or hits (yellow dots). **(Right)** Disintegration scheme of the ^{40}K isotope.

for the main radioactive isotopes of each material.

This information, previously shown in table 5.2, has been used to simulate the contribution of each significant isotope from each volume of the IAXO-D0 geometry. It has been a thorough study [227] where each isotope has been launched uniformly distributed inside each corresponding volume of the G4DML geometry described in section 6.3.1 with isotropic angular distribution. Not only the detector chamber, but also the lead shielding with its ^{210}Pb contribution has been considered for this study.

Almost all the pieces of the detector chamber are made out of copper and they have been stored and manipulated at sea level, so we expect them to contain a certain amount of ^{60}Co by cosmogenic activation. This activity A induced in the copper, with a decay constant λ, has been evaluated taking into account the time of exposure to cosmic rays, t_{exp}, and considering negligible the cooling time, t_{cool}, because it has never been stored underground or sheltered from cosmic rays:

$$A = R\,[1 - \exp(-\lambda t_{exp})]\,\exp(-\lambda t_{cool}) \tag{7.5}$$

where R is the production rate, that for the ^{60}Co it has been directly measured as the saturation activity, as it was shown in table 5.1.

The simulations to compute the materials radioactivity contribution to the total background have consisted of launching a large number of initial isotope disintegrations of each significant isotope from each geometry volume until $\sim 10^4$ interactions have been produced in the active gas of the detector. In the case of the lead shielding, only ~ 200 interactions have been obtained after more than 1000 hours of computational time. An example of an event produced by a ^{40}K disintegration from the copper of the Micromegas readout is shown in figure 7.19. In this example, an electronic capture ${}^{40}_{19}K \rightarrow {}^{40}_{18}Ar + \nu_e + \gamma$

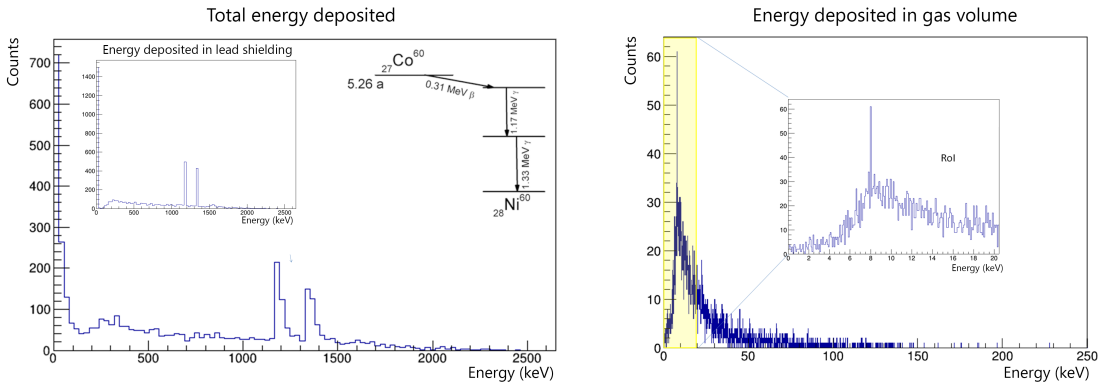

Figure 7.20: (Left) Total energy deposited in the geometry by events produced from 5×10^7 ^{60}Co disintegrations (425 equivalent years) from the copper pipe, where the 1.17 MeV and 1.33 MeV peaks are visible. The small plot shows the energy deposited by these events only in the lead shielding, where both peaks are also visible. **(Right)** Energy deposited in the gas volume by the same events from the left plot. The small plot is a zoom to the RoI where the axion signal is expected.

is observed, where an electron is generated as a consequence of the emission of the 1461 keV gamma by the ^{40}Ar. This electron interacts in the active gas and produces a detectable 1.23 keV energy deposit.

From these simulations it has been concluded that most of the energy from the events produced by radioactive disintegrations is efficiently shielded by the passive shielding. Figure 7.20 shows as an example the energy deposited in different volumes by events produced from 5×10^7 ^{60}Co disintegrations from the copper pipe, which considering the estimated activity (3.77×10^{-3} Bq), corresponds to ∼425 equivalent years. In the general plot, the 1.17 MeV and 1.33 MeV peaks from the ^{60}Co emission are visible, as well as in the plot that shows the energy deposited only in the lead shielding volume. On the other hand, the emission obtained in the gas shielding is smaller, and is specially reduced for lower energies where the IAXO RoI is.

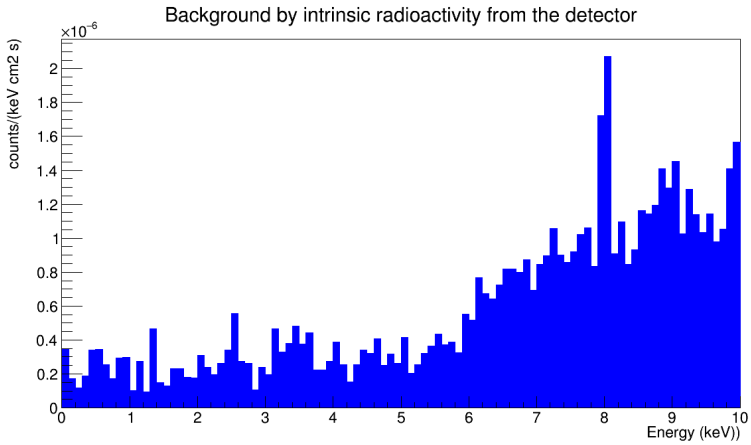

Figure 7.21: Total contribution to the raw background produced by the intrinsic radioactivity of the materials of the detector. The ^{210}Pb contribution from the lead shielding was not included because of low statistics.

As a whole, the raw background contribution from the intrinsic radioactivity of the detector, chamber and shielding is $< 6.39 \times 10^{-7}$ counts keV^{-1} cm^{-2} s^{-1}. Figure 7.21 shows the total raw background contribution in the IAXO RoI. More detailed information about specific contributions to the background will be discussed in the next section, after the analysis and the discrimination process.

7.3.7 Gas contamination

In order to evaluate the impact of the ^{39}Ar that naturally appears in the argon gas, a simulation has been performed from the gas volume itself. ^{39}Ar events have been launched uniformly distributed inside the gas volume with isotropic angular distribution. A total of 2×10^5 events have been simulated, which considering the activity of the ^{39}Ar, $\sim$1.01 Bq kg^{-1} [210], and the small mass of gas inside the chamber, $\sim$0.36 g, correspond to $\sim$17 equivalent years of emission.

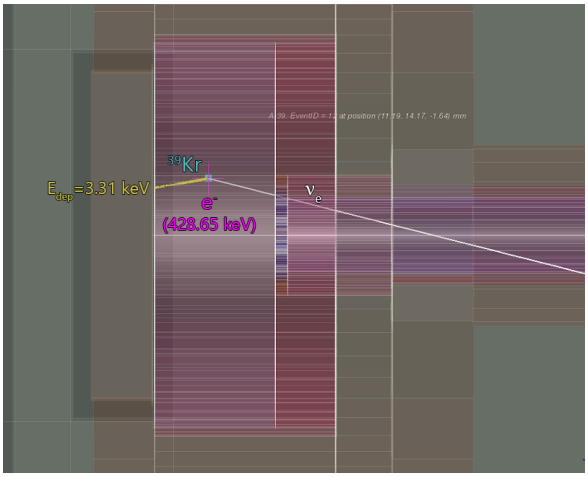

Figure 7.22: (Top) Example of an ^{39}Ar β^- decay, where a ^{39}Kr isotope is produced (blue square), as well as a $\overline{\nu}_e$ that leaves the shielding without interacting (white line) and an e^- (pink cross) that interacts in the gas and deposits an energy of 3.31 keV (yellow dots). **(Bottom)** The ^{39}Ar decay scheme.

Most of the events are produced by the electron produced at the β^- decay of the ^{39}Ar isotope: $^{39}_{18}Ar \rightarrow ^{39}_{19}K + e^- + \overline{\nu}_e$ as it is shown in figure 7.22. In this particular example, the electron left an energy of 3.31 keV in the gas. Such event could be indistinguishable from an event produced by an x-ray, so this contribution has to be studied.

The characterization observables of the events produced by the ^{39}Ar β^- decay from the active gas are shown in figure 7.23. They leave energy in all the IAXO RoI and also, most of the events have one single track. As we are only considering events in the RoI, all of them appear as quite small energy deposits (small $\sigma^2_{x,y}$ and σ^2_z). The most representative observable in this case for the discrimination process is the *distance to wall*, since most of the events spread across the full gas volume, reaching the readout borders.

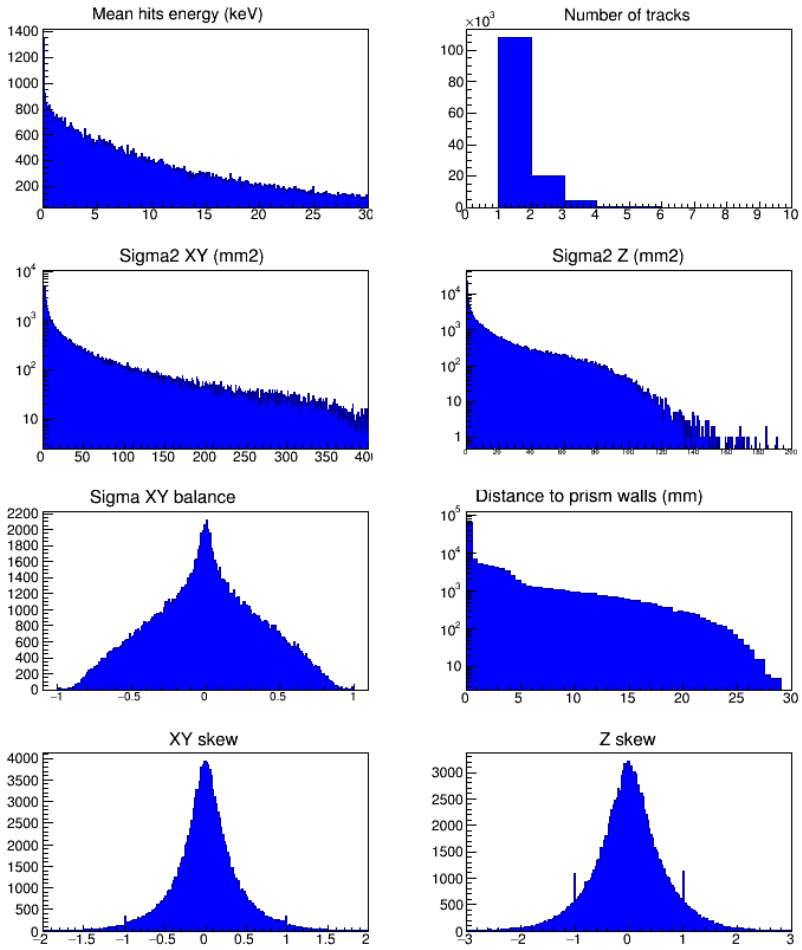

Figure 7.23: Characterization observables of events produced by the disintegration of the ^{39}Ar isotope of the IAXO-D0 detector gas. Y axis represents the number of events, and each x axis is labelled at the top for clearness, referencing the units if the observable is not dimensionless. The observables shown are the energy, the number of tracks, $\sigma^2_{x,y}$ and σ^2_z, the balance between σ_x and σ_y, the distance to the fiducial volume, γ_{xy} and γ_z.

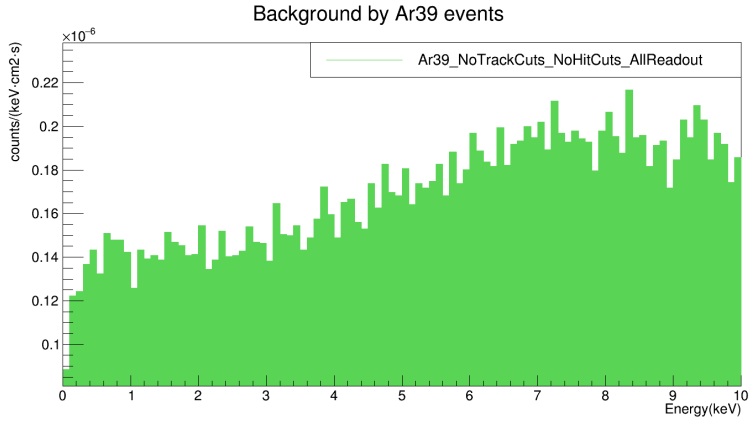

Figure 7.24: Raw background contribution from the ^{39}Ar of the active gas in the IAXO energy RoI.

Finally, figure 7.24 shows the raw contribution to the IAXO-D0 background of the events produced by ^{39}Ar decay from the gas of the detector in the IAXO energy RoI. This contribution for the [0,10] keV energy range will be $(1.71 \pm 0.01) \times 10^{-7}$ counts keV^{-1} cm^{-2} s^{-1}. It is one order of magnitude higher than the IAXO background objective, but it will be further reduced by the fiducial cuts after the discrimination process.

7.4 IAXO-D0 Background model for Ar+Isobutane

Once all the individual contributions to the background have been simulated, the next step has been to analyse them using REST software. As it was explained in section 7.2.1, the TRestG4Events have been transformed into TRestHitsEvents, and finally TRestTrackEvents, and the observables of each event type has been obtained along the process. A diffusion process has been applied to the TRestHitsEvents to simulate the drift of the electrons through the Ar+Isobutane mixture. Also, a hit reduction had to be performed previous to the the hit analysis to reduce the high number of TRestG4Hits produced by the simulations, as the step inside the gas volume was very small.

A similar analysis has been applied to the x-ray characterization in order to obtain the corresponding observables, and study which of them were more relevant and would define best the topology of an event produced by an x-ray in the IAXO energy RoI. Then a selection criterion has been defined by setting upper and lower cuts to certain observables. These cuts have been applied to every background contribution simulated and finally, individual background levels have been calculated and combined to obtain the total background for the IAXO-D0 prototype in CAST typical background units (counts keV^{-1} cm^{-2} s^{-1}).

In this section, the discrimination cuts will be justified and the IAXO-D0 background model will be detailed explained, paying special attention to the most relevant contributions.

7.4.1 Cuts definition and efficiency

Taking into account the x-ray characterization explained in section 7.2.2, the discrimination cuts have been defined in order to reject all the events that are not x-ray-like. The first cut applied has been to reject all the events with more than 1 track, because we expect most x-rays to leave all its energy in the gas at once via photoelectric effect. Although there are experimental reasons to consider two tracks events under certain circumstances, the observables are optimized for one-single track events, so the information obtained by the simulations study will be more significant if we consider only these last ones.

The observables that have been used for this discrimination process, as well as their

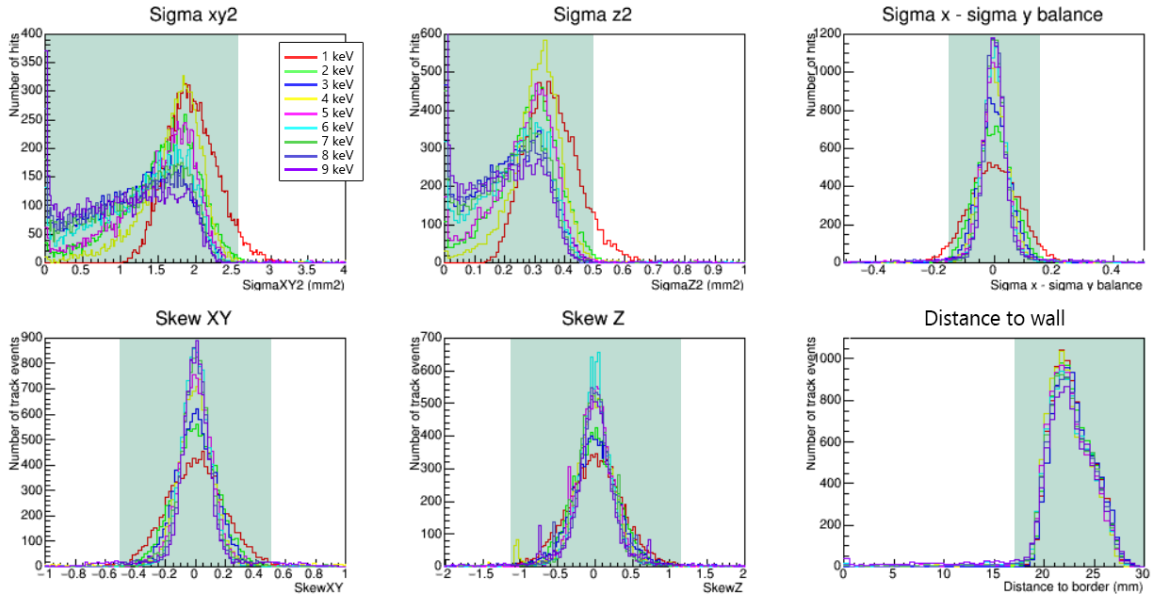

Figure 7.25: X-ray observables used to define the cuts for the background discrimination process. The green areas represent the events that would pass the cuts.

chosen values, are shown in table 7.3 and are visually represented in figure 7.25. Only events from the RoI [1, 10] keV have been considered. These observables are related with the position, the size, the shape and the symmetry of the energy deposit of the events.

These cuts to the observables leave only small, round-like and symmetric events. The σ^2_{xy} cut rejects all the events bigger than $\sim$10 mm^2 on the readout, which translates into 5-6 strips triggered per axis with a 0.5 mm pitch. The σ^2_z cut rejects all the events longer than 1.5 mm in the Z axis. The cut that limits the balance between σ_x and σ_y rejects all the events which deviation in both axis differ in more than 20%, leaving only round-like events. Finally, skewness cuts are also defined to assure that only symmetric events are considered.

Observable	Range	Efficiency (%) at 3 keV
σ^2_{xy} (mm^2)	[0, 2.6]	96.48±0.98
σ^2_z (mm^2)	[0, 0.55]	96.48±0.98
$\frac{\sigma_x-\sigma_y}{\sigma_x+\sigma_y}$ (1)	[-0.15, 0.15]	93.96±0.97
γ_{xy} (1)	[-0.5, 0.5]	93.37±0.97
γ_z (1)	[-1.12, 1.12]	90.69±0.95
d_w (mm)	[17, 30]	96.27±0.98

Table 7.3: Definition of the cuts for the background discrimination analysis. Their range values are obtained from the x-ray characterization. The first 5 cuts are related to the topological information of the event, and are referred to along the text as *x-ray cuts*. The last cut, d_w, which is the 2D fiducial cut, is often applied separately and used to select a smaller centred area of the readout. The efficiency of each cut applied individually for the 3 keV x-rays is also shown with its statistical error.

Energy (keV)	Cuts efficiency (%)
1	76.05±0.87
2	91.98±0.96
3	89.47±0.95
4	90.34±0.95
5	89.44±0.95
6	87.47±0.94
7	86.10±0.93
8	84.71±0.92
9	78.44±0.89

Table 7.4: Efficiency of all the discrimination cuts for one-single track x-rays in the [1, 10] keV range. All the cuts listed in table 7.3 has been applied. The statistical error is also shown.

The last discrimination cut that is indicated in table 7.3 is the *distance to wall*, d_w, and its range is defined such as only the events that are registered close to the center of the readout are kept. Considering that $d_w = 30\,\text{mm}$ means that the event is exactly at the center (i.e. the furthest distance from the fiducial prism wall as it can be), most of the events produced by x-rays in the RoI are contained in a small area of $\sim 6.8\,\text{cm}^2$ at the center of the readout, as it is shown in figure 7.25.

The efficiency of the cuts for the IAXO energy RoI is shown in table 7.4. It has been calculated as the percentage of events that pass the discrimination cuts at each energy. All the cuts listed in table 7.3 have been applied. We can see that the cuts are more efficient for energies between 2 and 6 keV, with only a $\sim$10% of efficiency loss.

Finally, another important cut that was only applied for cosmic contributions is whether or not the events leave any energy in any of the vetoes around the detector. From CAST experience it is known that only one veto over the detector is able to reject half of the background after the discrimination analysis was performed, i.e. a reduction of $\sim 10^{-6}\,\text{counts}\,\text{keV}^{-1}\,\text{cm}^{-2}\,\text{s}^{-1}$ of the total background.

7.4.2 Background model result

After all the known background contributions have been simulated, the x-ray characterization has been made and the discrimination cuts have been defined, the last step of the background study of IAXO-D0 has been to apply the cuts to all the individual contributions. This has been made using the *REST plot* tool, that allows the user to select all the files from each contribution and add them together, so the statistics can be higher with shorter simulations. It also applies the discrimination cuts by only plotting the events which observables fulfil the defined conditions.

Finally, a C++/Root script has been used to scale each background spectrum to be in the CAST-IAXO standard background units ($\text{counts}\,\text{keV}^{-1}\,\text{cm}^{-2}\,\text{s}^{-1}$), taking into

Background contribution	Background level before cuts counts keV^{-1} cm^{-2} s^{-1}	Background level after cuts counts keV^{-1} cm^{-2} s^{-1}	Discrimination cuts efficiency (%)
Cosmic μ	$(7.23 \pm 0.02) \times 10^{-4}$	$(3.9 \pm 0.8) \times 10^{-7}$	99.9
Cosmic $\mu^{(v)}$	$< 5.19 \times 10^{-8}$	$< 3.97 \times 10^{-8}$	-
Cosmic n	$(1.22 \pm 0.03) \times 10^{-5}$	$(8.2 \pm 1.5) \times 10^{-7}$	93.3
Cosmic n$^{(v)}$	$(8.1 \pm 0.9) \times 10^{-6}$	$(5.5 \pm 1.2) \times 10^{-7}$	93.3
Cosmic γ	$(5.9 \pm 1.7) \times 10^{-7}$	$< 4.17 \times 10^{-7}$	29.5
Total from cosmic rays	$(7.33 \pm 0.02) \times 10^{-4}$	$< 1.62 \times 10^{-6}$	99.8
Total from cosmic rays$^{(v)}$	$(8.8 \pm 0.9) \times 10^{-6}$	$< 1.00 \times 10^{-6}$	99.8
Environmental γ	$(4.8 \pm 1.4) \times 10^{-8}$	$< 2.24 \times 10^{-8}$	53.3
Radiogenic n	$(7.0 \pm 1.2) \times 10^{-14}$	$< 2.55 \times 10^{-14}$	63.5
Materials radioactivity	$< 6.39 \times 10^{-7}$	$< 4.56 \times 10^{-7}$	49.3
Ar gas radioactivity	$(1.71 \pm 0.01) \times 10^{-7}$	$(1.03 \pm 0.05) \times 10^{-8}$	94.0
Total from radioactivity	$< 1.01 \times 10^{-6}$	$< 5.11 \times 10^{-7}$	49.6
Total	$(7.34 \pm 0.02) \times 10^{-4}$	$(2.13 \pm 0.17) \times 10^{-6}$	99.7
Total $^{(v)}$	$(9.8 \pm 0.9) \times 10^{-6}$	$(1.51 \pm 0.12) \times 10^{-6}$	84.5

Table 7.5: IAXO-D0 background model. The background contributions from the different known sources are shown before and after the discrimination cuts were applied. Background values and errors were obtained by 7.2.1. Some values are upper limits due to non precise activity measurements or low statistics from the simulations (where the 95% C.L. was considered). The errors of the total background are obtained considering the most relevant contributions. (v) The vetoes rejection cuts were applied to these background values.

account their corresponding equivalent time, the energy range and the specific area of the readout. Table 7.5 shows each individual contribution as well as the total background before and after the application of the discrimination cuts. They are also shown the total contribution to the background coming from cosmic rays and radioactivity.

Some first conclusions can be obtained from these general results. The most important contribution to the background comes from cosmic rays, as expected. The raw background is dominated by events produced by cosmic muons, $\sim 7.2 \times 10^{-4}$ counts keV^{-1} cm^{-2} s^{-1}, followed by those produced by neutrons, which contribution is one order of magnitude lower, $\sim 1.2 \times 10^{-5}$ counts keV^{-1} cm^{-2} s^{-1}. Cosmic gammas barely contribute to the total raw background with $\sim 5.9 \times 10^{-7}$ counts keV^{-1} cm^{-2} s^{-1}, that is already at the level of the IAXO background goal. However, after the discrimination cuts are applied, the three contributions are reduced to the same order of magnitude, being $\sim 10^{-7}$ counts keV^{-1} cm^{-2} s^{-1} for each of them. The total contribution from cosmic rays (μ+n+γ) after the discrimination process is therefore $< 1.62 \times 10^{-6}$ counts keV^{-1} cm^{-2} s^{-1}. This is compatible with the background previously attributed only to cosmic muons in the CAST-Micromegas setups, where cosmic neutrons were never taken into account. Highly energetic cosmic gammas also seem to contribute to this result, but only an upper limit has been obtained because the equivalent simulated time and the resulting statistics are too low in comparison to the other two contributions to consider it at the same level of importance. Nevertheless, more simulations should be performed in the future in order to check this assumption.

Cosmic muons and neutrons leave energy in the vetoes around the detector, and the

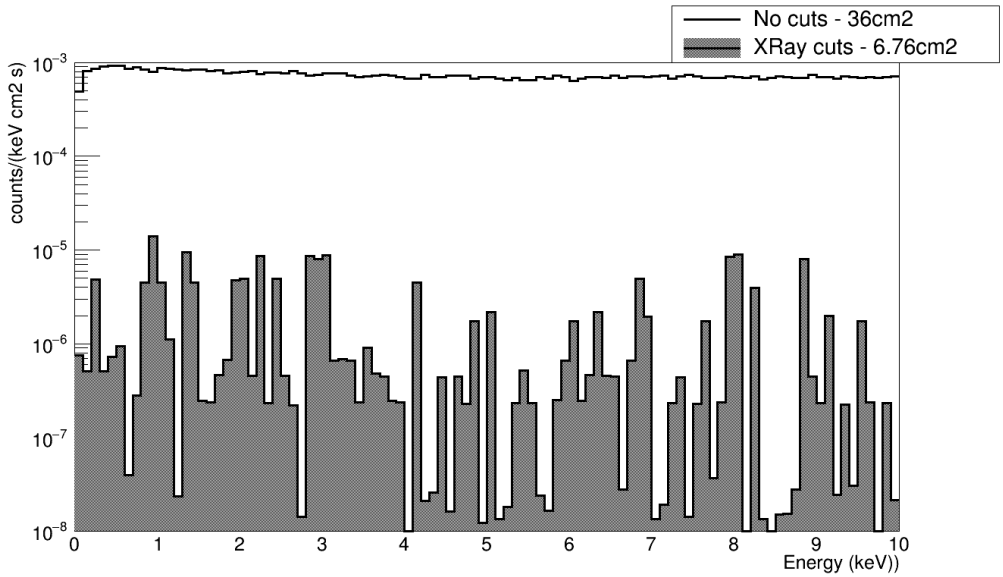

Figure 7.26: IAXO-D0 background model. The black line represents the total simulated background before the discrimination process. All the readout surface is considered (36 cm^2). The filled area represent the total simulated background after the discrimination process. Fiducial cuts were applied to consider only a central part of the readout (6.76 cm^2). The vetoes discrimination cuts are not taken into account.

simulations were performed considering a complete 4π veto coverage. This information can be used to reject events produced by cosmic particles and therefore, reduce the background. In table 7.5, the background values for cosmic muons considering only events that do not deposit energy in any of the six vetoes are shown (v). Further information about the shielding efficiency for muons and neutrons will be given later on the text.

The background component from radioactivity is not as important before cuts compared to the cosmic contribution, but it becomes relevant because the discrimination process is not as efficient to reject events coming from the intrinsic radioactivity of the detector materials. The biggest contribution comes from the contaminations of the materials of the detector and shielding, followed by the ^{39}Ar contamination from the target gas. The contribution from the environmental gammas is of the order of $\sim 10^{-8}\,\mathrm{counts\,keV^{-1}\,cm^{-2}\,s^{-1}}$, which proves that the improved passive shielding is satisfactorily reducing this component in comparison to the estimations made previously [43]. Finally, the radiogenic neutrons resulted irrelevant and the statistics were very low regardless the long equivalent simulated time. The total raw contribution from radioactivity is therefore $< 1.01 \times 10^{-6}\,\mathrm{counts\,keV^{-1}\,cm^{-2}\,s^{-1}}$, and after the cuts it is reduced by a 50%. This level of background is in agreement with the tests performed in the LSC underground laboratory with CAST-Micromegas detectors, and even though it is compatible with the IAXO background goal, a smaller contribution from radioactivity would be desirable. More details about specific materials contributions will be given later on this section.

Overall, the total background for the IAXO-D0 detector in the IAXO energy RoI ([0,10] keV) after the discrimination process is $(2.13 \pm 0.17) \times 10^{-6}\,\mathrm{counts\,keV^{-1}\,cm^{-2}\,s^{-1}}$

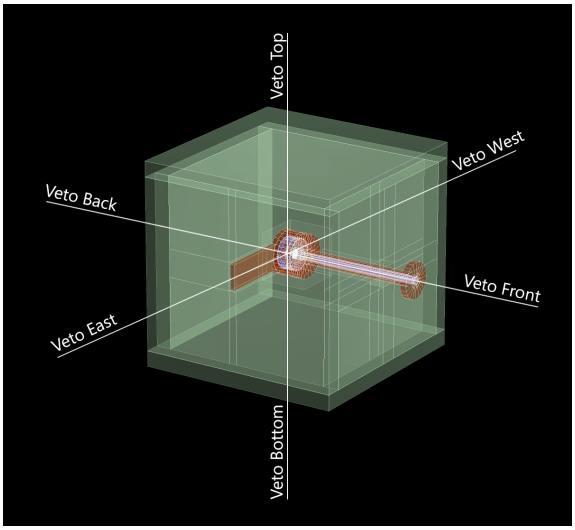

Veto(s) active	μ shielding efficiency (%)
Top	75.1 ± 0.7
Bottom	66.8 ± 0.8
Back	22.2 ± 5.2
Front	16.6 ± 3.5
East	11.8 ± 8.6
West	11.6 ± 8.8
All	100.0 ± 0.5
Top + West + Back	98.5 ± 0.5
Bottom + East + Front	89.3 ± 0.5

Figure 7.27: (Left) Veto placement at the IAXO-D0 simulated geometry. The front veto is the one that faces the magnet, and the east veto is where the electronics are attached. **(Right)** Cosmic μ shielding efficiency (i.e. the capability of the vetoes to tag events caused by muons) of the different vetoes or a combination of them. The statistical error is shown. Neither x-ray cuts or 2D fiducial cuts have been applied.

($(1.51 \pm 0.12) \times 10^{-6}$ counts keV^{-1} cm^{-2} s^{-1} considering the veto shielding). This involves a background reduction of the ∼99% taking into account the discrimination cuts from the x-ray characterization and the fiducial cut to consider a central and reduced area of the readout. Figure 7.26 shows the total simulated IAXO-D0 background in the IAXO energy RoI before and after the discrimination cuts.

After these general overview of the results, some more discussion can be made from the most relevant background contributions, such as the cosmic muons, the cosmic neutrons and the materials radioactive contaminations.

Cosmic muons

As far as the background studies have gone in the CAST and IAXO context, it was understood that the biggest contribution to Micromegas background came from muons. It was quantified to contribute $\sim 1.5 \times 10^{-6}$ counts keV^{-1} cm^{-2} s^{-1} [14], and this estimation was made by the comparison with underground measurements and the use of 1-2 plastic scintillator vetoes.

For this work, a total of 200 hours of muon contribution was simulated considering a geometry where the vetoes perfectly covers a solid angle of 4π of the detector, as it is shown in figure 7.27. Only two small openings for the interface pipe and the detector raquette are cut through the vetoes, which in real life would not be realistic. Vetoes cannot be placed in the side of the detector facing the magnet, and would exist some difficulties to fit a perfectly covering veto at the side where the electronics are attached.

This idealistic approach allows to study the efficiency of the vetoes rejecting events produced by muons and the importance of each veto. This was done by comparing the total number of events produced by cosmic muons with the number of events that do not leave any energy in one or a combination of the vetoes. The remaining events will be therefore detected and marked by the vetoes, and rejected from the background. The efficiency of the vetoes is shown in figure 7.27. From this study it is obtained that a full 4π veto coverage would shield ∼100% of the events produced by muons. The top veto the most relevant, being able to shield a 75% of the events by itself. Due to the directionality of the cosmic muons, the bottom veto is also relevant. The lateral vetoes are more inefficient by themselves, but combining them with the top or the bottom veto yields to a high rejection efficiency only using 3 vetoes. In the table, two different combination of vetoes are shown. The top+west+back combination is the most direct to translate to the experiment, because these sides of the shielding should be free from the setup restrictions: the connection to the electronics is made from the east side, and the connection to the magnet is made from the front side.

Also, it is important to remark that in this work, the detector is considered to be static with the bottom standing on the floor. These efficiency assumptions rely on the relative position of the detector to the zenith angle θ. As it was mentioned in section 7.3.1, muons follow an initial angular distribution of $\sim cos^2\theta$, which means that most of the muons will arrive vertically. If we suppose the detector to be mounted on an moved by the IAXO magnet, both front and back vetoes will become more relevant for the higher and lower positions of the sun tracking.

Considering a 4π muon coverage, the upper limit for the background contribution from cosmic muons after the discrimination cuts would be $< 3.97 \times 10^{-8}\,\mathrm{counts\,keV^{-1}\,cm^{-2}\,s^{-1}}$, for a 95% C.L. in all the readout area and the IAXO energy RoI. Note that table 7.5 shows two slightly different values for the background from cosmic muons when the vetoes are considered(v), before and after the discrimination process. This is due to the fact that from the almost 10^6 muons that were registered by the detector, two of them were not tagged by the vetoes. And then, those events did not pass the discrimination cuts. The values are given for a 95% C.L, and these upper limits are one order of magnitude lower than the IAXO background objective.

It is interesting also to understand how the discrimination cuts affect the total background produced by muons. As it was shown earlier in table 7.5, the discrimination efficiency of the cuts is a 99.9%. This high discrimination rate is due to the fact that muons leaves long and non-symmetric energy deposits that are out of the cuts ranges. There are some events that pass the cuts, but they will be vetoed thanks to the 4π veto coverage. Most of them are just a part of the muon tracks that cross the gas volume close to the chamber wall, where the readout is not able to measure the entire event, as it is shown in figure 7.28. This is due to the fact that the chamber is cylindrical and the readout is square shaped, so there will be some blind areas at the borders. This is not a real problem because the area where the axion signal is expected to be detected is the center of the readout, so fiducial cuts are an efficient way to remove remaining background from muons.

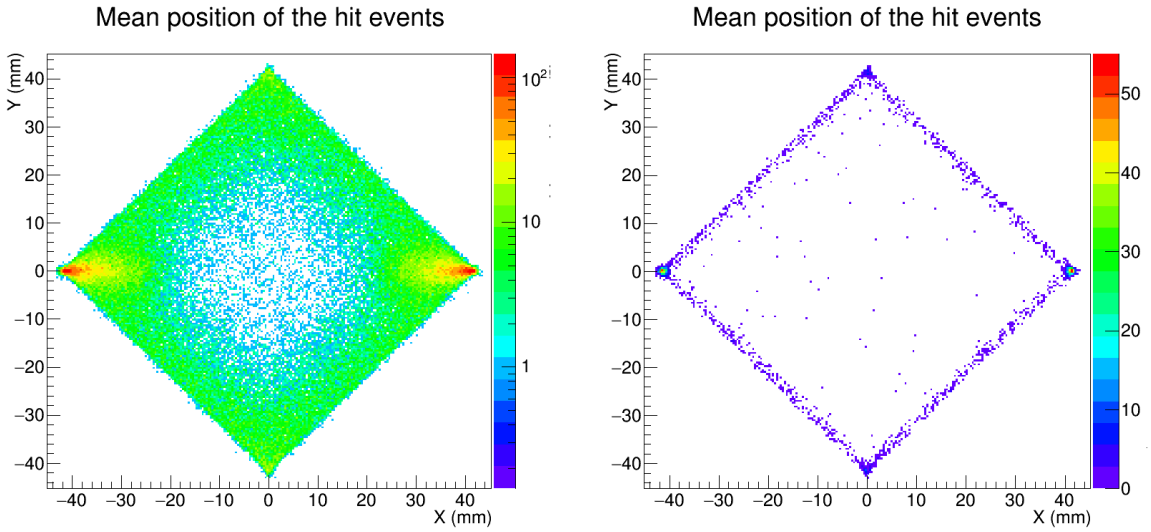

Figure 7.28: Mean position (weighted by the energy) of the hit events produced by muons in the IAXO energy RoI before **(left)** and after **(right)** the background discrimination cuts are applied. Most of the events that pass the cuts are detected close to the readout borders.

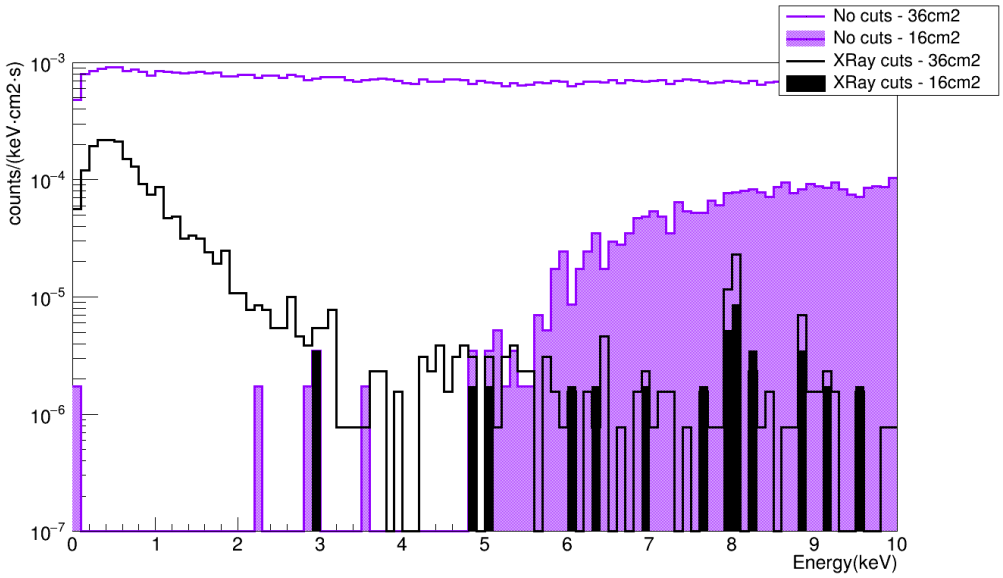

Figure 7.29: Background contribution from cosmic muons in the IAXO energy RoI. Raw background before the discrimination cuts are represented in purple and background after the discrimination process is represented in black. Lines represent background levels considering all the readout and solid areas represent background levels considering only a central area. Rejection from the vetoes is not considered in this plot.

Area considered	Background before cuts (counts keV^{-1} cm^{-2} s^{-1})	Background after cuts (counts keV^{-1} cm^{-2} s^{-1})	Cuts rejection (%)
36 cm^2	$(7.23 \pm 0.02)\times10^{-4}$	$(2.00 \pm 0.04)\times10^{-5}$	97.2 ± 0.1
16 cm^2	$(2.65 \pm 0.07)\times10^{-5}$	$(3.9 \pm 0.8)\times10^{-7}$	98.5 ± 0.3
6,76 cm^2	$(1.39 \pm 0.08)\times10^{-5}$	$(2.9 \pm 1.1)\times10^{-7}$	97.9 ± 0.8

Table 7.6: Background level from cosmic muons before and after the discrimination cuts considering different centred readout areas in the [0,10] keV energy range. 36 cm^2 corresponds to the complete readout and 6,76 cm^2 is the area from the x-ray characterization. The rejection factor from the application of the cuts is shown with its statistical error. Vetoes rejection cuts are not considered.

Figure 7.29 shows the background contribution from cosmic muons for the complete readout surface (36 cm^2) and a reduced central area (16 cm^2) that does not consider those events that are closer than 1 cm to the border of the readout. This fiducial cut is different from the one obtained from the x-ray characterization (6.76 cm^2) because the statistics for this smaller area were insufficient. In this plot, the lines represent the contribution to the background on the complete readout, and the solid areas represent the contribution considering only the central area. The fiducial cut results in a reduction of the low energy events up to $\sim$5 keV, leaving most of the axion signal expected range of energy free of background. Table 7.6 shows the different background levels for the different centred readout areas. The fiducial cut reduces the background in more than one order of magnitude before the discrimination cuts and two orders of magnitude after the cuts. And the cuts themselves reduce the background in more than 97%, resulting very efficient for this particular source of background.

With these considerations, the background level from events produced by cosmic muons after the x-ray discrimination cuts will be $(3.9 \pm 0.8)\times10^{-7}$ counts keV^{-1} cm^{-2} s^{-1}, with an upper limit of $< 3.97 \times 10^{-8}$ counts keV^{-1} cm^{-2} s^{-1} (95% C.L.) considering the discrimination from a 4π veto coverage. This limit is set by the fact that all the events produced by muons that passed the discrimination cuts are tagged by the vetoes, so they can be rejected. The background levels obtained from this study are compatible with the IAXO background goal and also, they resulted lower than the expected muon contribution from past CAST-Micromegas studies. This can be related to the fact that muons are not the only cosmic relevant contribution. And even though the results are encouraging, more simulations should be performed in order to cumulate more statistics and reduce the uncertainties.

Cosmic neutrons

Cosmic neutrons have resulted to be a more relevant contribution to the background than expected. In this work, a total of 96 hours of equivalent simulated time have been performed for both lower and higher energetic cosmic neutrons. A first interesting result has been that events produced by cosmic neutrons leave energy in the vetoes due to the large amount of secondary particles that they produce from its interactions with

Veto(s) active	Shielding efficiency for cosmic n (%)
Top	49.9 ± 6.5
Bottom	42.6 ± 8.1
Back	45.4 ± 7.4
Front	45.4 ± 7.4
East	45.0 ± 7.5
West	45.2 ± 7.4
All	66.8 ± 4.4

Table 7.7: Cosmic neutron shielding efficiency of the different vetoes, or the combination of them Statistical errors are shown. For veto positioning, refer to figure 7.27.

the shielding. Table 7.7 shows the shielding efficiency for the events produced by cosmic neutrons by each individual veto and the combination of all of them. This is, how effective are the vetoes to tag events produced by cosmic muons. These efficiencies were calculated in the same way described earlier for the cosmic muons. With a 4π veto coverage, a background reduction of 66% can be obtained for the cosmic neutron contribution. Individually, the shielding efficiency is similar for all of them, being the top one the most efficient and the bottom one the least efficient, probably due to geometrical reasons.

To obtain the background levels from cosmic neutrons, the quenching factor needs to be considered for those neutrons which interact in the gas via elastic scattering and produce a nuclear recoil. The quenching factor estimation was described earlier in this chapter by equations 7.3 and 7.4. Due to this factor, events with energies up to $\sim$30 keV that are produced by nuclear recoils will contribute to the [0,10] keV background.

The background contribution from nuclear recoils has been calculated separately. Thanks to the G4 observables provided by REST, events have been sorted depending on their type of interaction in the gas, so it is possible to apply a quenching factor only to the recoils (elastic interactions). Then, the final background in the RoI has been computed including all the contributions. Table 7.8 shows the background contribution from cosmic neutrons that produced a nuclear recoil in the gas separately from the rest of the interactions. Previously to the discrimination cuts, the nuclear recoils only account for a $\sim$10% of the total neutron interactions, so the background from this particular one is not significant. It is after the cuts are applied that this contribution becomes relevant. The energy deposit produced by a nuclear recoil is very similar to the energy deposit an x-ray would produce, so the discrimination cuts are not efficient.

On the other hand, the fiducial cuts are not as efficient as they were for the cosmic muon contribution. Figure 7.30 shows two hitmaps of the events produced by cosmic neutrons mean positions before (right) and after (left) applying the discrimination cuts. In both cases, all the events are homogeneously spread on the readout surface. A fiducial cut reducing the area considered turns in a maximum background reduction of a factor of $\sim$1.5.

Contribution	Area (cm^2)	Background before cuts (counts $keV^{-1}\,cm^{-2}\,s^{-1}$)	Background after cuts (counts $keV^{-1}\,cm^{-2}\,s^{-1}$)	Cuts rejection (%)
Nuclear recoils	36	$(4.2 \pm 0.3) \times 10^{-7}$	$(3.3 \pm 0.3) \times 10^{-7}$	20.7
	6.76	$(3.4 \pm 0.7) \times 10^{-7}$	$(3.0 \pm 0.7) \times 10^{-7}$	12.4
Other interactions	36	$(1.12 \pm 0.03) \times 10^{-5}$	$(8.7 \pm 0.8) \times 10^{-7}$	92.6
	6.76	$(1.4 \pm 0.3) \times 10^{-6}$	$(5.2 \pm 1.5) \times 10^{-7}$	64.0
Total	36	$(1.22 \pm 0.03) \times 10^{-5}$	$(1.19 \pm 0.09) \times 10^{-6}$	90.1
	6.76	$(1.8 \pm 0.3) \times 10^{-6}$	$(8.2 \pm 1.5) \times 10^{-7}$	54.1
Total (vetos)	36	$(8.1 \pm 0.9) \times 10^{-6}$	$(8.0 \pm 1.2) \times 10^{-7}$	93.4
	6.76	$(1.2 \pm 0.2) \times 10^{-7}$	$(5.5 \pm 1.2) \times 10^{-7}$	69.3

Table 7.8: Background contributions in the [0,10] keV energy range from cosmic neutrons depending whether or not a nuclear recoil occurs in the gas. The total contribution with and without the veto rejection is also shown, as well as the cuts rejection capability.

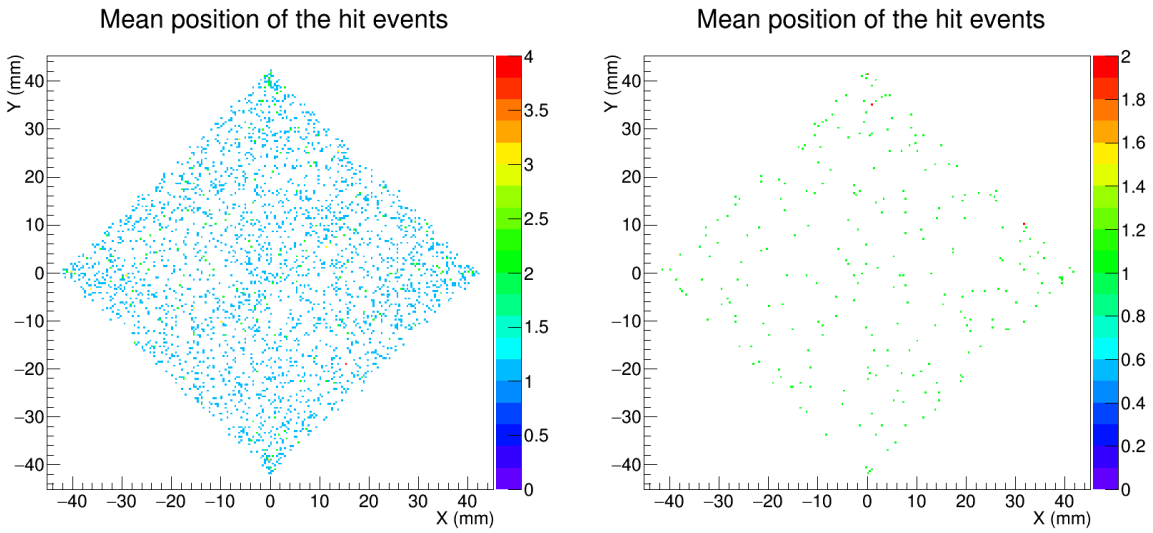

Figure 7.30: Mean position (weighted by the energy) of the hit events produced by cosmic neutrons in the [0,30] keV range before **(left)** and after **(right)** the background discrimination cuts are applied. The events are homogeneously spread on the readout.

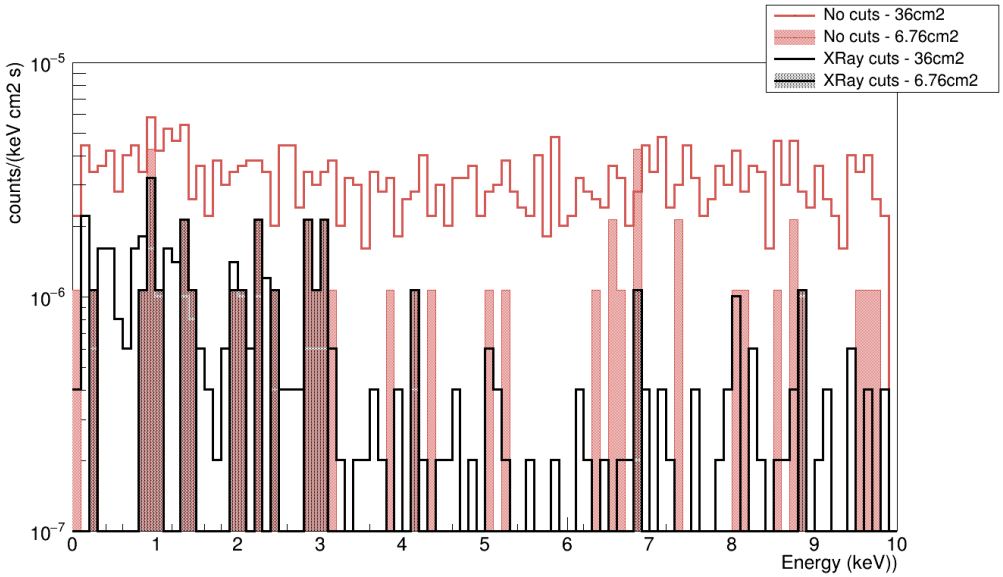

Figure 7.31: Background contribution from cosmic neutrons in the IAXO energy RoI. Raw background before the discrimination cuts are represented in red and background after the discrimination process is represented in black. Lines represent background levels considering all the readout and filled areas represent background levels considering only a central area. The vetoes rejection is not considered in this plot.

Finally, figure 7.31 shows the total background contribution after all the previous considerations for the IAXO energy RoI before (red) and after (black) the discrimination cuts, and for the total readout area (lines) and a reduced and central area (filled bars). In all the cases the background is homogeneously distributed in the energy RoI and it could be claimed that after the cuts, the background is reduced more efficiently for energies higher than $\sim$3 keV. More statistics would be desirable in order to fully understand if the cuts effectively reduce the events in any particular energy range.

With these considerations, the contribution to the IAXO-D0 background from events produced by cosmic neutrons after the discrimination process will be $(5.5 \pm 1.2) \times 10^{-7}$ counts keV^{-1} cm^{-2} s^{-1}, including the rejection from a 4π veto coverage. This contribution is comparable with the background produced by cosmic muons, which indicates that maybe the background typically attributed only to muons in the CAST-Micromegas context was actually a combination of both. The fact that neutrons also leaves energy in the vetoes reinforces this hypothesis and the need of further study of this particular background source.

Radioactivity from the detector components and shielding

The radiopurity of the materials is a key point to obtain a very low background detector, and even though all the materials used in the IAXO-D0 detector have been measured and are very radiopure, there is always room for improvement to low the background even more from this perspective. A big effort was made in order to simulate each contribution

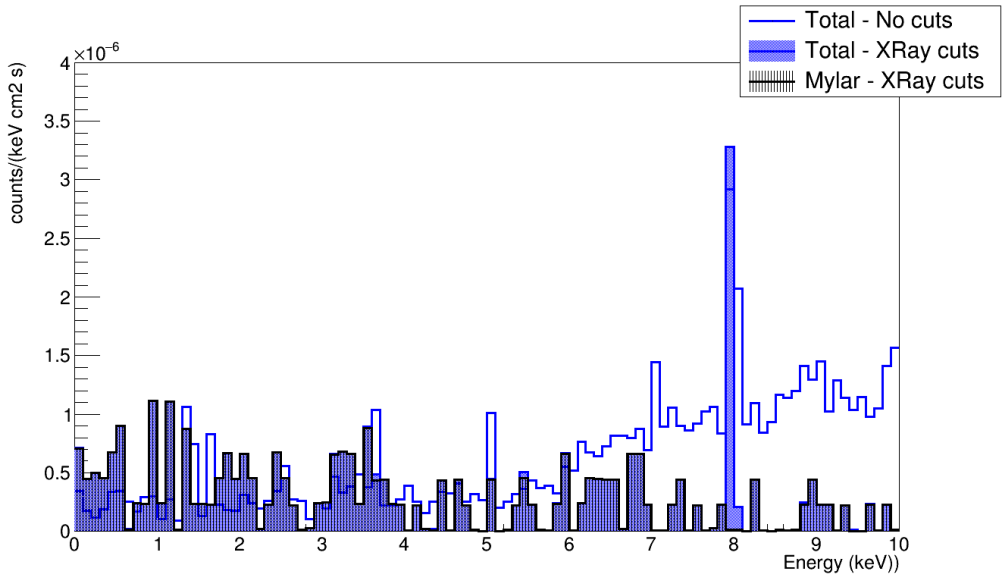

Figure 7.32: Background contribution from radioactivity of the detector and shielding materials in the energy RoI. The blue line represents the raw background before the discrimination cuts for all the readout area, and the blue filled histogram represents the background after the discrimination process and in the central area (6.76 cm^2). The black histogram represents the background after the discrimination process and in the central area (6.76 cm^2) of the Mylar window specifically.

of each relevant measured contamination from every volume of the geometry [227].

Large equivalent times were simulated for almost all the isotopes, with some exceptions due to the heavy computational weight, as it can be the ^{210}Pb from the lead shielding. Table 7.9 shows the activity, equivalent time and background before and after applying the discrimination cuts for each isotope of each detector part.

The combination of all these contributions result in the background spectra shown in figure 7.32. They are represented the raw background before the discrimination cuts, considering all the readout area, and the background after the discrimination process, considering only the central area. A reduction of background is observed mostly in the [5,10] keV region, with the exception of the 8 keV peak from the copper fluorescence. This peak in the final spectrum is mainly due to the shielding radiation, specifically from the ^{210}Pb component. Also, the Mylar window contribution to the background is shown, which seems to dominate the remaining background after the discrimination cuts.

Table 7.10 shows the contribution to the background from the most relevant isotopes and volumes. Almost ∼60% of the total background seem to come from the ^{238}U isotope radiation, mainly from the Mylar window and the Micromegas readout. It is shown also that the cosmogenic ^{60}Co produced in the copper parts of the detector is not a principal source of background of the IAXO-D0 detector.

These results, however, need some further discussion. Regarding the detector parts, the component that seem to contribute the most to the background is the Mylar

Detector part	Isotope	Activity (Bq/kg or Bq/m^2 (†))	Equivalent time (years)	Background before cuts (counts keV^{-1} cm^{-2} s^{-1})	Background after cuts (counts keV^{-1} cm^{-2} s^{-1})
Lead shielding	^{238}U	$< 3.30 \times 10^{-4}$	125.45	$< 8.71 \times 10^{-10}$	$< 5.61 \times 10^{11}$
	^{232}Th	$< 1.00 \times 10^{-4}$	224.24	$< 4.47 \times 10^{-10}$	$< 2.09 \times 10^{-11}$
	^{40}K	$< 1.20 \times 10^{-3}$	140.87	$< 7.60 \times 10^{-10}$	$< 4.66 \times 10^{-11}$
	^{210}Pb	< 80	0.01	$< 4.77 \times 10^{-8}$	$< 1.63 \times 10^{-7}$*
Copper chamber top flange	^{238}U	$< 6.20 \times 10^{-5}$	3050.46	$< 3.77 \times 10^{-11}$	$< 3.23 \times 10^{-12}$
	^{232}Th	$< 2.00 \times 10^{-5}$	9006.11	$< 1.81 \times 10^{-11}$	$< 1.30 \times 10^{-12}$
	^{60}Co	5.25×10^{-4}	342.86	$(4.86 \pm 0.11) \times 10^{-10}$	$(2.33 \pm 0.56) \times 10^{-11}$
Copper chamber	^{238}U	$< 6.20 \times 10^{-5}$	644.63	$< 1.25 \times 10^{-10}$	$< 1.75 \times 10^{-11}$
	^{232}Th	$< 2.00 \times 10^{-5}$	1427.39	$< 5.47 \times 10^{-11}$	$< 5.59 \times 10^{-12}$
	^{60}Co	5.25×10^{-4}	108.68	$(1.42 \pm 0.03) \times 10^{-9}$	$(1.08 \pm 0.22) \times 10^{-10}$
Copper pipe	^{238}U	$< 6.20 \times 10^{-5}$	4089.12	$< 2.93 \times 10^{-11}$	$< 3.56 \times 10^{-12}$
	^{232}Th	$< 2.00 \times 10^{-5}$	10726.08	$< 1.52 \times 10^{-11}$	$< 1.57 \times 10^{-12}$
	^{60}Co	4.59×10^{-4}	425.21	$(3.38 \pm 0.08) \times 10^{-10}$	$(2.98 \pm 0.57) \times 10^{-11}$
Copper strongback pattern	^{238}U	$< 6.20 \times 10^{-5}$	5539.75	$< 4.10 \times 10^{-11}$	$< 6.44 \times 10^{-12}$
	^{232}Th	$< 2.00 \times 10^{-5}$	34346.42	$< 7.78 \times 10^{-12}$	$< 1.80 \times 10^{-12}$
	^{60}Co	5.25×10^{-4}	6537.82	$(3.61 \pm 0.07) \times 10^{-11}$	$< (5.52 \pm 0.63) \times 10^{-12}$
Copper cathode	^{238}U	$< 6.20 \times 10^{-5}$	349.58	$< 4.28 \times 10^{-10}$	$< 8.05 \times 10^{-12}$
	^{232}Th	$< 2.00 \times 10^{-5}$	1806.17	$< 9.96 \times 10^{-11}$	$< 2.34 \times 10^{-12}$
	^{60}Co	5.25×10^{-4}	137.52	$(1.13 \pm 0.03) \times 10^{-9}$	$(3.07 \pm 1.02) \times 10^{-11}$
Copper raquette	^{238}U	$< 1.20 \times 10^{-5}$	4574.70	$< 5.52 \times 10^{-11}$	$< 2.05 \times 10^{-12}$
	^{232}Th	$< 4.10 \times 10^{-6}$	8703.09	$< 1.45 \times 10^{-11}$	$< 5.39 \times 10^{-13}$
	^{40}K	6.10×10^{-5}	2699.82	$(5.57 \pm 0.13) \times 10^{-11}$	$(6.95 \pm 3.47) \times 10^{-13}$
	^{60}Co	4.82×10^{-4}	156.65	$(8.47 \pm 0.22) \times 10^{-10}$	$(2.40 \pm 0.85) \times 10^{-11}$
MM readout (†)	^{238}U	$(2.60 \pm 1.4) \times 10^{-1}$	16.94	$(1.87 \pm 0.03) \times 10^{-8}$	$(7.75 \pm 1.47) \times 10^{-10}$
	^{232}Th	$< 9.30 \times 10^{-2}$	56.83	$< 4.17 \times 10^{-9}$	$< 3.38 \times 10^{-10}$
	^{40}K	$(5.70 \pm 2.5) \times 10^{-1}$	185.44	$(1.28 \pm 0.02) \times 10^{-9}$	$(7.59 \pm 1.39) \times 10^{-11}$
	^{60}Co	$< 3.10 \times 10^{-2}$	284.14	$< 8.72 \times 10^{-10}$	$< 1.16 \times 10^{-11}$
Kapton from MM readout (†)	^{238}U	$< 1.10 \times 10^{-1}$	1.00	$< 1.58 \times 10^{-7}$	$< 2.36 \times 10^{-9}$
	^{232}Th	$< 4.60 \times 10^{-2}$	3.81	$< 3.48 \times 10^{-8}$	$< 7.39 \times 10^{-10}$
	^{40}K	$< 7.70 \times 10^{-2}$	6.83	$< 2.58 \times 10^{-8}$	$< 2.75 \times 10^{-10}$
PTFE chamber inner cover	^{238}U	$< 6.20 \times 10^{-5}$	260.09	$< 3.60 \times 10^{-10}$	$< 1.94 \times 10^{-11}$
	^{232}Th	$< 4.10 \times 10^{-5}$	634.36	$< 1.49 \times 10^{-10}$	$< 1.04 \times 10^{-11}$
PTFE cathode inner cover	^{238}U	$< 6.20 \times 10^{-5}$	12672.97	$< 1.73 \times 10^{-11}$	$< 3.74 \times 10^{-12}$
	^{232}Th	$< 4.10 \times 10^{-5}$	22996.80	$< 9.35 \times 10^{-12}$	$< 3.04 \times 10^{-12}$
PTFE pipe inner cover	^{238}U	$< 6.20 \times 10^{-5}$	50454.25	$< 4.95 \times 10^{-12}$	$< 6.32 \times 10^{-13}$
	^{232}Th	$< 4.10 \times 10^{-5}$	105967.59	$< 2.32 \times 10^{-12}$	$< 5.36 \times 10^{-13}$
Mylar (†)	^{238}U	$< 2.90 \times 10^{-1}$	0.22	$< 3.22 \times 10^{-7}$	$< 2.69 \times 10^{-7}$
	^{232}Th	$< 8.00 \times 10^{-3}$	11.78	$< 5.65 \times 10^{-9}$	$< 7.73 \times 10^{-9}$
	^{40}K	$< 3.30 \times 10^{-2}$	27.19	$< 6.98 \times 10^{-9}$	$< 8.80 \times 10^{-10}$
	^{60}Co	$< 1.80 \times 10^{-3}$	249.22	$< 1.87 \times 10^{-9}$	$< 4.78 \times 10^{-9}$

Table 7.9: Background values and upper limits from the individual measured isotopes from each IAXO-D0 detector volume in the [0,10] keV energy range [227]. Background before cuts column show raw background values considering all the readout surface. Background after cuts column show the background values after the x-ray and fiducial cuts were applied, considering the central surface of 6.76 cm^2. Upper limits are given for those cases where the activity measurement is an upper limit. ^{60}Co activity from cosmogenic activation in the copper parts is estimated using equation 7.3.6. (∗) 95% C.L. (†) means that the activity of the contaminants is given in Bq/m^2 units.

Source	Background contribution (counts $\mathrm{keV}^{-1}\,\mathrm{cm}^{-2}\,\mathrm{s}^{-1}$)	% of the total radioactivity backround
Total ^{238}U	$< 2.72 \times 10^{-7}$	59.65
Shielding ^{210}Pb	$< 1.63 \times 10^{-7}$ *	35.84
Total ^{232}Th	$< 8.85 \times 10^{-9}$	1.94
Total ^{40}K	$< 1.00 \times 10^{-9}$	0.22
Copper cosmogenic ^{60}Co	$(2.33 \pm 0.27) \times 10^{-10}$	0.05
Mylar window	$< 2.87 \times 10^{-7}$	63.06
Micromegas readout	$< 4.57 \times 10^{-9}$	1.00
Chamber (without Mylar)	$< 2.78 \times 10^{-10}$	0.06
Total	$< 4.56 \times 10^{-7}$	
Total (measurements)	$(1.07 \pm 0.15) \times 10^{-9}$	

Table 7.10: Background levels after cuts (both x-ray and 2D fiducial) from different isotopes or detector parts, and their contribution to the total background from materials intrinsic radioactivity. Two values of total background are given: the sum of all contributions, regardless they are upper limits, and the addition of those contributions that come from precise measurements. (*) 95% C.L..

window. This is due to the fact that the Mylar foil used for the x-ray windows is extremely thin, so the samples that were measured to obtain the upper limits for the radioactive contaminants had a very small mass. These measurements were made with a ∼1 kg germanium gamma-ray ultra-low background detector of the University of Zaragoza operated underground at the LSC (see table 5.2), and only rather high upper limits could be obtained with samples with such a small mass. But there are no clear evidence that the real radioactive rates of this material are close to these upper limits. Therefore, the background contribution from the Mylar window can just be considered an upper limit, and other methods to measure the radioactive rates of this material need to be explored, or alternatively, to more massive samples need to be measured.

Also, from the analysis point of view, the discrimination cuts will be less efficient for the window emission due to its positioning. The window is placed at the cathode of the detector, so the gamma emission from this source will interact at the top of the gas volume and will be diffused in the same way as the x-rays that enters the chamber from the pipe.

The other apparently relevant contribution is the radiation from the lead shielding, more specifically, the radiation from the ^{210}Pb isotope. However, this contribution was very heavy computationally and even though a big amount of simulations have been performed ($\sim 5 \times 10^9$ events, which correspond to more than 1000 real hours of computation) only an equivalent time of ∼5 days has been obtained. And during this time, only 85 events have been registered, and none of them survived the discrimination cuts. This is why the contribution corresponds to the 95% CL for a Poisson distribution. Therefore, this result can only be considered an upper limit, and more statistics will be needed to prove this value. Further optimization of the simulations will probably be needed to fully understand this background source.

Area (cm^2)	Background before cuts (counts $keV^{-1}\,cm^{-2}\,s^{-1}$)	Background after cuts (counts $keV^{-1}\,cm^{-2}\,s^{-1}$)	Cuts efficiency (%)
36	$(1.709 \pm 0.001) \times 10^{-7}$	$(1.84 \pm 0.03) \times 10^{-8}$	89.2
6.76	$(6.8 \pm 0.1) \times 10^{-8}$	$(1.03 \pm 0.05) \times 10^{-8}$	84.8

Table 7.11: Background level in the [0,10] keV energy range from the ^{39}Ar natural radiation before and after the discrimination cuts considering different centred readout areas. 36 cm^2 corresponds to the complete readout and 6,76 cm^2 is the area from the x-ray characterization. The efficiency of the cuts in each case is also shown.

On the other hand, a significant result from this study is the background contribution from the Micromegas readout. The radioactivity rates from this component have been accurately measured, and the resulting background is almost two orders of magnitude lower than the IAXO requirements (i.e $\sim 10^{-7}$ counts $keV^{-1}\,cm^{-2}\,s^{-1}$). Also, the contamination from the chamber, taking into account the copper and the teflon parts, is well below this requirement.

Contamination from the gas: ^{39}Ar isotope

The last important background contribution to study is the radiation from the gas itself. Natural argon contains a certain amount of ^{39}Ar, which β^- decays producing an electron, that will consequently drift and produce a detectable signal. The activity of this isotope in natural argon gas is $1.01 + 0.02(stat) \pm 0.08(syst)$ Bq kg^{-1} [210].

The levels of background obtained from the ^{39}Ar of the IAXO-D0 gas are shown in table 7.11, where both values before and after the discrimination cuts are presented, as well as the efficiency of the cuts. The discrimination process resulted in a reduction of a ∼89% of the background for the entire detector readout surface, and a ∼85% for the central area. On the other hand, the fiducial cut is also efficient, reducing the background level in a factor of ∼2.5 in all the surface and a factor of ∼1.8 in the central area. Figure 7.33 shows the hitmap of the events in the [0,10] keV range produced by ^{39}Ar radiation before (left) and after (right) the cuts. In both cases, the events tend to cumulate at the borders of the readout, probably due to the fact that the gas chamber is cylindrical and the readout is square-shaped, so some incomplete events can be detected at the borders of the readout plane.

Finally, figure 7.34 shows the background contribution from the ^{39}Ar isotope for the IAXO energy RoI. The contributions after and before the cuts are shown, considering all the readout (36 cm^2) and a central smaller area (6.76 cm^2). Both the discrimination cuts and the fiducial cut have been very effective reducing this background, probably due to the fact that the energy deposits from this source are more extensive and not as symmetric than the ones produced by x-rays. Also, since most of the events spread across the full gas volume, they reach the readout borders, and the fiducial cut is able to reject them.

With all these considerations, the resulting contribution of the ^{39}Ar isotope from

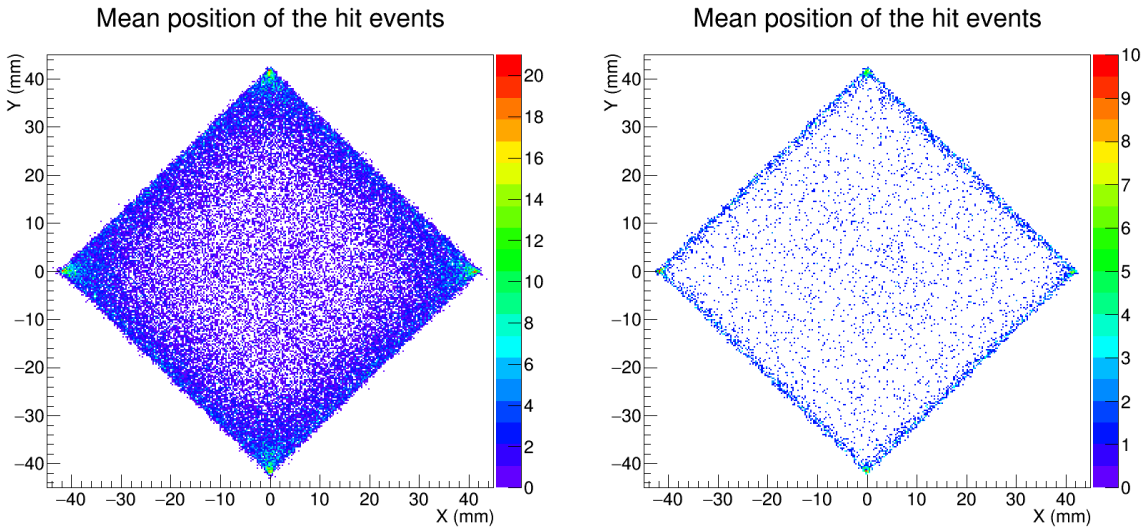

Figure 7.33: Mean position (weighted by the energy) of the hit events produced by the ^{39}Ar radioactivity in the [0,10] keV range before **(left)** and after **(right)** the background discrimination cuts are applied.

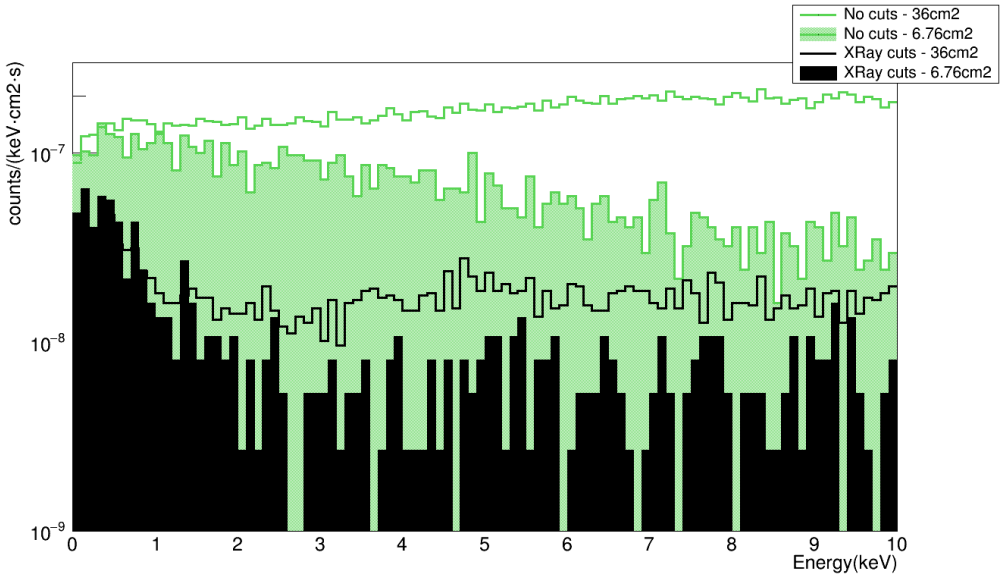

Figure 7.34: Background contribution from the ^{39}Ar isotope of the target gas in the IAXO energy RoI. Raw background before the discrimination cuts are represented in green and background after the discrimination process is represented in black. Lines represent background levels considering all the readout (36 cm^2) and filled areas represent background levels considering only a central area (6.76 cm^2).

the gas in the IAXO energy RoI is $(1.03 \pm 0.05) \times 10^{-8}$ counts keV^{-1} cm^{-2} s^{-1}. This value is five times lower than the estimations that were made previously for the CAST-Micromegas detectors [14], and it does not represent a principal contribution to the total IAXO-D0 background. Regardless, new approaches with Xe based mixtures are being explored to avoid this contribution.

7.5 Summary

One of the main requirements for the proposed x-ray detectors for IAXO is that they need to have very minimal levels of intrinsic radioactive background, and also, they need to implement techniques to reduce the external contributions. Therefore, a deep understanding of the radioactive background is required, so the simulation of a background model for the IAXO detectors is well motivated.

In this work, the background model of the IAXO-D0 prototype has been computed. REST software has been used both for the simulations and the analysis. REST is a very complete and modular framework based on C++/root with tools for acquisition, storage, and analysis of both simulated or experimental data from gaseous TPCs, allowing a direct comparison between them. This framework provides classes to store information for every possible representation of a TPC event, TRestEvents, that can be accessed and transformed by TRestProcesses. These TRestProcesses are able to obtain physical information from the TRestEvents, the observables, and store them inside the data structure of the TRestEvent itself. Also, metadata is stored to keep additional relevant information of the TRestEvents.

REST also provides tools for implementing a GDML geometry for simulation purposes. This has been used to define the IAXO-D0 prototype geometry with a good level of detail. The copper chamber, the Micromegas readout with its copper base, the cathode with the x-ray window, the pipe, all the inner Teflon covers and also passive lead shielding and a full 4π active cosmic veto coverage have been implemented.

Simulations of every single known source that may affect the background of the IAXO detectors have been carried out using the GEANT4 simulation toolkit that is integrated in the REST framework. These simulations have included cosmic muons, cosmic gammas of different energy ranges, cosmic neutrons, external gammas from the radioactivity of the walls, the radioactivity of the different materials of the detector and shielding, the neutrons produced in radioactivity fission reactions and finally, the possible ^{39}Ar contamination of the target gas.

All these contributions have gone through a REST analysis in order to obtain useful observables. The analysis steps have consisted on transforming the TRestG4Events from the GEANT4 simulations to TRestHitsEvents, that contain information about the position and energy of every event, by a TRestG4ToHitsProcess. Then, TRestHitsEvents have been transformed on TRestTrackEvents by a TRestHitsToTrackProcess. A track

is defined by a group of hits that are closer to each other than a certain distance. Along this process, observables have been computed for every event type by the TRestG4AnalysisProcess, TRestHitsAnalysisProcess and TRestTrackAnalysisProcess.

Also, an x-ray simulation in the IAXO RoI, [0,10] keV, has been carried out in order to obtain an x-ray characterization via their REST observables and define the selection criteria. From this study, it has been seen that events produced by an x-ray interaction have mostly one-single track, the energy deposit is rather small ($\sigma_{xy}^2 \lesssim 2.6\,\mathrm{mm}^2$, $sigma_z^2 \lesssim 0.55\,\mathrm{mm}^2$), and symmetric ($Balance_{\sigma_x\sigma_y} \sim 0$, $\gamma_{xy} \sim 0$, $\gamma_z \sim 0$) and they mostly hit at the center of the readout. An observable is also defined to register the distance from the TRestHitsEvents to the edge of the readout, *distance to wall*, in order to apply 2D spatial cuts on the readout surface.

Finally, the discrimination cuts have been applied to the individual background sources and the final background contributions have been computed, normalized to the standard counts keV^{-1} cm^{-2} s^{-1} background units. From this work, a final background level of $(2.13 \pm 0.17) \times 10^{-6}$ counts keV^{-1} cm^{-2} s^{-1} has been obtained for the IAXO-D0 prototype, that can be reduced to $(1.51 \pm 0.12) \times 10^{-6}$ counts keV^{-1} cm^{-2} s^{-1} if the information from the 4π cosmic veto coverage is taken into account.

As expected, the cosmic contribution to the background is dominant with $< 1.62 \times 10^{-6}$ counts keV^{-1} cm^{-2} s^{-1}, that can be reduced to $< 1.00 \times 10^{-6}$ counts keV^{-1} cm^{-2} s^{-1} if the information from the cosmic vetoes is considered. From this work it has been proven that this contribution does not only come from cosmic muons as it was previously thought, but also from cosmic neutrons. Another interesting result is that a 4π veto coverage is able to identify the $\sim 100\%$ of the cosmic muons that interact in the detector and also, the $\sim 67\%$ of the cosmic neutrons.

An upper limit has been estimated for the radioactivity contribution of the external and internal sources, $< 5.11 \times 10^{-7}$ counts keV^{-1} cm^{-2} s^{-1}. However, this limit is dominated by the radioactivity from the Mylar window, whose radioactive rates are not accurately measured, and from the radioactivity of the lead shielding, that has a big statistical error due to its heavy computational weight. A further study of this limit should potentially reduce the radioactivity contribution to the total IAXO-D0 background. On the other hand, the Micromegas readout contribution has resulted to be $< 4.57 \times 10^{-9}$ counts keV^{-1} cm^{-2} s^{-1}, which is well below the IAXO background needs, and also, it has been proven that the cosmogenic activation of the copper parts of the detector should not be a concern for the IAXO background. Finally, the contamination from the argon gas has turned out not as problematic as expected, only contributing as $(1.03 \pm 0.05) \times 10^{-8}$ counts keV^{-1} cm^{-2} s^{-1}.

Overall, this IAXO-D0 background model has shown that the Micromegas x-ray detectors designed for IAXO should be able to reach the desired background for the IAXO needs. Also, this background model sets a base for the next part of this work, which is the experimental measurement of the IAXO-D0 background prototype.

CHAPTER 8

IAXO-D0 ultra-low background prototype

Contents

8.1 Introduction

One of the goals in the IAXO experiment agenda has been the commissioning of an ultra-low background Micromegas detector prototype with the same design as the IAXO pathfinder in CAST (section 5.4.2) with all the upgrades and shielding improvements developed so far, but without the space limitations that the system in CAST used to have. This has been the principal motivation to build the IAXO-D0 prototype at the University of Zaragoza.

In this chapter, the experimental setup of the IAXO-D0 prototype and the Micromegas detector will be described, and the results of the characterization of the Micromegas detector will be presented.

8.2 Experimental setup

The experimental setup of IAXO-D0 is the last step from the design of the IAXO pathfinder where all the low background improvements learnt from the data taking

campaings at CAST and the benchmarks at the University of Zaragoza have been implemented. It can be divided into five parts: the chamber and its internal elements, the vacuum pipe and the calibration system, the gas system, the acquisition system with the new electronic cards based on AGET chips and finally the passive shielding.

The first and main objective of this prototype has been to test the performance of the improved design of the detector and the shielding in order to achieve the background level required for the IAXO and BabyIAXO experiments.

Further phases are planned for IAXO-D0 in order to study and fully test the detector performance and capabilities, such as its operation with other gases, the implementation of cosmic muon vetos and the study of the possible background dependence with the magnet movement.

(a)

(b)

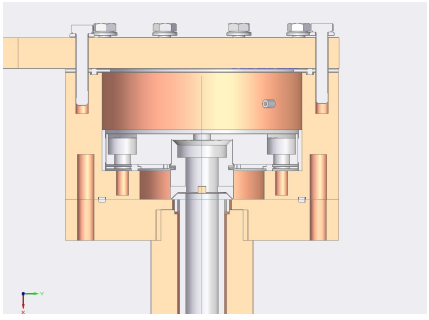

(c)

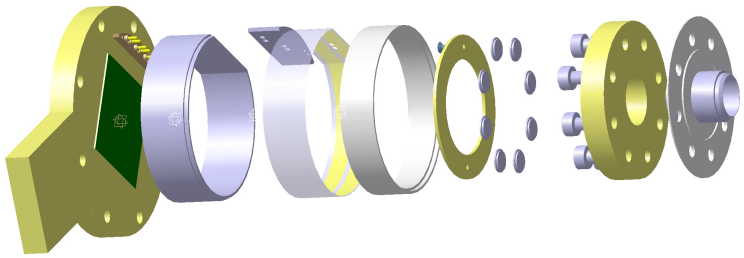

(d)

Figure 8.1: Pictures of (a) the built detector and (b) the detector pieces. (c) Scheme of the chamber. (d) Extruded scheme of the detector.

8.2.1 Chamber and internal components

The gas chamber consist of a cylindrical piece of 18 mm thick radiopure copper. One of the sides is closed by a 20 mm thick copper raquette where the readout is attached. This raquette provides a long enough support to route all the high-voltage and and the data paths out of the shielding, as shown in figure 8.1.

In the inner side of the chamber, a field shaper is used in order to create a homogeneous drift field and reduce border effects. It is printed on a flexible and radiopure multilayer circuit with polymide substrate. This circuit contains two 10 mm thick tracks that emulate the the typical conductor rings. The outer part of this circuit is used to bring the high-voltage connections from the detector board to the drift tracks and the cathode. This field shaper is coated by a 3 mm thick PTFE foil that acts as the inner shielding, preventing this way the possible fluorescence from the tracks without disturbing the electric field.

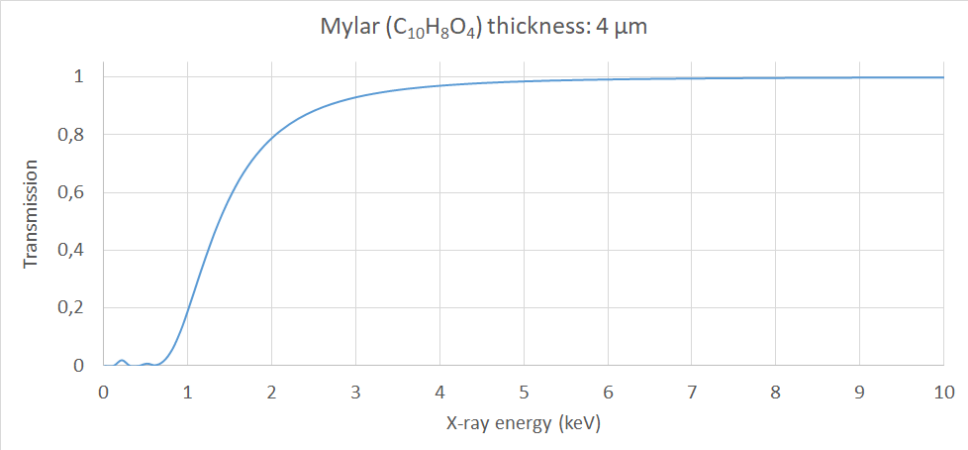

Figure 8.2: X-ray transmission of a Mylar foil of 4 μm thick [232] for the IAXO RoI.

The other side of the chamber is closed by the strongback with a spider-web design for the window support. This design was implemented taking advantage of the x-ray focusing telescope, allowing a smaller x-ray window that minimizes the strongback grid at the aperture surface. The x-ray window is a 4 μm aluminized mylar foil glued to the copper frame. The aluminized mylar is a radiopure material that is able to withstand the pressure difference between the gas volume inside the chamber and the vacuum pipe outside (with a leak rate $< 10^{-4}\,\mathrm{mb\,l\,s^{-1}}$) while being highly transparent to x-rays, as shown in figure 8.2. Also, on the inner part of the strongback, a copper ring is attached to act as the drift cathode.

The chamber has two gas ports that allow the operation of the detector in gas circulation mode. The overpressure guarantees a large quantum efficiency for x-rays in the energy range of interest. All the joints are gas-tight and the gaskets and o-rings used are made out of PTFE. Finally, the screws are made out of copper in order to remove possible radioactive contamination close to the chamber.

8.2.2 Calibration and vacuum system

Since this prototype aims to emulate the same working conditions, a detector of this characteristics would have in IAXO or BabyIAXO, the copper pipe that is meant to attach the x-ray telescope to the detector is also included in the design. This pipe is needed because of the external shielding that covers the detector (further described later in this section). It is a 30 cm long radiopure copper (Cu-ETP) pipe with a minimum wall thickness of 13 mm and an inner hole diameter of 24 mm. In order to replicate the running conditions of previous CAST-Micromegas setups, a turbo pump station (Pfeiffer Hi Cube 80) generates the needed vacuum ($< 10^{-4}$ mbar).

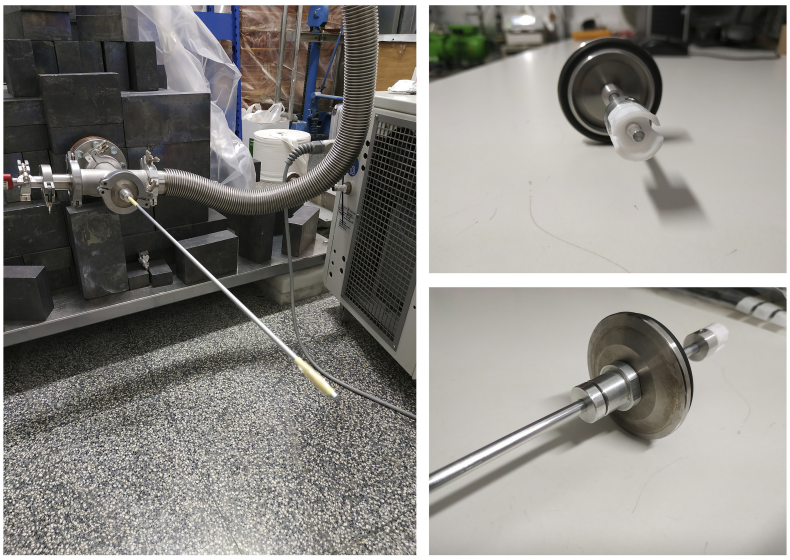

Figure 8.3: (Left) Calibrator attached to the exterior of the vacuum pipe. **(Right)** Frontal view of the ^{109}Cd source and the source holder, the vacuum tight o-ring and the back locking to tighten the source in place.

This new and narrower pipe, while reducing the radioactive background, brought a problem for the calibration system: the typical source used to calibrate these type of detectors has always been ^{55}Fe because of its main emission line at 5.9 keV. However, the available commercial ^{55}Fe calibration sources cannot be used because their diameter is larger than the internal pipe diameter. Thus, a ^{109}Cd source has had to be considered for the calibration runs. This isotope is commercially encapsulated in a smaller aluminium case, and therefore allowed designing a calibration system that brings the source through the pipe closer to the chamber Mylar window when needed. The main emissions from this source are summarized in table 6.1. We expect an energy spectra with a double peak at 19-22 keV and another peak at 8 keV due to the copper fluorescence.

The design of this calibration system is shown in figure 8.3. It is a vacuum tight assembly bolted to the copper pipe DN63 CF (ConFlat) flange located out of the Lead shielding. The source is placed in a PTFE source-holder at the end of an aluminium rod. This rod allows the movement of the source inside the pipe all the way to the detector Mylar window. When the calibration is finished, the source can be brought back to the

parking position and shielded thanks to a 3 mm thick aluminium plate to avoid undesired source contamination in the background data.

8.2.3 Gas system

A new gas system has been designed specifically for IAXO-D0 in order to allow a proper functioning with both Argon and Xenon. The conceptual design of the gas system is shown in figure 8.4. This design fulfils the requirements of all the possible scenarios: gas injection, open loop gas circulation, recirculation and recovery, vacuum cleaning and leak detection.

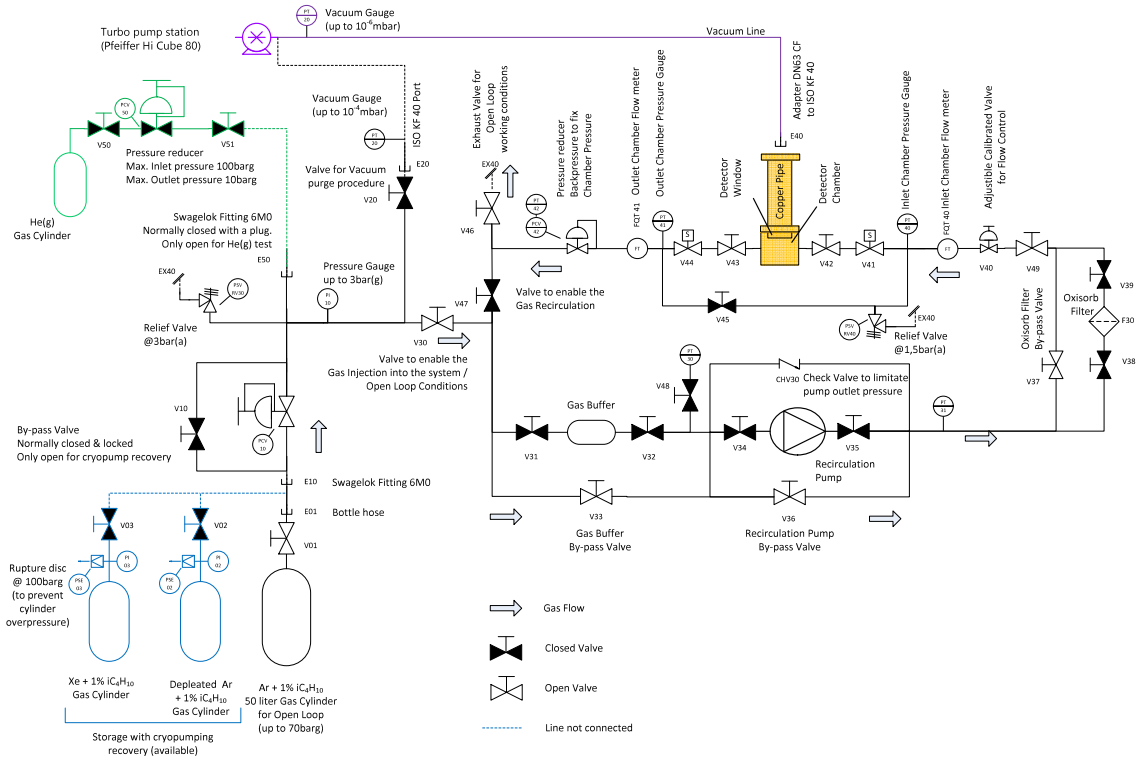

Figure 8.4: Comprehensive scheme of the IAXO-D0 gas system. This design allows gas injection, open loop gas circulation, recirculation and recovery, vacuum cleaning and leak detections.

The gas bottle is connected to the system with a relief valve to prevent any overpressure above 3 bar. Then, three valves are prepared for different procedures: a vacuum valve for the vacuum purging procedure, an inlet valve for the injection of helium for the gas leak detection procedure and an inlet port for the open loop gas circulation.

The next valve allows the gas injection to the system as well as the open loop circulation. Then, another valve sets the mode of the gas circulation: open loop or recirculation. If this valve is open for recirculation, the direction of the flow is marked by

a pressure controller/pressure transmiter valve (a Bronkhorst back-pressure) that stops the gas to pass through it. There is a gas buffer with a volume equal to the total volume of the total system that helps regulating the pressure, and it can be bypassed. If we are in recirculation mode, the gas then goes through a pump that keeps the flow at a constant rate. If we are in open loop circulation, the pump can be bypassed as well. Then, an Oxisorb filter is installed in order to clean the oxygen contamination of the gas in case of out-gassing when it is in recirculation mode. If we are in open loop circulation, this filter can be bypassed. Then, a calibrated valve controls the input gas flow of the chamber. A flowmeter and a manometer are installed both at the inlet and outlet ports of the detector chamber. A combination of a manual valve and an electro-valve controls the entrance of the gas inside the chamber. The detector can also be bypassed for cleaning and leak detection procedures. A relief valve prevents the chamber to reach pressures higher than 1.5 bar, which is important because the window could break. The pressure of the chamber is set with the back-pressure. Finally, an exhaust valve allows the exit of the gas from the system in open loop circulation.

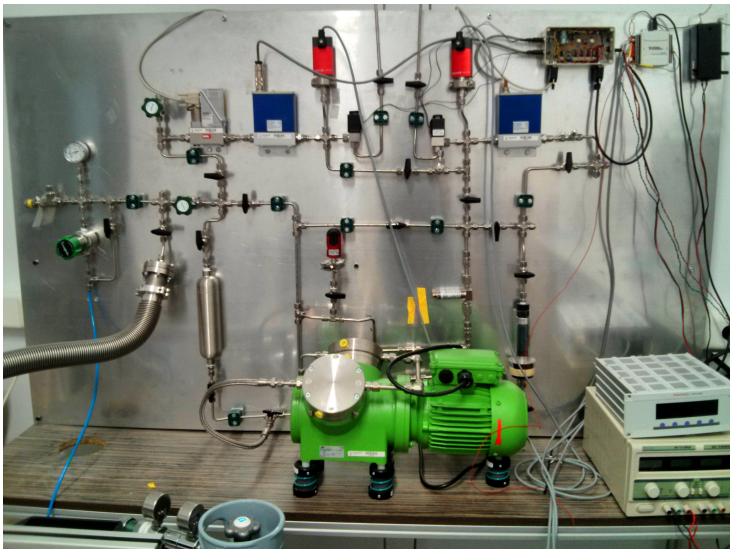

Figure 8.5: Picture of the fully operative IAXO-D0 gas system at the laboratory in the University of Zaragoza.

One of the main focuses has been to grant the gas purity and the absence of leaks. For these purposes, the system is prepared to perform vacuum cleaning before injecting the corresponding gases. Also, the exhaust, inlet and electro-valves have a $> 10^{-8}\,\mathrm{mbar\,l\,s^{-1}}$ leak rate. The ball valves for bypass and block purposes have a $< 10^{-3}\,\mathrm{mbar\,l\,s^{-1}}$ leak rate. Finally, the system allows the recovery of the gas by cryopumping.

Finally, the working conditions are controlled to avoid any damage to the detector. The information of the flowmeters, manometers and thermometer of the system is collected thanks to a slow control computer, which also allows to set the pressure of the backpressure and the conditions for the chamber electro-valves to close. It is also considered the suppression of the pressure pulsation generated by the pump by a non-reverse valve at the pump outlet. A picture of the gas system is shown in figure 8.5

During the gas system commissioning, several leak tests both in vacuum and overpressure modes were performed and they were all successfully passed with a $< 10^{-6}\,\mathrm{mbar\,l\,s^{-1}}$ leak rate. In this first stage of IAXO-D0, the system has been used only in open loop circulation, so neither the pump nor the Oxisorb filter were used. During the tests and the data taking, it performed well with very stable pressure and flow.

8.2.4 Electronics and acquisition system

When the primary charges reach the readout plane of the detector, electric signals are induced both on the mesh and the strips. In previous setups, the signal from the mesh was saved and used as the trigger for the acquisition. But in IAXO-D0, the new AGET electronics that acquire the signals from the strips features an auto-trigger functionality, so the signal from the mesh is only used to monitor the acquisition.

Readout electronics

IAXO-D0 prototype implements a new acquisition electronic card with four AGET chips (ASIC For Generic Electronics for TPCs (GET) [181]). They are 64-channel Front-End circuits that perform the detection, amplification and analog storage of the shaped signals from the strips. Figure 8.6 shows an example of a raw x-ray event acquired with the AGET electronic card. This design offers large flexibility with adjustable parameters like the sampling frequency, shaping time, gain and signal polarity. They are based on the AFTER ASIC [214] cards that were used in the last Micromegas setups in CAST, but they present new relevant features such as the auto-trigger functionality for each individual channel or decreased dead times for the measurements.

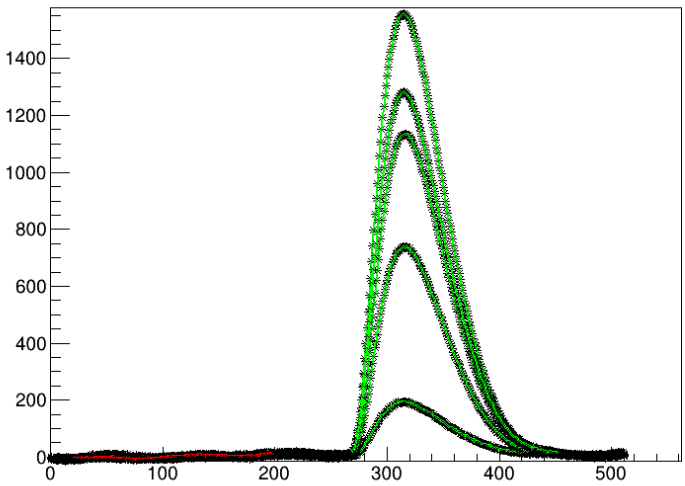

Figure 8.6: Example of a raw x-ray event acquired with the AGET electronic card. The baseline is marked in red and the signal pulses in green.

The concept of the acquisition system is shown in figure 8.7. The signals from the strips are carried to the connector footprint at the end of the raquette. An interface card is connected to the fingerprint by a SAMTEC GFZ connector and distributes the 240 physical channels of the detector in four sets of 60 channels, ending in ERNI connectors. Four ERNI-ERNI flexible cables connect the channels from the interface card to the Front-End card (FEC). The AGET chips are configured with a sampling time of 50 MHz for the 512 samples it takes for each channel, which gives a window of $\sim$10 μs. This temporal window is long enough to fit the maximum pulse duration taking into account the size of the active volume of the detector and the gas conditions.

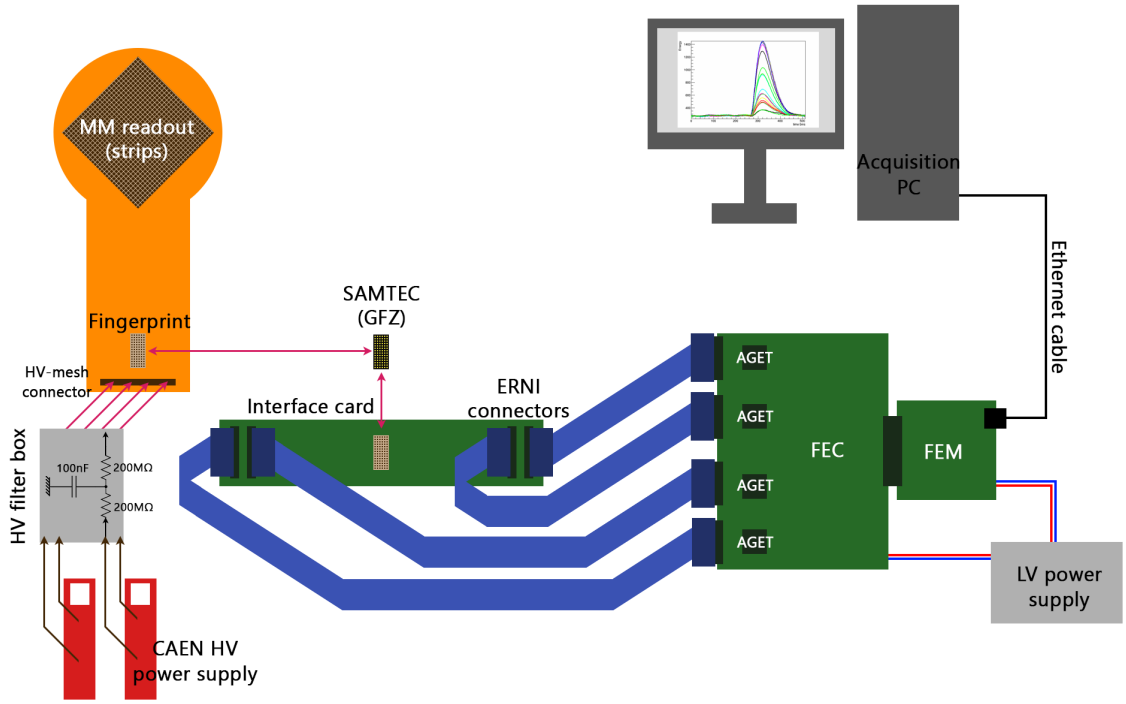

Figure 8.7: Conceptual scheme of the IAXO-D0 acquisition system. The signals from the strips are internally carried to the fingerprint of the raquette that is connected to a interface card via a SAMTEC GFZ connector. The interface card distributes the channels to the four AGET chips of the FEC card. The analogue information is digitalized in the FEM card and is sent to the PC by a Ethernet cable. The FEM and FEC cards are fed by a LV power supply and the detector is fed by a HV CAEN 2-fold power supply (mod. N471A) through a HV filter box.

The architecture of the AGET chip is shown in figure 8.8. Each channel of the AGET integrates a charge sensitive preamplifier (CSA) with adjustable gain, an analogue filter (shaper), a discriminator for multiplicity building and a 512-sample analogue memory based on a Switched Capacitor Array structure (SCA). It is used as a buffer where the analogue signal coming from the shaper is continuously sampled and stored. When the trigger marks the readout phase, the sampler is stopped and the 512 samples of each channel are read back, starting by the oldest sample. The analogue data from all the channels are multiplexed toward a single output to be sent to an external ADC in the FEC for digitalization. On the other hand, the filtered signal is also compared by the discriminator to a programmable threshold value set by a 8-bit DAC. When the signal

crosses the threshold, the discriminator output signal sets the hit channel register to an active level and forms a multiplicity signal with the other 63 discriminator signals.

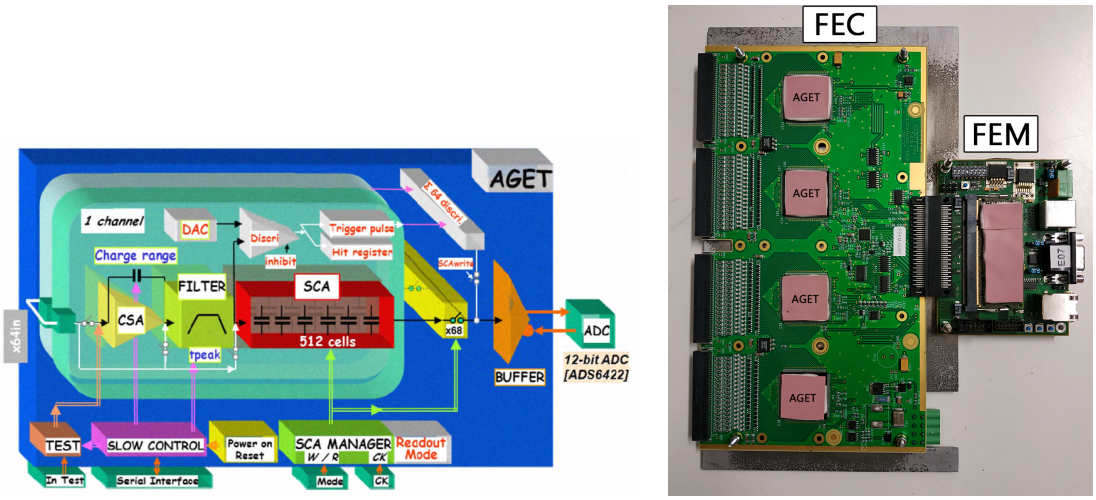

Figure 8.8: (Left) Architecture of the AGET chip [181]. **(Right)** Front-End Card (FEC) with four AGET chips connected to the FEMINOS digital card.

Finally, the ADC data from the FEC is collected by a FEMINOS digital electronic card [233], where a pedestal subtraction is performed and the final digital data is sent to the DAQ computer via Ethernet connection.

All the electronic stages have been grounded carefully. Both the AGET FEC and the FEMINOS as well as the mesh preamplifier are fixed inside a Faraday cage to minimize induced noises. Also, the mesh signal cables and HV cables are wrapped with a grounded metallic mesh to avoid any coupling. Finally, metallic braided cables are used to properly ground every component and to bring the ground inside the HV connection box.

HV connection filter box

To provide the high voltage to the detector parts, a HV-box has been designed to filter the current and reduce the noise. It consists of a plastic box with a copper layer in the inside to act as a Faraday cage. Inside it, RC low-frequency filters are implemented for each of the HV connections. Each RC filter has two resistances of 200 MΩ and a capacitor of 200 nF. It also implements BNC and SHV feedthroughs to assure clean connections. Both the drift and the mesh voltage were applied using a CAEN 2-fold HV power supply. For these first measurements, the field shaper rings were not fed.

Acquisition software

The data acquisition software is based on the software developed at CEA/Saclay for the FEMINOS card, and it is programmed using the REST libraries in order to produce

REST-compatible data files.

It is in an early stage of development, so it does not have any interface or visual control output, but it allows to initialize the electronics, to take pedestal runs and to start the acquisition. Each step uses a configuration file provided by the FEMINOS user's manual [234] where specific parameters can be defined such as the general threshold for the AGET chips, the readout mode, the size or the time of the run taken, etc. These parameters were studied in order to obtain the optimum data taking conditions:

- **SCA write clock:** The SCA write clock sets the SCA data writing frecuency, and translates in what we call the temporal window of the acquisition. By default, the reference clock is 100 MHz, i.e. 10 ns per temporal bin. Taking into account that the AGET chip counts with 512 bins per event, the default temporal window is $\sim$5 μs. The parameter *wck_divisor* is used to set the value of the divisor to set the SCA write clock and therefore, change the size of the temporal window. The SCA write clock is obtained by dividing the 100 MHz reference clock by *wck_divisor*. Valid values for the window clock divisor are [1, 255], leading to discrete frequency values of 100 MHz, 50 MHz, 33 MHz, 25 MHz, etc., down to a minimum sampling frequency of $\sim$392 kHz. In figure 8.9 are shown the pulses of ^{109}Cd calibration events with different window clock divisor values.

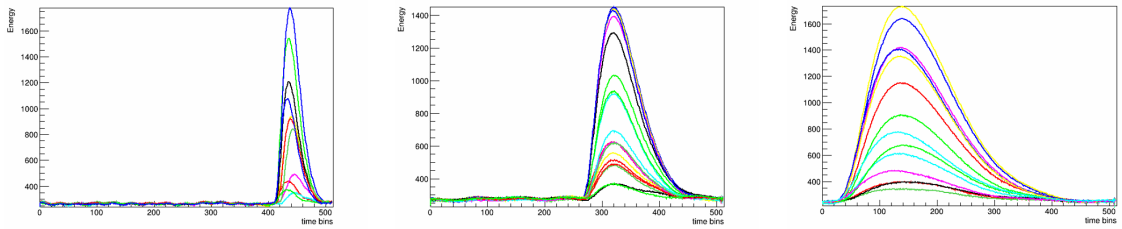

(a) *wck*=0x05 (50 ns/bin) (b) *wck*=0x02 (20 ns/bin) (c) *wck*=0x01 (10 ns/bin)

Figure 8.9: Pulses of ^{109}Cd calibration events with different window clock divisor (*wck*) values. Smaller clock divisor values translates into shorter temporal bins, what makes the pulses wider.

- **Trigger delay:** The *trig_delay* parameter is used to apply a fixed latency to the SCA stop order. The delay is expressed in 10 ns units and is programmable from 0 to 655.36 μs. Modifying this field makes the pulses to start earlier or later in the temporal window, as shown in figure 8.10. The pulses in these examples are placed too close to the end of the window because the tests have been carried out with a too big temporal window ($\sim$25 μs).

- **Gain:** The aget gain parameter sets the gain of the AGET channels, being able to select between 4 options: 120 fC (0x0), 240 fC (0x1), 1 pC (0x2) and 10 pC (0x3). One feature of the AGET chip is that you can set the gain of every channel individually. In our case, all the channels have been set at the same gain. Figure 8.11 shows pulses of ^{109}Cd calibration events with different aget gain parameters.

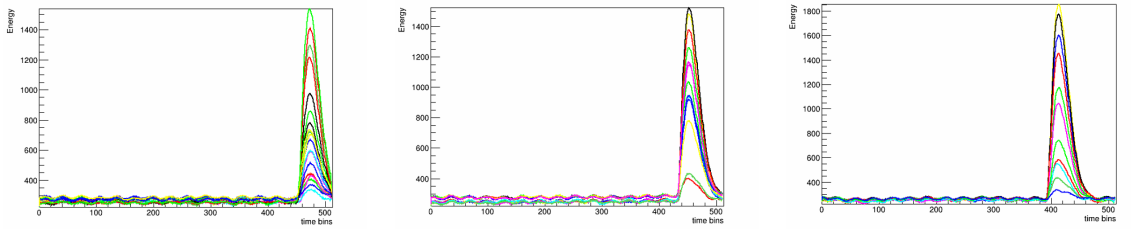

(a) *trig_delay*=0xC8 (2 μs) (b) *trig_delay*=0x12C (3 μs) (c) *trig_delay*=0x1F4 (5 μs)

Figure 8.10: Pulses of ^{109}Cd calibration events with different trigger delay values. Longer trigger delays make the pulse to start earlier at the temporal window.

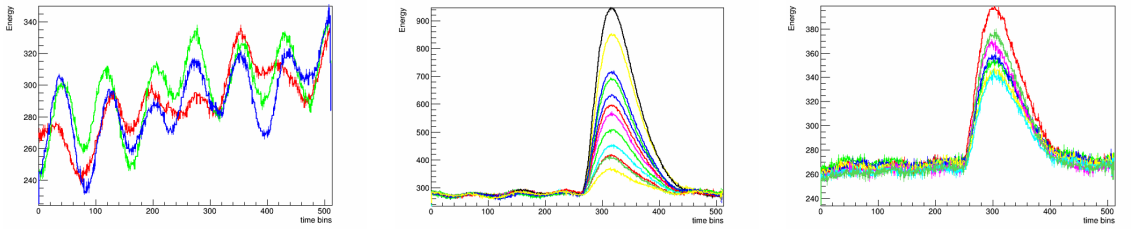

(a) *gain*=0x0 (120 fC) (b) *gain*=0x1 (240 fC) (c) *gain*=0x2 (10 pC)

Figure 8.11: Pulses of ^{109}Cd calibration events with different aget gain values. In the first example, the pulses are too amplified and therefore, noise triggers the acquisition and is kept as valid data.

- **Shaping time:** The *AGET time* parameter sets the period of time where the pulse is shaped along. This parameter has a range between 70 ns (0x0) and 1014 ns (0xF). Long shaping times (longer than the temporal extension of the initial pulse) will integrate the pulse, therefore eliminating the high frequency noise of the pulse. However, this implies a loss of temporal information since the shape of the pulse will be defined by the electronics. On the other hand, very short shaping times will maintain the temporal information, but at the expense of a noise increase and a worse estimation of the height of the pulse (i.e. the energy of the event). Examples of ^{109}Cd calibration events with different shaping times are shown in figure 8.12.

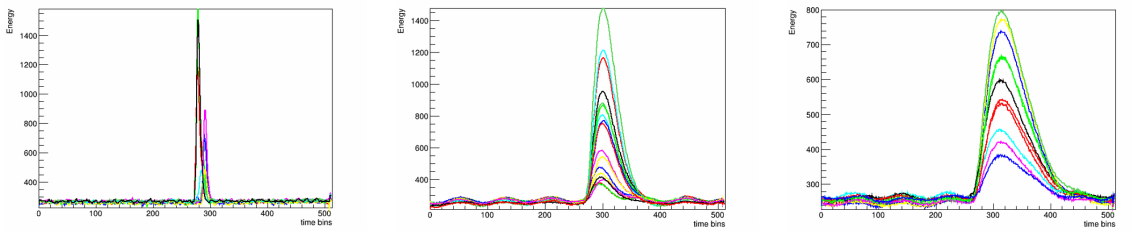

(a) *aget time*=0x0 (70 ns) (b) *aget time*=0x8 (579 ns) (c) *aget time*=0xF (1014 ns)

Figure 8.12: Pulses of ^{109}Cd calibration events with different shaping time values. Too short shaping times make the pulse too narrow and it looses information.

After all the tests, the chosen configuration for the data taking campaign has been a temporal window of $\sim$10 μs with bins of 20 ns (*wck_division* = 0x02); a trigger delay of 4 μs (*trig_delay* = 0x190); a gain of 240 fC (*aget gain* = 0x1) and a shaping time of 1014 ns (*aget time* = 0xF) for the Micromegas characterization and 897 ns (*aget time* = 0xD) for the data taking itself. The criterion followed to select these parameters has been to obtain pulses that are entirely contained in the time window, so no information is lost, while a long enough baseline is conserved in order to compute the energy threshold in the analysis process. An example of a signal event from one of the ^{109}Cd calibrations performed during the data taking campaign is shown in figure 8.13.

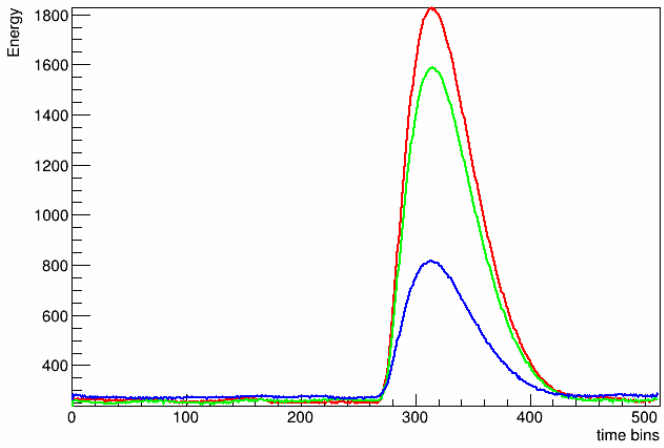

Figure 8.13: A signal event from one of the ^{109}Cd calibrations of the data taking campaing. The configuration parameters are: *wck_division* = 0x02 (20 ns), *trig_delay* = 0x190 (4 μs), *aget gain* = 0x1 (240 fC) and *aget time* = 0xF (1014 ns). The pulses start a little past the middle of the temporal window and the signals are completely contained inside the window. This configuration also allows to have a long enough base line for the posterior analysis.

8.2.5 Shielding

IAXO-D0 prototype puts together all the shielding improvements proved by the CAST experiment and the bench-tests performed by the GIFNA group so far in order to reach the lowest background level possible. These techniques are divided in passive and active shielding.

Passive shielding

The IAXO experiment will not have the geometrical limitation that CAST had for the passive shielding, so for IAXO-D0 the passive lead shielding has been doubled in size. The design consist on 20 cm of lead bricks around the detector chamber. Pictures of the shielding can be seen in figure 8.14.

There are two weak spots in this design. The first one is the electronic connections

Figure 8.14: (Left) Picture of the lead passive shielding of IAXO-D0. **(Right)** Picture of the side of the shielding where the electronic connections are placed. This is one of the weak spots of the shielding.

side. The raquette has to pass through the shielding to bring the electronic connections out. This raquette has been designed to fit inside the 10 cm thick CAST shielding, so it is not long enough to go through all the 20 cm. In this spot, the shielding is 5 cm thinner. The second weak spot is at the pipe side. The vacuum pipe has to go through the shielding in order to connect to the x-rays telescope. The design planned the minimum hole to fit the pipe.

One of the objectives of IAXO-D0 is to check if a thicker passive shielding would reduce the background. On one hand, a thicker layer of lead would stop more energetic external gammas. On the other hand, having a larger lead volume could increase the cosmic neutrons contribution or produce secondary particles which, after their interactions in vetoes, could help to veto these events. It is worth further studies on detector shielding.

Active shielding

Cosmic rays are one of the most important contributions to the background at sea level. Underground tests and active shielding improvements have proven to be key in order to reduce the background to the IAXO required levels.

The first time a CAST detector reached a background level below $10^{-6}\,\text{counts}\,\text{keV}^{-1}\,\text{cm}^{-2}\,\text{s}^{-1}$ at surface was with the implementation of two plastic scintillators as cosmic vetoes, one on top and another one at the back side [213]. Each plastic scintillator is attached to a photomultiplier tube (PMT) that collects the scintillation light from the plastic and transforms it into a detectable signal. This setup does not give any spatial information, but we are only interested in labelling the events produced by muons that interacts in the gas so we can reject them.

The design for IAXO-D0 is still in progress, and it involves the placement of 5-6 plastic scintillators that grants a $\sim 4\pi$ solid angle coverage for cosmic muons. A proposal

of the vetoes placement at IAXO-D0 is shown in figure 8.15. The main idea is that every muon that crosses the detector will leave energy in two of the scintillators for a better identification. Also, as seen in previous sections, active vetoes are able to identify cosmic neutrons as well, by detecting any secondary emission that the neutron can produce when interacting with the lead shielding or the detector itself.

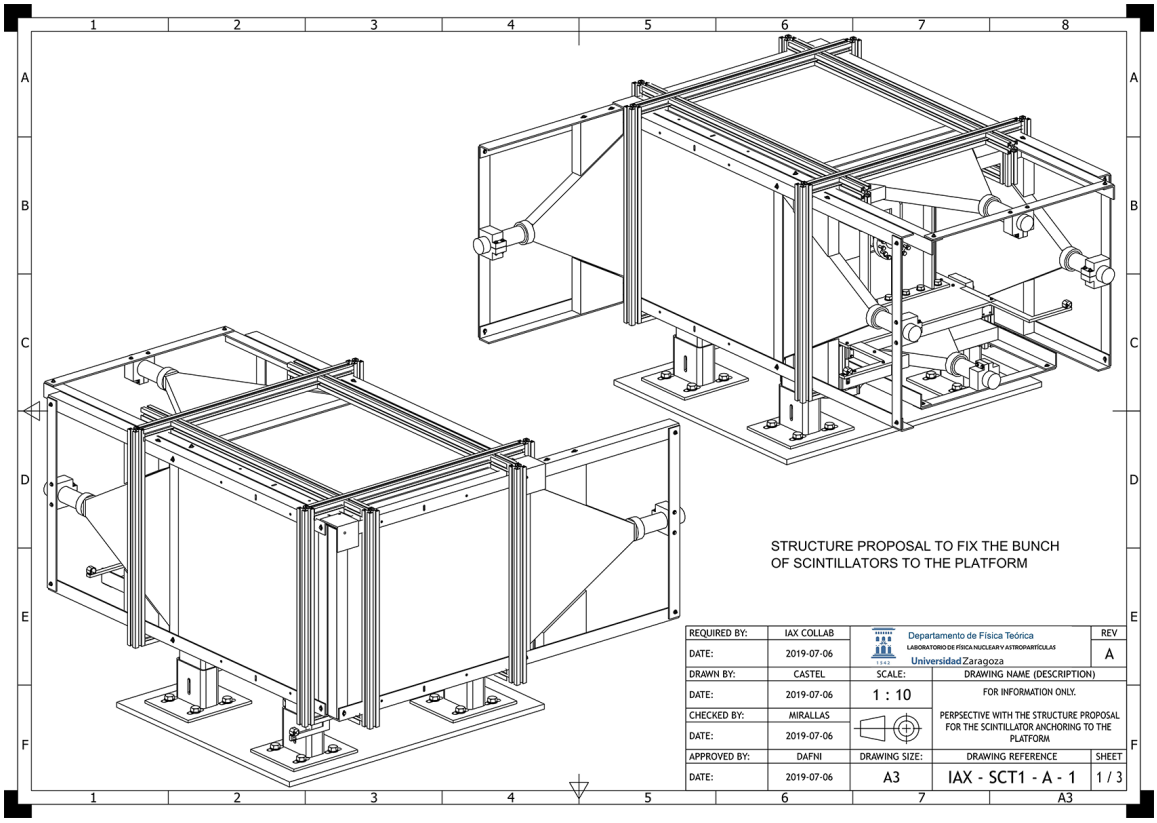

Figure 8.15: A proposal of the muon vetoes placement at the IAXO-D0 site. Five plastic vetoes would grant $\sim 4\pi$ solid angle coverage for cosmic muons.

The vetoes used in the last Micromegas setup in CAST were shipped back to Zaragoza in order to use them for IAXO-D0 together with some other spare vetoes. Also, other new alternatives are being considered because nowadays, the manufacture of vetoes with holes in the middle is possible, so they could be placed at the side of the detector that will face the magnet. These ideas are being discussed and some tests with the vetoes currently available are being done at IAXO-D0, so they can be implemented for the next data taking campaign.

8.3 Micromegas detector

The Micromegas detector implemented in IAXO-D0 is an actual spare detector from CAST, with the same design as the last one used in the IAXO pathfinder setup. In this section, the detector will be described and the results from the laboratory characterization will be presented.

8.3.1 Technical description

The detector for IAXO-D0 is an ultra-low background microbulk Micromegas from the R-branch of CAST detectors. It is made out of copper and kapton following the manufacturing process described in section 2.3.1. It has a 5 μm thick copper mesh suspended 50 μm over the anode by the means of insulation pillars. This mesh has a pattern of 3×3 holes lying over each pixel, with a pitch of 95 μm and about 41 μm border distance between each set of holes. A microscope picture of the mesh is shown in figure 8.16 (left). The active area of the detector is a square of $60 \times 60\, mm^2$, and it is patterned with 120 strips per axis, with a pitch of 500 μm. Each strip connects a row of pixels on both directions making the active area, but one direction is connected at the pixels level and the other in a back-layer. A scheme of the strips of the readout is shown in figure 8.16 (right). The pixels are $313 \times 313\, \mu m^2$ with a 40 μm spacing between them.

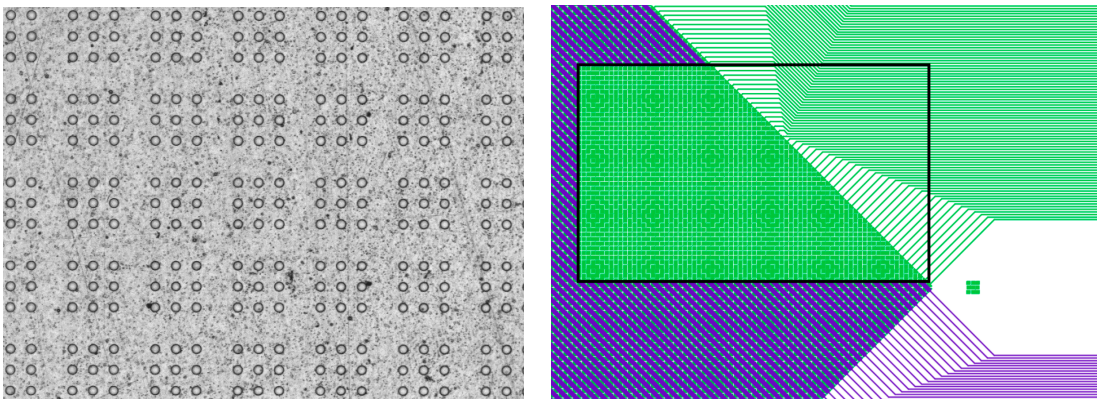

Figure 8.16: (Left) A microscope picture of the micromesh grid of the IAXO-D0 detector. **(Right)** Scheme of the strips of the readout in two layers: one axis is connected at the pixels level (green) and the other axis is connected at a top layer (purple). The top layer is removed inside the black rectangle for visualization purposes.

The signals from the strips are routed individually through the surface of the copper raquette to a fingerprint where the SAMTEC connector is plugged. Also, all the high voltage pads are implemented in the detector printed circuit board and routed through the surface of the raquette. They end in a SAMTEC HPF connector, where each pin is fed with the corresponding voltage from the HV-filter box. A picture of the detector as well as a scheme of the connections are shown in figure 8.17.

8.3.2 Detector characterization

Before starting the data taking campaign, an *in situ* characterization of the detector has been done to test its operational performance and to find its best operational point.

These tests have been performed using Ar+2%C_4H_{10} (isobutane) as the gas target for two main reasons. First, this particular mixture is usually used to test and characterize Micromegas detectors, so it exists a lot of data to compare with. And also, it is the gas

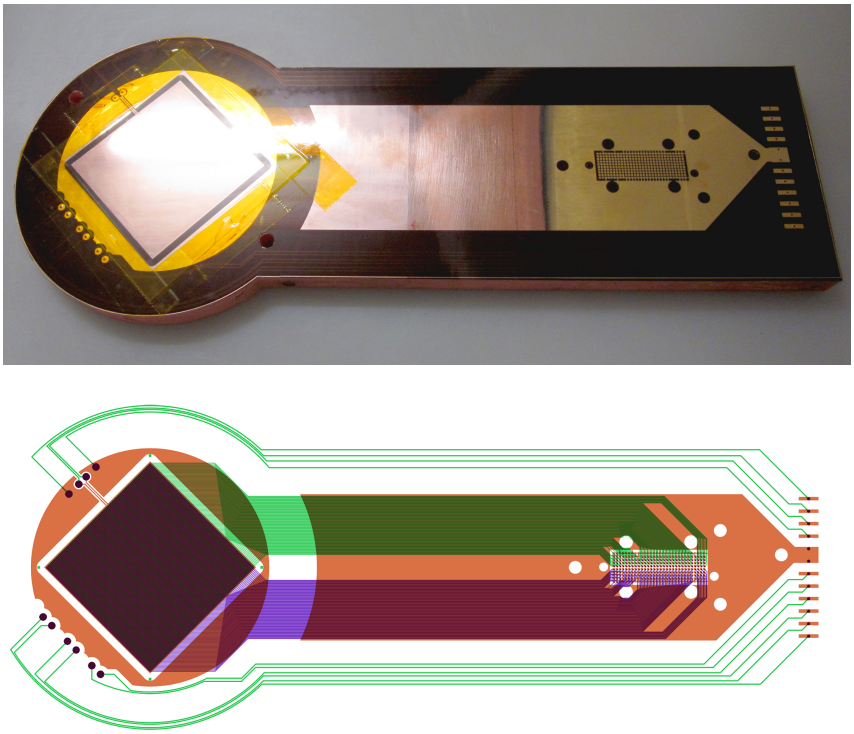

Figure 8.17: (Top) IAXO-D0 Micromegas detector. **(Bottom)** Schematics of the detector layers: (green) the bottom layer, that contains the paths and connection points of the mesh, drift and cathode high voltage and ground, and also the signal paths of the strips of one axis; (purple) the middle layer, that contains the signal paths of the strips of the other axis; (orange) top layer of grounding. Each individual strip is connected to the footprint at the end of the raquette, as well as the HV connections.

mixture that was used in the Micromegas detectors in CAST, so it has been used for the first IAXO-D0 data taking campaign as well. The operation pressure was 1.4 bar and the gas flow was set to 3 l/h. The gas system operated in open cycle to assure the maximum purity of the gas. Also, as a good practice, we let the gas flow during a few hours before taking any data in order for the target gas to be as clean as possible.

All the characterization measurements has been done with the ^{109}Cd calibration source at the calibration position in vacuum conditions. The signals from the mesh has been used only to monitor the process. On the other hand, the signals from the strips have been acquired and processed[1] in order to obtain the energy spectrum in ADC units for each measurement. A typical ^{109}Cd spectrum of the detector is shown in figure 8.18. Then, a C++/root macro has been used in order to fit the spectra peaks. This macro first finds the position of the peaks of the spectrum. Then, it estimates a background and fits it to a polynomial function of degree one. After that, it fits the higher peak, which is the copper 8 keV peak, to a Gaussian function. The second and the third higher peaks correspond respectively to the 22 keV and 19 keV peaks from the source. A first Gaussian fit is applied to the peaks individually. Then, a convoluted Gaussian fit is done using the

[1]The data analysis has been made using REST processes. The procedure to obtain the energy spectra will be described in full detail in the next section.

parameters of the individual fits. The mean errors obtained with this analysis are about the 0.1% in the peak determination for both peaks, and the 1.8% and 3.2% in the FWHM determination of the 8 keV and 22 keV peaks respectively.

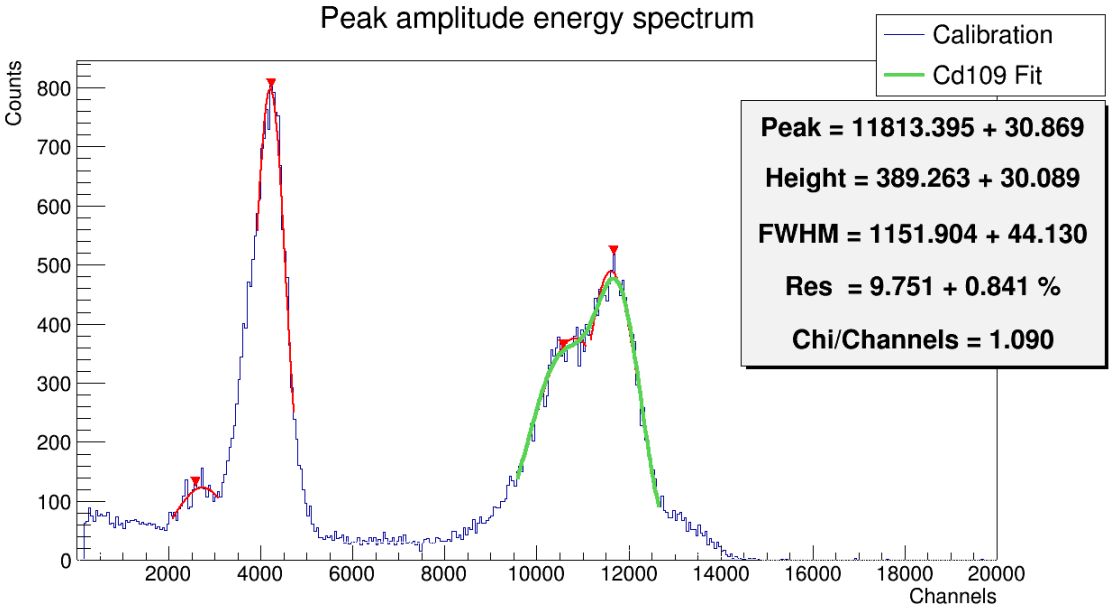

Figure 8.18: Typical ^{109}Cd energy spectrum obtained with the IAXO-D0 Micromegas. In this plot, the Gaussian fits of the peaks are shown. Red ones correspond to the individual fits, and the green one is the convoluted fit for the double peak.

Electron transmission

The first characterization measurement has been to obtain the electron transmission curve (also known as the electron transparency) of the Micromegas. This measurement gives information about the amount of electrons that passes through the mesh holes once they reach the readout plane.

The procedure has been to vary the drift voltage while keeping the mesh voltage fixed at 320 V. For each drift voltage value, a 10 minutes run has been taken and the spectrum has been analysed in order to find the position of both the 8 keV and 22 keV peaks.

The electron transmission curve for the IAXO-D0 Micromegas is shown in figure 8.19. The relative electron transmission is plotted as a function of the drift to amplification electric field ratio. The typical result for a microbulk Micromegas of this characteristics has been obtained: transmission starts low at low drift voltages because the drift field is not strong enough to bring the primary electrons to the readout before they recombine again with the gas molecules. When the drift voltage is higher, the transmission also increases until it reaches the plateau, where it remains constant until the drift voltage is too high, and then it decreases again. This happens because at higher drift voltages the drift field lines end on top of the mesh instead of passing through the holes. The plateu,

that is the region for which the mesh is transparent to primary electrons, corresponds to the drift voltages between 512 and 1040 V. Having a wide plateau means that the detector can work at optimal conditions in wide range of drift to amplification electric field ratios, and therefore the voltage fluctuations will have less impact in the detector performance.

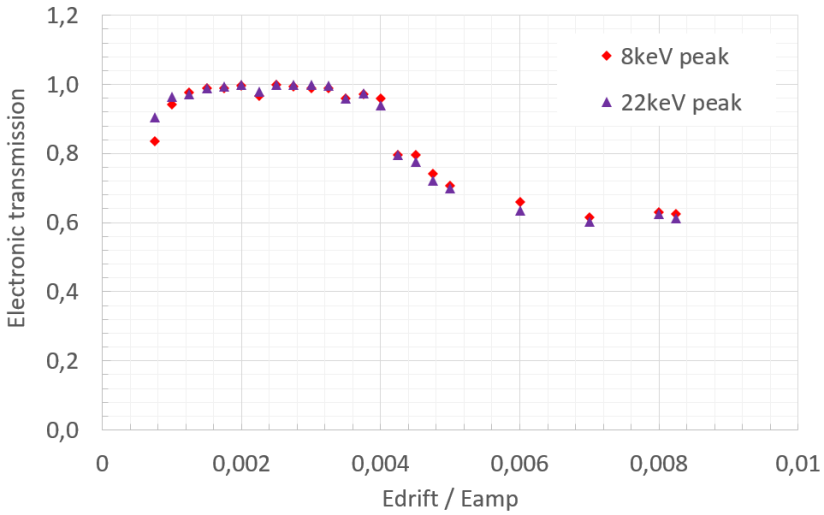

Figure 8.19: Electron transmission of the IAXO-D0 microbulk Micromegas detector as a function of the drift-amplification electric field ratio, in $Ar + 2\%iC_4H_{10}$ at 1.4 bar.

Even though we reached high drift voltages for this measurement, there were no sparks problems and the detector worked smoothly. The results are compatible with previous characterizations of similar detectors [14, 195].

Gain and energy resolution

The second measurement has been to obtain the gain and the energy resolution curves of the Micromegas. This measurement gives information about the amplification factor of the primary electrons charge and the precision of the detector measurements of this charge.

The procedure has been to vary the mesh voltage while keeping the same drift to amplification electric field ratio. We chose the point in the middle of the transmission curve plateau which had the best energy resolution in the previous measurement: E_{drift}/E_{amp}=0.002. For each run, the drift voltage has been chosen accordingly and the spectrum has been analysed in order to find the position and FWHM of the 8 keV and 22 keV peaks.

The relative gain curve for the IAXO-D0 Micromegas is shown in figure 8.20 (left). This curve has been obtained by plotting the position of the 8 keV and 22 keV peaks of the spectrum for each run as a function of the amplification field. The units of the gain are arbitrary ADC units because the electronic chain has not been calibrated. The main reason for not doing so has been that this particular detector had already been

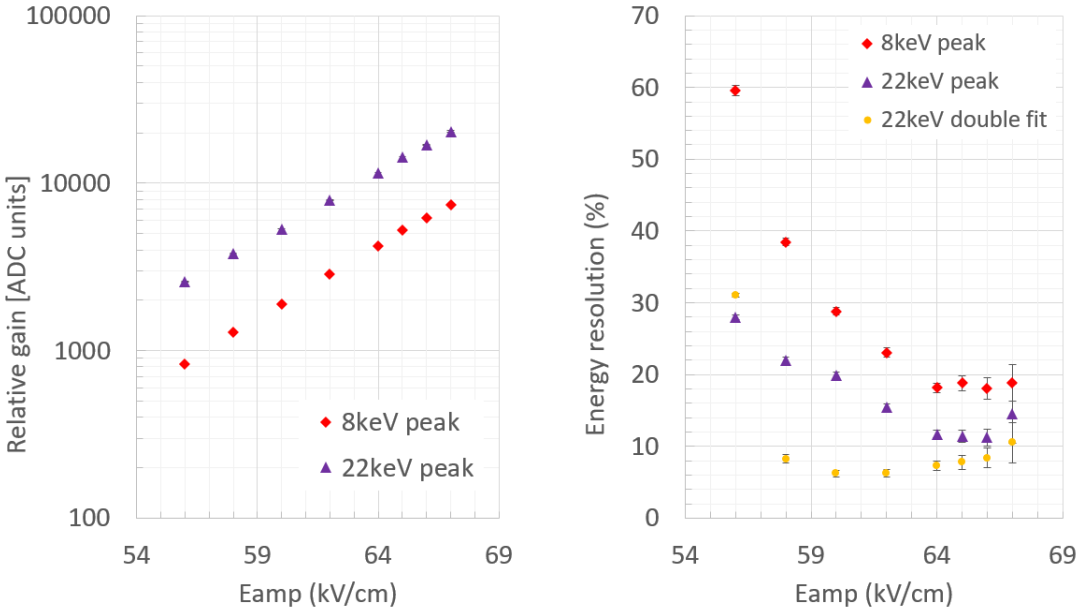

Figure 8.20: Left: Relative gain of the IAXO-D0 microbulk Micromegas detector as a function of the amplification electric field, in $Ar + 2\%iC_4H_{10}$ at 1.4 bar. For the gain, arbitrary ADC units are used. **Right:** Energy resolution of the IAXO-D0 microbulk Micromegas detector as a function of the amplification electric field, in $Ar + 2\%iC_4H_{10}$ at 1.4 bar. The energy resolution is expressed in FWHM percentage.

characterized in CAST [14] and the time has been a limiting factor. The main objective for this characterization has been to check that the detector performed as it was expected. So even though this plot is not directly comparable with previous measurements, the tendency is the expected one: the gain rises exponentially with the amplification field [48].

The energy resolution curve for the IAXO-D0 Micromegas is shown in figure 8.20 (right). It has been obtained by plotting the FWHM of the 8 keV and 22 keV peaks of the spectra of the previous runs as a function of the amplification field.

The FWHM (full width at half maximum) is an expression of the extent of function, given by the difference between the two points where the distribution value is equal to half of its maximum value. It is related with the Gaussian parameters by the expression:

$$FWHM(\%) = 100\frac{2\sqrt{2\,ln2}\,\sigma}{\mu} \simeq 235\frac{\sigma}{\mu} \tag{8.1}$$

where μ is the expected value of the Gaussian and σ its standard deviation.

The results are compatible with previous measurements, with the best energy resolution being 12% for the 22 keV peak and 18% for the 8 keV peak for an amplification field of 64 kV/cm (i.e V_{mesh}=320 V and V_{drift}=710 V).

As a final note, during this measurement rather high mesh voltages have been reached and the performance of the detector has been very stable.

CHAPTER 9

IAXO-D0 background measurements

Contents

9.1 Introduction

The main goals for the IAXO-D0 prototype built at the University of Zaragoza have been to test the main low background techniques that have been applied to the final design of the Micromegas detector, to study its radioactive background and to prove that it can reach background levels of the order of $\sim 10^{-7}$ counts keV^{-1} cm^{-2} s^{-1} in the IAXO energy RoI. These are important points for the IAXO experiment, and even though the IAXO pathfinder at CAST have already proven a suitable performance and very low background levels, this next generation helioscope will allow to implement all the ultra low background techniques learnt during the CAST experience with no limitations.

In this chapter, the conditions of the first IAXO-D0 data taking campaign will be described, as well as the acquisition procedure and the detector performance during the campaign. Then, the data analysis procedure using the REST software will be explained and a detailed description of the x-ray characterization will be given. Finally, the IAXO-D0 Micromegas background level results from this first data taking campaign will be presented.

9.2 First IAXO-D0 data taking campaign.

In this work it is showcased the first data taking campaign carried out with the IAXO-D0 prototype after its commissioning and test period. As it was described in the previous section, a spare Micromegas detector from the IAXO pathfinder was operated with a mixture of Ar+Isobutane (98/2)% with a 20 cm thick lead shielding and the new AGET based electronic cards. Muon vetoes were not installed due to technical issues, but they are already being tested *in situ* for the next campaign.

9.2.1 Data taking conditions

The first data taking campaign of IAXO-D0 started the sixteenth of July and concluded the twenty first of August of 2018. During these 37 days of data taking we were able to acquire ∼450 hours of background. Each background run was 20-23 hours long, and between background runs, a 10-20 minutes ^{109}Cd calibration run was taken.

The data taking conditions for this first campaign are shown in table 9.1 and they were chosen from the tests described previously in section 8.2.4 for the electronics, and section 8.3.2 for the detector optimum operational point. The gas conditions were chosen taking into account the quantum efficiency mentioned in section 6.4.1 and the small volume of the detector chamber: with a capacity of ∼0.9 l, the flux chosen allowed to renew the gas three times per hour, ensuring that the gas was always clean.

Detector	Mesh voltage (V_a)	320 V (i.e. 64 kV/cm)
	Drift voltage (V_d)	710 V (i.e. 130 V/cm)
Gas system	Pressure	1.4 bar
	Flux	3-4 l/h
Electronics	Gain	0x1
	Shaping time	0xD (i.e. 897 ns)
	Clock divisor	0x02 (i.e. 20 ns/bin)
	Trigger delay	0x190 (i.e. 400 ns)

Table 9.1: Experimental parameters set for the first IAXO-D0 data taking campaign to guarantee the optimum acquisition conditions. They are shown the parameter values and their physical meaning when needed.

During this data taking period some problems were found that hindered the normal working operation at some points. One recurrent inconvenient was that the new acquisition software tended to crash at the end of some runs. This was not a major issue, because the data was successfully saved, but it implied that after the crash happened, the detector needed to be ramped down and the electronic card reset. The technical error that caused the crashes was not easy to solve and the software priorities at that point were on a different stage, so the data taking had to be done regardless this problem. To avoid discrepancies, an extra calibration run was taken every time the system had to be reset.

Another inconvenient during the data taking campaign was that at the last week of july and the first week of august, maintenance in the electric system of the building was scheduled. This turned out to introduce a lot of electric noise that made it impossible to acquire any quality data during that period. Also, and maybe related to this problem, the power source of the acquisition computer broke, so it had to be replaced. This issue allowed us to implement some upgrades to the experimental system, like a UPS (uninterrupted power supply) to the acquisition computer.

These problems during the data taking period reduced the real acquisition time to 21 days out of the total 37 days of the campaign. And finally, the campaign was concluded when the gas bottle was drained.

9.2.2 Acquisition procedure

The acquisition procedure for this data taking campaign in the IAXO-D0 prototype started by setting the environmental conditions of the detector. The gas pressure and flow were set with the slow control and the gas system was configured from the gas panel to work in open cycle (i.e. we did not recover the gas once it passed through the chamber). The gas was let to circle through the system and chamber for at least one hour before taking any data. In parallel, the Pfeiffer vacuum pump was started in order to make vacuum inside of the pipe.

Once the environmental conditions of the data taking were reached, the electronic cards were initialized by the acquisition software. Then, a pedestals run was taken in order to measure the characteristic noise level of each of the channel's baselines in absence of signals. This run consists of an accumulation of a large number of measurements with all the strips where the mean value m_i and the standard deviation σ_i is calculated for each strip. This information is used to set the trigger of the individual channels. For this data taking campaign, a strip will trigger if its value s_i is above the mean value plus three times its standard deviation:

$$s_i \geqslant m_i + 3\sigma_i \tag{9.1}$$

Also, the Feminos card was programmed to update its internal pedestal subtraction (or equalization) constant table for the later data taking. When a strip triggers, the Feminos card performs a pedestal equalization in order to compensate for the physical mismatch between the baseline level of the different channels of the AGET chips. The updated equalization values of each channel are applied to obtain the same baseline level for all the channels after the equalization. This post-equalization baseline was chosen to be 250 ADC counts, which is the recommended value by the Feminos card provider.

After the pedestals run, the Micromegas amplification and the drift chamber voltages were ramped up to their optimum operational values. The drift shaper of the chamber allows to set the voltages at two intermediate rings in order to obtain a more homogeneous electric field inside the chamber, but for this first data taking campaign they were not used. The main reason behind it was to reduce the external noise of the signal produced by the HV connectors.

At this point the data taking conditions were reached. A 20 minutes long calibration run was taken before each background run by bringing the ^{109}Cd source closer to the chamber window through the vacuum pipe. When the calibration was finished, the source was brought back to the parking position and properly blocked, and finally the background run was set for 20-23 hours.

9.2.3 Micromegas detector performance

The study of the detector performance during the IAXO-D0 data taking campaign was done using the daily ^{109}Cd calibrations taken between background runs. These calibrations allowed to monitor *in-situ* if the detector was performing as expected. Then, for the offline analysis, a script was used in order to fit the peaks of reference to Gaussian functions, as it was previously described in in section 8.3.2.

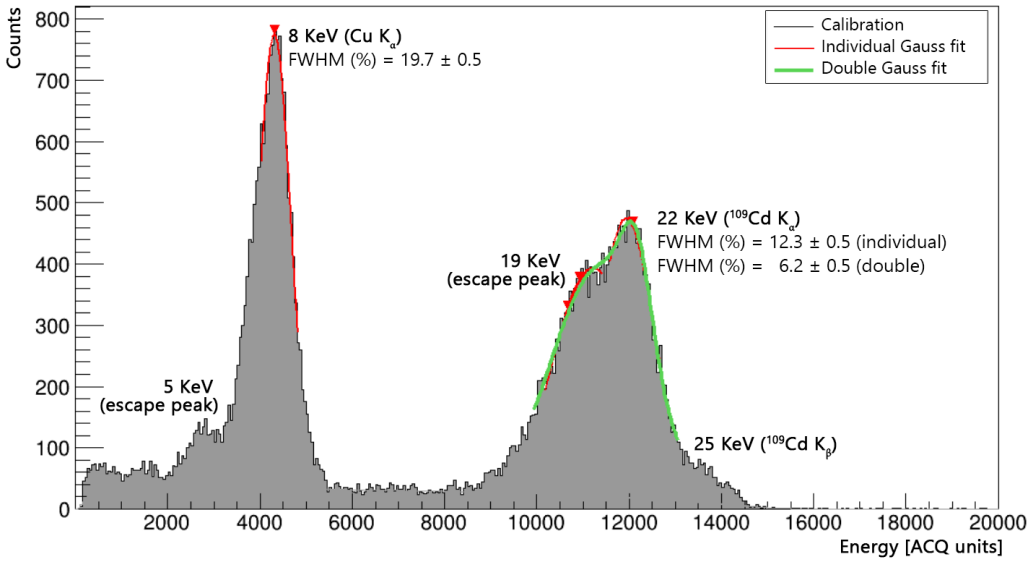

Figure 9.1: Energy spectrum of a ^{109}Cd calibration run (15/08/2018) with the 8 keV and 22 keV peaks fitted to Gaussian functions. The energy resolutions are also shown.

A typical ^{109}Cd spectrum measured with the IAXO-D0 Micromegas is shown in figure 9.1. The spectrum shows the expected shape already described in section 6.4.2 with the IAXO-D0 simulations: the highest peak correspond to the 8 keV fluorescence from the copper parts of the detector, and also at 5 keV it appears its escape peak; then the 22 keV x-ray from the ^{109}Cd source present a double peak with its corresponding 19 keV escape peak due to the energy resolution at those energies; and finally at the end of the spectrum we find the 25 keV emission from the ^{109}Cd source. At the beginning of the spectrum they are seen two small populations of events corresponding to the 1.4 keV emission of the aluminium from the window and also the 3 keV peak from the argon.

Gain stability

The stability of the gain of the detector is a good indicator of its performance. It is important for the consistency of the data to be acquired with a similar gain during the data taking period. The evolution of the gain during the IAXO-D0 data taking campaign is shown in figure 9.2. They are shown the positions of both the 8 keV and 22 keV peaks of the ^{109}Cd calibrations.

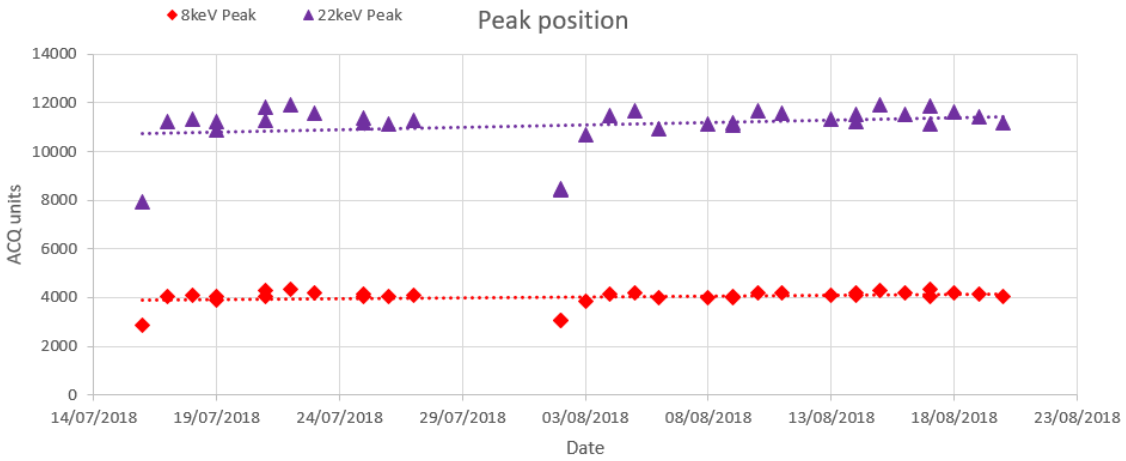

Figure 9.2: Gain stability during the IAXO-D0 data taking campaign for the 8 keV (red) and 22 keV (purple) peaks of the ^{109}Cd calibration runs. Days with two different values of the peak position correspond to those days when two calibrations had to be acquired due to the software problems.

The gain of the detector is stable for both peaks, specially for the 8 keV peak that is in the RoI. In this plot the problematic week at the end of july is visible, where the setup had to be reset many times. There are two dates when the gain drops below the normal tendency. This is because at the beginning of the data taking periods, the gas is not still in its optimum condition for the data taking.

Energy resolution

Another good indicator of the detector performance is the energy resolution, because it is directly related with the sensibility of the data acquisition. The calculation of the energy resolution was explained in section 8.3.2. The evolution of the energy resolution for both of the 8 keV and 22 keV peaks during the data taking campaign is shown in figure 9.3.

The energy resolution obtained with the IAXO-D0 Micrometas detector is stable during the data taking period, specially for the 8 keV peak. Regarding the 22 keV peak, for some calibration runs the 19 keV escape peak was not differentiated enough from the 22 keV peak for the fitting script to identify two peaks, so the double fit almost coincide with the value given by the individual fit. There is a specific day (14/08/2018) when the resolution of the 22 keV peak is worse than the rest. This was a problematic calibration because of some electronic noise that we were able to solve afterwards.

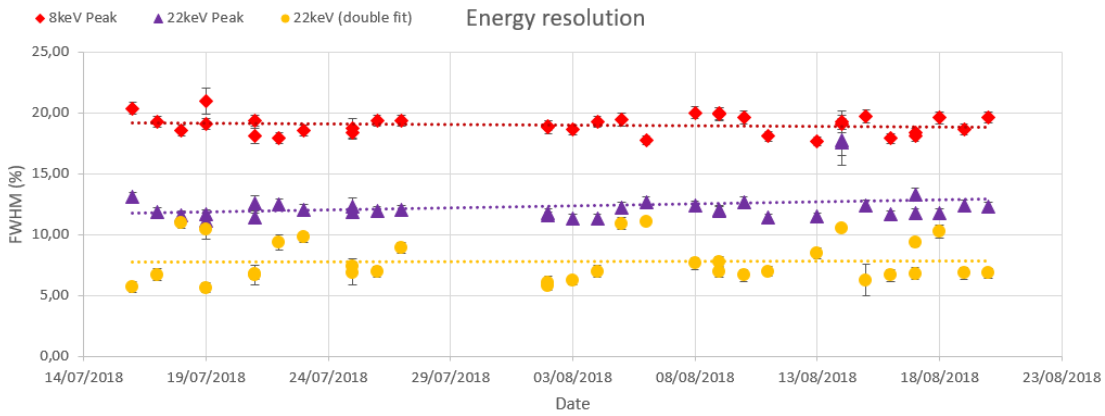

Figure 9.3: Energy resolution stability during the IAXO-D0 data taking campaign for the 8 keV (red) and 22 keV (purple) peaks of the ^{109}Cd calibration runs. It is also shown the energy resolution obtained with the double Gaussian fit for the 19 keV and 22 keV double peak (yellow) described in section 8.3.2. Days with two different values of energy resolution correspond to those days when two calibrations had to be acquired due to the software problems.

Spatial resolution

Finally, another indicator of the detector performance is the spatial resolution of the strips of the readout. It can happen that this type of detectors show dead areas which correspond to disconnected strips from the readout. This disconnected strips may come from a problem during the manufacturing process, from their posterior removal due to a shortcut with the mesh or from a bad connection with the electronic acquisition card. In our particular case, no strips had to be removed due to malfunctioning reasons.

Figure 9.4 show the information from the charge collected by all the ACQ channels for background (top) and calibration (bottom) runs along the data taking campaign. From this plots we see that some strips did not collect data properly, specially from the Y side of the readout. Although some of the malfunctioning strips seem consistently disconnected during all the data taking campaign (like the 25, 184, 188, 189, 194 or 210), some of them seem to fix themselves with time (like the 140, 161 or 198), and some of them seem to get worse with time (like the 143, 164, 219 or 222). This may indicate that the problem for many of the disconnected strips come from a bad connection at some point of the electronic chain. There is also a strip (222) that collects significantly more charge than its surrounding strips. This strip was identified as a problematic one, because it is internally connected with another strip (64), which is located at the center of the X axis and therefore, it collects more charge than the ones closer to the sides of the detector. This strip will have some consequences in the analysis, as it will be shown later on this chapter, but a proper use of the REST observables will mitigate this effect significantly.

It may seem that the amount of *bad* strips is too high, but for this particular application, the malfunctioning of disperse strips does not have a critical effect on the results. Usually, one single x-ray event triggers more than one strip (typically ∼4 per axis, as it will be shown later), and the possibility of one or two consecutive *bad* strips

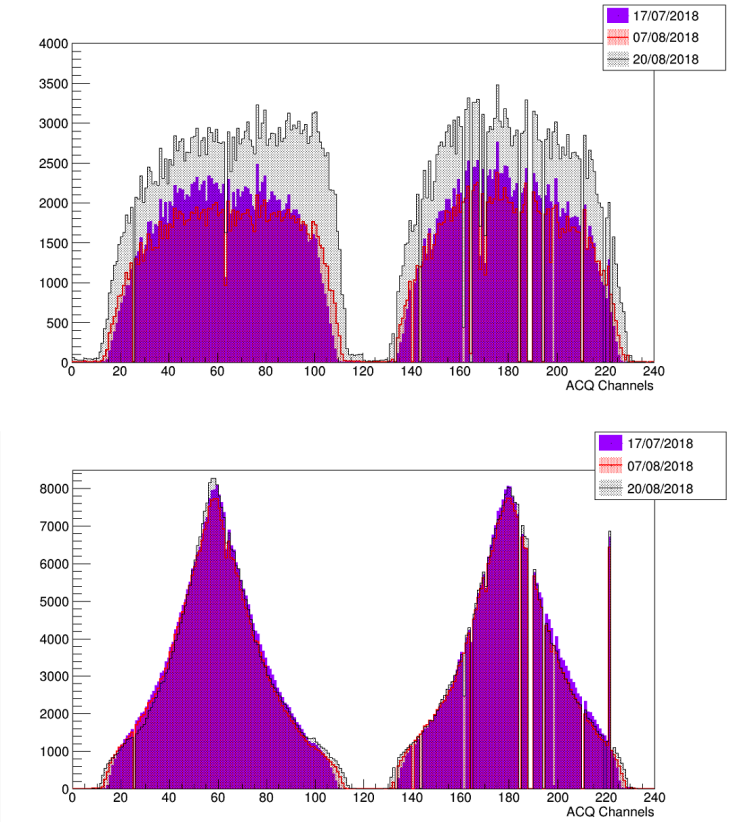

Figure 9.4: Information of the ACQ channels triggered for three IAXO-D0 **(Top)** background runs and **(Bottom)** calibration runs respectively from the beginning, middle and end of the data taking campaign. The first population correspond to the X strips (1-120 ACQ channels) and the second population, to the Y strips of the readout (121-240 ACQ channels).

contained in the 2D print of the event is considered in the analysis. This issue may have minor consequences, like a slight worsen of the energy resolution or the quality of some analysis observables, which are not desirable for the final IAXO detectors, but they are not significant for the conclusions of this work.

Finally, figure 9.5 show the cumulative distribution of the mean hit event position (i.e. hitmap) of a background (left) and calibration (right) run. An evident difference can be seen from the background run, where the events are homogeneously spread over the readout surface, in comparison with the calibration run, where there is an accumulation of events at the very center of the readout, that is the position over where the ^{109}Cd source is placed. In this calibration hitmap, the disconnected strips are noticeable.

Considering that the readout is $6\times6\,\mathrm{cm}^2$, the hitmaps show that very few events reach the borders. This can be due to the fact that the field shaper was not used during the data taking because of some electronic noise problems related to the HV connections. Although it would be preferable to have a more homogeneous drift electric field with no border effects, for the purpose of this data taking it was necessary to reduce the noise of the measurements. Note that for the case of the IAXO detectors, the most meaningful

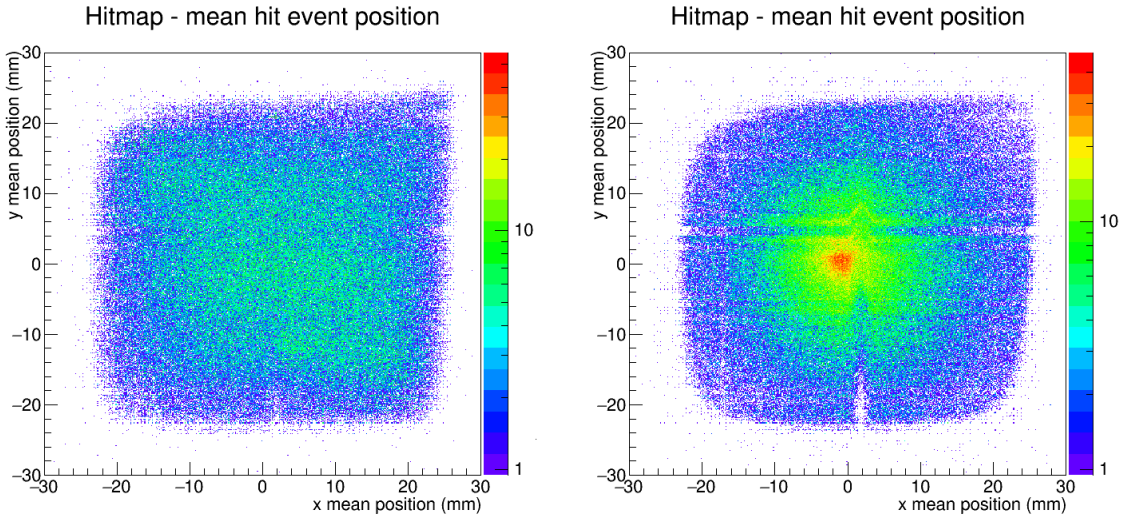

Figure 9.5: Hitmap of the mean positions **(Left)** of the hit events of all the IAXO-D0 background runs and **(Right)** of a ∼7.5 hours calibration run.

part is the center of the readout and the borders are usually not considered for the signal recognition.

Also, the hitmap and the channel activity histograms show a non ideal situation for an optimum performance, because there are a few problematic strips at the middle part of the readout, that is the area where we would expect an axion signal. An extra effort will be necessary in order to improve the strips connection and improve the spatial resolution of the detector.

9.3 Data analysis with REST

REST software has been used to perform the main part of the analysis process of the acquired data with the IAXO-D0 prototype. It is the first time the very same analysis software has been used for both experimental data and simulations in the CAST-Micromegas context, so this is one important step in the IAXO data treatment philosophy. Some external scripts have been used as well for some of the features that are not implemented in the REST framework yet since it is still in a development stage.

9.3.1 General procedure

The first part of the analysis has been to use the REST processes in order to transform the raw pulses acquired with the electronics to REST/root compatible TRestRawSignalEvents. Then, a series of REST processes have been applied in order

to transform these signals[1] into energy deposits or hits, and finally to group the near hits into tracks, obtaining a TRestTrackEvent output file with observables from each analysis process. Each of these event types were fully described in section 6.2.1, and a conceptual scheme of the work-flow is shown in figure 9.6.

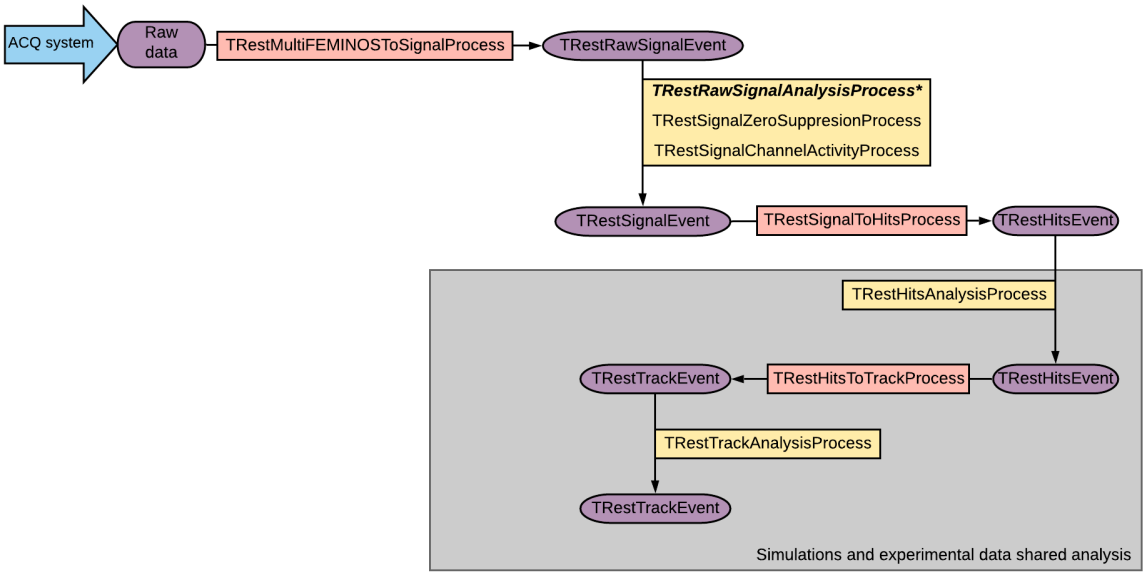

Figure 9.6: Scheme of the REST analysis steps for the experimental data. The purple ovals represent the different event types, the red rectangles are the processes that transform one event type into another, and the yellow rectangles are the processes that performs transformations or calculate the observables for each type of event. (∗) Note that in this case, we have a process that both performs an analysis and transforms the event type.

One of the advantages of using the REST software is that even though this analysis starts from experimental data, they can be processed up to the point where the same analysis that was already used for the simulations can be applied. There is no need to define other processes because the data will have the same software structure, so the only difference between both analysis will be the steps from the raw data to the TRestHitEvents.

1. **TRestMultiFEMINOSToSignalProcess** translates the binary acquisition data format to a TRestRawSignalEvent using the information of the run and pedestal configuration. This process is programmed taking into account the architecture of the electronic card (Feminos) and it is prepared for acquisition systems with multiple cards. In our case, only one card is used. The outputs are TRestRawSignalEvent with raw signals (pulses) from each strip of the readout that triggered for each event.

2. **TRestRawSignalAnalysisProcess** obtains all the observables related to the signals and their shape. This is a special process because, before calculating the observables, it transforms the TRestRawSignalEvents into TRestSignalEvents by

[1] In this work, the word *signal* related with the REST analysis refers to the electrical signal, or pulse, that is measured and transformed by the electronic card. Do not mistake with the axion positive signal.

assigning the charge and time stamp to each signal. Then, it obtains observables related to the shape of the pulse, like the base line, the rise time, etc. All these observables were described in section 6.2.1.

3. **TRestSignalZeroSuppresionProcess** eliminates all the bins from the signals that do not contain any physical information, what is commonly called a *zero suppression*. This process checks each time bin of the signal and only saves the ones that pass a certain threshold, that is obtained with information of the baseline and some other parameters set by the user. It is useful in order to reduce the digital weight of the analysed data without loosing any relevant physical information.

4. **TRestSignalChannelActivityProcess** registers the charge collected by each strip of the detector in a histogram, giving information about the activity of every electronic channel (strip). This process is very useful in order to check whether or not there are *bad strips* i.e. strips that do not work properly or are disconnected.

5. **TRestSignalToHitsProcess** transforms TRestSignalEvents into TRestHitsEvents. For each signal, the x or y position is determined by the position of the strip that triggered. To obtain the z position, a new method was implemented in this work, where the top of the signal pulse is fitted with a Gaussian function. The bin that corresponds to the center of the Gaussian is considered the time when the signal was measured. Then, using the information of the sampling time and the drift velocity of the gas at the IAXO-D0 specific conditions, the relative z position of the signal within the TRestSignalEvent is obtained. Some examples of fitted signal are shown in figure 9.7. The reason for the implementation of this method was that sometimes, specially for signals with lower energy, the shape of the pulse was dominated by the electronic noise, so finding the center of the peak simply as the highest value of the signal was not accurate enough. Finally, the energy of the hit is defined as the height of this Gaussian over the signal baseline and the user set threshold.

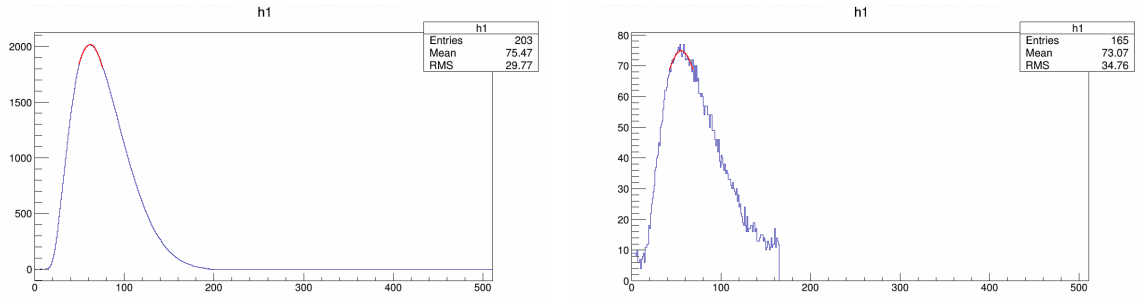

Figure 9.7: Examples of the Gaussian fit performed by the analysis method in TRestSignalToHitsProcess to obtain the time of the signal. **(Left)** A smooth signal of ∼3.9 keV. **(Right)** A more noisy signal of ∼0.15 keV.

6. **TRestHitsAnalysisProcess** to obtain the hits observables related with the energy and shape of the energy deposit. The most useful ones for the data analysis will be the number of hits, that correspond directly with the number of strips that

triggered for each event; the xy energy balance $\frac{E_x - E_y}{E_x + E_y}$ that will give information about the difference in the energy collection between each axis of strips; the $\sigma^2_{x,y}$ and σ^2_z, that will give information about the size of the event; the xy sigma balance $\frac{\sigma_x - \sigma_y}{\sigma_x + \sigma_y}$ as well as the skewness, that will give information about the shape and symmetry of the event; and finally, the distance of the hits to the fiducial walls of the $(60 \times 60\,\text{mm}^2) \times (30\,\text{mm})$ fiducial prism.

7. **TRestHitsToTrackProcess** to search for hits closer than a selected distance to define tracks, where this minimum distance is chosen by the same criterion as the one used for the simulation analysis: two tracks will be considered as such if there are two or more non triggered consecutive strips (i.e. 2 mm of distance between tracks).

8. **TRestTrackAnalysisProcess** to obtain the tracks related observables, the most useful ones being the number of tracks and the balance between the total energy and the track with maximum energy of the of the TRestTrackEvent ($Balance_x = \frac{E_x - E_x^{max}}{E_x + E_x^{max}}$ and $Balance_y = \frac{E_y - E_y^{max}}{E_y + E_y^{max}}$).

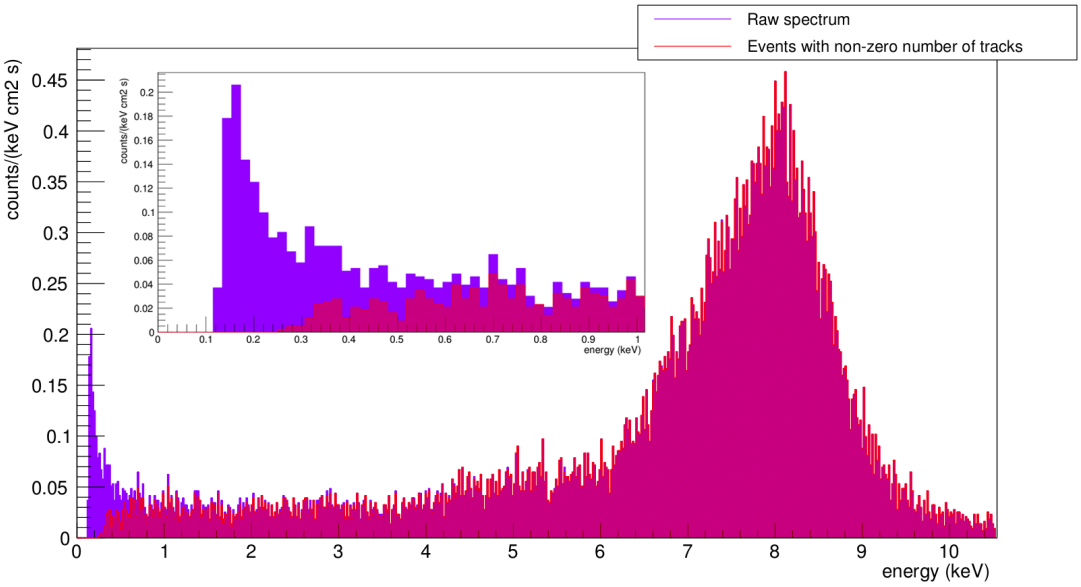

Figure 9.8: Calibrated energy spectrum of a raw ^{109}Cd calibration run (purple) and the same spectrum but only considering events with at least one track in both X and Y dimensions (red) to remove the noise. The energy threshold in this case is ∼0.25 keV.

The second part of the analysis has consisted on the energy calibration of the acquired spectra. For this purpose, the energy spectra of all the runs, both calibration and background, have been generated with the REST plots tool. Only two cuts have been applied in order to remove the noise at low energy: they have only been considered the events with non-zero number of tracks in either x or y dimension. Figure 9.8 shows a ^{109}Cd calibration run energy spectrum with and without these cuts and their effect at low energy. The energy threshold resulting is ∼0.25 keV after applying the noise cuts, which is already an improvement from the previous CAST Micromegas setups.

Once all the energy spectra have been obtained, the script explained in 8.3.2 has been used to fit both the 8 keV and the 22 keV peaks for all the daily ^{109}Cd calibration runs. Then, each background run has been calibrated in energy considering the ^{109}Cd calibration performed the same day the run was taken. This has been done using an external C++/root macro that takes the calibration information for each background run, as well as the total time of the run and the surface of the detector readout considered, and then it rescales both axis of the histogram to obtain the background level in counts $\mathrm{keV}^{-1}\,\mathrm{cm}^{-2}\,\mathrm{s}^{-1}$ plotted as a function of the energy in keV.

The third part of the analysis has consisted on the x-ray characterization in a similar way than the characterization described in section 7.2.2 for simulated data. With this characterization, that will be further explained in the next section, the discrimination cuts for the data observables have been obtained.

Finally, the last step of the analysis has been to apply these discrimination cuts to every background run and the IAXO-D0 background levels have been studied.

9.3.2 X-rays characterization

A good x-ray characterization in the axion energy RoI is a key step of the analysis. It is needed a deep understanding of how an x-ray produced by the axion (the axion signal) would be seen by the IAXO detector. The ideal scenario for this study would be to illuminate the detector with a source that emits x-rays in the range of 2-6 keV and study the events produced by such emission.

In previous CAST-Micromegas setups, these characterizations used to be done with a ^{55}Fe source, because this isotope emits a 5.9 keV x-ray. But as it has already been mentioned, due to mechanical issues, a ^{109}Cd source had to be used for the IAXO-D0 detector calibrations of the first data taking campaign. This isotope emits a 22 keV x-ray that is out of the axion energy RoI, but even though these x-rays are not the best sample for the axion x-ray characterization, they interact with the copper of the detector and 8 keV fluorescent x-rays are produced. These x-rays are in the axion energy RoI and can be used as an alternative for the axion signal characterization.

For this purpose, a 20 hours long ^{109}Cd calibration run was performed on IAXO-D0 in the data taking conditions. The stability of the gain and the energy resolution of the run are shown in figure 9.9. The 8 keV peak remains very stable during the run. These data have been analysed using the REST procedure described in the previous section, and the main observables have been studied. The most representative observables for the x-ray characterization have been the ones from the TRestHitsEvents and TRestTrackEvents, which are the ones that give the topological information and describe the shape of the energy deposit. Thanks to the previous CAST studies we have a solid knowledge of what an x-ray event should look like when measured with a Micromegas detector: one-single track events that leave a small, punctual or round-like and symmetric energy deposit. Also, some considerations can be obtained from the observables from the

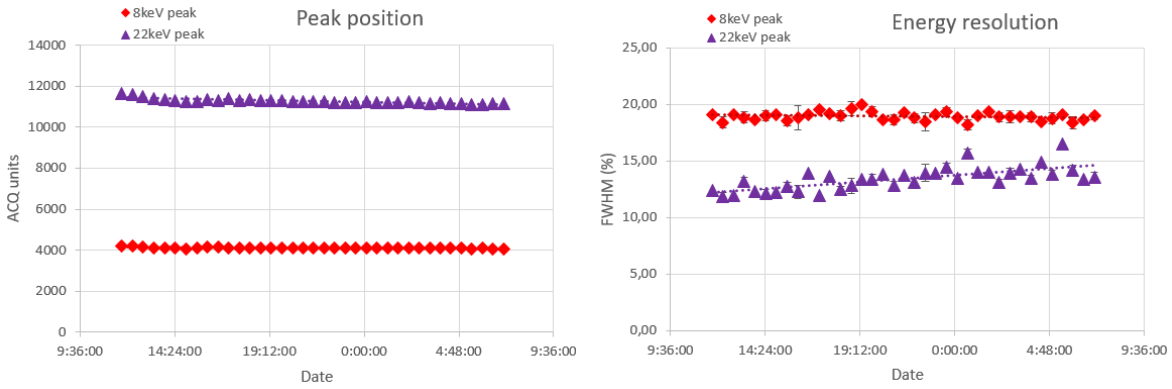

Figure 9.9: Stability of the relative gain **(right)** and the energy resolution **(left)** of the IAXO-D0 20 hours long ^{109}Cd calibration run during the measurement period. Purple triangles correspond to the gain and energy resolution of the 22 keV peak of the ^{109}Cd spectrum and red diamonds correspond to the 8 keV peak from the copper fluorescence.

TRestSignalEvents even though the signal shape analysis is not in a very advanced stage.

Figure 9.10 shows the hit and track observables from the 8 keV events (19% FWHM), which have been used for this x-ray characterization. Some initial information can be obtained from these plots:

- In the hits energy spectrum it is shown the population of events chosen for this study (blue area) in comparison to the total energy spectrum of this run (grey line).

- The number of hits histogram correspond directly to the number of strips triggered for each event. In the plot it is shown the sum of the x and y strips that triggered, so we can see that these events vary from 1-2 and up to 8-9 strips per axis, with a pitch of 500 μm between strips.

- The number of tracks in x and y direction are shown, $N_{tracks,x}$ and $N_{tracks,y}$. As it has already been mentioned, energy hits are considered to form a track if they are up to 2 mm away from each other. We would expect most of the x-ray events to have one single track, but we see that there is a considerable large population of two tracks events. These events will be studied separately because the observables are optimised for one track events.

- The balance between the energy collected by the x and y strips present a gaussian-like distribution around zero. Considering its definition, $\frac{E_x - E_y}{E_x + E_y}$, we see that for most of the events the energy collection from both axis is comparable. A small shift to the positives values can be appreciated, but it can be explained by the fact that there were more malfunctioning Y strips than X strips. Overall, this plot shows the expected behaviour for this observable considering x-ray events.

- The mean positions hitmap clearly shows a bigger accumulation of events at the center of the readout where the ^{109}Cd source is positioned. But it shows as well that some strips are not working properly, specially in the y direction. There is

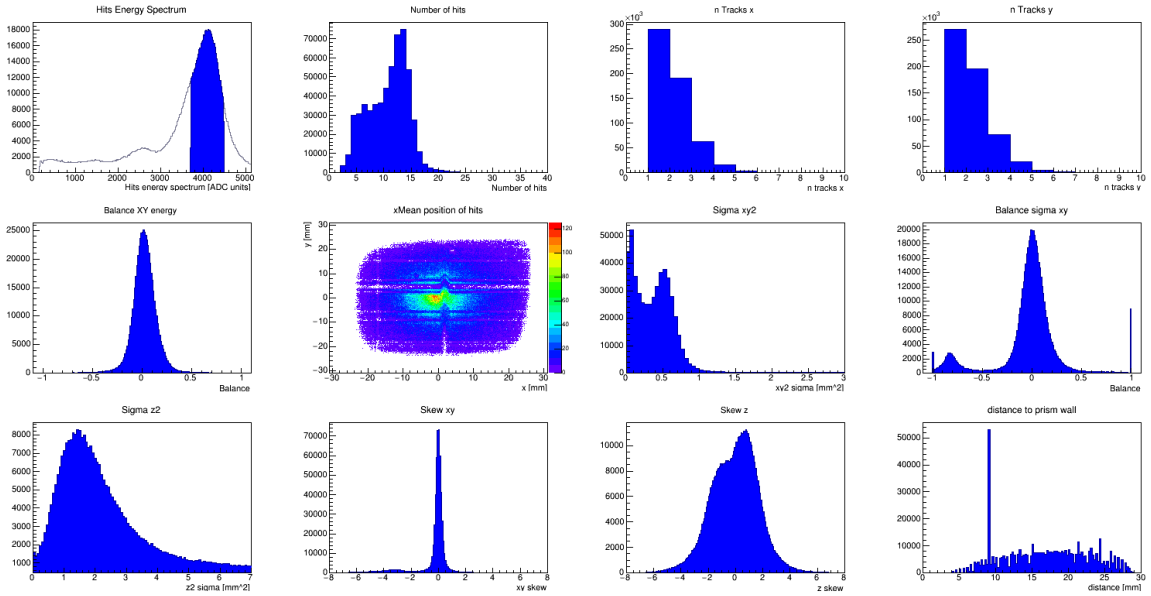

Figure 9.10: Hit and track observables of the 8 keV x-rays from the 20 hours long ^{109}Cd calibration run. From the upper left corner: Hits deposited energy; number of hits; number of tracks in x direction; number of tracks in y direction; balance between the energy collected by the x and y strips; x-y mean positions; $\sigma^2_{x,y}$ i.e. 2D extension of the energy deposit on the readout; balance between the σ_x and the σ_y; σ^2_z i.e. temporal extension of the energy deposit; skewness in the x-y plane; skewness in the temporal direction; distance of the hits to the fiducial prism wall. Further explanation can be found in the text below.

a region around $x = 2$ mm where the y mean position seems to behave differently compared to its surroundings. This will be discussed later, but this perturbation is related with the two tracks events and the internally connected y strip mentioned in section 9.2.3. As it was already explained, most of the observables are optimized for one-single track events because the observable calculations are made at the TRestHitEvent stage, where the tracks are still note defined. And even though the calculation of observables related with the position is weighted, the result for two or more tracks events can be less significant.

- The $\sigma^2_{x,y}$ observable is important because it gives information about the 2D extension of the energy deposit on the Micromegas redout. The 8 keV x-rays are smaller than 1 mm^2, which is equivalent to ∼4-5 strips triggered per direction with a pitch of 0.5 mm. Also, two different populations of events can be distinguished below and above $\sigma^2_{x,y} \sim 0.25\,\text{mm}^2$. This effect will be discussed later on in this section.

- The balance between the standard deviation from the mean positions of the x and y axis, σ_x and σ_y, present mainly a gaussian-like distribution around zero. We can see also a smaller population of events with values around ∼-0.8. Considering the observable definition, $\frac{\sigma_x - \sigma_y}{\sigma_x + \sigma_y}$, this means that these events are wider in the y direction. This effect is caused by the events with more than 1 track in the y direction and the internally connected y strip mentioned in section 9.2.3 that gives fake pulse of small energy (less than 1 keV). As it was mentioned before, the σ_x and σ_y observables are defined at the hits analysis level, and takes into account all the hits of the hit events

despite they are in the same track or not. This will be further discussed later on this section. Finally, some events have a sigma balance observable equals to 1 or -1, and correspond to those events with where only one strip was triggered in one of each directions while the other direction had more than one strip triggered.

- The σ_z^2 observable gives information about the temporal length of the event. It is relevant because it is the only topological information that we can obtain from the measured events with the IAXO-D0 setup. From this characterization we can see that the x-ray events are smaller than 4 mm^2 in the temporal direction (z direction). Again, this observable is also calculated at the hits analysis level, so it does not take into account the hits within the same track but the hits within the entire TRestHitsEvent, and therefore can give misleading information for events with more than one track.

- The skewness (γ_{xy}, γ_z) is a measure of the geometrical asymmetry of the event. It is a statistical parameter that indicates how a distribution deviates from its mean value. Taking into account our definition of this observable shown in equation 6.2.3, a hit event with skewness ∼0 will be symmetrical. On the other hand, a positive value of a hit skewness means that the position of the hit is smaller than the mean position of the hit event, and in the same way, a negative value of a hit skewness means that the position of such a hit is bigger than the mean position of the hit event.

  From the γ_{xy} observable plot we see that the 8 keV x-rays show a Gaussian distribution centred at $\gamma_{xy} = 0$, which means that most of the events are symmetrical on the readout plane. We see a small population around $\sim \gamma_{xy} = -3$ that is caused by the same problematic y strip for the events with 2 or more tracks and it will be addressed later on this section.

  From the γ_z observable plot we see two population of events centred around $\gamma_z \sim -1$ and $\gamma_z \sim 1$. Events with $\gamma_z < 0$ correspond to those where some noise was recorded at the readout before the physical event reached the readout. This first events prior the main event usually trigger one single strip with a very small charge. On the other hand $\gamma_z > 0$ correspond to those events where the main charge is deposited first and then, some other strips with less charge trigger. Most of the one-single track events have $\gamma_z \simeq 0$.

- Finally, the distance-to-wall, d_w, observable indicates the distance of the closest hit of the hit event to the fiducial prism. Accordingly to this definition, $d_w \simeq 0$ mm means that the event contains hits very close to the walls of the fiducial volume, and $d_w \simeq 30$ mm corresponds to the events at the center of the readout. In the plot we can see that the 8 keV x-rays occur towards the center of the readout, and there are very few events with hits close to the edge. This plot also show the cumulation of events with a hit at $d_w \simeq 9$ mm, which correspond to the problematic Y strip already mentioned.

A detailed study of these data has been done in order to identify the best x-ray population sample to define the discrimination cuts. One-single track events and two track

events have been studied separately, and some considerations about the signal observables have been made as well.

One-single track events study

From the CAST Micromegas experience we expect that the x-rays in the axion RoI interact via photoelectric effect in the target gas and therefore they will leave one single energy deposit that will be detected as a one-single track event (i.e. one track on each direction). This is why the observables are defined to be optimum for these kind of events. In this section, the study of one-single track events produced by the 8 keV x-rays from the long ^{109}Cd calibration run will presented. Note that the notation *one-single track* is referring to the number of physical events produced in the TPC, but this will translate into one track in both x and y strips, $N_{tracks,\,x} = 1$ and $N_{tracks,\,y} = 1$, which leads to two total number of tracks for the TRestTrackEvent in the analysis.

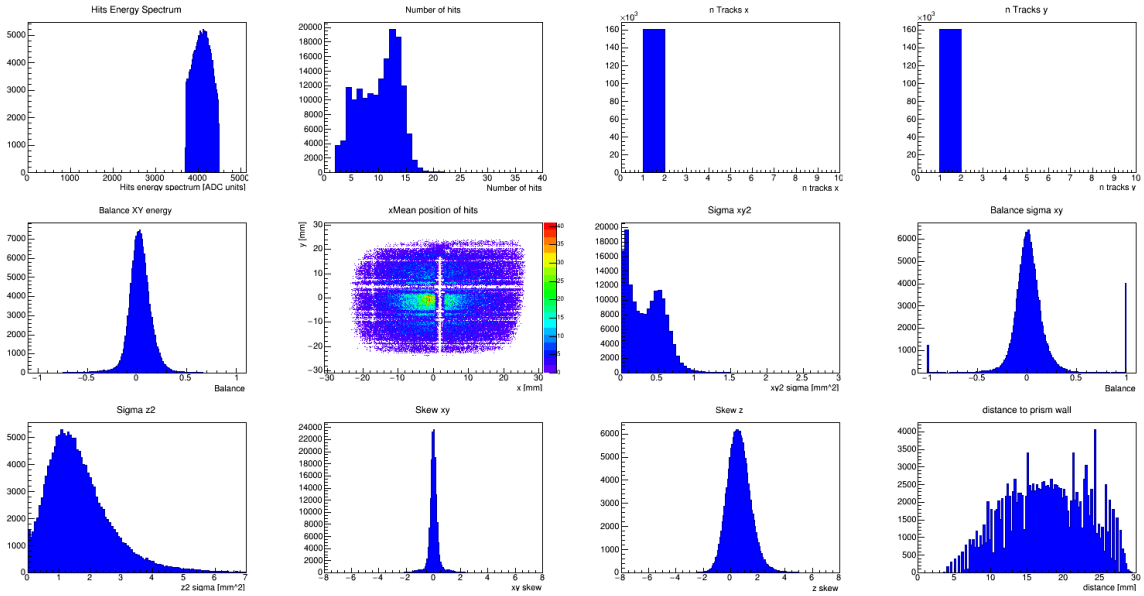

Figure 9.11: Hit and track observables of the one-single track 8 keV x-rays from the 20 hours long ^{109}Cd calibration run. From the upper left corner: Hits deposited energy; number of hits; number of tracks in x direction; number of tracks in y direction; balance between the energy collected by the x and y strips; x-y mean positions; $\sigma^2_{x,y}$ i.e. 2D extension of the energy deposit on the readout; balance between the σ_x and the σ_y; σ^2_z i.e. temporal extension of the energy deposit; skewness in the x-y plane; skewness in the temporal direction; distance of the hits to the fiducial prism wall.

Figure 9.11 shows the most relevant hits and tracks observables for this population of events and can be compared with figure 9.10 as a reference of how the one-single track condition change the rest of the observables distributions. The first consequence is that the number of events is reduced by a ∼3.5 factor, which is a big reduction and a reason to also consider two tracks events under certain circumstances. The second straight forward consequence is that the effects observed in figure 9.10 produced by the problematic y strip do not appear for this event population, and the behaviour of the observables fit with the

expectations for typical x-ray events: rather small energy deposits (with less than 15 hits i.e. strips triggered in total), where the total charge of the event is equally distributed between the x and y strips and also, its topological distribution on the readout plane is round-like and symmetric (as it is shown in the σ_x and σ_y balance and the xy skewness).

Regarding the spatial distribution, the hitmap shows a higher density of events at the center of the readout, over where the source is placed, and now we can perfectly see some bad strips in both x and y directions that affects the center of the readout plane. This bad strips match with the ones previously identified in section 9.2.3. The distance-to-wall observable also shows that the events are distributed towards the center of the readout.

The temporal observables show that most of the events have a $\sigma_z^2 \simeq 1.5$, with translates into an extension of $\sim$2.5 mm, or $\sim$0.1 μs considering a drift velocity of $\sim$2.5 cm μs^{-1} for the mixtures of Ar+Isobutane (2%) at 1.4 bar (see figure 6.11 for gas mixtures properties). With this considered population of events, the skewness in the temporal direction shows a Gaussian-like shape but it is not centred at zero as it would be expected for symmetrical events. The distribution is shifted towards the positive values, peaking at $\gamma_z \simeq 0.5$, which can be explained from the way the condition of *one-single track* event is imposed. As it has already has been mentioned, acquired data events are two-dimensional, which means that the number of tracks is computed separately for the x and y axis. A one-single track event will have one track per axis, which in most of the cases correspond to the scenario where the same physical event deposited charge in both x and y strips. But it can happen that the entire charge of an event is registered by a single strip in one direction, and a noisy strip triggers in the other, so the TRestTrackEvent end up with one track per axis but from different physical events. This difference in the time of the events can shift the temporal skewness distribution.

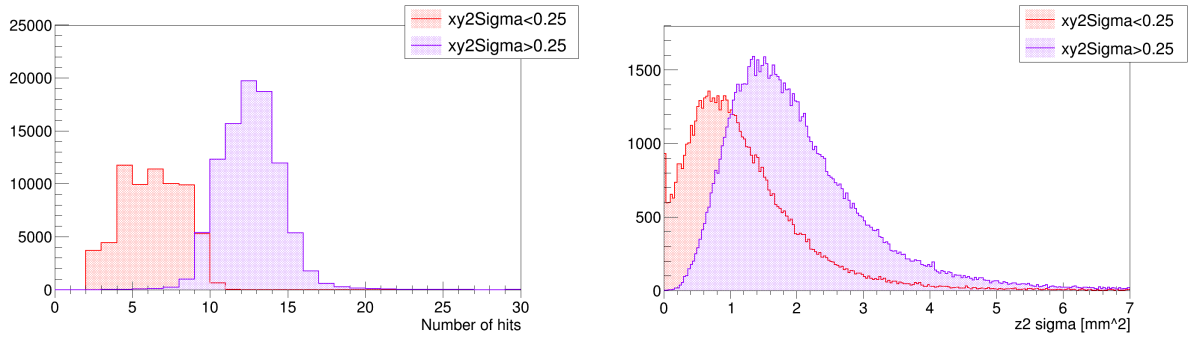

Figure 9.12: Correlation between the size of the events on the Micromegas readout, $\sigma_{x,y}^2$, **(Left)** and the number of hits (i.e. strips that triggered) **(Right)** and the temporal extension of the events for the 8 keV x-rays with one-single track from the 20 hours long ^{109}Cd calibration run. Bigger events ($\sigma_{x,y}^2 \gtrsim 0.25\,\text{mm}^2$) will have more hits and a bigger σ_z^2.

Finally, an important remark has to be made about the $\sigma_{x,y}^2$ observable, where two different populations of events can be very well distinguished, below and above $\sigma_{x,y}^2 \sim 0.25\,\text{mm}^2$. This effect is correlated with the number of hits (i.e. strips that triggered) of the event, as it is shown in figure 9.13, and also with its temporal extension σ_z^2. This could be explained by the fact that the 8 keV x-rays are produced in the copper

parts of the detector chamber. Taking into account that the walls of the chamber are internally shielded by a PTFE layer, most of the events would come from the copper cathode at the furthest part of the chamber from the readout, or from the copper raquette that acts as the base of the Micromegas readout. This way, the events produced in the copper cathode will interact at the top part of the chamber and will travel a longer distance through the gas. Therefore, they will diffuse more and will turn into bigger events.

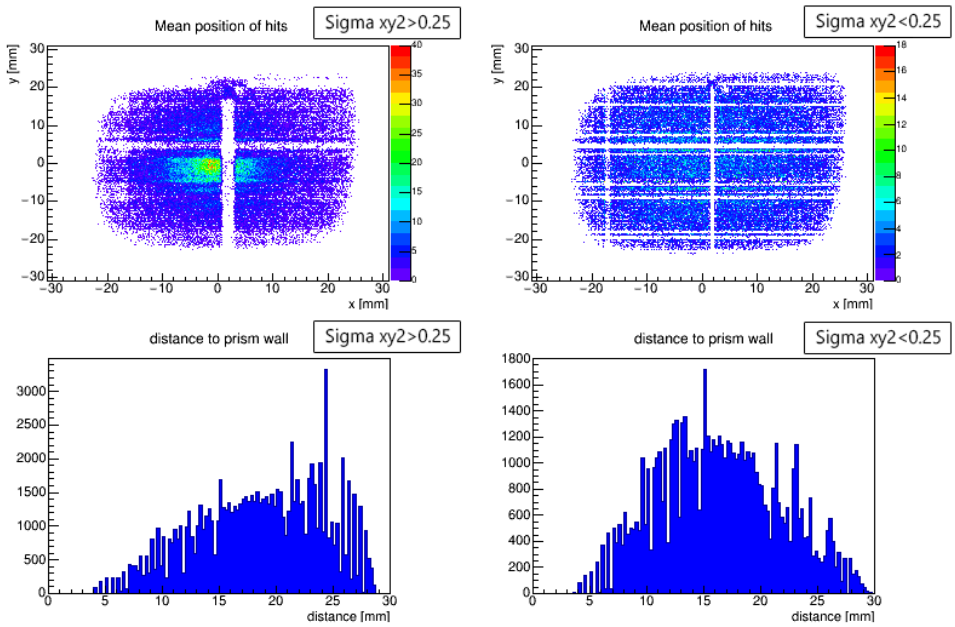

Figure 9.13: Mean position hitmap and the distance to the fiducial prism wall of the 8 keV x-rays with one-single track from the 20 hours long ^{109}Cd calibration run with **(Left)** $\sigma^2_{x,y} > 0.25\,\mathrm{mm}^2$ and **(Right)** $\sigma^2_{x,y} < 0.25\,\mathrm{mm}^2$.

The same conclusion can be reached from the hitmaps in figure 9.13, where it is shown the mean position of the 8 keV events with $\sigma^2_{x,y} > 0.25\,\mathrm{mm}^2$ (left) and with $\sigma^2_{x,y} < 0.25\,\mathrm{mm}^2$ (right). We see that events with bigger 2D print will be more frequently produced at the center of the chamber as a product of the calibration x-rays that come from the pipe interacting with the copper cathode. On the other hand, events with smaller 2D print are homogeneously spread on the readout surface.

This effect is actually very interesting because it allows us to correlate the 2D size of the event with its temporal coordinate, so we can apply a cut in the z-direction to only consider the 8 keV x-rays that interacted at the furthest part of the chamber and are a more representative sample than the ones produced close to the readout. Figure 9.14 shows the hit event observables from this specific event population and the results fit with the expected behaviour of an event population produced by x-rays coming from the pipe. This information will be used in the following step of the analysis in order to define the cuts for the background discrimination process.

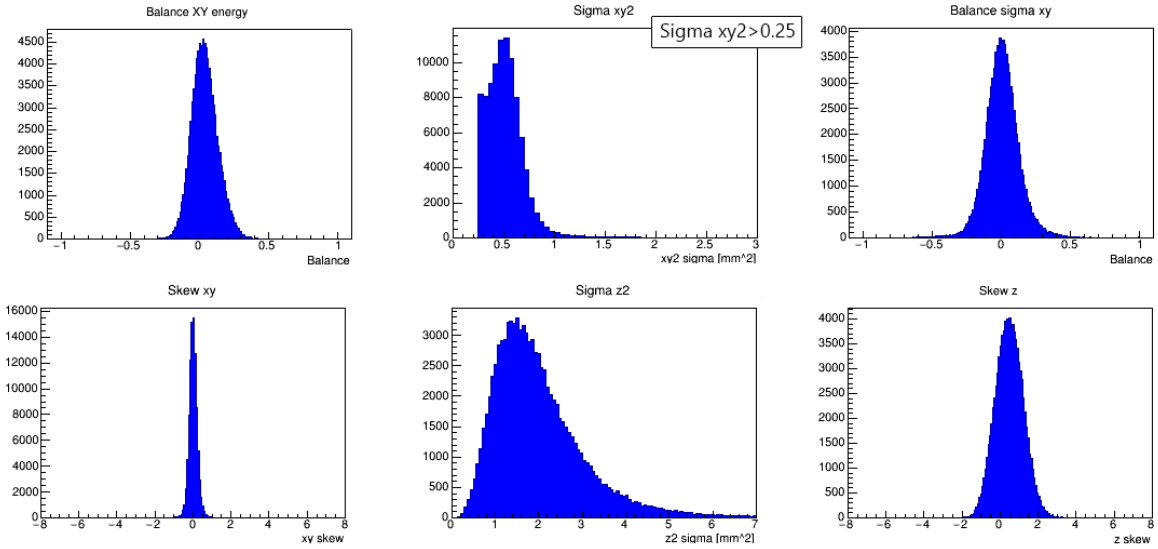

Figure 9.14: Hit event observables of the 8 keV x-ray events with one-single track and $\sigma^2_{x,y} > 0.25$ that will be used for the background discrimination process. In this figure, starting from the top left corner, the following observables are shown: balance between the energy collected by the x and y strips; $\sigma^2_{x,y}$ i.e. 2D extension of the energy deposit on the readout; balance between the σ_x and the σ_y; skewness in the x-y plane; σ^2_z i.e. temporal extension of the energy deposit; skewness in the temporal direction.

Two tracks events study

Although we expect that events produced by x-rays will have one-single energy deposit, from the IAXO-D0 ^{109}Cd calibration data we obtain a not negligible amount of 8 keV x-rays events with two tracks. These *two tracks events* can have two tracks in either x or y direction, while in the other they only have one track, or they can have two tracks in both x and y directions. It turns out that from all the events at the 8 keV peak, ∼28% of them have one-single track, i.e. only one track per direction, and ∼45% of them have two tracks, i.e. two tracks in at least one direction but no more than four tracks in total. Two tracks events turn out to be an important part of the total 8 keV x-rays.

This not negligible amount of two tracks events can be caused due to the fact that the trigger threshold of the acquisition electronic card was set very low, so small noise could actually have been recorded as a physical signal. An example of a two track event is shown at the top of figure 9.15. Studying these events, we can see that some of them are caused by the problematic Y strip (Y=20,8 mm) that is internally connected, as it is shown at the bottom of figure 9.15. This effect is also shown in the distance-to-wall observable in figure 9.17.

Since these two tracks events cannot be discarded, a separated study needs to be done in order to check if the same observables that have been used for one-single track events will be suitable, or instead a new set of cuts needs to be defined in order to consider them for the total background. A very important observable for this purpose is the energy balance between the total energy of the event in each direction (E_x and E_y) and the energy

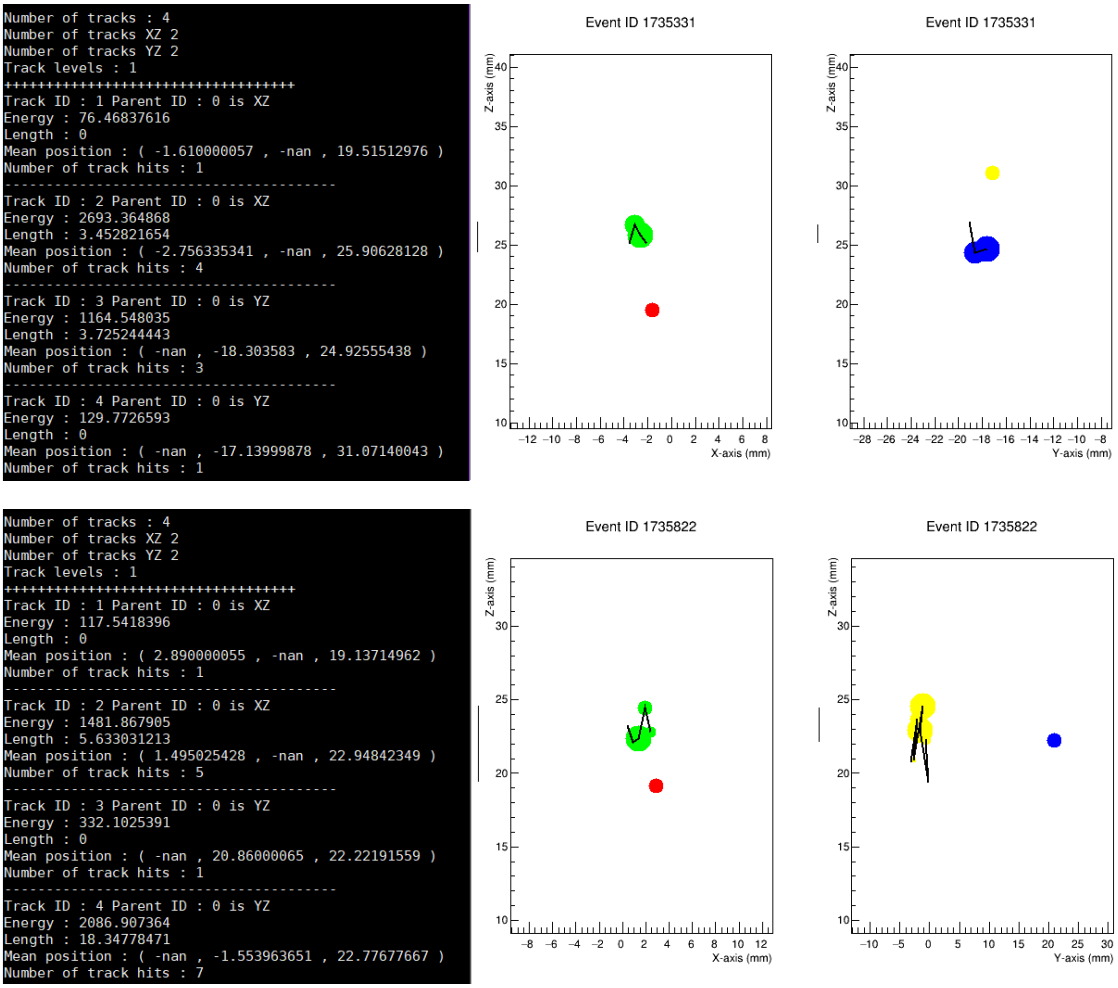

Figure 9.15: Visualization of a 8 keV track events from a ^{109}Cd calibration run with 2 tracks per axis. On the left, some information about the number of tracks of the event, the energy and mean position of the tracks is shown. **(Top)** An example of an x-ray event with two tracks, where one of them has almost all the energy of the event and the other one is probably noise. **(Bottom)**. Another example like the top one, but in this case, the problematic y strip at y=20.8 mm triggered with a small energy.

of the most energetic track in that direction (E_x^{max} and E_y^{max}):

$$Balance_x = \frac{E_x - E_x^{max}}{E_x + E_x^{max}} \quad \text{and} \quad Balance_y = \frac{E_y - E_y^{max}}{E_y + E_y^{max}} \tag{9.2}$$

This observable allows us to select only those events which the total energy of the event is concentrated mostly in one of the tracks. Figure 9.16 shows the energy balance for the x and y strips, where different regions are limited depending on the percentage of the energy of the most energetic track related to the total energy. In previous CAST analysis, two track events with a most energetic track down to 85% of the total energy of the event (i.e. $Balance_{x,y} < 0.08$) were considered for the background estimations. In this case, events with a most energetic track with the 85% of the total energy are a ∼52% of the total two track events, and a ∼23% of the total number of events.

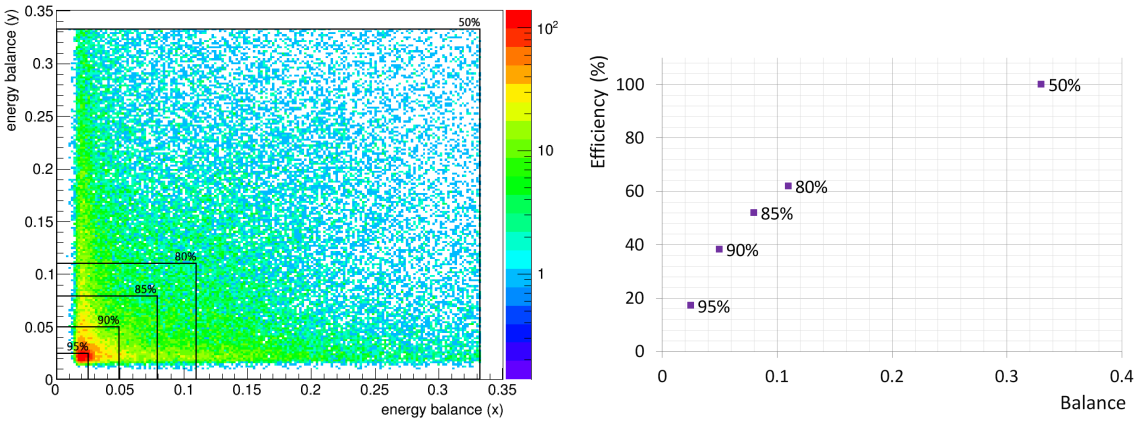

Figure 9.16: (Left) Balance$_x$ versus Balance$_y$ observables for events with two tracks per direction. The regions illustrate different energy balance cuts. The minimum percentage of the energy of the most energetic track respect to the total energy is shown for each region. **(Right)** Percentage of the events that pass certain energy balance cuts. In the plot, the minimum percentage of the energy of the most energetic track respect to the total energy is shown for each balance cut.

Figure 9.17 shows the main hit and track observables for the 8 keV x-rays with two tracks events. Even though the observables are optimized for one-single track events, they do not change significantly for the two tracks events with the energy balance conditions. This is because the observables are weighted and it is imposed that the second track of the event has to be lighter, so it does not affect the final result. The same two populations of events depending on their $\sigma^2_{x,y}$ is visible, and the size of the events in both the xy plane and the z direction are compatible with the ones obtained for the one-single track events.

However, there is a small population visible at the balance between the σ_x and σ_y, and also at the xy skewness observable. These populations are correlated and they correspond to the internally connected strip previously mentioned. This strip is placed at $\sim$y=21 mm, so the balance and the skewness of these events are shifted towards the negative values of both observables. These events will not be taken into account for the background estimates of this work.

With all these considerations, figure 9.18 shows the main observables of the 8 keV x-rays with two tracks events where the most energetic track has at least the 85% of the total energy (i.e. $Balance_{x,y} < 0.08$), and $\sigma^2_{x,y} > 0.25$. These observables are compatible with the ones obtained for one-single track events at the same conditions (figure 9.14), and also compatible with the expected behaviour of an energy deposit left in the gas by an x-ray. Therefore, there is no need to define different discrimination cuts for the two tracks events.

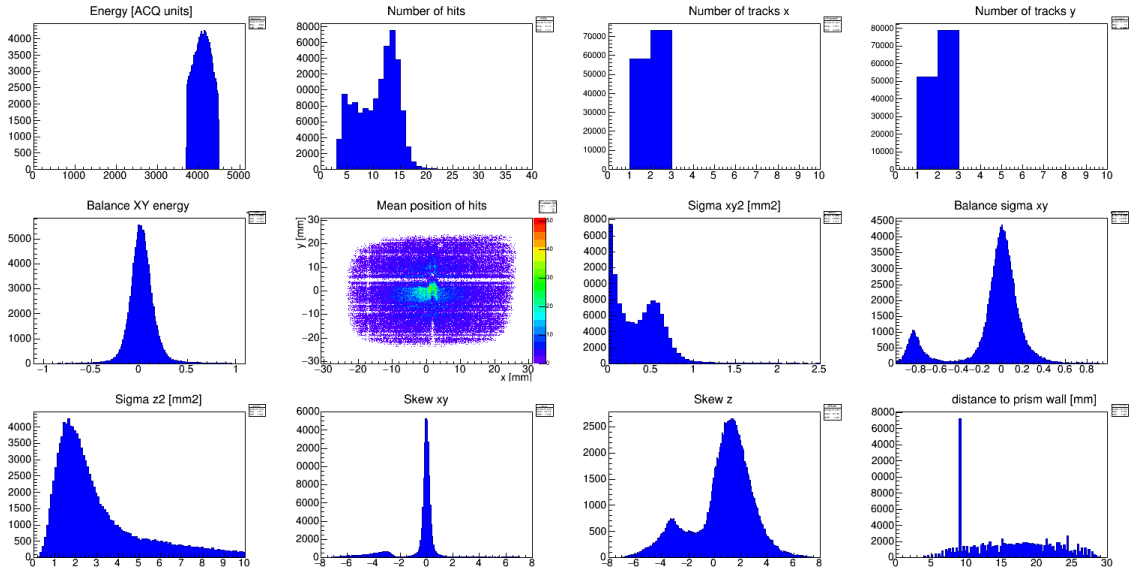

Figure 9.17: Hit and track observables of the 8 keV x-ray two tracks events. In this figure, starting from the top left corner, the following observables are shown: TRestHitEvent deposited energy; number of hits; number of tracks in x direction; number of tracks in y direction; balance between the energy collected by the x and y strips; x-y mean positions; $\sigma^2_{x,y}$ i.e. 2D extension of the energy deposit on the readout; balance between the σ_x and the σ_y; σ^2_z i.e. temporal extension of the energy deposit; skewness in the x-y plane; skewness in the temporal direction; distance of the hits to the fiducial prism wall.

Signal observables study

In previous CAST background discrimination analysis, some discriminants from the shape of the signal pulse were also used. Although the pulse shape analysis in this version of the code is not very complex, some considerations can be made from the signal observables.

The most meaningful signal observables are the rise time and the rise slope. The rise time is defined as the time between the first point over the signal analysis threshold and the maximum amplitude point of the signal, and the rise slope is the rate between the amplitude and the rise time of the signal. A graphic definition is shown in figure 9.19. The observables are the average value of the individual rise time (or rise slope) of each signal in the signal event.

Comparing the mentioned observables between a IAXO-D0 background run and a ^{109}Cd calibration run (figure 9.19), the rise time average is pretty similar for both runs, but a different behaviour is observed in the rise slope observable. The events from the background run have a smaller rise slope, which is compatible with shorter and wider signal pulses. On the other hand, the events from the ^{109}Cd calibration run are bigger, which fits with higher and sharper signal pulses. Also, the two peaks correspond to the 8 keV and 22 keV events. Since the amplitude has ADC arbitrary units, and the rise time has time bin arbitrary units, the units of the rise slope observable are also arbitrary.

If we take the same one-single track 8 keV events with $\sigma^2_{x,y} > 0.25$ that have

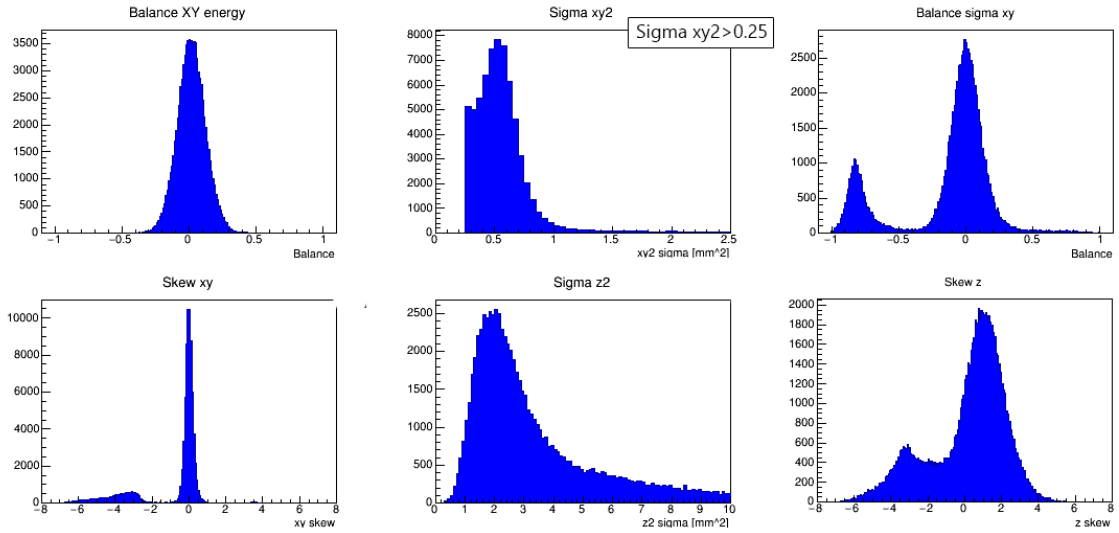

Figure 9.18: Hit event observables of the 8 keV x-ray two tracks events and $\sigma^2_{x,y} > 0.25$ that will be used for the background discrimination process. In this figure, starting from the top left corner, the following observables are shown: balance between the energy collected by the x and y strips; $\sigma^2_{x,y}$ i.e. 2D extension of the energy deposit on the readout; balance between the σ_x and the σ_y; skewness in the x-y plane; σ^2_z i.e. temporal extension of the energy deposit; skewness in the temporal direction.

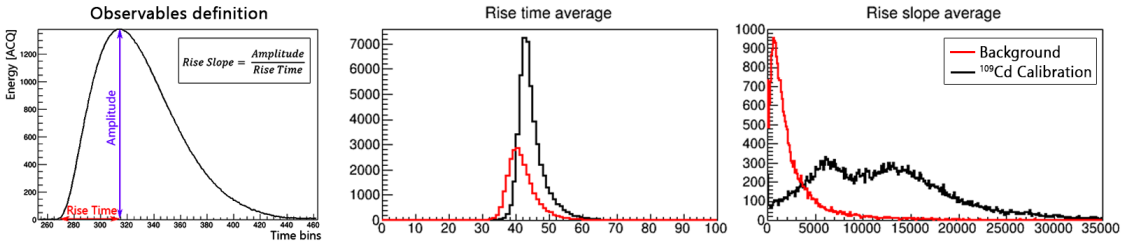

Figure 9.19: **(Left)** Definition of the signal observables: *rise time* and *rise slope*. The energy is expressed in ACQ units. **(Center)** Histograms of the rise time **(Right)** and rise slope observables for a background run (red) and a ^{109}Cd calibration run (black).

been considered previously as the most representative population of events for the x-ray characterization, we obtain that these events have an evident cut at low values of rise slope, as it is shown in figure 9.20.

Applying a cut using the rise slope observable (rise slope ∼3000) to the background and calibration runs, we find that events with small rise slope correspond to low energy events below 2 keV. On the other hand, the cut barely reduces a ∼6% the total number of events in the calibration run, and ∼0.6% the number of one-single track and 8 keV events, resulting in a very efficient cut for the population of events chosen for the x-ray characterization. Nevertheless, this cut has to be taken with precaution because it is heavily dependent to the energy of the event. A calibration with ∼3 keV x-rays would be needed in order to prove the efficiency of the cut for that particular energy.

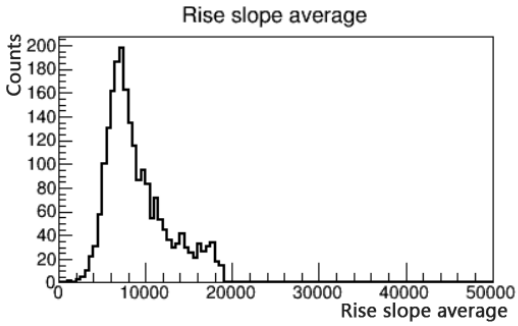

Figure 9.20: Rise slope average observable for one-single track 8 keV events with $\sigma^2_{x,y} > 0.25$ from a ^{109}Cd calibration run.

9.4 IAXO-D0 Micromegas background study

After the x-ray characterization, the following steps have been to process all the data taken in this first campaign with the REST software and calibrate in energy all the background spectra using the corresponding ^{109}Cd calibration runs. A first value of the IAXO-D0 prototype background can be obtained before the discrimination process is applied.

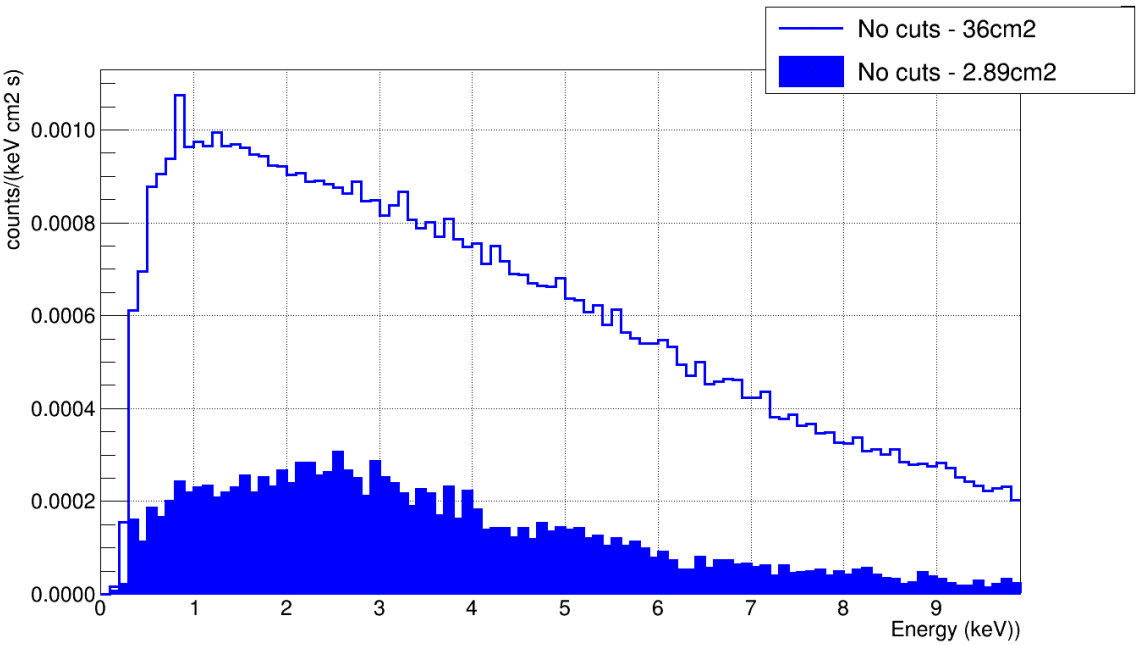

Figure 9.21: Background energy spectrum of the IAXO-D0 prototype before the analysis process. The line correspond the background of the entire readout surface (36 cm^2), and the filled histogram correspond to the background of a central smaller area with the size of the window aperture (2.89 cm^2). The background is reduced in a factor of ∼5 with the fiducial cut.

Figure 9.21 shows the raw background energy spectra in the IAXO energy range of interest, where only two cuts were applied in order to discard the low energy noise: they were only considered the events with non-zero number of tracks in either x or y

dimension. This first cut has an efficiency of ∼95% and it mainly discards events with energy below ∼0.2 keV. The background obtained for all the readout surface (36 cm^2) is $5.93 \pm 0.01 \times 10^{-4}$ counts $keV^{-1}\,cm^{-2}\,s^{-1}$, and it is reduced when only the window area is considered (2.89 cm^2) to $1.28 \pm 0.02 \times 10^{-4}$ counts $keV^{-1}\,cm^{-2}\,s^{-1}$.

Once the raw background has been obtained, the next step has been to apply the discrimination process to the background runs, and finally the final background level has been computed. As it was already explained, the discrimination process consists on discarding all the events which observables do not match with the x-rays observables. This has been done by applying cuts to the background runs so only the events whose observables are in the range of the cuts have been kept.

In this section, the cuts for the background discrimination are shown, as well as their efficiency, and the background level of the IAXO-D0 prototype after the discrimination analysis is presented.

9.4.1 Discrimination cuts and efficiency

Using the information provided by the x-rays characterization, some discriminants have been defined based on the most significant observables for x-ray recognition. One-single track and two track events have been studied separately and both have lead to similar characterization observables (illustrated in figures 9.14 and 9.18).

The specific values of the observables that have been used as discrimination cuts are shown in table 9.2. First, the cuts at track event level allow us to only keep one-single track events, i.e. events with one track in both x and y dimensions, or two track events, i.e. events with more than two tracks in total but up to two tracks per axis, with its most energetic track containing at least the 85% of the total energy. Then, the cuts at hit event level have been applied to these two populations of events separately. The observables that have been chosen for the discrimination process are the balance between the energy collected by the x and y strips, the balance between the position standard deviation σ_x and σ_y, the 2D extension of the event print on the readout, or σ_{xy}^2, the two-dimensional symmetry, or γ_{xy}, and finally the temporal extension of the event, σ_z^2.

The fiducial cut has also been applied at hit event level with the distance-to-wall, d_w, observable. This cut is either off when all the readout surface is considered, or it only keeps the events that happen in the central square of $8.5 \times 8.5\,mm^2$, i.e. the events that are at a distance of 21.5 mm of the fiducial prism wall or further. This surface of 2.89 cm^2 correspond to the size of the cathode window where the x-rays are expected to come from. This observable is defined so the events need to be fully contained in the area to be considered.

Finally, the only cut defined at signal event level has been the rise slope average, and has been applied separately as a most optimistic background result. Further pulse-shape analysis needs to be developed in order to fully understand the cuts at this level.

Observable	Value or range	Comment
Cuts at track event level		
$N_{tracks,x}$	1	Cuts for one-single track events.
$N_{tracks,y}$	1	
$N_{tracks,x}$	< 3	Cuts for two tracks events.
$N_{tracks,y}$	< 3	
$N_{tracks,x} + N_{tracks,y}$	> 2	
$Balance_{x,y}$	< 0.08	
Cuts at hit event level		
E_x - E_y Balance	[-0.3, 0.3]	Hit shape cuts that describe a small, punctual like and symmetric energy deposit. These cuts are defined to be optimal for one-single track events.
σ_x - σ_y Balance	[-0.3, 0.3]	
σ_{xy}^2	[0.25, 0.7]	
σ_z^2	[0.2, 4]	
γ_{xy}	[-0.5, 0.5]	
d_w (mm)	[21.5, 30]	This is the fiducial cut that is applied to consider only the center of the readout when needed.
Cuts at signal event level		
Rise Slope Average	> 3000	This cut is applied separately due to its low efficiency at 3 keV (see table 9.3).

Table 9.2: Background discrimination cuts and their corresponding values. They have been chosen so the efficiency at the center of the readout for the 8 keV x-rays one-single track and σ_{xy}^2 >0.25 representative population was higher than 90% for each individual cut.

The values for the discrimination cuts have been chosen so the efficiency at the center of the readout for the 8 keV x-rays one-single track representative population was higher than 90% for each cut individually. Table 9.4 shows the efficiency of each individual cut at 8 keV and 3 keV, considering all the readout or only the central part, for both one-single track and two tracks events. The efficiency has been obtained by the percentage of events with σ_{xy}^2 >0.25 that pass each specific cut. These values have been computed from the long ^{109}Cd calibration run.

Since the observables are defined to be optimum for one-single track events, some of the cuts are not as efficient for two tracks events. Also, the rise slope average cut leads to a very low efficiency for 3 keV events. This might look like a problem at first sight because the axion signal is expected to be a 3-4 keV x-ray at the center of the readout. But since our calibration source does not emit at 3 keV, the events that are being discarded actually come from secondary x-rays from the walls of the chamber. As it was already discussed, the x-ray sample in this work is not the ideal one for a proper characterization.

9.4.2 Background level for IAXO-D0

Once the x-ray characterization has been done and the discrimination cuts have been defined, the final step has been to process al the acquired data using the REST analysis

Observable	Value or range	Efficiency (%) at 8 keV		Efficiency (%) at 3 keV	
		All readout ($36\,cm^2$)	Window ($2.89\,cm^2$)	All readout ($36\,cm^2$)	Window ($2.89\,cm^2$)
One-single track events					
E_x - E_y Balance	[-0.3, 0.3]	99.2	99.3	92.5	90.9
σ_x - σ_y Balance	[-0.3, 0.3]	96.9	98.3	85.2	88.4
σ_{xy}^2	[0.25, 0.7]	87.4	91.7	92.9	93.7
σ_z^2	[0.2, 4]	94.2	95.7	79.0	89.7
γ_{xy}	[-0.5, 0.5]	96.4	97.2	92.6	92.0
Rise Slope Average	> 3000	99.1	99.2	*11.3*	*9.8*
Two tracks events					
E_x - E_y Balance	[-0.3, 0.3]	99.1	99.4	88.9	91.6
σ_x - σ_y Balance	[-0.3, 0.3]	76.9	98.6	67.0	88.1
σ_{xy}^2	[0.25, 0.7]	66.5	89.6	66.6	90.1
σ_z^2	[0.2, 4]	63.4	59.6	39.7	46.4
γ_{xy}	[-0.5, 0.5]	75.9	96.7	69.9	89.3
Rise Slope Average	> 3000	97.8	98.0	*10.9*	*8.2*

Table 9.3: Efficiency of the cuts for one-single track and two tracks events from the x-ray population with σ_{xy}^2 >0.25 of a IAXO-D0 ^{109}Cd calibration at 8 keV and 3 keV (with a resolution of the 19% FWHM). Statistical errors of the efficiency for the one-single track events is less than 2% in all cases, and in the case of two tracks events, less than 4%.

chain described in section 9.3.1: the TRestRawSignalEvents have been processed in order to obtain TRestTrackEvent outputs with all the signal, hits and tracks observables computed. Then, the cuts have been applied by the REST plots tool to the background energy spectra and a root macro has been used to calibrate the background spectra with its corresponding calibration run, and to scale it to express it in the standard IAXO background units ($counts\,keV^{-1}\,cm^{-2}\,s^{-1}$). Finally, the background values for the different scenarios that were described along this section have been computed using equations 7.2.1.

Table 9.4 shows the background levels obtained for the IAXO-D0 prototype in the IAXO energy RoI ([1,10] keV) under different considerations. One-single track events and two track events have been treated separately, and their contribution to the background has been computed applying only the cuts at hit event level, that are related to the three-dimensional topology of the event, and also applying the signal event level cut, which refers to the rise slope of the signal pulses (see table 9.2 for specific values), both for the entire readout surface ($36\,cm^2$) and the smaller central area that is the size of the x-ray window ($2.89\,cm^2$).

The total background has been calculated as the combination of one-single track and two tracks events individual backgrounds after the discrimination cuts. Figure 9.22 shows the total background spectra of the IAXO-D0 prototype before and after the discrimination cuts for all the readout surface. The discrimination process results in a background reduction of $\sim 10^2 - 10^3$ depending on the energy region, which was

Events	Cuts applied	Surface considered	Background level ($\mathrm{keV^{-1}\,cm^{-2}\,s^{-1}}$)
One-single track	Hit cuts	All readout	$(2.08 \pm 0.06) \times 10^{-6}$
		Window	$(1.7 \pm 0.2) \times 10^{-6}$
	Hit and signal cuts	All readout	$(5.7 \pm 0.3) \times 10^{-7}$
		Window	$(1.2 \pm 0.2) \times 10^{-6}$
Two tracks	Hit cuts	All readout	$(2.6 \pm 0.2) \times 10^{-7}$
		Window	$(4.0 \pm 0.9) \times 10^{-7}$
	Hit and signal cuts	All readout	$(1.9 \pm 0.2) \times 10^{-7}$
		Window	$(3.8 \pm 0.9) \times 10^{-7}$
Total	Hit cuts	All readout	$(2.34 \pm 0.07) \times 10^{-6}$
		Window	$(2.1 \pm 0.2) \times 10^{-6}$
	Hit and signal cuts	All readout	$(7.6 \pm 0.4) \times 10^{-7}$
		Window	$(1.5 \pm 0.2) \times 10^{-6}$

Table 9.4: Background of the IAXO-D0 prototype for the IAXO energy RoI [0,10] keV. The background coming from one-single track and two tracks events are computed separatedly, and the total background is the combination of both. For *hit cuts*, only the cuts at hit event level have been applied, and for *hit and signal cuts*, both hit and signal event level cuts have been applied (see table 9.2). The surfaces considered for the background calculation are: all the readout ($36\,\mathrm{cm^2}$) or a central area of the size of the window ($2.89\,\mathrm{cm^2}$).

expected from previous CAST discrimination analysis experience. Two tracks event contribute approximately one order of magnitude less than the one-single track population of events, but their contribution is still significant. Taking into account that the most conservative scenario would be the case where only cuts at hit event level have been applied, the total background obtained for the IAXO-D0 prototype for ∼450 hours of background is $(2.34 \pm 0.07) \times 10^{-6}\,\mathrm{counts\,keV^{-1}\,cm^{-2}\,s^{-1}}$ for the total readout area and $(2.1 \pm 0.2) \times 10^{-6}\,\mathrm{counts\,keV^{-1}\,cm^{-2}\,s^{-1}}$ for the central reduced window area. These results are compatible with previous background values that have been measured for identical detectors in similar setups.

Figure 9.23 shows the total IAXO-D0 background after the discrimination process, as well as the individual contributions of the one-single track events and two tracks events populations for all the readout surface. The main contribution to the background comes from the one-single track events at low energies, while at energies above ∼5 keV, two tracks events become more significant. The small cumulation of events at 8 keV is compatible with the copper fluorescence. Also, this spectra show a bigger cumulation of events in the range of 1-3 keV, which remembers the shape of the simulated muon spectrum after the discrimination cuts. Figure 9.24 show the hitmap of the events that pass the discrimination cuts for both 0-10 keV and 0-3 keV range. The cumulation of events at low energies comes from events that interact near to the readout borders and therefore, they are compatible with secondary emissions from the gas chamber.

Taking this into consideration, it is clear that the application of a fiducial cut rejecting the events that are near to the readout borders can reduce the background level.

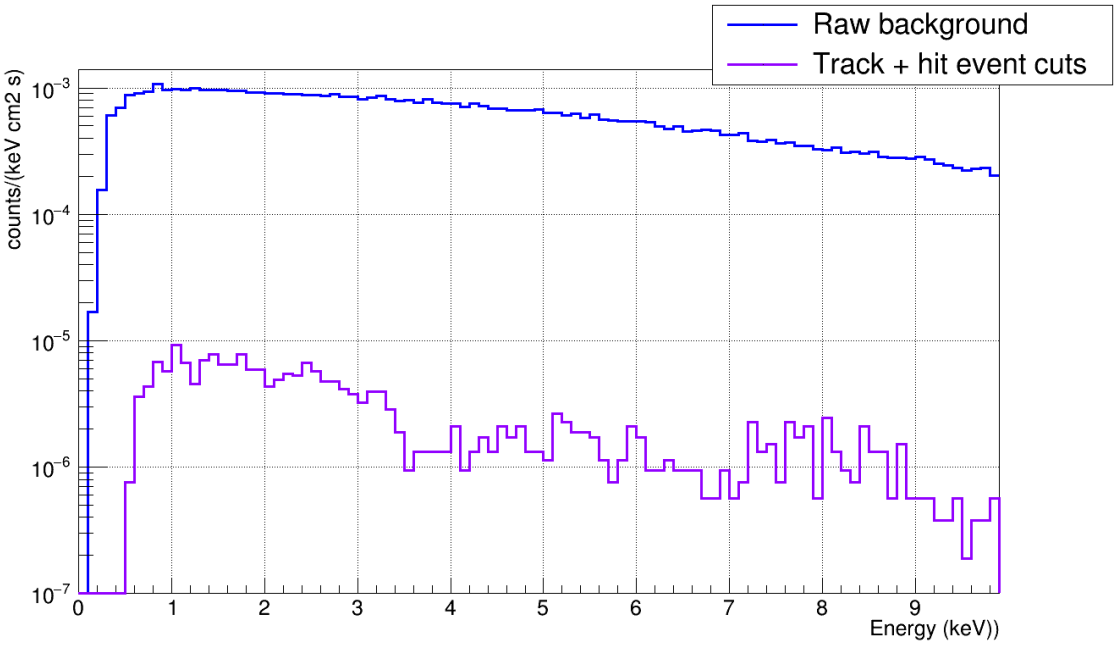

Figure 9.22: Background of the IAXO-D0 prototype for the IAXO energy RoI. These spectra correspond to ∼450 hours of background and all the readout surface (36 cm^2). The raw background spectrum (blue line) is plotted versus the background spectrum after the discrimination cuts (purple line). One-single track and two tracks events have been considered, and the cuts at hit event level have been applied.

Figure 9.25 shows the IAXO-D0 background after the discrimination cuts and also, at the reduced window area. In this spectrum, the events at low energy are no longer dominant, and the copper fluorescence peak at 8 keV as well as its escape peak 5 keV are visible.

Finally, the cut at signal level seem to be very energy dependent, reducing mostly the contribution from the lower part of the spectrum. This could be a good cut because in this case, it is rejecting low energetic background events from fluorescences and secondary emission from the detector chamber. Even though, whether or not this cut would reject low energetic x-rays coming from the pipe needs to be further studied with a proper x-ray calibration in the complete energy range of interest. This is why this cut has been applied separately as an optimistic background estimation, obtaining a total of 401 ± 6 counts spread over all the readout surface, and only 65 ± 2 counts for the window reduced area for the total background data taking campaign (errors for 1σ standard deviation). These results lead to values of background of $(7.6 \pm 0.4) \times 10^{-7}$ counts $\mathrm{keV}^{-1}\,\mathrm{cm}^{-2}\,\mathrm{s}^{-1}$ for all the readout and $(1.5 \pm 0.2) \times 10^{-6}$ counts $\mathrm{keV}^{-1}\,\mathrm{cm}^{-2}\,\mathrm{s}^{-1}$ for the window reduced area. This levels of background are comparable and even lower than the best background obtained for the CAST Micromegas detectors including the vetoes reduction, which supports the need of implementing a more complete pulse-shape analysis.

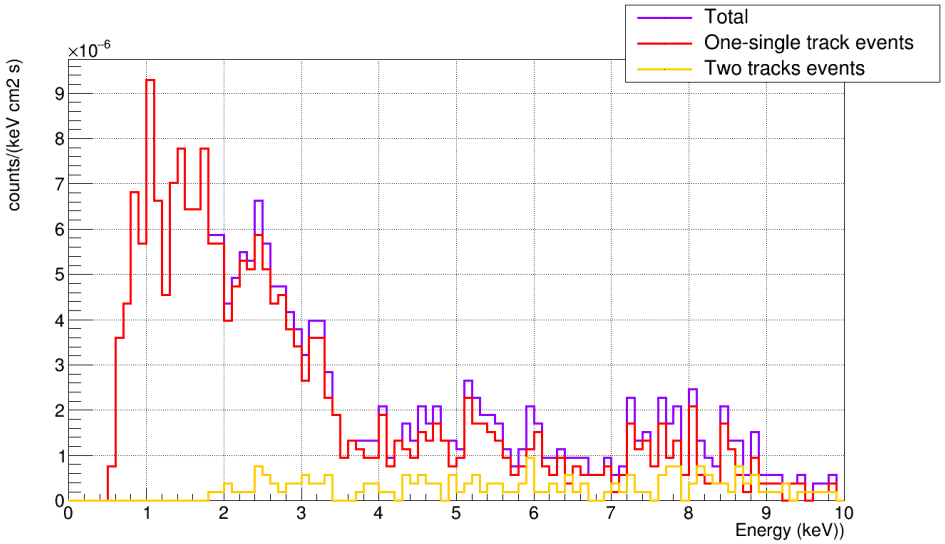

Figure 9.23: Background of the IAXO-D0 prototype for the IAXO energy RoI after the discrimination cuts. The background from one-single track events (red line) and from two tracks events (yellow line) are compared, and the total background is the combination of both (purple line). These spectra correspond to ∼450 hours of background and all the readout surface (36 cm^2), and only hit event level cuts were applied (see table 9.2).

9.5 Summary

The IAXO-D0 prototype has been commissioned at the University of Zaragoza as a part of the IAXO project agenda. It has been motivated by the need of proving the detector performance and background level for the latest Micromegas design used in CAST, which showed the best performance and lowest background levels among the CAST detectors, without the space limitations of the CAST helioscope.

The commissioning involved the design of new calibration and gas systems, and also the upgrade of the acquisition electronic cards to the new AGET-based technology. One of the IAXO *pathfinder* spare radiopure Micromegas detector has been implemented with a mixture of Ar+Isobutane (98/2)% as the drift gas and with an enlarged external lead shielding. Also, the acquisition system has been updated to be compatible with the REST software.

The first data taking campaign with the IAXO-D0 prototype started the sixteenth of July of 2018 and it took ∼450 hours of effective background data, with daily calibrations with a ^{109}Cd source. During the data taking campaign, the Micromegas detector showed stable performance with no sparks and also, very stable gains for the 8 keV and 22 keV peaks of the calibration spectrum. The energy resolution obtained has been ∼19% FWHM at 8 keV and ∼12% FWHM at 22 keV (∼8% FWHM for the 19-22 keV peak of the source).

REST software has been used for the data analysis. First, the raw data from the acquisition has been formatted to a root TRestRawSignalEvents file, and then, a TRestSignalAnalysisProcess has calculated the corresponding observables from the data

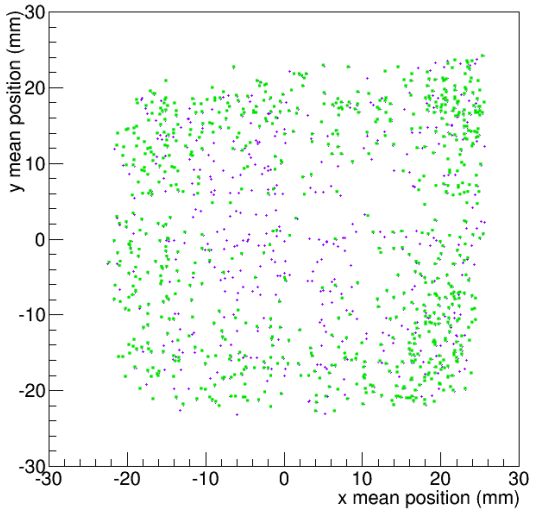

Figure 9.24: Mean hit event position hitmap of the one-single track events on the IAXO-D0 readout for the IAXO energy RoI after the discrimination cuts. Purple crosses represent all the events that passed cuts and the green dots represent the events in the range of [0,3] keV. The low energy events that pass the cuts hit the readout near to the borders.

pulses. After a *zero suppression*, the TRestSignalEvent files have been transformed to TRestHitsEvent files with information about the position and the energy of the events. Then, A TRestHitsAnalysisProcess has computed the observables at hit event level, and finally, tracks have been searched from close hits and saved into a TRestTrackEvent file. A last TRestTrackAnalysisProcess has obtained the observables at track event level.

To define the event rejection criteria, an x-ray characterization has been done in order to know how the observables from x-ray events look like, and therefore, to be able to reject all the events that do not fit in such definition. For this purpose, the 8 keV event population from a long ^{109}Cd calibration has been used. The study of their observables has shown that the 2D extension of the charge of the event on the readout surface, i.e. the σ_{xy}^2 observable, allows introducing a temporal discriminant to reject events that are produced too close to the anode, and are unlikely to have been produced by x-rays coming from the pipe. One-single track events and two tracks events were studied separately, and the conclusion from the x-ray characterization has been that x-ray events leave small and symmetric energy deposits on the readout of the detector. From these conclusions, the discrimination cuts have been defined as limits for the most representative observables with an efficiency of $\gtrsim$90% for the selected initial event population.

Finally, the background data have been properly calibrated with the information from the daily ^{109}Cd runs and the discrimination process has been applied. The background levels obtained for ∼450 hours of data taking and for the most conservative scenario have been $(2.34 \pm 0.07) \times 10^{-6}$ counts keV^{-1} cm^{-2} s^{-1} for the total readout area and $(2.1 \pm 0.2) \times 10^{-6}$ counts keV^{-1} cm^{-2} s^{-1} for the central reduced window area. These results are compatible with previous background values taking into account that the cosmic vetoes are not implemented.

From this work, it has been proved that the background levels required for

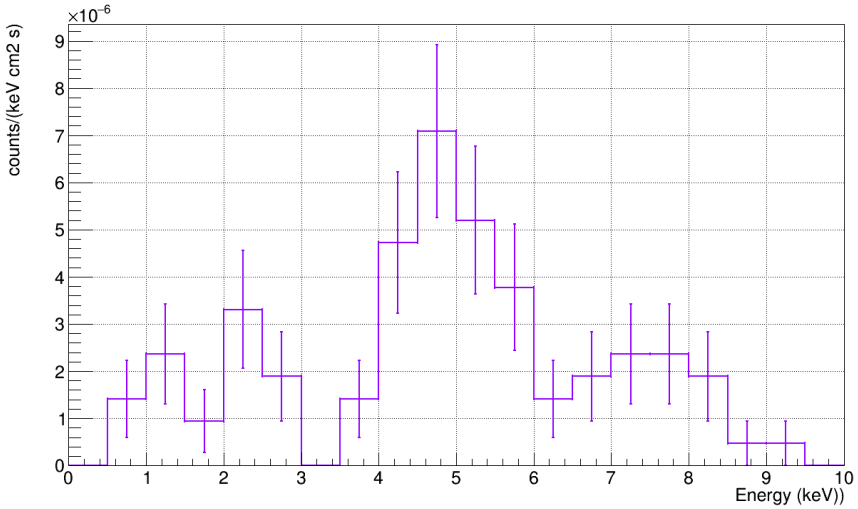

Figure 9.25: Background of the IAXO-D0 prototype for the IAXO energy RoI after the discrimination cuts at the reduced window area ($2.89\,\mathrm{cm}^2$). This spectrum correspond to ∼450 hours of background and only hit event level cuts were applied (see table 9.2).

IAXO ($\sim 10^{-7}\,\mathrm{counts\,keV^{-1}\,cm^{-2}\,s^{-1}}$) are at reach with the current detector design. An improvement on the pulse-shape analysis can lead to further reductions of the background, as it was preliminary explored, and the implementation of an efficient active shielding to avoid cosmic contribution would most likely be enough to reach the desired background level for IAXO. These options are already being explored.

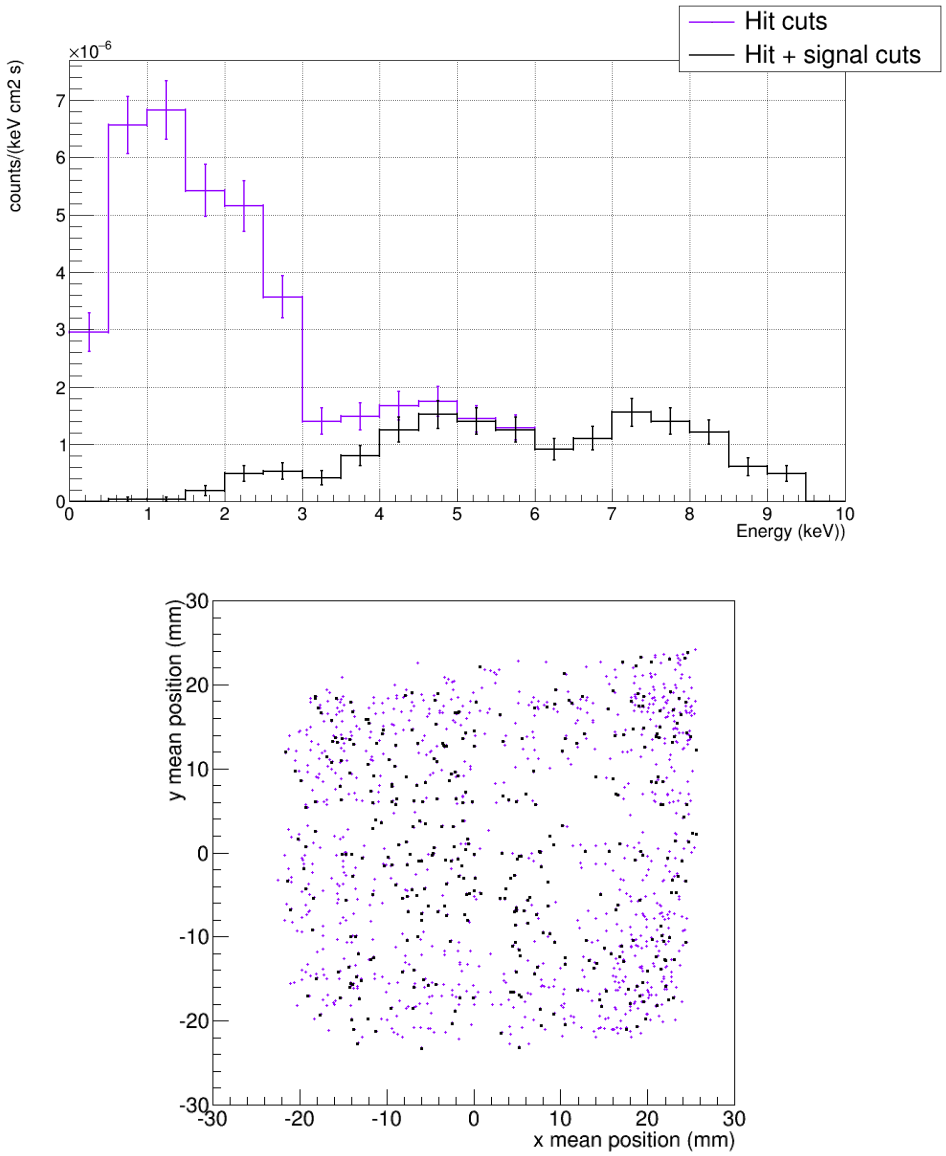

Figure 9.26: Comparison between the background obtained for the IAXO-D0 prototype in the IAXO energy RoI when only cuts at hit event level are applied (purple) with the one obtained when cuts at both hit and signal event level are applied (black) (see table 9.2 for cut values). These spectra correspond to ∼450 hours of background and all the readout surface (36 cm^2). (**Top**) Background enery spectra. **(Bottom)** Main hit events position hitmap.

CHAPTER 10

IAXO-D0 background: discussion and future prospects

Contents

10.1 Introduction

The main project of this *thesis* has been the study of the radioactive background of the IAXO-D0 detector prototype, performing both simulations and laboratory work. This prototype is based on the last Micromegas setup used in CAST that was attached to an x-ray focusing telescope, and provided the lowest background level up to date in a CAST detector, $(1.0 \pm 0.2) \times 10^{-6}$ counts keV^{-1} cm^{-2} s^{-1} in the [2,7] keV CAST RoI [155]. From this design, and without the restrictions of the CAST site, the IAXO-D0 setup has further implemented the background reduction techniques with an enlarged lead shielding, new AGET electronics with autotrigger features and new analysis software (REST).

A deep understanding of the radioactive background of the x-ray detectors is important in order to achieve the IAXO requirements for axion searches. Since backgrounds of the order of $\sim 10^{-6}$ counts keV^{-1} cm^{-2} s^{-1} has already been achieved in CAST, the detectors for the new fourth generation helioscope will need backgrounds of the order of $\sim 10^{-7}$ counts keV^{-1} cm^{-2} s^{-1} in the [0,10] keV IAXO RoI, or below, in order to properly increase the detector's FOM, f_D.

The goal of this work has been to develop a complete background model for the IAXO-D0 prototype with the new REST software, and on the other hand, to commission

the prototype at the TREX laboratory of the University of Zaragoza and also, to take and analyse the first background measurements. For both parts, a whole new analysis has been developed from scratch, following the concepts of the previous CAST analysis, but with the new REST philosophy and tools.

In this chapter, the main conclusions of this work will be reviewed. First, some comments about the REST based analysis will be made regarding the common steps and the differences in the treatment of experimental and simulated data. Then the background obtained from the simulated IAXO-D0 background model will be compared with the background obtained from the first IAXO-D0 data taking campaign, to see the level of agreement between both of them. And finally, some brief considerations will be made about the future prospects and next steps in order to work towards the BabyIAXO helioscope.

10.2 Simulated *versus* experimental background

To close this work, some final considerations will be done about the agreement between the simulated background model and the results from the first data taking campaign of the IAXO-D0 prototype.

10.2.1 Final comments about REST

One of the main advantages of using REST as the analysis software for experimental and simulated data has been that the same processes can be applied to both of them, and the same physical observables are obtained. Figure 10.1 shows the complete scheme of the REST analysis for simulated data (from the restG4 package) and for the laboratory acquisition system.

In this work, the common point for simulated and experimental data starts at the TRestHitsEvent level: simulated TRestG4Events transforms into TRestHitsEvents directly and then, a TRestElectronDiffusionProcess applies the corresponding gas diffusion to the position of the hits. Finally, a TRestHitsReductionProcess merges hits that are closer to each other than the minimum distance detectable by the readout pattern. On the other hand, raw data from experimental acquisition is processed into TRestRawSignalEvents to fit the REST data format, and then a TRestRawSignalAnalysisProcess transforms them into TRestSignalEvents. Also, a *zero suppression* is applied to reduce the computational weight of the files. The TRestSignalChannelActivityProcess is a small process that obtains the number of triggers per channel, for monitoring purposes. Then, the TRestSignalEvents are transformed to TRestHitsEvents, and the common point of both analysis is reached.

From this point onwards, the TRestHitsEvents from experimental and simulated data have the same format, and the same processes can be applied to both. However, there

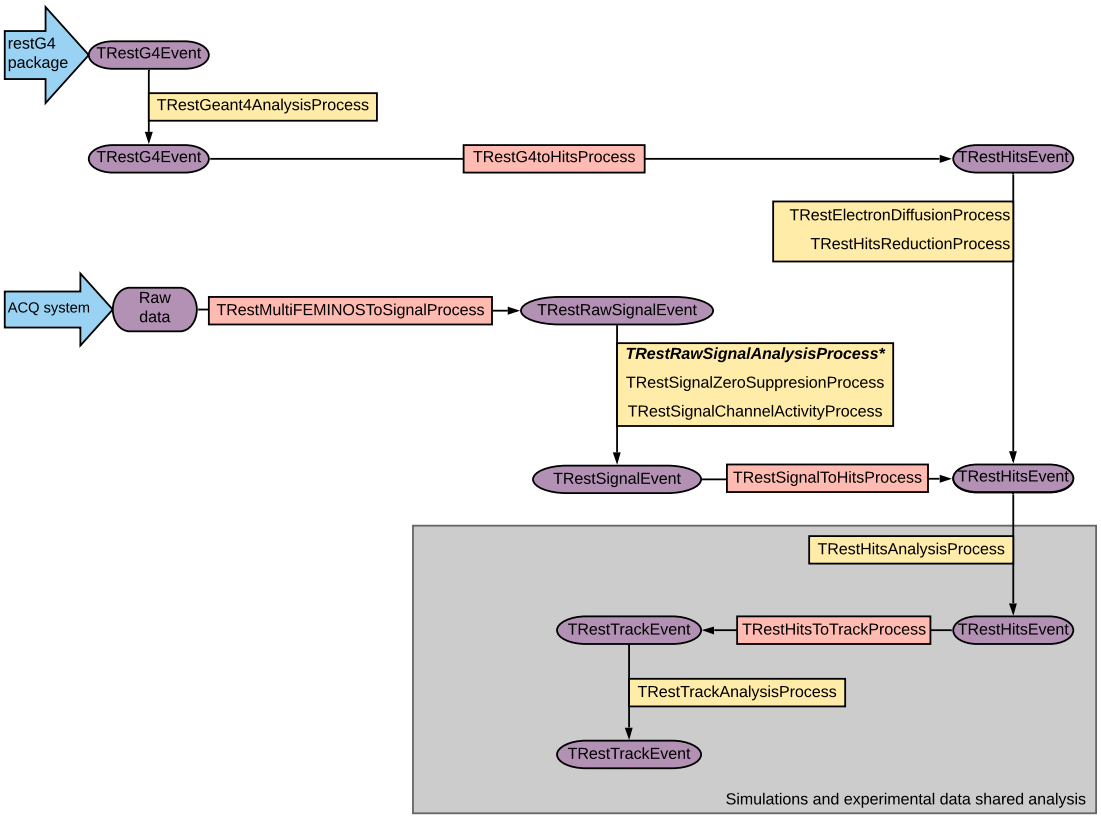

Figure 10.1: Complete REST analysis scheme for experimental and simulated data. It is a combination of the individual diagrams 7.1 and 9.6. The purple ovals represent the different event types, the red rectangles show the processes that transform one event type into another, and the yellow rectangles are the processes that performs transformations or calculate observables for each type of event. The common part of the analysis for simulated and experimental data is highlighted. (*) This process both transforms the TRestRawSignalEvents into TRestSignalEvents and also, obtains observables from the TRestSignalEvent.

is a difference between them due to the approach of this analysis flow: TRestHitsEvents from experimental data inherit their position from TRestSignalEvents. For each TRestHit, the z coordinate comes from the position of the maximum of the pulse of the TRestSignal in the time window, taking into account the drift velocity of the gas. And the x or y coordinate come form the channel of the strip that collects the charge. Therefore, TRestHits from experimental data will only have xz or yz position. On the other hand, TRestHits from GEANT4 simulations will have their three-dimensional position that is inherited from the corresponding TRestG4Hits.

A possible solution for this discrepancy could be to add an extra step in the simulated data analysis, starting with the output of the TRestG4ToHitsProcess. The TRestHitsEvent could be transformed to a TRestSignalEvent by means of a TRestHitsToSignalProcess, where the three-dimensional energy deposit would produce one pulse in one of the strips of the readout. Some extra processes would be required to correctly shape the signal accordingly to the desired acquisition card. At this point, the

simulated data would have the same structure than the TRestSignals from the acquisition, and the same analysis could be used onwards.

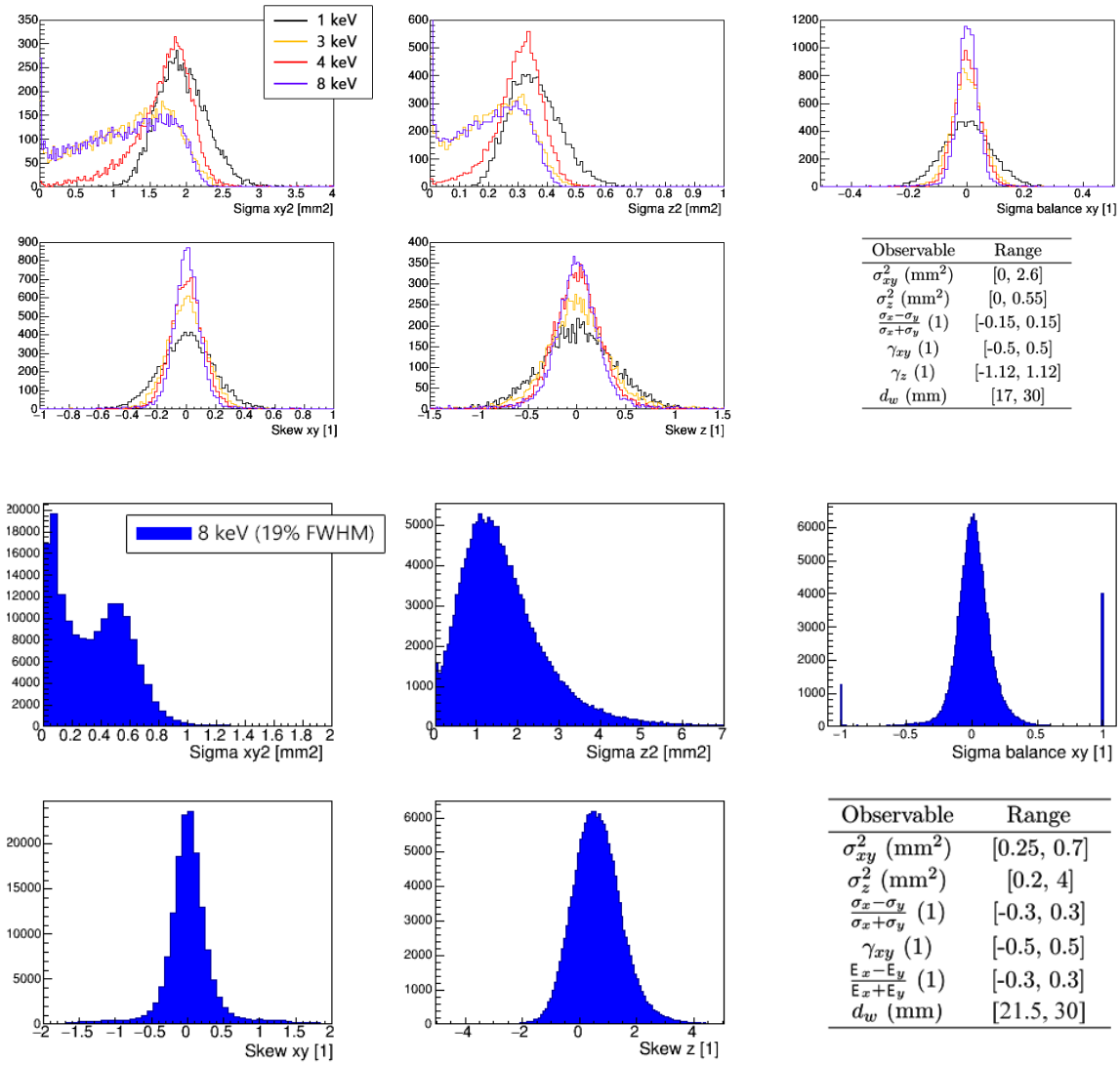

Observable	Range
σ_{xy}^2 (mm^2)	[0, 2.6]
σ_z^2 (mm^2)	[0, 0.55]
$\frac{\sigma_x-\sigma_y}{\sigma_x+\sigma_y}$ (1)	[-0.15, 0.15]
γ_{xy} (1)	[-0.5, 0.5]
γ_z (1)	[-1.12, 1.12]
d_w (mm)	[17, 30]

Observable	Range
σ_{xy}^2 (mm^2)	[0.25, 0.7]
σ_z^2 (mm^2)	[0.2, 4]
$\frac{\sigma_x-\sigma_y}{\sigma_x+\sigma_y}$ (1)	[-0.3, 0.3]
γ_{xy} (1)	[-0.5, 0.5]
$\frac{E_x-E_y}{E_x+E_y}$ (1)	[-0.3, 0.3]
d_w (mm)	[21.5, 30]

Figure 10.2: (Top) Observables of the simulated x-ray calibration in the IAXO energy RoI. Only a few representative x-ray energies are shown. From the upper left corner: the 2D extension of the TRestHitEvent σ_{xy}^2; the temporal extension σ_z^2; the balance between σ_x and σ_y; the 2D skewness or asymmetry of the TRestHitEvent γ_{xy}; and the temporal skewness γ_z. **(Bottom)** The same observables but in this case, of the 8 keV copper fluorescence peak of the long ^{109}Cd calibration (19% FWHM). In both cases, the values of the discrimination cuts at hit event level that have been chosen for the background studies are also shown.

This difference between the TRestHits implies that some observables, like the balance between the charge collected by the x or y strips, can only be calculated from experimental data, while other observables like the mean three-dimensional position only make sense for simulated data. Nevertheless, this detail was taken into account for the definition of the observables, and most of those used for the x-ray characterizations and the discrimination process are valid for every TRestHitEvent.

Note that most of the observables that have been used in this work to define the discrimination criteria are TRestHitsEvent observables. This is mostly due to the fact that TRestSignalEvents were not simulated, so the expected behaviour of TREstSignalEvents produced by x-rays was not available for study. Nonetheless, previous CAST-Micromegas analysis did use the information of the shape of the detected pulses, commonly called pulse-shape analysis, in order to discriminate x-rays from background. A preliminary cut has been explored from the observable that describes the rise rate of the pulses (see section 9.3.2), but further development need to be done in this direction. This cut has not been considered for the results that are summarized in this section.

Figure 10.2 shows the same observables for the simulated x-ray calibration, described in section 7.2.2, and for the 8 keV x-ray peak from the copper fluorescences of the experimental ^{109}Cd calibration, described in section 9.3.2. These observables have been used in order to define the discrimination criteria for the background studies of IAXO-D0[1], and all of them are computed in the same way for both simulated and experimental data.

Although the observables are computed in the same way, there seem to be some discrepancies in how x-rays are described from the simulations and the acquisition, and some further commentary is required. The 2D size of the charge deposit is described by the σ_{xy}^2 observable. In the case of simulated events produced by x-rays, the upper limit can be set at $\sigma_{xy}^2 \lesssim 0.26\,\text{mm}^2$ for the majority of the energy range. The exception are the 1 keV x-rays, that interact sooner in the gas volume, and therefore they are more affected by diffusion. This upper limit implies a standard deviation of $\sigma \sim$1.6 mm from the mean position of the TRestHitEvent. For a readout with a pitch of 0.5 mm, this deviation translates into 4-6 strips triggered in both x and y directions. On the other hand, for experimental events produced by x-rays, the upper limit of this observable would be $\sigma_{xy}^2 \lesssim 1\,\text{mm}^2$, which translates into 4-5 strips triggered in both directions. Therefore, the slight difference between both distribution is not significant when the granularity of the readout is taken into account. Also, the distribution of the events produced by 3 keV x-rays shows the effect of the absorption of the argon at 3.19 keV and the corresponding escape peak, as previously discussed in section 6.4.1. Excited argon atoms by the incident 3 keV x-rays will relax by emitting whether an Auger electron of $\sim$ 3 keV that will immediately produce further ionization, or a $\sim$ 3 keV x-ray fluorescence, that can escape and therefore, produce a low energetic escape peak.

The differences between the σ_z^2 observable seem to be larger between simulations and experimental data acquisition. The extension in the temporal direction is rather small for the simulated x-rays in the RoI, with a maximum deviation of only $\sigma_z \sim$0.7 mm. But this deviation is bigger for the experimental events, around $\sigma_z \sim$1.7-2 mm. This difference is more significant, but also understandable, because the measurement of the z position in a TPC is not trivial. In the case of IAXO-D0, there is no way to measure the absolute

[1]Actually, the γ_z observable has only been used for the discrimination criterion of the simulated background, whereas the balance between the E_x and E_y energy has been used for the discrimination criterion of the experimental background. Figure 10.2 shows the γ_z for both of them just for the sake of comparison.

z position, so the only temporal information is relative among the TRestHits of the same TRestHitEvent. This observable can be easily distorted by noise.

On the other hand, in terms of xy symmetry, both sets of data are in very good accordance. The balance between σ_x and σ_y show a Gaussian distribution around zero, meaning that the energy deposits are symmetrical in the xy plane. This is also supported by the γ_{xy} that is also a Gaussian distribution around zero, meaning that there is no preference direction for the charge deposits to deviate from the medium value. Note that the bins at $Balance_{\sigma_x,\sigma_y} = \frac{\sigma_x-\sigma_y}{\sigma_x+\sigma_y} = 1$ and -1 correspond to very small events that triggered very few strips.

Finally, the temporal skewness is also slightly different between experimental data and simulations. From the simulations perspective, γ_z shows what would be expectable for a symmetric x-ray deposit: a Gaussian distribution around z. But experimental events present a distribution centred in ∼1. As it was seen in section 9.3.2, $\gamma_z > 0$ correspond to those events where the main charge is deposited first and then, some other strips with less charge trigger. As it was argued before, temporal observables can be easily distorted by experimental noise.

An important detail that should not be ignored is that the sample used for the experimental x-ray characterization actually comes from the fluorescences produced in the copper chamber as a reaction of the radioactive source used for the calibrations. A relation was found between the σ^2_{xy} and the diffusion of the events (section 9.3.2) that allowed us to apply a cut in the z direction, so only events produced close to the cathode were considered. But still, this is not a perfect sample to perform a proper x-ray characterization. This issue will be solved in the near future, because a Micromegas detector like the one used in IAXO-D0 was calibrated at CERN using a CAST facility called *x-ray beam*, that was designed to calibrate x-ray detectors at different energies. It consist of a line where free electrons are accelerated with a high electric field until they hit a target, producing x-rays with a characteristic energy that depends on the transition lines of the material of the target. At the other side of the line, an x-ray detector can be placed and the different x-rays can be properly measured. This facility allows us to study events produced by x-rays of different energies in the RoI that enter the chamber through the pipe. This information can be used to properly define a selection criterion, even allowing the definition of different sets of energy dependent discrimination cuts for a more precise identification of x-ray-like events.

10.2.2 The background of IAXO-D0

The last topic to address is the comparison and discussion of the results from the simulated background model and the data taking campaign with the IAXO-D0 prototype. Table 10.1 shows the background levels obtained for IAXO-D0 before and after the discrimination process for the IAXO energy RoI. Overall, the results seem to be conclusive and in good agreement with each other.

Discrimination cuts	Area	Simulated background ($\mathrm{keV^{-1}\,cm^{-2}\,s^{-1}}$)	Experimental background ($\mathrm{keV^{-1}\,cm^{-2}\,s^{-1}}$)
No cuts	All readout	$(7.34 \pm 0.02) \times 10^{-4}$	$(5.93 \pm 0.01) \times 10^{-4}$
X-ray cuts	Central area	$(2.13 \pm 0.17) \times 10^{-6}$	$(2.1 \pm 0.2) \times 10^{-6}$

Table 10.1: Background level of the IAXO-D0 prototype from experimental data and simulations in the IAXO RoI [0,10] keV. The *no cuts* row refers to the background level before the discrimination cuts have been applied, where all the readout surface has been considered ($36\,\mathrm{cm^2}$). The *x-ray cuts* row refers to the background level after the discrimination process has been performed, where two different sets of cuts have been applied (see table 7.3 for the cuts applied to the simulated data and table 9.2 for the cuts applied to the experimental data). Errors have been computed following equation 7.2.1.

Considering first the background before the discrimination process, the level of the simulated background has resulted to be $(7.34 \pm 0.02) \times 10^{-4}\,\mathrm{counts\,keV^{-1}\,cm^{-2}\,s^{-1}}$ for the complete readout surface ($36\,\mathrm{cm^2}$). On the other hand, the background level that has been obtained from the IAXO-D0 data taking campaign is $(5.93 \pm 0.01) \times 10^{-4}\,\mathrm{counts\,keV^{-1}\,cm^{-2}\,s^{-1}}$, also for the complete readout surface and taking into account one-single track and two tracks events whose most energetic track has at least the 85% of the total energy (i.e. $Balance_{x,y} < 0.08$, see section 9.3.2). Both levels are in the same order of magnitude, and the simulations predict a ∼20% higher background.

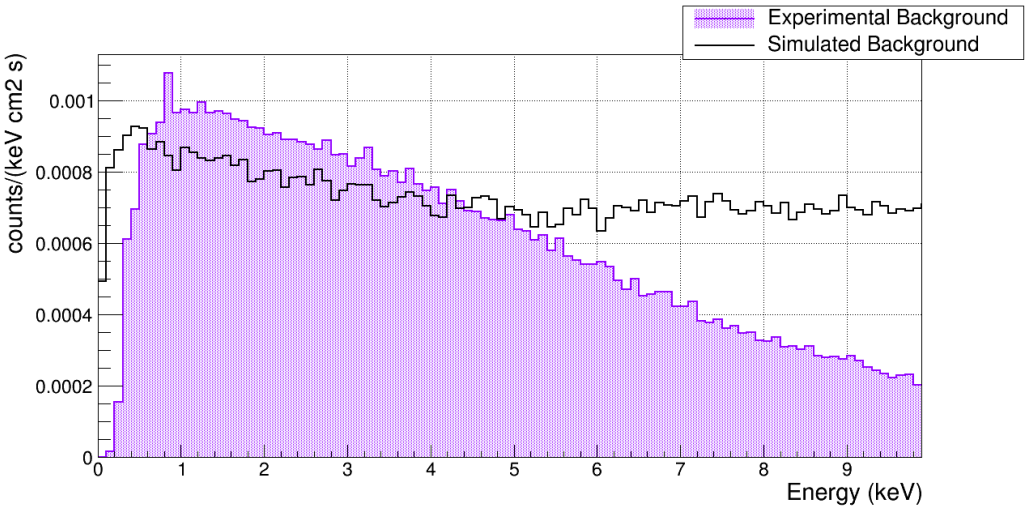

Figure 10.3: Experimental (purple) and simulated (black) background in the IAXO energy RoI before the discrimination process. All the readout surface is considered ($36\,\mathrm{cm^2}$). Simulated background follow a more flat tendency than the experimental one, that slowly decreases with the energy.

Figure 10.3 shows the comparison of the simulated and experimental backgrounds in the IAXO RoI before the discrimination process. It is shown that, even though the background level integrated in the energy RoI is similar for both cases, their tendency is quite different. Simulated background is flatter, with a light decrease in the lowest energy range. However, experimental background seem to decrease towards the end of the spectrum, with a difference of almost one order of magnitude. On one hand,

this experimental background tendency is well known from previous CAST-Micromegas setups (see for example figure 5.1). And on the other hand, the simulated background before cuts is completely dominated by the cosmic muons, whose raw contribution is $(7.23 \pm 0.02) \times 10^{-4}$ counts keV^{-1} cm^{-2} s^{-1}. This discrepancy may come from some misunderstanding of the muons simulations, or some topological effects that are not being taken into account. It can also be explained if the temporal window of the acquisition is not long enough to fit the most energetic events. This way, we would be detecting only part of them, that would cumulate at a lower part of the spectrum. This effect would not occur in the simulations. There is also a difference in energy threshold, due to the cuts applied to the experimental data to reduce noise at the low part of the spectrum.

Finally, the background level after the discrimination process for the IAXO RoI and a central area of the readout, has resulted to be in very good agreement for both background studies. The values that have been obtained are $(2.13 \pm 0.17) \times 10^{-6}$ counts keV^{-1} cm^{-2} s^{-1} for the simulated background, and $(2.1 \pm 0.2) \times 10^{-6}$ counts keV^{-1} cm^{-2} s^{-1} for the experimental background. The central area that has been considered to obtain the background values has been chosen differently for each study. For experimental data, a central area of 2.89 cm^2 has been considered because it is the aperture area of the detector window. On the other hand, for the simulations, a general area of 6.76 cm^2 has been chosen from the x-ray characterization. Figure 7.3 shows that x-rays in the [0,10] keV energy range coming from the pipe will unlikely interact further than 1.3 cm from the center of the readout. However, for the muons contribution, a bigger area of 16 cm^2 has been considered due to the very low statistics at the center of the readout.

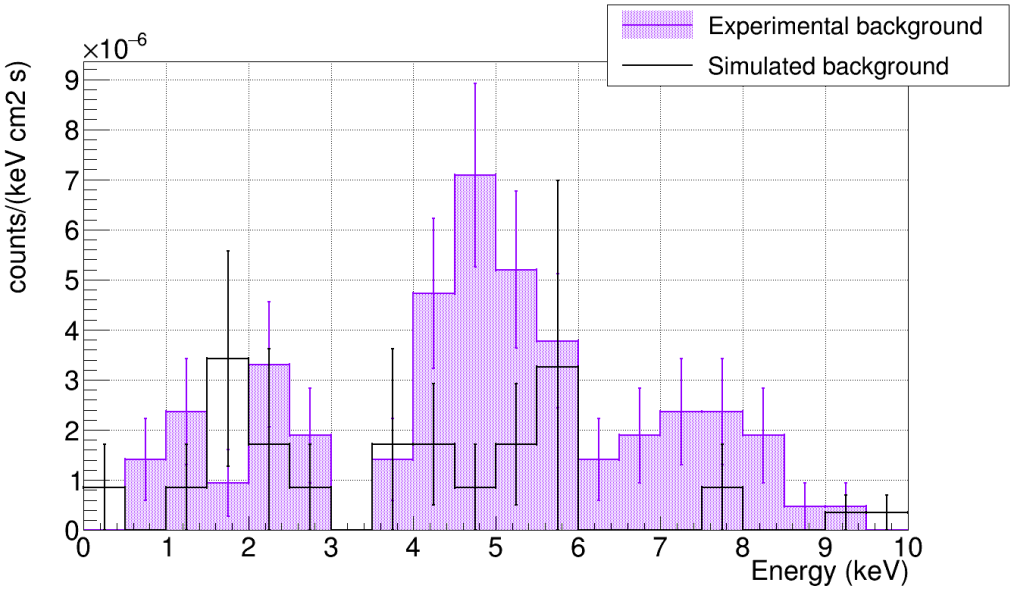

Figure 10.4: Experimental (purple) and simulated (black) background in the IAXO energy RoI after the discrimination process. Only a central area of the readout surface is considered (2.89 cm^2 for experimental data and 6.76-16 cm^2 for simulations). Experimental data shows the 8 keV copper fluorescence as well as the 5 keV escape peak of the argon. Also, at 1.4 keV could be seen from the emission from the aluminum of the Mylar window. The same tendency can be guessed from the simulations, although the statistics are very low.

Figure 10.5 shows the comparison between the simulated and experimental backgrounds in the IAXO RoI after the discrimination process. They are both compatible in magnitude, although the few final statistics from the simulations produce rather high error bars (errors have been obtained using equation 7.2.1). The 8 keV peak of the copper fluorescence is visible, as well as the escape peak at 5 keV. One could argue that the 1.4 keV emission from the aluminium in the Mylar window is contributing at the beginning of the spectrum as well.

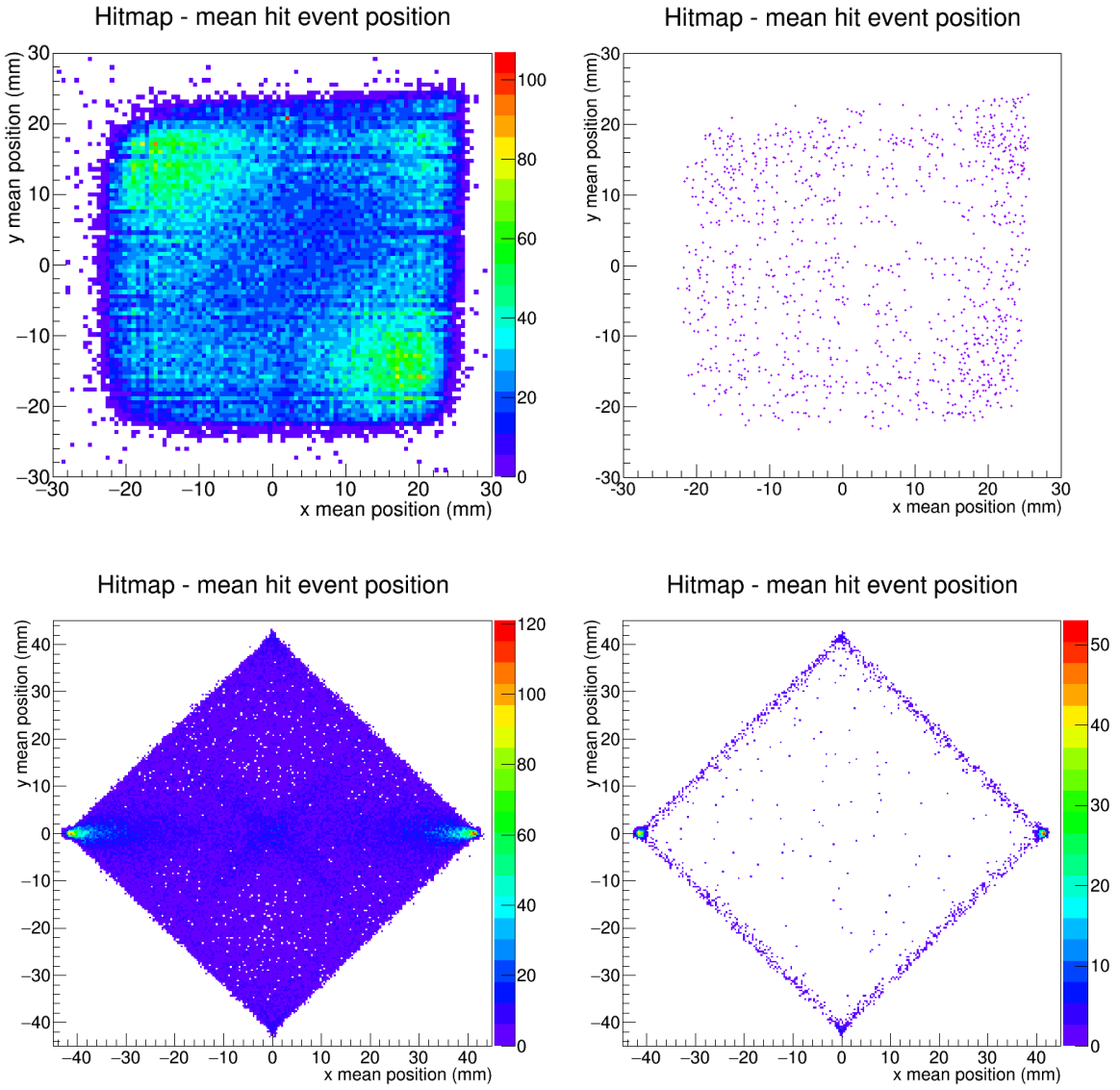

Figure 10.5: Background hitmaps of the TRestHits mean position: **(Top)** from the IAXO-D0 prototype data taking; **(Bottom)** from the simulated background model (cosmic muons and cosmic neutrons); **(Left)** before the discrimination process; **(Right)** after the discrimination process.

Previous CAST-Micromegas background spectra after their corresponding discrimination processes were usually dominated by the 8 keV peak rather than the 5 keV

one (like those shown in 5.5 or 5.11). This can be due to the different discrimination criteria used. In this work, the cuts are based on the 8 keV population of events, while in previous CAST analysis, the x-ray characterization was typically carried out using the 5.9 keV peak of a ^{55}Fe source.

To close this section, figure 10.5 shows different hitmaps of the TRestHits mean position for both experimental and simulated data, before and after the discrimination process. Note that the simulation hitmaps only take into account the cosmic muons and neutrons contributions, since they are the ones with higher impact on the background. The readout is rotated 45° in the simulations hitmap because this is how the readout is actually placed inside the geometry, and the three-dimensional position conserves this rotation. On the other hand, although the readout is physically rotated 45° in the IAXO-D0 detector, the position of the TRestHits is defined by the channel of the strip triggered, which translates directly into x or y distance by means of the REST readout configuration, so the rotation is lost.

Even though the readout of the IAXO-D0 Micromegas detector is $6\times6\,\mathrm{cm}^2$, barely any event is registered at the first centimetre from the borders. This can be due to the fact that the field shaper was not used for this data taking campaign, so the drift field could produce some border effects. Although a homogeneous drift field in all the gas volume is desirable, the border effects are not very significant for this particular application.

Also, the hitmaps before the discrimination cuts show a cumulation of events at two of the corners. Taking into account the position of the readout, these are the east-west corners, which are parallel to the floor. Since these hitmap plots show weighted medium positions, these cumulations of events are compatible with muons that cross perpendicularly the gas volume at the edges of the gas chamber (x$\sim$-40 mm or x$\sim$40 mm). This effect is visible both for simulations and experimental data.

Finally, the hitmaps after the discrimination cuts show that the background events are homogeneously distributed over the detector surface. The simulations also show a cumulation of events at the borders of the readout, that is compatible with incomplete events produced by muons at the blind sections of the gas chamber (remember that we are simulating a square readout surface inside a cylindrical chamber). This higher density of events at the exterior region of the readout is also visible for the experimental background, but the effect is more subtle, probably because of the electric field border effects. Nevertheless, the relevant area of an x-ray detector for axion searches in an enhanced helioscope is the center of the readout, so the border effects will be rejected by means of the fiducial cuts.

Overall, the main conclusion of this work is that the current understanding of the radioactive background of Microbulk Micromegas detectors is accurate and realistic, and they fulfil the experimental needs for an enhanced axion helioscope x-ray detector. Furthermore, the IAXO background requirements for x-ray detectors are at reach with a few known improvements, like active cosmic vetoes, a better x-ray characterization or the implementation of pulse-shape analysis.

10.3 Future prospects: towards BabyIAXO

The next big milestone for the IAXO project is the commissioning of the BabyIAXO helioscope at DESY (Hamburg). This is why some simulation and test bench studies related to the x-ray Micromegas detectors are planned among the IAXO group from the University of Zaragoza. In this section, some of these prospects will be shown.

10.3.1 Simulation studies

REST is a versatile software that is being used by several groups of the IAXO collaboration. In this section, some of the software related studies that are currently ongoing in the context of IAXO-D0 and BabyIAXO will be presented.

Background model for Xe based mixtures

All the work here presented explored the background of the IAXO-D0 prototype with a mixture of Ar+C_4H_10 (98/2)%. The main reasons behind this decision are that previous CAST-Micromegas setups, such as the IAXO *pathfider*, have always been operated with a variation of this gas mixture. Also, as it was seen from the quantum efficiency study (section 6.4.1), this mixture provides high efficiency for the CAST and IAXO energy ranges of interest at a low enough pressure (∼1.4 bar) that allows using thin differential windows for the TPC chamber.

However, argon based mixtures present a decrease in efficiency at ∼3.2 keV, which corresponds to the absorption energy (K-edge) of the Ar atoms. Also, natural argon can contain a certain amount of β^- emitter ^{39}Ar isotope. This contribution to the background has been studied in this work and turned out of the order of $10^{-8}10^{-6}$ counts keV^{-1} cm^{-2} s^{-1} after the discrimination process. Although is not a dominant contribution, other gas mixtures are considered for the IAXO detectors to avoid this background.

The most promising are the xenon penning mixtures. Xe+C_4H_10 (99/1)% has the advantage of providing high quantum efficiencies for the IAXO RoI at lower pressures (∼0.5 bar). This fact makes that thinner differential windows can be also considered, which would reduce the contribution to the background as well as the energy threshold for x-rays. Also, Xe+TMA[2] mixtures have been broadly used in the context of the TREX project, and it has proven to be suitable mixtures to work in ultra-low background TPCs for rare event searches [**?**, 19].

In this context, the development of a similar background model but with xenon based mixtures for the target gas would be required to prove the level of background and

[2]Trimethylamine (TMA) is an organic compound with the formula $N(CH_3)_3$.

to check its improvement. This is already a work in progress in the IAXO group at the University of Zaragoza. A preliminary approach has been done in [227] for the background component from the intrinsic radioactivity of the IAXO-D0 materials. This work will be complemented with more simulations carried out with the newest versions of the REST software.

Cosmic vetoes optimization

The REST-GDML geometry of the IAXO-D0 prototype that has been implemented in this work for the background model contain cosmic vetoes, but they are rather idealistic. They are just 5 cm thick plates that completely cover all the six sides of the detector's lead shielding (see figure 6.9). The main reason is that cosmic vetoes in this work have had the purpose of covering the complete solid angle of the detector in order to study the background reduction with the maximum coverage. Therefore, the realistic aspect of them, such as the placement of the photomultipliers or the available commercial sizes and shapes have not been taken into account.

Some studies are being carried out in the University of Zaragoza regarding this topic. The idea is to prove the background reduction of more realistic vetoes configurations. For this purpose, new REST-GDML geometries will be implemented, and studies about the hit distribution of the cosmic muons and neutrons at the cosmic vetoes are ongoing. Also, some approaches are being considered in order to optimize the simulation code, so higher statistics can be collected in a reasonable time period.

Finally, this work has shown that the contribution from cosmic neutrons dominates the background of the detectors after the discrimination cuts and the veto rejection. Therefore, the shielding designs are being revised in order to take this contribution into account.

Radiopure electronics background

Also in the context of the REST simulation studies, a group from the ICCUB/SiUB[3] at the University of Barcelona is developing a background model for their new proposed AGET based electronic cards for BabyIAXO (see section 4.4.1).

The simulation procedure has been similar to the one explained in this work: the geometry of the electronic card has been generated with the REST-GMDL tool, and the different contributions from the different materials have been simulated using the restG4 tool. The activity of each component considered in these simulations are shown in table 10.2, and were obtained in one of the screening programs of the TREX project [235]. These simulations have been carried out for different positions of the electronics related to the detector chamber. Finally, a REST analysis has been performed and a similar

[3] A collaboration between the Institute of Cosmos Sciences (ICCUB) and the Instrumentation Service of the Physics Faculty (SiUB) of the University of Barcelona.

discrimination process has been applied. Actually, the same discrimination cuts described in section 7.4.1 have been used in order to obtain comparable results with the IAXO-D0 background model computed in this work.

Component	Quantity (per board)	Units	^{40}K	^{60}Co	^{137}Cs	^{226}Ra	^{228}Ra	^{228}Th	^{232}Th	^{235}U	^{238}U
Capacitors	106	mBq/unit	5.29	<0.036	<0.043	5.29	-	8.75	8.52	-	10.4
Resistances	128	μBq/unit	83.6	<0.2	104	4.1	-	4.4	4.4	-	85
AGET Chip	1	mBq/unit	0.83	-	-	0.48	0.16	0.47	-	-	8.77
Diodes	64	μBq/unit	-	-	-	-	-	-	2.9	2.6	1.4

Table 10.2: Activity of the radioactive contaminants of the electronic components of the new AGET electronic cards [182]. The activity is given by unit of each component.

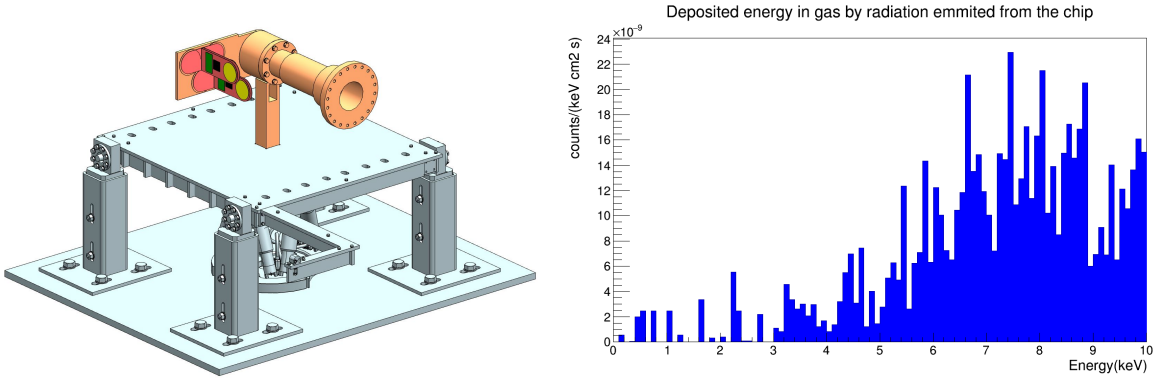

Figure 10.6: (Left) Scheme of the new radiopure electronic cards designed for BabyIAXO placed at the detector's raquette. **(Right)** Background contribution from the new AGET-based radiopure electronic card after the discrimination process, placed at ∼6.8 cm from the external border of the detector's raquette. The plot corresponds to the background of one AGET card (by C. Cogollos [182]).

Figure 10.6 (right) shows the background contribution of the new radiopure AGET-based electronics situated at ∼6.8 cm from the external border of the detector's raquette, that has a total length of 20 cm before it reaches the chamber of the detector. The placement of the electronic cards is illustrated in figure 10.6 (left). Most of the contribution from the electronic cards happens at the end of the spectrum, leaving the low energies range free of background, which is desirable for axion detection purposes.

The total integrated background after the discrimination process is $< 2 \times 10^{-8}$ counts keV^{-1} cm^{-2} s^{-1} for an energy range of [0,8] keV. This upper limit has been obtained taking into account the worse scenario of the radioactivity rates, so there is room for improvement. Although these are preliminary results, they seem promising so far for the IAXO background requirements, and the idea of radiopure electronics for rare event searches detectors seem viable.

10.3.2 IAXO-D0 prototype

Finally, the plans for the IAXO-D0 prototype are long term. Some further upgrades are currently in the agenda of the IAXO group at the University of Zaragoza. In this section, some of these upgrades will be mentioned.

X-ray calibration

As previously discussed, the x-ray characterization performed in this work from the 8 keV copper fluorescence peak suited the needs for this first data taking campaign, but is not the most adequate x-ray characterization. Ideally, one would like to characterize the x-rays detector in the range of the expected axion signal, i.e. in the 2-5 keV range.

For this purpose, the SR-Micromegas detector that was used in the last data taking campaign in CAST, and that is identical to the IAXO-D0 detector, was installed in the *x-ray beam* facility at the CAST laboratory, at CERN. Several calibrations were performed with x-rays in the [0,10] keV range for both Ar+C_4H_10 (97.7/2.3)% at 1.4 bar and Xe+C_4H_10 (98.5/1.5)% at 0,5 bar.

Also, a new ^{55}Fe source has been recently acquired to perform the new daily calibrations of the IAXO-D0 prototype at the University of Zaragoza. This source emits x-rays at 5.9 keV, so it will be more appropriate for future x-ray characterizations and analysis.

Cosmic vetoes implementation

The implementation of the cosmic vetoes at the IAXO-D0 prototype has already started at the University of Zaragoza. Some spare plastic scintillators that were used as cosmic vetoes in previous CAST setups were available, and one of them has already been tested in coincidence with the Micromegas detector. A new strategy has needed to be adopted because for previous Micromegas setups, the trigger for the vetoes acquisition was provided externally. However, on the current IAXO-D0 setup, the AGET electronics have auto-trigger for the strips, so no external trigger is needed. The solution has been to connect the output signal from the photomultiplier of the veto to one of the non used AGET channels. In this way, all the information is digitalized by the AGET card at the same time, and the veto signal is stored within the TRestRawSignalEvent.

In the near future, the IAXO-D0 prototype will count with 5-6 vetoes to test a full 4π solid angle coverage. The collaboration with the INR/RAS[4], from Russia, is bringing new ideas about the cosmic vetoes, because of the possibility of manufacturing squared-shaped plastic scintillators, even with a hole in the middle. This would add the possibility

[4]Institute for Nuclear Research (INR) and Russian Academy of Sciences (RAS).

of placing vetoes at the six sides of the detector, even in the side that would face to the magnet and have the passing pipe.

Movable platform

Finally, it is important to consider that the IAXO and BabyIAXO x-ray detectors will be moving along with the magnet during the solar tracking. In principle, the performance of the detectors should not be affected by the detector movement, as it has been proven by the CAST-Micromegas setups.

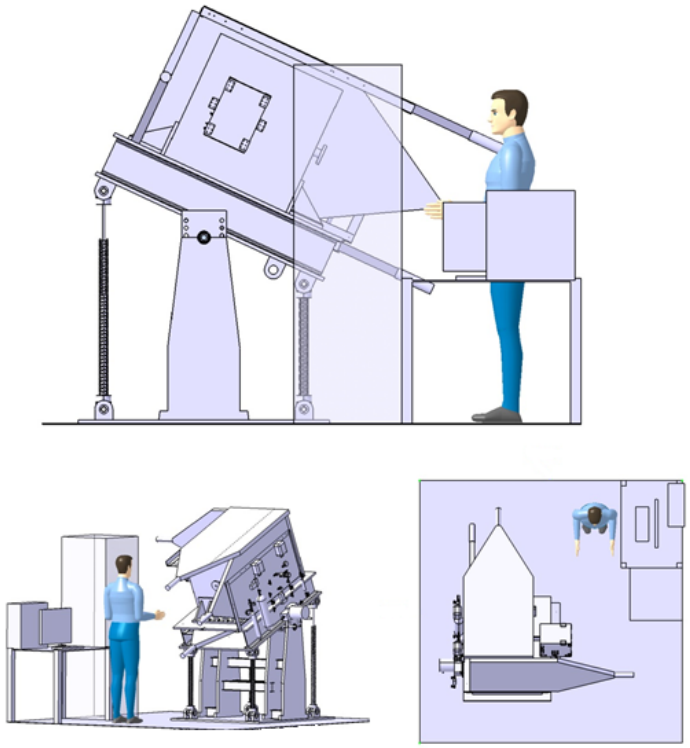

Figure 10.7: Conceptual Design of a ±30° movable platform with the IAXO-D0 passive and active shielding.

However, some sources of background like the cosmic muons or neutrons have a specific angular distribution, so the position of the detector with respect to zenith angle may result in a change of the background observables. To study these possible changes in the background or the detector performance, and also, to provide a test bench facility for detector stability testing.

This is a very preliminary idea which is still in the design state. Figure 10.7 shows a feasible and realistic design of a movable platform that would hold the lead shielding weight. Moreover, the IAXO-D0 prototype will be moved to another laboratory at the University of Zaragoza that would fit the structural requirements to build such platform.

Summary and conclusions

The main concept of a **particle gaseous detector** is that radiation passing through a gas can ionize atoms or molecules if the energy delivered is higher than the ionization potential of the gas. This is known as primary ionization, and can be caused by different charged and non-charged particles via several processes. Then, the application of an external electric field in the medium, or the conversion region, can make the produced charge pairs to move, or drift, towards the electrodes. Electrons will move towards the anode with a drift velocity that depends on the gas composition and pressure. Along its path, collisions with the gas atoms or molecules will affect the spread of the primary ionization, what is known as diffusion. Also, there are some effects that can reduce the charge production in the conversion region, such as electron recombination or attachment. When the electrons reach the anode, they usually enter the amplification region. A very strong electric field, or amplification field, can accelerate the electrons so they are able to ionize more atoms, producing an electron avalanche and therefore, amplifying the initial charge. Finally, charges moving within the amplification electric field will induce a current, i.e. a detectable signal at the electrodes.

The gaseous detector concept has been adopted by many particle physics detection techniques for rare event searches, the most representative being the **Time Projection Chambers (TPCs)**. These detectors consist of a gas chamber, where an electric field is applied, and some sort of patterned anode plane, where the charge amplification and detection occur. Specifically, **Micromegas readouts** are of interest due to their flexible designs in terms of patterning, high granularity, good energy resolution and potential radiopurity. They consist of a metallic micromesh that acts as the cathode of the amplification region, that is suspended over a pixelated anode by means of insulating pillars. The main manufacturing techniques are bulk and microbulk, being the latest one the best in terms of energy resolution and gap homogeneity. The main properties to characterize a Micromegas detector are the electron transmission, i.e. the fraction of initial electrons that pass through the mesh holes to the amplification region; the gain, i.e. the multiplication factor of the electrons in the amplification gap; and the energy, position and time resolution, i.e. the accuracy in the determination of the energy, position and temporal dimension of the event.

Axions are hypothetical elementary particles that were proposed as the most compelling solution to the strong CP problem of Quantum Chromodynamics (QCD). By acquiring a potential, axions absorb the CP violating term of the Lagrangian. They are characterized by their mass, m_a, and their coupling constant to other particles, g_{ai}. Both of them depend on the arbitrary symmetry breaking scale, f_a of the $\mathrm{U}(1)_{PQ}$ symmetry. There are different axion models where some couplings are allowed and some other are not,

but all of them agree that axions couple to photons with a coupling constant $g_{a\gamma}$. Even though f_a is arbitrary, some astrophysical and cosmological observations have constrained the $g_{a\gamma} - m_a$ parameter space of the axions. And beyond the QCD predicted axions, it extends a whole category of particles called **Axion-Like Particles (ALPs)**, that are well motivated by different extensions of the Standard Modell (SM). Some axions and ALPs *hints* are found when they are invoked as a solution for unexplained astrophysical observations, like the intergalactic transparency to very high energetic (VHE) photons or the anomalous cooling of stellar objects. Moreover, due to their weakly interacting nature, they are suitable candidates to be part or the totality of the dark matter of the Universe.

An interesting property from the experimental point of view is that axions and photons can oscillate in the presence of a magnetic field, which is called the **Primakoff effect**. Well known solar physics predict the emission of axions from the core of the Sun via plasma photons conversion. These axions would escape from the Sun and travel to Earth, where they could convert back to x-ray photons via inverse Primakoff effect inside a laboratory magnet. **Helioscopes** are experiments that use this idea to search for solar axions. A powerful magnet tracks the Sun so an axion-photon conversion can occur, and then, x-ray detectors would be able to measure an excess over the background at $\sim$keV energies. The figure of merit of an enhanced helioscope predicts better sensitivities for long magnets with high magnetic field, whose bores aperture are covered by x-ray optics. These optics are meant to focus the photon conversion flux into a small spot on the readout plane of an x-ray detector. The best figure of merit for detectors and optics stands for high efficiencies, small spot area and very low background.

The CERN Axion Solar Telescope (CAST), has been searching for solar axions for more than 15 years, and a limit of the axion-photon constant coupling has been obtained at $g_{a\gamma} < 0.66 \times 10^{-10}\,\mathrm{GeV}^{-1}$ for axion masses of $m_a \lesssim 0.02\,\mathrm{eV}$. From the expertise of this experiment, the new **International AXion Observatory (IAXO)** has been proposed. With a dedicated magnet and x-ray optics specially built for axion searches, and also, with improved low background microbulk Micromegas x-ray detectors, IAXO predicts to reach sensitivities of $g_{a\gamma} \sim 10^{-12}\,\mathrm{GeV}^{-1}$ for axion masses up to $m_a \lesssim 0.25\,\mathrm{meV}$. This would allow IAXO to probe completely unexplored regions of the parameter space, having potential for discovery. In the context of the IAXO international Collaboration, a **BabyIAXO** helioscope has been proposed for a short-term commissioning in order to prove all the technologies required for IAXO, to test improvements in order to enhance it even further and also, to aim for new physics discovery.

In this context, a deep understanding of the **radioactive background** of the detector is important in order to identify the most problematic sources and shield the detectors from them. From the CAST experience and from several bench tests and related projects at the University of Zaragoza and the Canfranc Underground Laboratory (LSC), the principal sources of background that can affect the IAXO Mircomegas detectors are cosmic muons and cosmic neutrons, that can be shielded with active vetoes; external high energy gammas that can be reduced by dense and high-Z materials passive shielding, like lead or copper; the intrinsic radioactivity of the detector itself, that is reduced by

using radiopure materials; and the radioactivity of the Micromegas active gas, in this case, argon mixtures. Also, background can be reduced by identifying the nature of the detected events thanks to the topological information that the Micromegas readouts provide. A small pattern granularity together with offline rejection algorithms allow identifying x-ray signals and rejecting background. CAST has been able to prove most of these techniques together in the so called IAXO *pathfinder* setup, where backgrounds of $(1.0 \pm 0.2) \times 10^{-6}\,\mathrm{counts\,keV^{-1}\,cm^{-2}\,s^{-1}}$ have been reached at surface for the [2,7] keV energy RoI.

IAXO-D0 is a IAXO detector prototype based on the *pathfinder* setup but with some improvements, like a larger passive shielding, new AGET-based electronics with autotrigger capabilities, a gas system prepared to operate with xenon gas mixtures, and a new acquisition and analysis software. The work of this thesis has consisted in two parts: the computational simulation of a background model of IAXO-D0, and the commissioning, data taking, analysis and background study of the prototype.

To produce the **IAXO-D0 background model**, the new REST framework has been used. It is a C++/root based software that provides tools for acquisition, storage, simulation, treatment and analysis of data taken with gaseous TPCs, allowing direct comparison between experimental data and simulations. Different TRestEvent types store information of experimental pulses, simulated GEANT4 tracks, energy deposits or energy tracks. Also, other TRestProcesses can access them and obtain and process the physical informations via observables. These observables can be used to identify and characterize the different events that can be detected in a TPC.

The IAXO-D0 detector and shielding geometry has been implemented in the REST software and a complete simulation of all the known background sources has been carried out. Also, a simulation of [0,10] keV x-rays has allowed characterizing x-ray induced events, and discrimination cuts have been defined from their observables. These discrimination cuts have been applied to all of the individual background source, resulting in a total background of $(2.13 \pm 0.17) \times 10^{-6}\,\mathrm{counts\,keV^{-1}\,cm^{-2}\,s^{-1}}$ for the central area of the readout and the [0,10] keV energy RoI. From this work, a low background level has been obtained for the IAXO-D0 prototype, which is of the same order of the IAXO *pathfinder* background. Note that the rejection from the vetos is not considered in this result due to very low statistics, so lower background levels are at reach. Also, some of the radioactivity measurements are not very precise, specially the ones from the window, which effectively increase the simulated background. Furthermore, it was learnt that cosmic neutrons are a very important source of background that persists after the discrimination process, and that cosmic vetoes are not only tagging events produced by muons, but also by neutrons. This result is a motivation to revise the shielding designs for BabyIAXO.

On the other hand, during 2017, the **IAXO-D0 prototype** was commissioned at the University of Zaragoza, along with the gas system installation, the electronics upgrade and the Micromegas characterization. The detector of IAXO-D0 is actually a IAXO *pathfinder* spare Micromegas, so good performance from it was expected and achieved. The first data taking campaign was carried out during 2018, with approximately 400

hours of background data and daily calibrations with a ^{109}Cd source. REST software has also been used for the data processing and analysis, and the same strategy has been followed: an x-ray characterization has been performed using the data of a long ^{109}Cd calibration run, and a representative population of events produced by the 8 keV x-rays form the copper fluorescence has been chosen to define the discrimination cuts. Then, background runs have been calibrated in energy, and the discrimination cuts have been applied. The resulting experimental background of the IAXO-D0 prototype is $(2.1 \pm 0.2) \times 10^{-6}$ counts keV^{-1} cm^{-2} s^{-1} for the central area of the readout and the [0,10] keV energy RoI. This result is very promising taking into account that cosmic vetoes were not installed for this first data taking campaing, so a further reduction of the background levels could be achieved easily in the near future.

Overall, both experimental and simulated background levels are in good agreement, and some better knowledge of the cosmic contribution to the background has been learnt. From this work, some paths are left to be explored towards the BabyIAXO commissioning, like the revision of the shielding to reject cosmic neutrons, the computation of a background model for xenon based mixtures, the implementation of the cosmic vetoes at the IAXO-D0 prototype or the optimization of the code to obtain even more realistic simulations and better statistics.

Resumen y conclusiones

Los **detectores gaseosos de partículas** se basan en que la radiación que pasa a través de un gas puede ionizar los átomos o moléculas de dicho gas, siempre y cuando la energía intercambiada sea mayor que el potencial de ionización del gas. Esto se conoce como ionización primaria, y puede estar causada por diferentes partículas con carga eléctrica o neutras, a través de diversos procesos. Si se aplica un campo eléctrico externo en el medio gaseoso, o también llamada región de conversión, los electrones e iones producidos por la ionización se moverán hacia los electrodos. Concretamente, los electrones derivarán hacia el ánodo con una velocidad de deriva que depende de la composición del gas y de la presión. A lo largo de su deriva, las colisiones con los átomos y moléculas del gas hacen que la ionización primaria se disperse, fenómeno conocido como difusión. Además, existen efectos que pueden hacer que la producción de carga en la zona de conversión se reduzca, como pueden ser la recombinación o el *attachment*. Cuando los electrones llegan al ánodo, entran en la zona de amplificación. Un campo eléctrico intenso, o campo de amplificación, acelera los electrones haciendo que ionizen el medio y formen una avalancha, amplificando de esta forma la carga inicial. Finalmente, las cargas en movimiento en el seno de un campo eléctrico producirán una corriente en los electrodos, creando una señal detectable.

El concepto de los detectores gaseosos ha sido adoptado por muchas técnicas de detección de física de partículas, concretamente en la búsqueda de eventos raros. Las más representativas son las **cámaras de proyección temporal (TPCs)**. Estos detectores consisten en una cámara de gas en la que se aplica un campo eléctrico, y en el ánodo sitúa algún tipo de plano de lectura pixelado, en el que ocurre la amplificación de la carga y la detección de la misma. Concretamente, los **planos de lectura Micromegas** despiertan especial interés debido a su flexibilidad en el diseño de sus patrones con elevada granulariad, y a su buena resolución en energía y potencial radiopureza. Estos planos de lectura consisten en micro-mallas metálicas, que actúan cómo cátodo para la región de amplificación, y que está suspendida sobre el ánodo pixelado por medio de pilares aislantes. Las principales técnicas de fabricación de estos detectores se llaman *bulk* y *microbulk*, y las Micromegas fabricadas con esta última, sobresalen en términos de resolución en energía y homogeneidad del gap de amplificación. Las caracteríticas principales de un detector Micromegas son la transmissión electrónica, es decir, la fracción de electrones iniciales que pasan a través de los agujeros de la malla a la zona de amplificación; la ganancia, es decir, el factor de multiplicación de los electrones en la zona de amplificación; y la resolución en energía, posición y tiempo, es decir, la exactitud con la que se puede determinar la energía, la posición o la dimensión temporal de un evento, respectivamente.

Los **axiones** son partículas elementales hipotéticas que fueron propuestas como una

solución atractiva al problema CP fuerte de la cromodinámica cuántica (QCD). El axión es capaz de absorber el término del Lagrangiano que viola la simetría CP acquiriendo un cierto potencial. Los axiones están caracterizados por su masa, m_a y su constante de acoplo a otras partículas, g_{ai}. Ambos parámetros dependen de la escala arbitraria de ruptura de la simetría $\mathrm{U}(1)_{PQ}$, f_a. Existen diferentes modelos teóricos de axiones entre los que hay discrepancias sobre los acoplos permitidos, pero todas ellas concuerdan en que los axiones pueden acoplarse a photones con una constante de acoplo $g_{a\gamma}$. Y aunque f_a en principio es arbitraria, existen observaciones astrofísicas y cosmológicas que restringen el espacio de parámetros de los axiones, $g_{a\gamma} - m_a$. Más allá de los axiones que vienen predichos por la QCD, existe una amplia categoría de partículas llamadas de **tipo-axiones (ALPs)**, y que están muy bien motivadas por diferentes extensiones del modelo estándar (SM). De hecho, algunas *pistas* de los axiones y ALPs se encuentran cuando dichas partículas son capaces de resolver observaciones astrofísicas que no se acaban de comprender. Algunos ejemplos serían la excesiva transparencia del universo a los fotones de alta energía (VHE), o el enfiamiento anómalo de algunos objetos estelares. Además, debido a que axiones y ALPs interaccionan débilmente con el resto de materia, son perfectos candidatos para ser una parte, o la totalidad, de la materia oscura del universo.

Una propiedad interesante de los axiones desde el punto de vista experimental es que axiones y fotones pueden oscilar en presencia de un campo magnético fuerte, conocido como **efecto Primakoff**. La emisión de axiones desde el núcleo del Sol por medio de la conversión de los fotones del plasma está basada en predicciones bien entendidas de la física solar. Estos axiones escaparían del Sol y viajarían hasta la tierra, dónde podrían volver a transformarse en fotones a través del efecto Primakoff inverso en un imán lo suficientemente potente. Los **helioscopios** son experimentos que usan esta idea para buscar axiones solares. Constan de un potente imán que sigue la trayectoria del Sol para que la conversión de axión-fotón pueda ocurrir en su interior, y pueda ser medida por un detector de rayos-x como un exceso sobbre el fondo a energías de ∼keV. La figura de mérito de un helioscopio de última generación predice mejores sensibilidades para imanes largos y con campos magnéticos intensos, y cuya apertura esté cubierta por ópticas de rayos-x. Dichas ópticas focalizarían el flujo de fotones de conversión en un área muy pequeña (*spot*), sobre el plano de lectura de un detector de rayos-x. La mejor figura de mérito para las ópticas y los detectores se consigue con eficiencias altas, tamaños de spot pequeños y con muy bajo nivel de fondo radiactivo.

El experimento *CERN Axion Solar Telescope*, o CAST, es un helioscopio que lleva más de 15 años buscando axiones solares. El mejor límite obtenido para la constante de acoplo axión-fotón es de $g_{a\gamma} < 0.66 \times 10^{-10}\,\mathrm{GeV}^{-1}$ para axiones con masas de $m_a \lesssim 0.02\,\mathrm{eV}$. Partiendo de la experiencia ganada con este experimento, el nuevo *International AXion Observatory*, o IAXO, ha sido propuesto. Contará con un imán dedicado y ópticas de rayos-x, ambos optimizados para física de axiones, y también con detectores de rayos-x con ultra bajo fondo de tipo microbulk Micromegas. Con estas características, las predicciónes para IAXO en términos de sensibilidad llegarían a $g_{a\gamma} \sim 10^{-12}\,\mathrm{GeV}^{-1}$ para axiones con masas de $m_a \lesssim 0.25\,\mathrm{meV}$. Este nivel de sensibilidad permitiría a IAXO sondear zonas completamente inexploradas del espacio de parámetros de axiones y ALPs, teniendo

potencial de descubrimiento. En el contexto de la Colaboración internacional de IAXO, el helioscopio **BabyIAXO** ha sido propuesto como un proyecto a más corto plazo, con el objetivo de probar todas las tecnologías requeridas por IAXO, así como testear mejoras que también podrían ser implementadas, y por supuesto, para buscar nueva física.

En este contexto, un conocimiento profundo del **fondo radiactivo** de los detectores es de suma importancia para poder identificar las fuentes más problemáticas y blindar el detector. De la experiencia ganada en CAST y de diferentes proyectos relacionados de la Universidad de Zaragoza y el Laboratorio Subterráneo de Canfranc (LSC), las principales fuentes de fondo que podrían afectar a los detectores Micromegas de IAXO han sido identificadas. Son principalmente muones y neutrones cósmicos, que pueden ser rechazados con blindaje activo (vetos); fotones externos de alta energía, que pueden ser reducidos gracias a blindajes pasivos con materiales densos y de alto número atómico, como el plomo o el cobre; también la radiactividad intrínseca de los materiales del detector, que pueden reemplazarse por otros más radiopuros; y finalmente, la radiactividad natural del gas activo del detedctor, que en este caso es argon. Otra forma de reducir el fondo radiactivo es identificando la naturalieza de los eventos detectados gracias a la información topológica de los planos de lectura Micromegas. La conjunción de planos pixelados con algoritmos de rechazo da como resultado la capacidad de identificar eventos producidos por rayos-x, y rechazar de esta forma los eventos de fondo. CAST ha testeado la mayoría de estas técnicas de reducción de fondo en uno de sus sitemas llamado IAXO *pathfinder*, para el que se consiguieron valores de fondo de $(1.0 \pm 0.2) \times 10^{-6}\,\text{cuentas}\,\text{keV}^{-1}\,\text{cm}^{-2}\,\text{s}^{-1}$ a nivel del mar y en el rango de energía de [2,7] keV.

IAXO-D0 es un prototipo de los detectores de IAXO basado en el diseño del *pathfinder*, pero con algunas mejoras, como un mayor blindaje pasivo, nuevas tarjetas electrónicas con chips AGET y autotriger, un sistema de gas preparado para operar con xenon, y una nueva adquisición y software de análisis. El trabajo de esta tesis ha consistido en dos partes: la simulación de un modelo de fondo para IAXO-D0, y la puesta en marcha, toma de datos, análisis y estudio de fondo del prototipo.

Para generar el **modelo de fondo de IAXO-D0**, se ha usado un framework llamado REST. Es un software basado en C++/root que provee de herramientas para adquisición, almacenamiento, simulación, tratamiento y análisis de datos tomados con TPCs, permitiendo una comparación directa entre datos experimentales y simulaciones. Diferentes tipos de TRestEvent guardan información sobre pulsos, *tracks* de GEANT4, depósitos de energía o trazas de energía. Además, otros TRestProcesses puede acceder a estos objetos y obtener y procesar su información física por medio de *observables*. Dichos observables pueden ser usados para identificar y caracterizar los diferentes eventos que pueden ocurrir en una TPC.

La geometría del detector de IAXO-D0, así como su blindaje, han sido implementados en REST, y una simulación completa de cada una de las fuentes de fondo radiactivo conocidas ha sido llevada a cabo. Además, una simulación de rayos-x entre [0,10] keV ha permitido caracterizar los eventos producidos por dichos rayos-x. A partir de esta información, se han definido los cortes de discriminación de fondo, y se han

aplicado a cada una de las contribuciones individuales, obteniendo de esta forma un fondo radiactivo de $(2.13 \pm 0.17) \times 10^{-6}\,\text{cuentas}\,\text{keV}^{-1}\,\text{cm}^{-2}\,\text{s}^{-1}$ para la zona central del plano de lectura y en la región de energía de [0,10] keV. De este trabajo se ha obtenido un nivel bajo de fondo radiactivo para el prototipo IAXO-D0, del mismo orde que el obtenido en el sistema de IAXO *pathfinder*. Hay que tener en cuenta que el rechazo de eventos mediante los vetos no ha sido considerado para este resultado debido a la baja estadística de las simulaciones, pero en caso de hacerlo, se pueden llegar a conseguir niveles de fondo más bajos. Además, algunas medidas de radiactividad de algunos componentes del detector no son demasiado precisas, lo que aumenta el valor de fondo de forma artificial. Otra de las conclusiones de esta parte es que se ha comprobado que los neutrones cósmicos son una parte importante del fondo radiactivo, cosa que hasta ahora se atribuía solo a muones. Este resultado podría motivar la revisión del diseño de los blindajes para BabyIAXO.

Por otro lado, a lo largo del 2017, el **prototipo IAXO-D0** se puso en marcha junto con un nuevo sistema de gas y las tarjetas electrónicas mejoradas. También se realizó una caracterización de las Micromegas. Como el detector de IAXO-D0 es uno de los detectores de repuesto del IAXO *pathfinder*, se sabía de antemano que este detector respondía perfectamente. La primera campaña de toma de datos se llevó a cabo en 2018, con aproximadamente 400 horas medidas de fondo y calibraciones diarias con una fuente de ^{109}Cd. El software de REST se ha usado también para el procesamiento y el análisis de los datos tomados con IAXO-D0, y se ha seguido la misma estrategia que para las simulaciones: se hizo una caracterización de rayos-x mediante una calibración especialmente larga con la fuente de ^{109}Cd, y después, se eligió una muestra representativa de rayos-x de 8 keV producidos por la fluorescencia del cobre, para obtener los cortes de discriminación. Después, los fondos fueron calibrados en energía y se les aplicó el proceso de discriminación. El resultado para el fondo experimental de IAXO-D0 es $(2.1 \pm 0.2) \times 10^{-6}\,\text{cuentas}\,\text{keV}^{-1}\,\text{cm}^{-2}\,\text{s}^{-1}$ para el área central del plano de lectura y el rango de energía [0,10] keV. Este resultado es esperanzador teniendo en cuenta que los vetos de rayos cósmicos no estaban instalados en esta primera campaña de toma de datos. Por lo tanto, se pueden esperar reducciones de fondo cuando se instalen en un futuro próximo.

Como conclusión, ambos niveles de fondo experimental y simulado concuerdan, y además se llegado a conocer mejor la contribución de los rayos cósmicos al fondo radiactivo del detector. Este trabajo deja algunos caminos abiertos a seguir hacia la puesta en marcha de BabyIAXO. Por ejemplo, la revisión del blindaje para rechazar también neutrones cósmicos, el cálculo de un modelo de fondo para IAXO-D0 con xenon en lugar de argon, la implementación de los vetos en IAXO-D0 y la optimización del código de simulación para conseguir resultados todavía más realistas y mejores estadísticas.

Bibliography

[1] S. N. Ahmed. *Physics and Engineering of Radiation Detection.* (2007). Academic Press. 4

[2] D. R. Nygren and J. N. Marx. *The Time Projection Chamber.* (1978). Physics Todays, Today 31N10 46. 5, 21

[3] P. Rebourgeard J. P. Robert, Y. Giomataris and G. Charpak. *MICROMEGAS: A high granularity position-sensitive gaseous detector for high pbook-flux environments.* (1996). Nucl. Instrum. Meth. A, 376:29. 5, 22, 23

[4] M. Tanabashi et al. *Pbook Data Group.* (2018). Physical Review D 98, 030001. 6, 8, 9, 10, 38, 47, 157

[5] U. Fano. *Ionization Yield of Radiations. II. The Fluctuations of the Number of Ions.* (1947). Physical Review 72, 26. 6

[6] G.D. Alkhazov. *Ionization Fluctuations in Gases.* (1972). Soviet Physics Technical Physics, Vol. 16, p.1540. 7

[7] E.P. de Lima et al. *Fano factors of rare gases and their mixtures.* (1982). Nucl. Instr. and Meth. 192 575. 7

[8] B. Obelic D. Srdoc and I. Krajcar Bronic. *Statistical fluctuations in the ionisation yield of low-energy photons absorbed in polyatomic gases.* (1987). J. Phys. B 20 4473. 7

[9] M. Scharff J. Litndhard and H. E. Schiott. *Range concepts and heavy ion ranges. (Notes on atomic collisions, II).* (1963). Mat. Fys. Medd. Dan. Vid. Selsk. 33(14):1-42. 7

[10] H.H. Andersen and J.F. Ziegler. *Hydrogen Stopping Powers and Ranges in All Elements.* (1977). Vol. 2 of. 7

[11] H. A. Bethe. *Zur Theorie des Durchgangs schneller Korpuskularstrahlen durch Materie.* (1930). Ann. Phys. 5, 324. 7

[12] F. Bloch. *The slow down of rapidly moving pbooks in their passing through solid matter.* (1933). Ann. Phys. 16, 285. 7

[13] M. J. Berger et al. *XCOM: Photon Cross Sections Database, National Institute of Standarts and Technology (NIST).* https://www.nist.gov/pml/xcom-photon-cross-sections-database. 11

[14] J.G. Garza. *Micromegas for the search of solar axions in CAST and low-mass WIMPs in TREX-DM.* (2015). PHD Thesis, Universidad de Zaragoza, http://zaguan.unizar.es/record/47876. 12, 93, 97, 101, 106, 107, 130, 148, 151, 156, 173, 185, 204, 205

[15] O. Klein and T. Nishina. *Uber die Streuung von Strahlung durch freie Elektronen nach der neuen relativistischen Quantendynamik von Dirac.* (1929). Zeitschrift für Physik, Volume 52, Issue 11-12, pp. 853-868. 13

[16] R. Veenhof S. Biagi. Magboltz: transport of electrons in gas mixtures. http://magboltz.web.cern.ch/magboltz. 14, 16, 17, 19, 128

[17] W. Riegler W. Blum and L. Rolandi. *Pbook Detection with Drift Chambers.* (1993). Springer-Verlag. 15, 21

[18] A. I. Bolozdynya et al. *Noble Gas Detectors.* (2006). WILEY-VCH. 17

[19] D. C. Herrera. *Development of a Micromegas Time Projection Chamber in Xe-based Penning Mixtures for Rare Event Searches.* (2014). 2015 JINST TH 002. 17, 27, 251

[20] F. J. Iguaz. *Development of a time projection chamber prototype with micromegas technology for the search of the double beta decay of 136XE.* (2012). PHD Thesis, Universidad de zaragoza, http://zaguan.unizar.es/record/5731. 18, 27

[21] A. Tomas. *Development of Time Projection Chambers with Micromegas for Rare Event Searches.* (2013). PhD Thesis, Universidad de Zaragoza, http://zaguan.unizar.es/record/12540. 19, 130, 149, 156, 157

[22] H. Raether. *Electron avalanches and breakdown in gases.* (1964). Butterworths. 18

[23] G. D. Alkhazov. *Statistics of electron avalanches and ultimate resolution of proportional counters.* (1970). Nucl. Instrum. Meth. A89 155. 19

[24] S. Ramo. *Currents Induced by Electron Motion.* (1939). Proc, IRE 27. 20

[25] W. Shockley. *Currents to Conductors Induced by a Moving Point Charge.* (1938). J. Appl. Phys. 91. 20

[26] H. Geiger and E. Rutherford. *An electrical method of counting the number of alphapbooks from radio-active substances.* (1908). Proc. Royal Soc. A, 81:141. 21

[27] H. Geiger and W. Muller. *Electron counting tube for measurement of weakest radioactivities.* (1928). Die Naturwissenschaften, 16:31. 21

[28] M. Longair. *C.T.R. Wilson and the cloud chamber.* (2014). Astropbook Physics Volume 53, Pages 55-60. 21

[29] G. Charpak et al. *The use of multiwire proportional counters to select and localize charged pbooks.* (1968). Nucl. Instrum. Meth. A62 262. 21

[30] A. Oed. *Position sensitive detector with microstrip anode for electron multiplication with gases.* (1988). Nucl. Instrum. Meth. A263 351. 22

[31] O. Schafer. Working principle of a tpc. https://www.lctpc.org/e8/e57671. 23

[32] G. Charpak et al. *Micromegas, a multipurpose gaseous detector.* (2002). Nucl.Instrum.Meth. A478 26-36. 23

[33] D. Attie et al. *Towards smaller gap microbulks.* (2014). JINST 9 C04013. 24, 28

[34] (CAST Collaboration). *New CAST limit on the axion-photon interaction.* (2017). NPHYS4109. 24, 47, 50, 65, 91, 108, 109, 110

[35] F. J. Iguaz et al. *TREX-DM: a low-background Micromegas-based TPC for low-mass WIMP detection.* (2016). Eur. Phys. J. C 76:529. 24, 104, 159

[36] H. Lin et al. *Design and commissioning of a 600 L Time Projection Chamber with Microbulk Micromegas.* (2018). JINST 13 no.06, P06012. 24, 104

[37] G. Vasseur et al. *Operation of the T2K time projection chambers.* (2012). JINST 7 C02040. 24

[38] A. Zibell et al. *Micromegas detectors for the upgrade of the ATLAS muon spectrometer.* (2014). JINST 9 C08013. 24

[39] D. Neyret et al. *New pixelized Micromegas detector for the COMPASS experiment.* (2009). JINST 4 12004. 24

[40] B. Peyaud et al. *KABES: A novel beam spectrometer for NA48.* (2004). Nucl. Instrum. Meth. A535 247. 24

[41] G. Charles et al. *Micromegas detectors for CLAS12.* (2013). Nucl. Instrum. Meth. A718 414. 24

[42] (N-TOF Collaboration) S. Andriamonje et al. *The MICROMEGAS neutron detector for CERN n-TOF.* (2002). Nucl. Phys. B. 24

[43] (IAXO Collaboration) I. G. Irastorza el al. *The International Axion Observatory IAXO. Letter of Intent to the CERN SPS committee.* (2013). CERN-SPSC-2013-022, http://inspirehep.net/record/1510349. 25, 47, 48, 50, 66, 71, 84, 94, 107, 157, 172

[44] A. Delbart et al. *New developments of Micromegas detector.* (2001). Nucl. Instrum. Meth. A461 84. 25

[45] I. Giomataris et al. *Micromegas in a bulk.* (2006). Nucl. Instrum. Meth. A560 405. 25

[46] S. Andriamonje et al. *Development and performance of Microbulk Micromegas detectors.* (2010). JINST 5 P02001. 25, 26, 27

[47] T. Dafni. *A Search for Solar Axions with the MICROMEGAS Detector in CAST.* (2005). PHD Thesis, Darmstadt Tech. U., http://inspirehep.net/record/1332791. 27

[48] M. E. Rose and S. A. Korff. *An Investigation of the Properties of Proportional Counters.* (1941). Phys. Rev. 59, 850. 28, 205

[49] T. Alexopoulos et al. *The ATLAS muon Micromegas RD project: towards large-size chambers for the s-LHC.* (2009). JINST 4 P12015. 29

[50] T. Franke and V. Peskov. *Innovative applications and developments of Micro-Pattern gaseous detectors.* (2014). Engineering Science Reference, IGI Global. 29

[51] F. Wilczek. *Asymptotic freedom: From paradox to paradigm.* (1978). Phys. Rev. Lett. 40 279. 33

[52] S. Weinberg. *The U(1) Problem.* (1975). Phys. Rev. D 11 3583. 35

[53] G. 't Hooft. *Symmetry Breaking through Bell-Jackiw Anomalies.* (1976). Phys. Rev. Lett. 37(1):8. 35

[54] G. 't Hooft. *Computation of the quantum effects due to a four-dimensional pseudopbook.* (1976). Phys. Rev. D 14, (12):3432. 35

[55] C. A. Baker et al. *Improved experimental limit on the electric dipole moment of the neutron.* (2006). Phys. Rev. Lett. 97 131801. 36

[56] R. D. Peccei and H. R. Quinn. *CP Conservation in the Presence of Pseudopbooks.* (1977). Phys. Rev. Lett., 38(25):1440. 36, 39

[57] R. D. Peccei and H. R. Quinn. *Constraints imposed by CP conservation in the presence of instantons.* (1977). Phys. Rev. D 16 1791. 36, 39

[58] S. Weinberg. *A New Light Boson?* (1978). Phys. Rev. Lett. 40 223. 36

[59] F. Wilczek. *Problem of Strong P and T Invariance in the Presence of Instantons.* (1978). Phys. Rev. Lett. 40 279. 36

[60] Y. Asano et al. *Search For A Rare Decay Mode $K^+ \to \pi^+$ Neutrino Anti-Neutrino And Axion.* (1981). Phys. Lett. B 107 159. 39

[61] J. E. Kim. *Weak-Interaction Singlet and Strong CP Invariance.* (1979). Phys. Rev. Lett. 43(2):103. 40

[62] A. I. Vainshtein M. A. Shifman and V. I. Zakharov. *Can confinement ensure natural CP invariance of strong interactions?* (1980). Nuclear Physics B 166(3):49. 40

[63] D. B. Kaplan. *Opening The Axion Window.* (1985). Nucl. Phys. B 260 215. 41

[64] M. Dine et al. *A Simple Solution to the Strong CP Problem with a Harmless Axion.* (1981). Phys. Lett. B 104 199. 41

[65] A. R. Zhitnitsky. *On Possible Suppression of the Axion Hadron Interactions.* (1980). Sov. J. Nucl. Phys. 31 260. 41

[66] G. G. Raffelt. *Pbook Physics from Stars.* (1999). Ann. Rev. Nucl. Part. Sci. 49 163–216. 41, 42

[67] G. G. Raffelt. *Astrophysical axion bounds.* (2008). Lect. Notes Phys. 741 51-71. 41, 42

[68] P. Gondolo and G. Raffelt. *Solar neutrino limit on axions and keV-mass bosons.* (2009). Phys.Rev. D79, 107301. 9. 41

[69] G. G. Raffelt. *Astrophysical axion bounds diminished by screening effects.* (1986). Phys. Rev. D33 897. 42

[70] A. Ayala et al. *Revisiting the Bound on Axion-Photon Coupling from Globular Clusters.* (2014). Phys. Rev. Lett. 113 191302. 42, 48, 88

[71] P.B. Stetson G. Raffelt J. Redondo A. R. Valcarce N. Viaux, M. Catelan and A.Weiss. *Neutrino and axion bounds from the globular cluster M5 (MGC 5904).* (2013). Phys. Rev. Lett. 111, 231301. 42, 48, 87

[72] A. H. Corsico et al. *The Potential of the variable DA white dwarf G117 - B15A as a tool for fundamental physics.* (2001). New Astron. 6 197-213. 42, 48, 87

[73] M. Giannotti A. Friedland and M. Wise. *Constraining the Axion-Photon Coupling with Massive Stars.* (2013). Phys.Rev.Lett. 110 061101. 42

[74] M. Giannotti P. Carenza, T. Fischer and A. Mirizzi. *Improved axion emissivity from a supernova via nucleon-nucleon Bremsstrahlung.* (2008). Lect. Notes Phys. 741 51-71. 43

[75] R. Essig J. H. Chang and S. D. McDermott. *Supernova 1987A Constraints on Sub-GeV Dark Sectors, Millicharged Pbooks, the QCD Axion, and an Axion-like Pbook.* (2019). arXiv:1906.11844 [hep-ph]. 43

[76] A. Payez et al. *Revisiting the SN1987A gamma-ray limit on ultralight axion-like pbooks.* (2015). JCAP 1502 006. 43

[77] J. Jaeckel and A. Ringwald. *The Low-Energy Frontier of Pbook Physics.* (2010). Annual Review of Nuclear and Pbook Science 60: 405–437. 43

[78] E. Masso and R. Toldra. *On a Light Spinless Pbook Coupled to Photons.* (1995). Phys. Rev. D52: 1755–1763. 43

[79] A. Ringwald. *Exploring the Role of Axions and Other WISPs in the Dark Universe.* (2012). Phys.Dark Univ. 1: 116–135. 43

[80] S. Dubovsky N. Kaloper A. Arvanitaki, S. Dimopoulos and J. March-Russell. *String Axiverse.* (2010). Phys.Rev. D81 123530. 43

[81] A. Ringwald M. Goodsell M. Cicoli, M. Goodsell and A. Ringwald. *The type IIB string axiverse and its low-energy phenomenology.* (2012). JHEP 1210 146. 43

[82] A. Ringwald. *Searching for axions and ALPs from string theory.* (2012). arXiv:1209.2299. 43

[83] L. Okun. *Limits Of Electrodynamics: Paraphotons?.* (1982). Sov.Phys.JETP 56 502. 43

[84] B. Holdom. *Two U(1)s and Epsilon Charge Shifts.* (1986). Phys.Lett. B166 196. 43

[85] S. Davidson and M. E. Peskin. *Astrophysical bounds on millicharged pbooks in models with a paraphoton.* (1994). Phys. Rev. D49 2114–2117. 43

[86] S. M. Carroll. *Quintessence and the rest of the world.* (1998). Phys. Rev. Lett. 81 3067–3070. 43

[87] P. Brax and K. Zioutas. *Solar Chameleons.* (2010). Phys. Rev. D82 043007. 43

[88] M. Goodsell J. Jaeckel J. Redondo P. Arias, D. Cadamuro and A. Ringwald. *WISPy Cold Dark Matter.* (2012). JCAP 1206, 013. 43, 88

[89] I. G. Irastorza and J. Redondo. *New experimental approaches in the search for axion-like pbooks.* (2018). Prog.Part.Nucl.Phys. 102 89-159. 44, 86

[90] F. Zwicky. *On the Masses of Nebulae and of Clusters of Nebulae.* (1937). Astrophys.J. 86: 217. 44

[91] (Planck Collaboration) N. Aghanim. *Planck 2018 results. VI. Cosmological parameters.* (2018). arXiv:1807.06209 [astro-ph.CO]. 44

[92] G. G. Raffelt S. Hannestad, A. Mirizzi and Y. Y. Wong. *Neutrino and axion hot dark matter bounds after WMAP-7.* (2010). JCAP 1008 001. 45

[93] A. Mirizzi G. Raffelt M. Archidiacono, S. Hannestad and Y. Y. Y. Wong. *Axion hot dark matter bounds after Planck.* (2013). JCAP 1310 020. 45

[94] P. Sikivie. *Axion cosmology.* (2008). Lect.Notes Phys. 741 19–50. 45

[95] O. Wantz and E. P. S. Shellard. *Axion Cosmology Revisited.* (2010). Phys. Rev. D82 123508. 45, 46

[96] E. Armengaud et al. *Physics potential of the International Axion Observatory (IAXO).* (2019). Prepared for submission to JCAP. arXiv:1904.09155 [hep-ph]. 46, 84, 86, 87

[97] (ADMX Collaboration) S.J. Asztalos et al. *SQUID-Based Microwave Cavity Search for Dark-Matter Axions.* (2010). Phys. Rev. Lett. 104 041301. 47, 50, 51

[98] (HESS Collaboration) A. Abramowski et al. *Measurement of the extragalactic background light imprint on the spectra of the brightest blazars observed with H.E.S.S.* (2013). Astron. Astrophys. 550. 46

[99] (Fermi-LAT Collaboration) M. Ackermann et al. *The Imprint of The Extragalactic Background Light in the Gamma-Ray Spectra of Blazars.* (2012). Science 338 1190–1192. 46

[100] G. Galanti A. De Angelis and M. Roncadelli. *Relevance of axion-like pbooks for very-high-energy astrophysics.* (2011). Phys.Rev. D84 105030. 46, 47, 87

[101] D. Horns and M. Meyer. *Indications for a pair-production anomaly from the propagation of VHE gamma-rays.* (2012). JCAP 1202 033. 46, 47, 87

[102] (HESS Collaboration) F. Aharonian et al. *A Low level of extragalactic background light as revealed by gamma-rays from blazars.* (2006). Nature 440 1018–1021. 46, 87

[103] (MAGIC Collaboration) M. Teshima et al. *Discovery of Very High Energy Gamma-Rays from the Distant Flat Spectrum Radio Quasar 3C 279 with the MAGIC Telescope.* (2008). Proc. 30th Int. Cosm. Ray Conf. Vol.3 1045-1048. 46, 87

[104] (MAGIC Collaboration) E. Aliu et al. *Very-High-Energy Gamma Rays from a Distant Quasar: How Transparent Is the Universe?.* (2008). Science 320 1752. 46, 87

[105] D. Horns M. Meyer and M. Raue. *First lower limits on the photon-axion-like pbook coupling from very high energy gamma-ray observation.* (2013). Phys.Rev. D87 no. 3, 035027. 47, 87

[106] A. H. Corsico et al. *The rate of cooling of the pulsating white dwarf star G117-B15A: a new asteroseismological inference of the axion mass.* (2012). arXiv:1205.6180 [astro-ph.SR]. 48, 87

[107] A. H. Corsico et al. *An independent limit on the axion mass from the variable white dwarf star R548.* (2012). JCAP 1212 010. 48, 87

[108] T. Battich et al. *First axion bounds from a pulsating helium-rich white dwarf star.* (2016). star, JCAP 1608 062. 48, 87

[109] A. H. Corsico et al. *An asteroseismic constraint on the mass of the axion from the period drift of the pulsating DA white dwarf star L19-2.* (2016). JCAP 1607 036. 48, 87

[110] A. H. Corsico et al. *Constraining the neutrino magnetic dipole moment from white dwarf pulsations.* (2014). JCAP 1408 054. 48

[111] K. Zuber S. Arceo-Diaz, K. P. Schroder and D. Jack. *Constraint on the magnetic dipole moment of neutrinos by the tip-RGB luminosity in ω-Centauri.* (2015). Astropart. Phys. 70 1-11. 48, 87

[112] O. Straniero et al. *Axion-Photon Coupling: Astrophysical Constraints.* (2015). Proceedings, 11th Patras Workshop on Axions, WIMPs and WISPs (Axion-WIMP 2015): Zaragoza, Spain, June 22-26, 2015, pp. 77-81. 48

[113] J. Redondo M. Giannotti, I. Irastorza and A. Ringwald. *Cool WISPs for stellar cooling excesses.* (2016). JCAP 1605 057. 48

[114] R. C. Dohm and P. E. D. Skillman.n. *The ratio of blue to red supergiants in sextans a from hst imaging.* (2002). astro-ph/0203284. 48, 88

[115] K. B. W. McQuinn et al. *Observational Constraints on Red and Blue Helium Burning Sequences.* (2011). Astrophys. J.740 48. 48, 88

[116] M. Giannotti A. Friedland and M. Wise. *Constraining the Axion-Photon Coupling with Massive Stars.* (2013). Phys. Rev. Lett. 110 061101. 48, 88

[117] P. Sikivie. *Experimental Tests of the Invisible Axion.* (1983). Phys. Rev. Lett. 51, 1415. 49, 50

[118] K. vanBibber et al. *Design for a practical laboratory detector for solar axions.* (1989). Phys. Rev.D 39 2089. 49, 58

[119] D. M. Lazarus et al. *A Search for solar axions.* (1992). Phys. Rev. Lett. 69 2333. 49

[120] S. Moriyama et al. *Direct search for solar axions by using strong magnetic field and X-ray detectors.* (1998). Phys.Lett. B 434 I.1–2, 147-152. 49, 66

[121] Y. Inoue et al. *Search for sub-electronvolt solar axions using coherent conversion of axions into photons in magnetic field and gas helium.* (2002). Phys.Lett. B 536 18-23. 49, 66

[122] K. Zioutas et al. *A decommissioned LHC model magnet as an axion telescope.* (1999). Nucl. Instrum. Meth. A 425 480. 50, 61

[123] S. J. Asztalos et al. *Improved RF cavity search for halo axions.* (2014). Phys. Rev. D 69, 011101. 50, 51

[124] B. M. Brubaker et al. *First Results from a Microwave Cavity Axion Search at 24 μeV.* (2017). Phys. Rev. Lett. 118, 061302. 51

[125] B. T. McAllister et al. *The ORGAN Experiment: An axion haloscope above 15 GHz.* (2017). Physics of the Dark Universe 18 67-72. 51

[126] J. Redondo and A. Ringwald. *Light shining through walls.* (2011). Contemp. Phys. 52 211. 51

[127] (OSQAR Collaboration) R. Ballou et al. *New exclusion limits on scalar and pseudoscalar axionlike pbooks from light shining through a wall.* (2015). Physical Review D 92, 092002. 52

[128] K. Ehret et al. *New ALPS Results on Hidden-Sector Lightweights.* (2010). Phys. Lett. B 689 149. 52

[129] R. Bahre et al. *Any Light Pbook Search II – Technical Design Report.* (2013). JINST 8 T09001. 52

[130] (BFRT collaboration) G. Ruoso et al. *Limits on Light Scalar and Pseudoscalar Pbooks from a Photon Regeneration Experiment.* (1992). Z. Phys. C 56, 505. 52

[131] (PVLAS Collaboration) E. Zavattini et al. *New PVLAS results and limits on magnetically induced optical rotation and ellipticity in vacuum.* (2008). Phys. Rev. D. 77, 032006. 52

[132] E. A. Paschos et al. *A Proposal for solar axion detection via Bragg scattering.* (1994). Phys. Lett. B 323 367. 52

[133] (SOLAX Collaboration) F. T. Avignone et al. *Experimental Search for Solar Axions via Coherent Primakoff Conversion in a Germanium Spectrometer.* (1998). Phys. Rev. Lett. 81 5068. 52

[134] (DAMA/LIBRA Collaboration) R. Bernabei et al. *Search for solar axions by Primakoff effect in NaI crystals.* (2001). Phys. Lett. B 515 6. 52

[135] (COSME Collaboration). *Pbook Dark Matter and Solar Axion Searches with a small germanium detector at the Canfranc Underground Laboratory.* (2002). Astropart. Phys. 16 325. 52

[136] (CDMS Collaboration) Z. Ahmed et al. *Search for Axions with the CDMS Experiment.* (2009). Phys. Rev. Lett. 103 141802. 53

[137] E. Armengaud et al. *Axion searches with the EDELWEISS-II experiment.* (2013). JCAP 11, 067. 53

[138] Z. Krecak A. Ljubicic, D. Kekez and T. Ljubicic. *Search for hadronic axions using axioelectric effect.* (2004). Lett. B599 143–147. 53

[139] A. Kayunov A. Derbin, I. Drachnev and V. Muratova. *Search for solar axions produced by Compton process and bremsstrahlung using axioelectric effect.* (2012). JETP Lett. 95 379. 53

[140] A. Derbin et al. *Search for axioelectric effect of solar axions using BGO scintillating bolometer.* (2014). Eur. Phys. J. C 74:3035. 53

[141] (CAST Collaboration) S. Andriamonje et al. *Search for 14.4-keV solar axions emitted in the M1-transition of Fe-57 nuclei with CAST.* (2009). JCAP 0912 002. 53

[142] (Borexino Collaboration) G. Bellini et al. *Search for Solar Axions Produced in p(d; 3He)A Reaction with Borexino Detector.* (2012). Phys.Rev. D85 092003. 53

[143] D. Budker et al. *Cosmic Axion Spin Precession Experiment (CASPEr).* (2014). Phys. Rev. X 4 021030. 53

[144] J. Redondo. *Solar axion flux from the axion-electron coupling.* (2013). JCAP 1312 008. 56, 57

[145] et al. K. Barth. *CAST constraints on the axion-electron coupling.* (2013). JCAP 1305 010. 56, 85

[146] G. G. Raffelt. *Plasmon decay into low mass bosons in stars.* (1988). Phys. Rev. D 37 1356. 57

[147] (CAST Collaboration) S. Andriamonje et al. *An improved limit on the axion-photon coupling from the CAST experiment.* (2007). JCAP 0704:010. 57, 58, 59, 84

[148] M. H. Pinsonneault J. N. Bahcall and S. Basu. *Solar Models: current epoch and time dependences, neutrinos, and helioseismological properties.* (2001). Astrophys. J. 555, 990. 57

[149] M. H. Pinsonneault. J. N. Bahcall. *What do we (not) know theoretically about solar neutrino fluxes?.* (2004). Phys. Rev. Lett. 92 121301. 57

[150] I. G. Irastorza et al. *Towards a new generation axion helioscope.* (2011). JCAP 1106. 59, 60, 66

[151] L. Struder et al. *The European Photon Imaging Camera on XMM-Newton: The pn-CCD camera.* (2001). Astron. Astrophysics 365 L18. 63

[152] S. Cebrian et al. *Background study for the pn-CCD detector of CERN Axion Solar Telescope.* (2007). Astropbook Astrophysics 28 205. 63

[153] D. Autiero et al. *The CAST time projection chamber.* (2007). New J. Phys. 9 171. 63

[154] J. Castel et al. *Background assessment for the TREX Dark Matter experiment.* (2018). arXiv:1812.04519 [astro-ph.IM]. 63, 94, 97, 98, 149, 163

[155] F.Aznar et al. *A Micromegas-based low-background x-ray detector coupled to a slumped-glass telescope for axion research.* (2015). JCAP12, 008. 64, 70, 108, 241

[156] M. Chefdeville et al. *An electron-multiplying 'Micromegas' grid made in silicon wafer post-processing technology.* (2006). Nucl. Instrum. Meth. A 556 490. 64

[157] X. Llopart et al. *Timepix, a 65k programmable pixel readout chip for arrival time, energy and/or photon counting measurements.* (2007). Nucl. Instr. Meth. Phys. Res. A 581, 485-494. 64

[158] C. Krieger et al. *An InGrid based Low Energy X-ray Detector.* (2014). Proceedings of the 10th Patras Workshop on Axions, WIMPs and WISPs 147-150. 64

[159] M. Kuster et al. *The X-ray Telescope of CAST.* (2007). New J. Phys. 9, 169. 64, 130

[160] J. Altmann et al. *Mirror system for the German x-ray satellite ABRIXAS: I. Flight mirror fabrication, integration, and testing.* (1998). Proc. SPIE 3444 350. 64

[161] (CAST Collaboration) K. Zioutas et al. *First results from the CERN Axion Solar Telescope (CAST).* (2005). Phys. Rev. Lett. 94, 121301. 65

[162] (CAST Collaboration) E. Arik et al. *Probing eV-scale axions with CAST.* (2009). JCAP 0902 008. 65

[163] (CAST Collaboration) S. Aune et al. *CAST search for sub-eV mass solar axions with 3He buffer gas.* (2011). Phys. Rev. Lett. 107, 261302. 65

[164] (CAST Collaboration) M. Arik et al. *CAST solar axion search with 3He buffer gas: Closing the hot dark matter gap.* (2014). Phys. Rev. Lett. 112, 091302. 65, 66

[165] (CAST Collaboration) M. Arik et al. *New solar axion search in CAST with 4He filling.* (2015). Phys.Rev. D92 no.2, 021101. 65

[166] H. H. J. ten Kate. *The atlas superconducting magnet system at the large hadron collider.* (2008). Physica C 468, no.15-20 2137–2142. 69

[167] F. A. Harrison et al. *The nuclear spectroscopic telescope array (NuSTAT) high-energy x-ray mission.* (2013). Astrophysical Journal 770 103. 70

[168] et al. I.G. Irastorza. *Gaseous time projection chambers for rare event detection: results from the T-REX project. I. Double Beta decay.* (2016). JCAP 1601 01, 033. 73, 94

[169] et al. I.G. Irastorza. *Gaseous time projection chambers for rare event detection: Results from the T-REX project. II. Dark matter.* (2016). JCAP 1601 01, 034. 73

[170] J. Kaminski C. Krieger, K. Desch and M. Lupberger. *Operation of an InGrid based X-ray detector at the CAST experiment.* (2018). EPJ Web Conf. 174 02008. 74

[171] C. Enss A. Fleischmann and G. Seidel. *Metallic Magnetic Calorimeters.* (2009). Enss C. (eds) Cryogenic Pbook Detection, pp 151-216. Topics in Applied Physics, vol 99. Springer, Berlin, Heidelberg. 74

[172] L. Gastaldo S. Kempf, A. Fleischmann and C. Enss. *Physics and applications of metallic magnetic calorimeters.* (2018). Journal of Low Temperature Physics 193 no. 3 365–379. 74

[173] S. Pirro and P. Mauskopf. *Advances in Bolometer Technology for Fundamental Physics.* (2017). Ann. Rev. Nucl. Part. Sci. 67 161–181. 74

[174] D. Poda and A. Giuliani. *Low background techniques in bolometers for double-beta decay search.* (2017). Int. J. Mod. Phys. A32 no. 30, 1743012. 74

[175] L. Ravera et al. *The X-ray Integral Field Unit (X-IFU) for Athena.* (2014). Space Telescopes and Instrumentation 2014: Ultraviolet to Gamma Ray 91442L. 74

[176] B. Cabrera. *Introduction to TES Physics.* (2008). Journal of Low Temperature Physics 151 82–93. 74

[177] (IAXO Collaboration). *BabyIAXO Experiment Proposal to the DESY PRC.* (2019). 74

[178] F. Jansen et al. *XMM-Newton observatory. I. The spacecraft and operations.* (2001). Astron. Astrophys. 365 L1–L6. 77

[179] M. Civitani et al. *Cold and Hot Slumped Glass Optics with interfacing ribs for high angular resolution x-ray telescopes.* (2016). Ultraviolet to Gamma Ray, vol. 9905 of Proceedings of the SPIE, p. 99056U. 78

[180] T. Schiffer. *GridPix detector and ultra thin window developement.* (2019). Talk given at 9th General IAXO Coll. Meeting. 80

[181] S. Anvar et al. *AGET, the GET Front-End ASIC, for the readout of the Time Projection Chambers used in Nuclear Physic Experiments.* (2011). IEEE Nuclear Science Symposium Conference Record, NP2.S-65, 745. 81, 104, 193, 195

[182] D. Costa D. Gascon J. Mauricio C. Cogollos, E. Picatoste and J. Miralda. Radiopure electronics for the micromegas detector for iaxo, (2019). Poster for the 15th Patras Workshop on Axions, WIMPs and WISPs. 81, 253

[183] X. Chen et al. *PandaX-III: Searching for neutrinoless double beta decay with high pressure136Xe gas time projection chambers.* (2017). Sci. China Phys. Mech. Astron. 60 no. 6, 061011. 81

[184] C. O. Heinke and W. C. G. Ho. *Direct Observation of the Cooling of the Cassiopeia A Neutron Star.* (2010). Astrophys. J. 719 L167–L171. 88

[185] C. O. Heinke W. C. G. Ho P. S. Shternin, D. G. Yakovlev and D. J. Patnaude. *Cooling neutron star in the Cassiopeia A supernova remnant: Evidence for superfluidity in the core.* (2011). Mon. Not. Roy. Astron. Soc. 412 L108–L112. 88

[186] J. Redondo A. Ringwald M. Giannotti, I. G. Irastorza and K. Saikawa. *Stellar Recipes for Axion Hunters.* (2017). JCAP 1710 no. 10, 010. 88

[187] J. Redondo M. Giannotti, I. Irastorza and A. Ringwald. *Cool WISPs for stellar cooling excesses.* (2016). JCAP 1605 no. 05, 057. 88

[188] L. Verde J. L. Bernal and A. G. Riess. *The trouble with H0.* (2016). JCAP 1610 no. 10, 019. 88

[189] (CMB-S4 Collaboration) K. N. Abazajian et al. *CMB-S4 Science Book, First Edition.* (2016). arXiv:1610.02743 [astro-ph.CO]. 88

[190] R. Z. Ferreira and A. Notari. *Observable windows for the QCD axion through N_{eff}.* (2018). arXiv:1801.06090 [hep-ph]. 88

[191] F. Takahashi R. Daido and W. Yin. *The ALP miracle: unified inflaton and dark matter.* (2017). CAP 1705 no. 05, 044. 88

[192] F. Takahashi R. Daido and W. Yin. *The ALP miracle revisited.* (2017). arXiv:1710.11107 [hep-ph]. 88

[193] S. Aune et al. *Low background x-ray detection with Micromegas for axion research.* (2014). JINST 9, P01001. 92, 93, 94, 99, 102, 103, 108

[194] G. Luzon et al. *Characterization of the Canfranc underground laboratory: Status andfuture plans.* (2006). Proceedings, 6th International Workshop on The identification of dark matter (IDM). 92

[195] F.J. Iguaz et al. *Characterization of microbulk detectors in argon and neon based mixtures.* (2012). JINST, 7:P04007. 94, 204

[196] F. Aznar et al. *Assessment of material radiopurity for Rare Event experiments using Micromegas.* (2013). JINST 8, C11012. 94

[197] S. Cebrian et al. *Radiopurity of Micromegas readout planes.* (2011). Astropart. Phys. 34, 354. 94

[198] A.S. Barabash et al. *The BiPo-3 detector for the measurement of ultra low natural radioactivities of thin materials.* (2017). JINST 12, P06002. 94

[199] J. F. Ziegler. *Terrestrial cosmic rays.* (1996). IBM Journal of Research and Development, Volume 40, Issue 1, pp. 19-39. 95, 149, 157, 159

[200] S. Cebrian. *Cosmogenic activation of materials.* (2017). International Journal of Modern Physics A, Vol. 32, No. 30, 1743006. 96, 97

[201] G.Heusser. M. Laubenstein. *Cosmogenic radionuclides in metals as indicator for sea level exposure history.* (2009). Applied Radiation and Isotopes 67, 750–754. 96

[202] S. Cebrian et al. *Cosmogenic activation in germanium and copper for rare event searches.* (2010). Astropart. Phys. 33, 316–329. 96

[203] C. Zhang et al. *Cosmogenic activation of materials used in rare event search experiments.* (2016). Astropbook Physics Volume 84, Pages 62-69. 96

[204] Yu.N. Shubin et al. Mendl-2: Neutron reaction data library for nuclear activation and transmutation at intermediate energies., (1995). https://www-nds.iaea.org/publications/iaea-nds/iaea-nds-0136.htm. 96

[205] R. Silberberg and C. H. Tsao. *Partial Cross-Sections in High-Energy Nuclear Reactions, and Astrophysical Applications. I. Targets With z <= 28.* (1973). Astrophysical Journal Supplement, vol. 25, p.315-333. 96

[206] S. Agostinelli et al. *GEANT4-a simulation toolkit.* (2003). Nucl. Instr. and Meth. A 506:250–303. 96, 112, 117

[207] J.J.Back and Y.A.Ramachers. Activia: Calculation of isotope production cross-sections and yields., (2008). Nucl. Instrum. Meth A. 586, 286. http://universityofwarwick.github.io/ACTIVIA/. 96

[208] I. Coarasa et al. *Cosmogenic and primordial radioisotopes in copper bricks shortly exposed to cosmic rays.* (2016). Journal of Physics: Conference Series 718 (2016) 042049. 96

[209] L.P. Ekstrom S.Y.F. Chu and R.B. Firestone. The lund/lbnl nuclear data search., (1999). http://nucleardata.nuclear.lu.se/toi. 97, 135

[210] F. Calaprice et al. P. Benetti. *Measurement of the specific activity of ^{39}Ar in natural argon.* (2007). Nuclear Instruments and Methods in Physics Research Section A: Accelerators, Spectrometers, Detectors and Associated Equipment, 574(1):83-88. 97, 149, 166, 183

[211] J. Amare et al. *Cosmogenic production of tritium in dark matter detectors.* (2018). Astropbook Physics 97 96-105. 97

[212] S. Nisi et al. *ICP-MS measurement of natural radioactivity at LNGS.* (2017). International Journal of Modern Physics A, Vol. 32, No. 30, 1743003. 98

[213] J. G. Garza et al. *X-ray detection with Micromegas with background levels below 10-6 keV-1cm-2s-1.* (2013). JINST 8, C12042. 100, 101, 104, 199

[214] D. Calvet et al. *AFTER, an ASIC for the Readout of the Large T2K Time Projection Chambers.* (2008). Nuc. Science, IEEE Trans. 55, 1744. 103, 104, 193

[215] J. Santiard et al. *Gasplex: A Low noise analog signal processor for readout of gaseous detectors.* (1994). CERN-ECP-94-17. 104

[216] J. Galan. *A data analysis and simulation framework for micropatterned readout detectors.* (2016). 8th symposium on large TPCs for low-energy rare event detection. 104

[217] Rest: Rare event searches with tpcs framework. https://sultan.unizar.es/rest/index.html. 112

[218] Root data analysis framework. https://root.cern.ch. 112

[219] J. Allison et al. *GEANT4 developments and applications.* (2006). IEEE Transactions on Nuclear Science, 53:270–278. 112, 117

[220] (GEANT4 Collaboration). Physics reference manual., (2005). http://geant4.cern.ch. 112, 117

[221] Garfield++: simulation of tracking detectors. https://garfieldpp.web.cern.ch/garfieldpp. 112

[222] W. Pokorski G. Santin. R. Chytracek, J. McCormick. *Geometry Description Markup Language for Physics Simulation and Analysis Applications.* IEEE Trans. Nucl. Sci., Vol. 53, Issue: 5, Part 2, 2892-2896. http://lcgapp.cern.ch/project/simu/framework/GDML/gdml.html. 117

[223] P. L. Bartlett and A. T. Stelbovics. *Calculation of electron-impact total-ionization cross sections.* (2002). Physical Review A 66, 012707. 129

[224] J.A. Garcia. *Solar Axion search with Micromegas Detectors in the CAST Experiment with 3He as buffer gas.* (2015). PHD Thesis, Universidad de Zaragoza, http://zaguan.unizar.es/record/31618. 130

[225] P. Abbon et al. *The Micromegas detector of the CAST experiment.* (2007). New Journal of Physics 9(6). 130

[226] P. Abbon et al. *Micromegas for Axion Search and Prospects.* (2007). Journal of Physics Conference Series 65(1):012010. 130

[227] Cristina Margalejo Blasco. *Modelo de fondo para IAXO-D0, prototipo del experimento IAXO (International AXion Observatory).* (2018). http://zaguan.unizar.es/record/76133. 148, 149, 164, 180, 181, 252

[228] Peter K. F. Grieder. *Cosmic rays at Earth, researcher's reference manual and data book.* (2001). Elsevier. 149, 150, 154, 159

[229] J. Matthews J.J. Beatty and S.P. Wakely. *Pbook Data Group.* (Revised October 2017). http://pdg.lbl.gov/2017/reviews/rpp2017-rev-cosmic-rays.pdf. 150, 154

[230] P. F. Smith and J. D. Lewin. *Dark Matter Detection*, volume 187. (1990). 159

[231] M.M Be. V. Chiste. Lne - lnhb/cea table de radionucleides, (2006). http://www.nucleide.org/DDEP_WG/Nuclides/U-238_tables.pdf. 163

[232] E.M. Gullikson B.L. Henke and J.C. Davis. *X-ray interactions: photoabsorption, scattering, transmission, and reflection at E=50-30000 eV, Z=1-92.* (1993). Atomic Data and Nuclear Data Tables Vol. 54 (no.2), 181-342 http://henke.lbl.gov/optical_constants/. 189

[233] D. Calvet. *A New Versatile and Cost Effective Readout System for Small to Medium Scale Gaseous and Silicon Detectors.* (2013). Nuclear Science Symposium and Medical Imaging Conference (NSS/MIC), IEEE. 82. 195

[234] D. Calvet. *FEMINOS Card. User's Manual.* (2015). Version 2.12. 196

[235] S. Cebrian et al. *Radiopurity assessment of the energy readout for the NEXT double beta decay experiment.* (2017). JINST 12 T08003. 252